UNIVERSITY OF SOUTHAMPTON

FACULTY OF PHYSICAL SCIENCES AND ENGINEERING

Electronics and Computer Science

Characterisation of Droplet-Compartmentalised Chemical Oscillator Networks Using Computer Vision

by

Kai Ming, Chang

Thesis for the degree of Doctor of Philosophy

February 2018

Supervisors: **Dr Maurits de Planque**

Dr Klaus-Peter Zauner

ABSTRACT

The challenge of overcoming limitations in computing technology drives the development of unconventional computing materials and architectures. Microfluidic and droplet-in-oil technology is a field of study that allows a large number of communicating chemical droplets of different compositions to be efficiently produced as a new form of engineering and computing substrate. To develop this technology, this project utilises the Belousov-Zhabotinsky (BZ) chemical oscillator of different compositions as aqueous droplets in an asolectin in hexadecane system. Previous studies were limited to structured homogeneous solutions and emulsions or to arrays of micrometre-sized droplets of identical composition. In comparison, this project uses millimetre-sized droplets enabling wave patterns to be observed while using droplets of different compositions coupled in different topologies. These droplet array topologies are defined using laser-cut acrylic (PMMA) with complex designs. This allows the effect of changing individual BZ components to be observed over many repeats and in different topologies. Wave characteristics of different BZ droplet compositions are statistically analysed over many repeats with computer vision techniques. Changing H_2SO_4, $NaBrO_3$, malonic acid and ferroin concentrations changes the oscillation lifetime, frequency and total wave count as well as the amplitude and area of each peak. When droplets are coupled in arrays of more than one droplet, wave sources are formed at droplet interfaces but without wave propagation through the interface and no change to wave characteristics. If the coupled droplet becomes exhausted, the wave source at that interface disappears and other wave sources become dominant. To study wave propagation through droplet interfaces, a BZ composition using both malonic acid and 1,4-cyclohexanedione is developed. These droplets have a shorter induction phase and waves that can propagate through droplet interfaces of at least 20 droplets over 55 mm. Arrays of up to 399 droplets are formed and stable for at least 4 hours. Microfluidic devices are important for future applications as they allow forming large networks of coupled droplets in different topologies to be scaled up and precisely controlled. To test the compatibility of BZ with polydimethylsiloxane (PDMS) microfluidic devices, BZ droplets were mixed in situ and observed in a millifluidic chip for at least 3 hours. These developments reveal opportunities to study and advance future applications of BZ or other chemical droplets in large arrays of coupled droplets for future applications in unconventional computing.

Table of Contents

List of Tables

List of Figures

Academic Thesis: Declaration Of Authorship

I, Kai Ming, Chang declare that this thesis and the work presented in it are my own and has been generated by me as the result of my own original research.

Characterisation of Droplet-Compartmentalised
Chemical Oscillator Networks Using Computer Vision

I confirm that:

1. This work was done wholly or mainly while in candidature for a research degree at this University;
2. Where any part of this thesis has previously been submitted for a degree or any other qualification at this University or any other institution, this has been clearly stated;
3. Where I have consulted the published work of others, this is always clearly attributed;
4. Where I have quoted from the work of others, the source is always given. With the exception of such quotations, this thesis is entirely my own work;
5. I have acknowledged all main sources of help;
6. Where the thesis is based on work done by myself jointly with others, I have made clear exactly what was done by others and what I have contributed myself;
7. Parts of this work have been published as:

   K. M. Chang, M. R. R. de Planque, and K. P. Zauner, "Fabricating millifluidic reaction-diffusion devices: Droplet-in-oil networks structured by laser cutting," in *2016 IEEE Symposium Series on Computational Intelligence (SSCI)*, 2016, pp. 1-7.

   K. M. Chang, M. R. R. de Planque, and K. P. Zauner, “Towards Functional Droplet Architectures: a Belousov-Zhabotinsky Medium for Networks,” unpublished.

Signed: .....

Date: .....

Acknowledgements

I would like to thank my supervisors Prof. Maurits de Planque and Prof. Klaus-Peter Zauner who gave crucial guidance and expertise throughout this project, as well as my predecessors Dr. Philip King and Dr. Gareth Jones for their guidance at the start of the project. I would also like to acknowledge the Future and Emergent Technologies Grant FP7-248992 “NEUNEU” from the European Union for funding my predecessors up to 2014 and getting this project started. Special thanks to Prof. George Attard and Dr. Srinanda Dasmahapatra for their advice during and after the viva sessions, as well as Prof. George Attard’s student, Duncan Parker, for his input on BZ chemical mixtures. I would also like to thank the members of the CHB lab for their patience and help, especially Dr. Prameen Kalikavunkal and Dr. Sumit Kalsi whom I have sought guidance from repeatedly, and Prof. Hywel Morgan for allowing the use of his labs. I would also like to thank Dave Batt and the ECS for providing the computers for this project and iSolutions for providing the research file store for storing the data. Many thanks also to my previous supervisors Prof. Jonathan Swingler, Prof. Ling Wang, Prof. Philippa Reed, Prof. Shuncai Wang and Prof. Nicholas Green as well as lab technician Tim Hartley for their help during my previous projects. Finally, I would like to thank my parents and family for their support throughout my life.

Abbreviations

1D = one dimensional

2D = two dimensional

3D = three dimensional

AOT = Aerosol OT system using dioctyl sulfosuccinate sodium salt

AU = Arbitrary Units

BZ = Belousov-Zhabotinsky

CHD = 1,4-Cyclohexanedione

Conc. = Concentration

MA = Malonic acid

MA-CHD BZ = Malonic acid and 1,4-Cyclohexanedione mixture Belousov-Zhabotinsky solution

Osc. = Oscillation

PDMS = polydimethylsiloxane

PMMA = acrylic / poly (methyl methacrylate)

v/v = volume in volume ratio

Chapter 1 Introduction

The challenge of advancing computing technology drives innovation in both manufacture and design. As this becomes more difficult due to limitations of the von Neumann architecture [1] and components reaching molecular size [2], there is an increasing interest to explore using different substrates and paradigms. This has resulted in the field of unconventional or non-classical computing technologies. Some use different methods of structuring traditional silicon-based circuits [3] and programming their software [4] while others use new substrates such as chemicals [4] and biomolecules [5]. These systems take advantage of interactions on the macro and microscopic level to produce parallel and distributed processing systems, which are more efficient at solving certain problems while having better fault tolerance and evolvability [4]. It is hoped that future advances in this field will allow the creation of systems that can mimic information processing methods in nature and biology as well as supplement existing electronics [6]. However, a common challenge for research in this field is that methods of compartmentalising the components while allowing communication needs to be developed alongside the mechanisms themselves so that their starting states and interactions can be purposefully positioned and controlled.

Compartmentalised reaction networks have certain reaction components in inhomogeneous distribution in a 1D, 2D or 3D geometry with engineered interfaces among the compartments. The nature of the chemicals, the coupling and the geometry of the network depend on the intended application. For these networks to function, it is essential that the chemicals in neighbouring compartments can interact with each other. In other words, these compartments need to be "coupled" and allowed to communicate. This requires barriers between these compartments, which could take a variety of forms and with varying degrees of connection efficiency and selectivity. Existing compartmentalisation methodologies include defining physical channels and wells in a substrate material, conjugating specific chemicals to defined regions in a microfluidic channel or on a paper strip, and immersing aqueous droplets in an oil phase. Among the transport methods used, diffusive coupling has the highest potential to be scaled up for larger networks required for functional architecture with hundreds or thousands of compartments. In such cases, active transport as in conventional microfluidics and lateral

flow assay applications is at present less feasible. For such diffusion-coupled systems, millimetre to micrometre scale provides practical timescales given typical molecular diffusion rates. Therefore, compartmentalisation methodologies that have been explored so far build on the progress in micromanufacturing. Most work to date concerns aqueous droplets in an oil phase where interdroplet diffusion implies transport over an interdroplet lipid bilayer, which could contain biological channels or pores. Modulating the coupling strength can be achieved either spatially or chemically. Aspects of diffusive coupling such as selectivity and spatial arrangement are essential for the development of diffusive reaction networks. This new field opens up possibilities for creating new devices for unconventional computing due to their good scalability and precision in making large numbers of droplets, which can have different behaviours for different effects when coupled together [7].

To contribute to the field of unconventional computing, this project studies using droplet-in-oil compartmentalisation for coupling oscillatory chemical reactions. Oscillatory chemicals allow interactions to be observed over many cycles for a longer time, and has more complex interactions giving richer behaviours. Droplet-in-oil compartmentalisation is chosen for this as it allows the compartment size to be scaled up and down as needed between the micro to millimetre scale. Additionally, when encapsulated in a lipid membrane, these droplets can form a semipermeable membrane, that only allows selective interaction between the chemicals they contain. These droplets also mimic the structure of living cells, which separate themselves from their environment with their own cell membrane while allowing certain interactions with the outside. This method of compartmentalisation is also flexible as future devices that can be scaled up in complexity or topographic size while allowing individual droplet components to be scaled down in physical size to the nanometre scale. This project focuses on contributing new information on these substrates for their eventual use in unconventional computing.

Specifically, the Belousov-Zhabotinsky (BZ) reaction is chosen as it is a well-studied system in reaction-diffusion computing, which utilises a chemical reaction's behaviour over time for computation [8]. Using BZ makes studying reaction-diffusion computing through droplet-in-oil compartmentalisation simpler as it has also been shown to couple between droplets through oil and lipid membranes and as free solutions [9]. It is also a relatively simple [10] and well-modelled mechanism [11] which can oscillate for a long time without

replenishing its chemical substrates [10, 12, 13]. The visual pattern formed also makes this reaction easier to observe and analyse while using the delicate and fragile droplet-in-oil compartmentalisation method, as no extra components such as electrodes are necessary to obtain measurements. As no measurement instruments are needed to be in direct contact with the mixture, disruptions to the observation can also be minimised. To use the BZ solution as the unconventional computing substrate, its mechanism of reaction, wave behaviour and other previous methods of using and manipulating these behaviours needs to be understood. Other methods of unconventional computing also offer insight into methods of implementing new computing substrates. Additionally, the field of droplet-in-oil compartmentalisation needs to be understood to determine the methods and challenges of implementing these systems for use in complex topologies for unconventional computing.

The BZ reaction forms a variety of patterns spontaneously due to interaction between the initial mixture of chemical species. This emergent pattern can be stationary such as Turing patterns or periodic over time and space, and can be controlled by the initial composition of the BZ solution as well as the BZ compartmentalisation [10, 14]. Historically, purely aqueous reactions were observed in well-stirred systems which could be influenced by injecting different ions [13]. Unstirred systems were also studied due to their ability to spontaneously form patterns [13]. These chambers can be selectively coupled using electrodes [15], through a porous membrane [16] or via capillary tubes [17]. Aerosol-OT systems are similar to unstirred systems, where the wave behaviour can be influenced by changing the BZ composition and ratio between aqueous mixture and oil, despite being a continuous unstructured system [12, 18]. When structure is imposed using shapes in polymer membranes [19] or projected light [8, 20], the wave paths and interactions are further controlled.

Droplet-in-oil compartmentalisation is a method that allows compartmentalisation of larger droplets of BZ mixture. These droplets can be coupled by having them in direct contact such that only their membranes separate them or even slightly further apart such that there is also a layer of hydrophobic medium such as oil in between, though only in micrometre scale distances. This additional method of coupling through oil is due to BZ releasing both aqueous and hydrophobic chemical species [10]. This means that droplet-in-oil compartmentalisation allows for the exploration of spatial topology, droplet

neighbours, lipid membrane and oil properties as additional factors that can influence the patterns formed from BZ oscillations [10, 12]. In the case of this project, droplets are considered “coupled” once they have touched each other in the droplet array and can no longer move, as the interface formed when they touch should have only a small separating distance and hence should allow interdroplet communication.

The large variety of these methods shows the robustness of this reaction despite individual compartments being scaled up and down in physical size. The variety of compartmentalisation and control techniques also allows for testing the scalability and complexity of topological structures that can be formed using droplet-in-oil compartmentalisation. However, most networks so far use relatively small sub-millimetre diameter droplets such that wave patterns cannot be observed. The arrays experimented with are also smaller with less than a dozen droplets each unless they are used in a petri dish of evenly spaced droplets without structure. Most methods also use droplets, free solutions or emulsions with homogeneous composition, so the effect of coupling droplets of different compositions and oscillation characteristics is not greatly studied [10].

To test the feasibility and stability of creating structured droplet networks, the droplets need to be observed in different states and wave behaviours interacting in networks of varying complexity. To allow such patterns and other behaviours to be observed, larger millimetre sized droplets are used as the droplet size is significantly larger than the wave width, so wave patterns can form instead of the droplets becoming uniformly oxidised and reduced as in smaller droplets. Using droplets of this size is also relatively novel, as most studies are conducted with continuous free solution, which has no physical barriers between compartments, or micrometre to millimetre sized droplets, which are observed to oxidise and reduce uniformly without wave pattern observations. Using larger droplets also allows droplets of different chemical composition to be more easily manipulated and tracked in a complex system, such that they can be placed in specific locations in droplet arrays to observe their effect on the wave patterns in the array. Using larger droplets may also reduce the surface area to volume ratio of the droplets, changing the quantity of intermediate species lost from the droplet to the surroundings.

As the droplets used are a larger size, it is not necessary to use highly accurate fabrication techniques such as clean room wet etching. Acrylic (PMMA) laser cutting is chosen as a

suitable fabrication method for this size range, with complex topographies able to be designed, fabricated and improved in a short time. These advantages are crucial for rapid-prototyping of these design topologies. Techniques of designing and fabricating these PMMA structures are developed as well as the methodology of using them for observing BZ arrays. A technique of producing multi-layer designs using this method is also developed and tested to allow designs with freestanding structures for “loop” designs. This method also tests the compatibility of PMMA with BZ droplets, which are acidic and produce many interacting intermediates to oscillate.

Once the substrate and fabrication methods are shown to be viable, methods of controlling the behaviour of these arrays could be analysed for future studies in using these substrates for unconventional computing. By characterising the effect of different droplet compositions and coupled neighbours, arrays could be designed with these couplings to produce a desired behaviour. Different droplet array topologies are also tested to determine the scalability and complexity of this technique for future use in unconventional computing. To do this, both linear and non-linear arrays are tested. Each experiment is also performed with several repeats of the same droplet array topology and composition to allow some statistical analysis of their behaviour to be performed. This is important as each repeat is slightly different despite identical initial conditions. This requirement is made easier by the large number of arrays that can be observed the same time using the PMMA laser cut structures.

As a very large quantity of data needs to be analysed, a technique of automating the analysis is also developed. Basic computer vision techniques are employed to extract fixed regions of interest based on their positions on the petri dish, smooth the frames to remove noise, select a colour channel for the highest contrast then to remove the background baseline and analyse the peaks of the graph obtained. Specifically, macros using ImageJ convert the images recorded into a space-time plot, which allows the wave direction, source and times to be presented in a single image. As some designs have multiple space-time plots that need to be analysed at a time, another macro was developed to stitch these different space-time plots into a single image to be compared. The pixel intensity at different parts of the space-time plot can be measured to produce a graph of the oscillations for each droplet in the array. Macros in Origin Lab then smooth the data, remove the background baseline, analyse the peaks in the graph and present the changes

to different parameters in graphs, which can be used to compare between different droplets for any interactions. Further macros are then developed to summarise and combine the wave data for several droplet analysis files for statistical analysis and summarised graphs. A more detailed explanation of these macros is shown in Section 3.8 and 3.9.

To determine their normal behaviour when used with this novel combination of PMMA and droplet-in-oil compartmentalisation, droplets of different malonic acid (MA) BZ composition in one-droplet arrays are first characterised. First, time-based phase changes are observed so that the optimum observation time of BZ arrays can be determined. Common behaviours between different droplets are identified. These phases of behaviour are then characterised quantitatively between single droplets of different composition in an effort to understand how changing each BZ component affects the oscillation behaviour. The characterisation studies for different droplet composition yielded results that could be used to manipulate droplet behaviours when coupled in arrays.

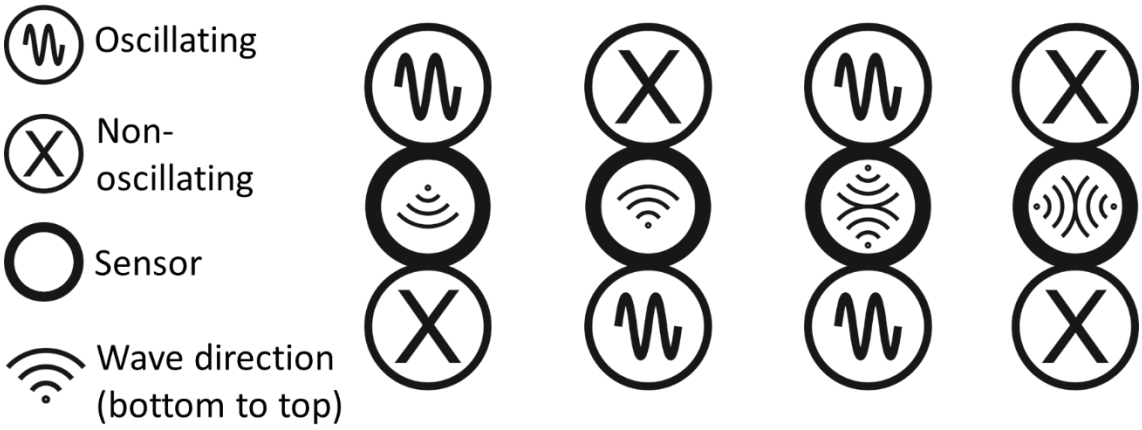

Figure 1.1 Schematic of BZ droplet-in-oil arrays of different behaviours and the result of their influence on the wave behaviour of a sandwiched “sensor” droplet. This is shown using real droplets in Section 6.2.

These droplets must then be tested in arrays of coupled droplets to determine the stability of the droplet interface bilayer, which is crucial to both coupling the droplets and maintaining the topology of arrays containing droplets of different compositions. With the challenge of creating stable droplets understood, the changes in wave pattern behaviour and the wave characteristics can then be performed and compared with their behaviour in

single droplets. To test if the understanding of the system is correct, arrays such as those shown in Figure 1.1 are created following the characterisation results previously obtained to see if the wave behaviour responds accordingly. While it is confirmed that waves do not propagate through droplet interfaces in MA BZ, significant differences in wave pattern behaviour can be observed.

BZ droplets using only malonic acid have waves that do not propagate through droplet interfaces. This limits the interactions between droplets of different composition and makes observing their behaviours in arrays more difficult. To solve this, a BZ composition using both malonic acid and 1,4-cyclohexanedione (CHD) is tested (MA-CHD BZ droplets). These droplets combine the advantages of both MA and CHD BZ, where they have a shorter induction time and have waves that propagate through droplet interfaces. As with MA BZ, MA-CHD BZ droplets are characterised as single droplets in different compositions, and then characterised as droplets in arrays to determine their stability in the droplet-in-oil system and effectiveness in producing oscillations that propagate through the droplet interface. Parameters such as the age of the CHD, ratio of MA to CHD and ferroin concentration are tested to give insight into its mechanism and their effects on wave propagation.

With this information, longer droplet arrays are tested to observe their long-term stability and push the limits of manipulating their behaviours. These arrays proved to be stable for 4 hours up to overnight, confirming that they can be used to observe the evolution of wave behaviour. This is shown in Figure 1.2. However, 1D topologies are not enough for future applications of this technology, so new topologies are developed to test the feasibility of using non-linear 2D topologies. A “Y-shaped” and “multiple Y-shaped” array is designed as this is a simple design combining many linear arrays, which also has a meeting point where a single droplet is coupled to two others are acute angles. The wave behaviour at these meeting points can also be observed for any unique effects. This is followed up with observing even more complex topologies such as BZ arrays structured into maze shapes, like in Figure 1.3, as well as into loops providing feedback, which provided even more complex observations that were difficult to analyse. Initial work is also done to use initiator droplets to form wave sources at specified locations of the array.

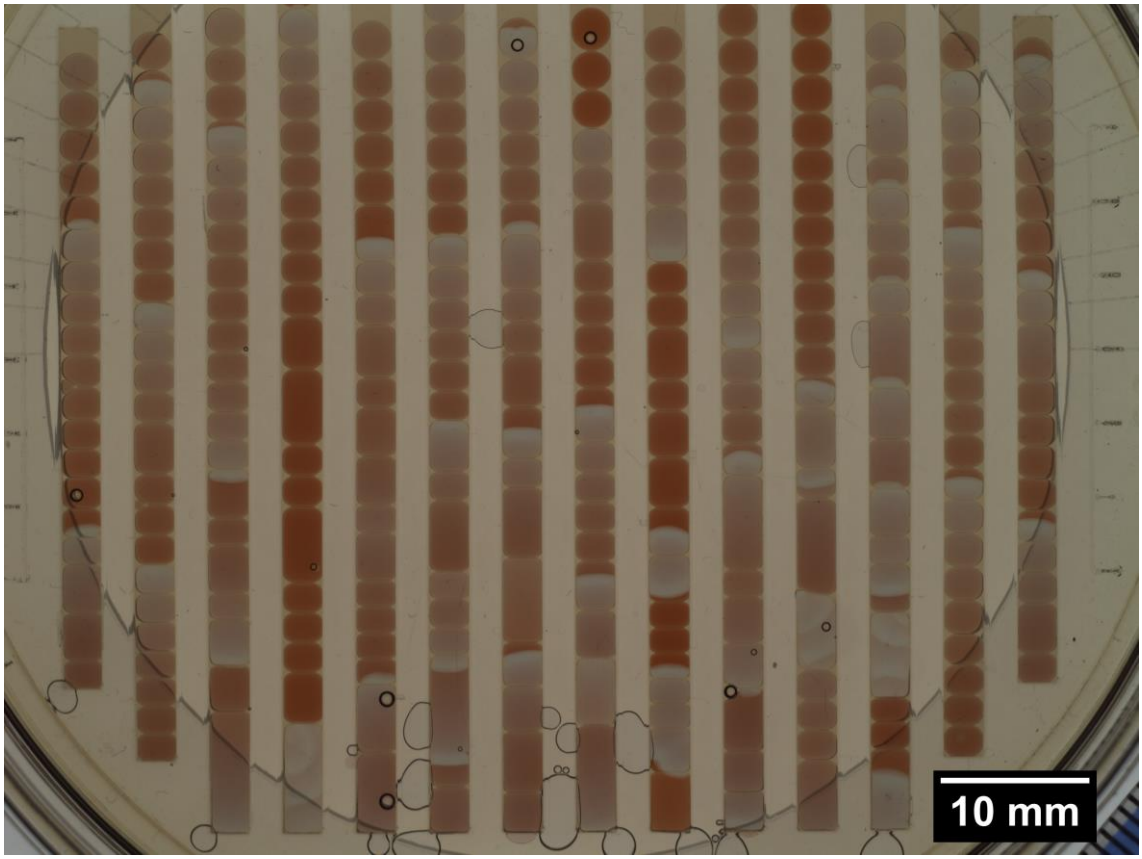

Figure 1.2 Arrays of 20+ MA-CHD BZ droplet droplets of identical composition with waves propagating through most droplet interfaces. Each droplet is 5 µl but some have fused to form larger droplets. Arrays structured using laser-cut PMMA in 90 mm petri dish. Arrays stable for 4-hour observation time. Image taken at approximately 2 hours after solutions mixed.

Initial work into analysing such complex topologies is developed in an effort to address the non-symmetrical and large number of meeting points. These features made the standard space-time plot techniques used for 1D arrays obsolete. A modification of the standard method uses the same ImageJ macro techniques to rotate the Y-shaped and “fish” structure arrays to obtain and stitch together the many space-time plots from the same array and to repeat this across multiple arrays of different orientations. However, this technique is not possible for extremely complex arrays such as mazes, so computer vision is applied to analyse the full image. The difference between images is calculated to remove the background and highlight wave fronts. The results are then fed into ImageJ’s built-in particle analyser, which uses optical flow techniques to automatically classify and track each wave while analysing their characteristics. While this initial work in computer vision

techniques is simplistic, it shows that further development of these techniques enables detailed analysis of wave features and patterns even in complex topographies.

Future networks need to be fabricated with very high reproducibility and in very high volume, so it would be necessary to eventually automate the process of mixing droplets of different compositions and positioning them in arrays of varying complexity. Microfluidic devices are effective at scaling up the production such droplet arrays and automating the process [21]. For this purpose, initial tests are performed in the millifluidic chip developed by King *et al.* in [22]. This allows large BZ droplets in arrays to be mixed in situ and observed to test their compatibility in polydimethylsiloxane (PDMS) microfluidic devices, which is non-trivial due to the acidic pH and many intermediates produced. Another problem to overcome when using large droplets as in this project is that BZ droplets produce CO_2 bubbles, which can destroy the array and disrupt observations. The chip fabrication is modified to accommodate these considerations and initial experiments with BZ droplets are carried out. These enabled the observation of stable BZ droplet arrays of up to 4 droplets in length for up to 5.5 hours with continuously flowing asolectin in hexadecane oil.

We conclude with Chapter 9 summarising the results of compartmentalising oscillating BZ droplet-in-oil arrays in complex topologies and observing droplet communication. Due to the large amount of generated video data, simple computer vision techniques are employed to characterise the wave behaviour, which is non-trivial as each droplet oscillates for many cycles that evolve over time. While stable arrays of interacting BZ droplets with complex topology can be formed, these same fabrication techniques are versatile and can be applied to other unconventional computing substrates. The initial work in confirming the compatibility of BZ droplets with simple PDMS microfluidic devices shows that future efforts in rapid-prototyping of microfluidic devices for studying BZ waves is viable. As such, future experiments in creating new unconventional computing devices and substrates can be devised to further develop the field.

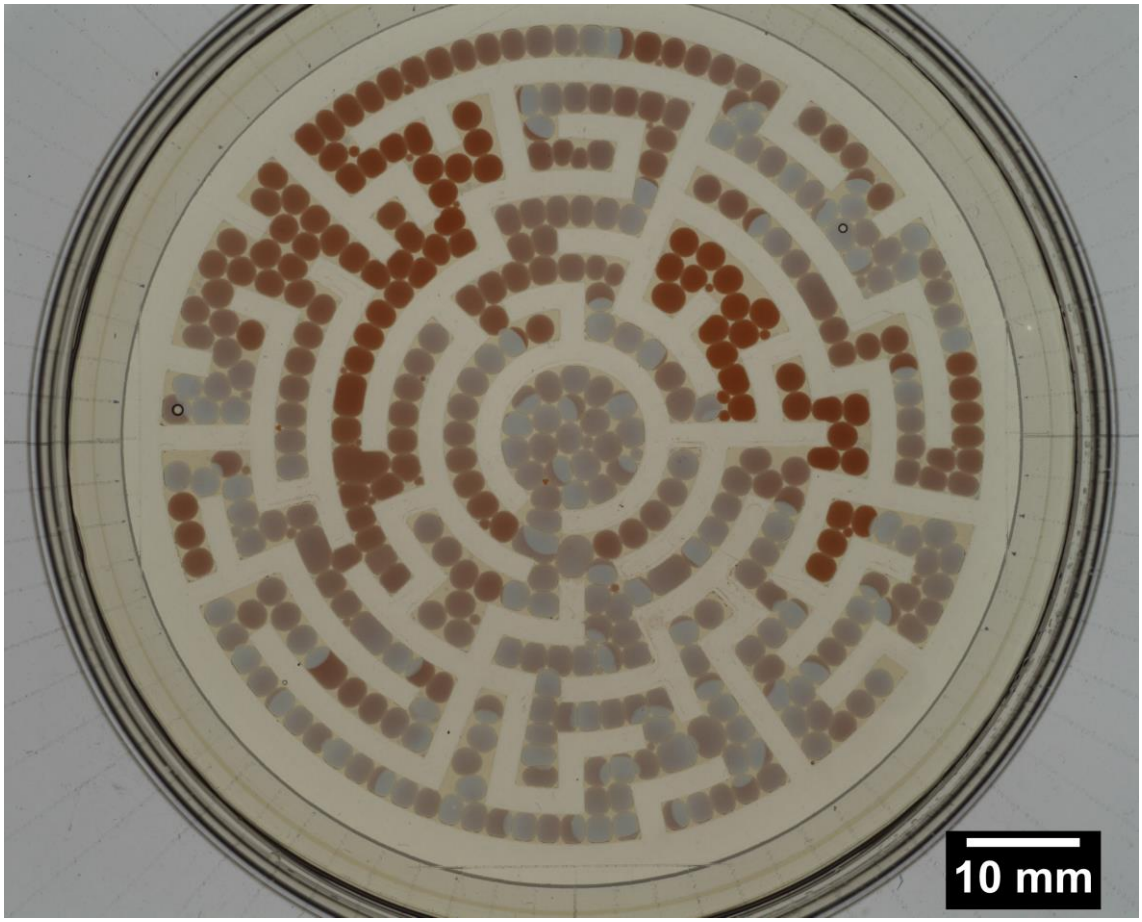

Figure 1.3 Circular maze array initially containing 399 MA-CHD droplets of identical composition, of which 376 remain unfused for a 94% survival rate. Waves observed to pass through most droplet interfaces. Image taken at approximately 2 hours after solutions mixed.

Chapter 2 Literature Review

2.1 Unconventional computing

In order to research the needs of a compartmentalised reaction network for unconventional computing, short review of classical computing and unconventional computing is done to insight into the advantages and disadvantages of unconventional computing as well as the solutions to the challenges faced when implementing such systems. The methodologies used in these other efforts can be studied to give insight into how development of a microfluidic version of this technology can proceed.

Alternatives to classical computing methods are sought in order to overcome challenges in advancing computing, especially as computing becomes more complex and decentralised. Improvements in classical computers can also be obtained when changing the structuring of the components from the conventional von Neumann architecture used, which is relatively inefficient when communicating between many interconnected distributed systems as it relies on a centralised and shared hardware for communication and memory. An alternative hardware structuring method proposed where smaller independent nodes contain their own dedicated memory and communication hardware, allowing them to process information without continuous communications with the centralised system [3]. Another method of improving classical computing is by using chemical programming methods, which utilise emergent behaviours from the interactions of individual components [4]. To further increase the complexity of computations, new components can also be implemented in existing architectures that can change the output. A component called the “memristor” was developed which autonomously changes the resistance of connections based on previous inputs, which is more efficient compared to calculating such inputs and outputs in the conventional method using many more components and instructions [23]. A common theme between these improvements to classical computing methods is the usage of smaller independent distributed nodes forming an emergent behaviour based on the node’s own rules instead of a large centralised system that needs constant communication.

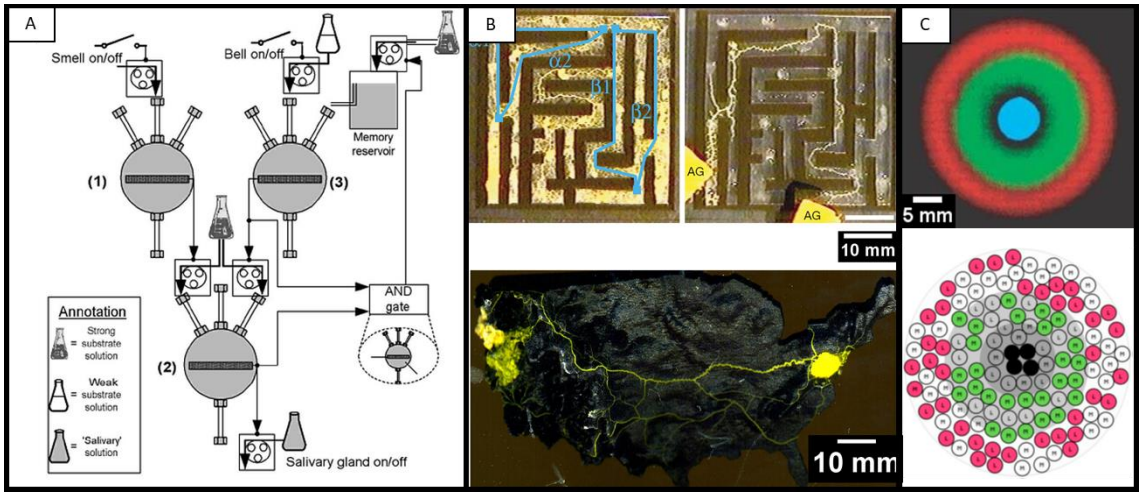

Figure 2.1 (A) Cells in separate chambers with different inputs such as food, temperature and CO_2. Reproduced from [24]. (B) Examples of how *Physarum polycephalum* is used to compute the shortest distance between two points. Maze image on top reproduced from [25] and 3D terrain of West-East USA shortest path image from [26]. (C) Example of how genetically modified cells produce colour pattern based on concentration of specific detected chemical and type of cell detecting chemical. Highest concentration at the middle of the ring. Reproduced from [27]. Schematic reproduced from [28].

Using these principles, several unconventional computing systems were previously developed using living cells. Cells inside growth chambers are coupled using electronic measurements of their living processes such as pH and CO_2 respiration. These measurements trigger other systems that increase the quantity of food and oxygen needed for the cells to grow, affecting their growth rate and hence their outputs (Figure 2.1 (A)) [24]. However, in this system the spatial positions of these chambers relative to each other is not matter. In other work, living cells were used where their positions relative to the environment or other cells would produce outputs for unconventional computing calculations. An example is when *Physarum polycephalum* slime moulds were used to calculate the shortest path through a maze. In this case, plastic was used to control where the mould was allowed to grow, forcing it to calculate its path towards a source of food (Figure 2.1 (B)) [25, 26, 29]. By projecting light at specific regions to inhibit growth, its peristaltic behaviour is changed and the robotic system using peristaltic measurements for control will autonomously change its behaviour [30, 31]. Efforts in structuring neuron cells caused changes the direction of their electrical signals [32, 33]. These previous examples all used identical cells with identical rules of behaviour. Further complexity was achieved

using cells when cells genetically engineered to produce different enzymes to react with the presence of a chemical. This development used both the spatial position of a chemical source and the different types of cells in different positions around this chemical source to produce colour changes that depend on the cells present (Figure 2.1 (C)) [27]. This achievement shows that behaviours that are even more complex can be achieved by controlling the rules of individual independent computing nodes at the same time as the inputs and spatial structure in networks [28].

However, using complex systems such as living cells is difficult to control as many independent variables can affect the outputs of the system. Living cells also need complex systems in order to regulate their environment to keep them healthy enough for use and may change in behaviour if unhealthy. Additionally, each cell may not have identical responses even within the same sample, causing significant differences in behaviour that may not be practical for a computing system that needs to be reproduced over many iterations. As such, one method is by using enzyme-based systems. Human-made substrates limit the number of inputs that can affect the output while improving the reproducibility of the system.

One such substrate is deoxyribonucleic acid (DNA) and ribonucleic acid (RNA), which allows specifically designed molecules to be made which only interact with their complementary counterpart. As many combinations could be made and allowed to interact in the same container without structuring, it is theorised that even very complex computational problems could be solved by diffusion processes alone [34]. Recent efforts allowed structured individual DNA molecules to detect chemical inputs to release medicines [35], act as a counter device [36] and guiding joints to structure the self-assembly of crystal structures [37, 38]. However, DNA is still a relatively new and expensive technology for fabricating and decoding these strands [39], such that it may not be practical for use in more complex computing systems yet.

A more established alternative is enzymes. Enzymes are proteins that have a specific “active site” shape meant to catalyse only specific reactions. This allows a small quantity to be reused over many iterations if recovered and for selective reactions to be performed even in a mixture with many different substrates. Enzymes have the advantage where they can be additionally controlled by coenzyme and inhibitor molecules, which increase or

decrease their activity respectively [40-42]. One current application is enzyme-linked immunosorbent assays (ELISA), which combine both enzymes and antibodies in order to detect specific antibodies to produce an output. As the enzymes are compartmentalised by attaching them to the surface of plastic plates, different solutions can be added without initiating the reaction and washed away, enabling multiple steps of the reaction to be performed [43]. Another application of enzyme computing includes injecting enzymes directly into a reaction chamber with unknown substrates, where only the correct sequence is able to trigger the logic gate sequence to form the final output [44]. Another application is to use the enzymes attached to pH sensitive polymers, which would autonomously stop and restart the reaction as the reaction is completed over many iterations [45].

A particularly interesting development in enzyme computing is in using droplet-in-water systems where each droplet has its own enzyme inside and is separated by a lipid membrane. This allows the relatively expensive enzymes to be concentrated but used in small quantities inside individual droplets. One of the three droplet coupled droplets has a membrane treated with α-hemolysin pores, and so allows lactose substrate to diffuse inside only that droplet. The lactase enzymes inside that droplet convert the lactose into glucose, which travels to the next droplet where glucose oxidase enzyme converts it into H_2O_2. H_2O_2 does not need α-hemolysin pores to diffuse into the final droplet, and so can enter to form the final fluorescent colour change in resorufin using the horseradish peroxidase enzyme. The membrane is particularly important as it allows a small quantity of enzyme and substrate to be used to produce a significant colour change, as both are concentrated only inside their respective droplets. Each droplet can also contain its own reaction conditions, making the specific reaction to occur inside even more efficient. Additionally, this shows that lipid membranes can be used to change the coupling of the system, producing behaviours that are even more complex. This is shown in Figure 2.2 (A) [46]. A short review of enzymes and their prices on Sigma-Aldrich was performed for future use but was not used and is shown in Appendix B.

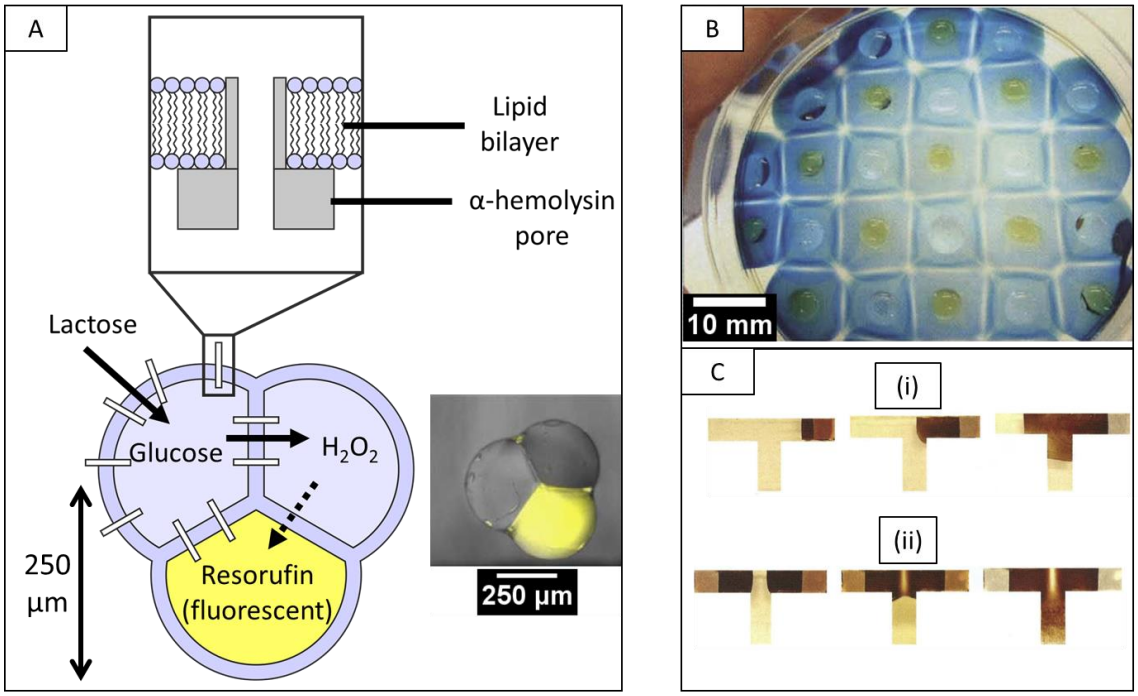

Figure 2.2 (A) Three water-in-water droplets containing different enzymes separated by lipid bilayers. Lipid bilayer restricts movement of large molecules such as enzymes, allowing them to be used in concentrated by small quantities. Membrane permeability changed by introducing α-hemolysin, allowing glucose and lactose to pass through only glucose droplet. Lactose converted into glucose by lactase enzyme. Glucose diffuses into another droplet to be converted into H_2O_2 by glucose oxidase enzyme. H_2O_2 diffuses through bilayer directly to third droplet containing horseradish peroxidase, which uses H_2O_2 to turn resorufin fluorescent. Inset is a photo of the real droplets. Reproduced based on [46]. (B) Voronoi diagrams of 1 cm squares computed from agar-palladium processors. Reproduced from [47]. (C) Palladium-iodide XOR-gate. In (i) only one input is received. In (ii) both inputs received, forming a pattern in the output in the centre. Reproduced from [48].

Enzymes are still relatively expensive substrates with a narrow and unique range of reaction conditions. Furthermore, many of the enzyme reactions need specific indicators to show that the reaction has completed, where not all enzymes work with those reaction conditions. This makes designing a system for computing using enzymes more complex and difficult as many factors need to be taken into account and can stop the reaction from occurring.

Chemical computing gives an alternative that is even less sensitive to environmental conditions and contaminants compared to enzymes. Chemical computing uses simple

chemical reactions to produce complex outputs. One method that was explored is using indicator displacement assays, which are relatively complex with specific indicator dyes bound to their molecular structure. These dyes are displaced only when a specific chemical analyte comes into contact, causing the surrounding solution to have a significant colour change [49, 50]. The variety of analytes that can be studied can be expanded by using specific antibodies or protein sequences [51]. This returns to the disadvantages of using enzymes and DNA, but shows its flexibility in being used in combination with other unconventional computing methods.

One disadvantage of the chemical computing methods described is that the reaction is complete once the colour change has occurred, and does not evolve over time or depending on the spatial positions of these substrates. The complexity of chemical computing can be increased using reaction-diffusion processes, where the concentration of reactants and products change over time and space, forming complex patterns and behaviours [52]. One such reaction-diffusion process uses the non-oscillatory palladium-iodide reaction. This reaction diffuses away from the source of iodide over time and forms a dark precipitate. When two waves meet, the reaction stops and a light coloured region is left at the meeting point. This is because the reaction consuming palladium in front of the dark colour, so there is not enough reactants to continue the reaction where two waves meet, demonstrating how the simple diffusion over time and space causes large effects to its final pattern [53]. Compartmentalising this reaction gives structure to the diffusion of the input reactants so that they can be made to meet at specified locations, further increasing the usefulness of this autonomous behaviour. A Voronoi diagram (Figure 2.2 (B)) [47] and XOR-gate (Figure 2.2 (C)) [48] computation was developed by only structuring where the starting reactants are and the paths of diffusion.

A subset of chemical computing uses oscillatory or “chemical clock” reactions. These reactions have an abrupt change in its appearance after a time, and can “oscillate” because the products formed are not in equilibrium [54]. As before, reactants and products diffuse away from their sources and interact, but these waves eventually disappear and the process restarts. Examples of these include the Vitamin-C clock [55], Bray-Liebhafsky reaction, BZ reaction Briggs-Rauscher reaction [56], arsenite-iodate-chlorite, chlorite-iodate-malonic acid (CIMA) and chlorine dioxide-iodate-malonic acid systems [57, 58]. In a system without structuring, the spatial patterns start at random locations and propagate

through the whole solution randomly. These patterns can be manipulated by changing factors such as the concentration of each reactant, the ratio between aqueous mixture and oil and properties of the oil and lipid membrane [58]. These studies are similar to that of the BZ reaction, which is a more widely studied reaction and the focus of this project.

By structuring these different substrates and using their unique properties, different computational problems were solved for their specific applications. A common theme is that these substrates calculate the inputs and outputs using their autonomous self-assembly when exposed to their environments. By structuring and compartmentalising these substrates, these already complex behaviours can be further controlled and concentrated in specialised regions. The benefits of this include simplifying the inputs, outputs or system designs, greater efficiency in operation, modifying the sequence of processes or even preventing processes from occurring.

2.2 Belousov-Zhabotinsky chemical reaction

Specifically, the Belousov-Zhabotinsky (BZ) reaction is chosen as it is a well-studied system in reaction-diffusion computing, which utilises a chemical reaction's behaviour over time for computation [8]. Using BZ makes studying reaction-diffusion computing through droplet-in-oil compartmentalisation simpler as it has also been shown to couple between droplets through oil and lipid membranes and as free solutions [9]. It is also a relatively simple [10] and well-modelled mechanism [11] which can oscillate for a long time without replenishing its chemical substrates [10, 12, 13]. The visual pattern formed also makes this reaction easier to observe and analyse while using the delicate and fragile droplet-in-oil compartmentalisation method, as no extra components such as electrodes are necessary to obtain measurements. As no measurement instruments are needed to be in direct contact with the mixture, disruptions to the observation can also be minimised. To use the BZ solution as the unconventional computing substrate, its mechanism of reaction, wave behaviour and other previous methods of using and manipulating these behaviours needs to be understood.

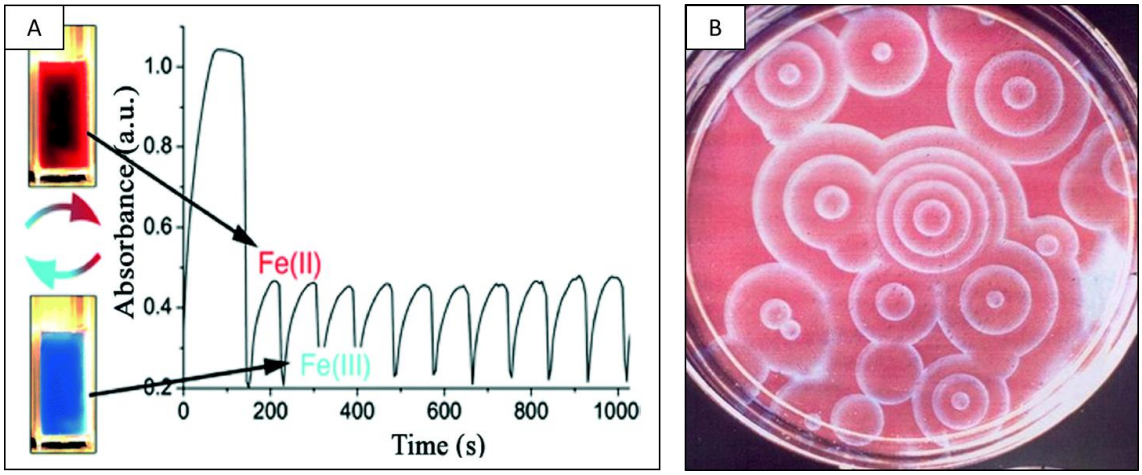

Figure 2.3 (A) The BZ reaction solution oscillates between red and blue colour over time. Reproduced from [10]. (B) Unstirred BZ reaction forming waves. Reproduced from [59].

The excitability of this reaction allows it to mimic natural systems such as neural networks and enable the construction and connection of logic gates using the waves formed [15, 60, 61], making it a suitable substrate for studying compartmentalised reaction networks for unconventional computing. The main components of the BZ reaction are acid, bromate oxidant, organic species reductant and metal catalyst. Of these, only the oxidant bromate (BrO_3^-) species is consistently used in the form of $NaBrO_3$ or $KBrO_3$, whereas the catalyst is varied using many metal complex ions with ligands such as Ce, Mn, Fe, Ru, Co, Cu, Cr, Ag, Ni and Os [62]. Sulphuric acid H_2SO_4 is the main acid used currently [63], though there are cases of using HNO_3 as well [64, 65]. Currently, malonic acid is the mainly used organic species reductant [63], but due to the CO_2 gas produced as the reaction occurs, alternatives have been researched. Some of these alternatives are also termed as “uncatalysed” because a catalyst is not required for the oscillatory reaction to occur, but it is added as an optical indicator to improve observations [66, 67]. One prominent alternative is 1,4-cyclohexanedione (CHD) which produces bubble-free reactions [68-71]. Other alternatives usually contain phenols, amines and aminophenols, while aliphatic amines and hydroxo compounds do not oscillate without a catalyst [72]. Many research groups use the recipe consisting of sulphuric acid, sodium bromate, sodium bromide, malonic acid and ferroin, though even these have variations in concentration [63].

This complex reaction is described by the Field-Körös-Noyes mechanism [73, 74]. This was simplified with the Oregonator model, which modelled both the reversibility of each

reaction and how a significant positive feedback can occur to amplify tiny perturbations of the steady state to initiate oscillations at the start of the reaction [54], but the effect of the total organic concentration on the magnitude of oxidised catalyst produced is much smaller than predicted [75]. Another alternative model is the Brusselator model that was used in one study for microscopic scales [76]. Both models predict the emergence of wave patterns that propagate via reaction-diffusion and have been used for computer simulations [76, 77]. A more detailed mechanism is the Gyorgyi-Turanyi-Field (GTF) model [11]. This is the most detailed mechanism consisting of 80 reaction equations and 26 components, which was later simplified to 42 reactions and 22 species [78, 79]. Each model is formulated for its own reactants and is modified and refined for new reactants and conditions. The Gao-Fösterling malonic acid (GaF-MA) model was modified to include the effect of oxygen inhibition on a cerium and malonic acid BZ mixture instead of ruthenium [80]. Another alternative model is the Missoula-Budapest-Marburg (MBM) model that predicts competition between bromination of malonic acid and the oxidation of bromomalonic and malonic acid. However, all models may not be able to predict the behaviour of BZ accurately, as there are still many reaction mechanisms that are unknown [81].

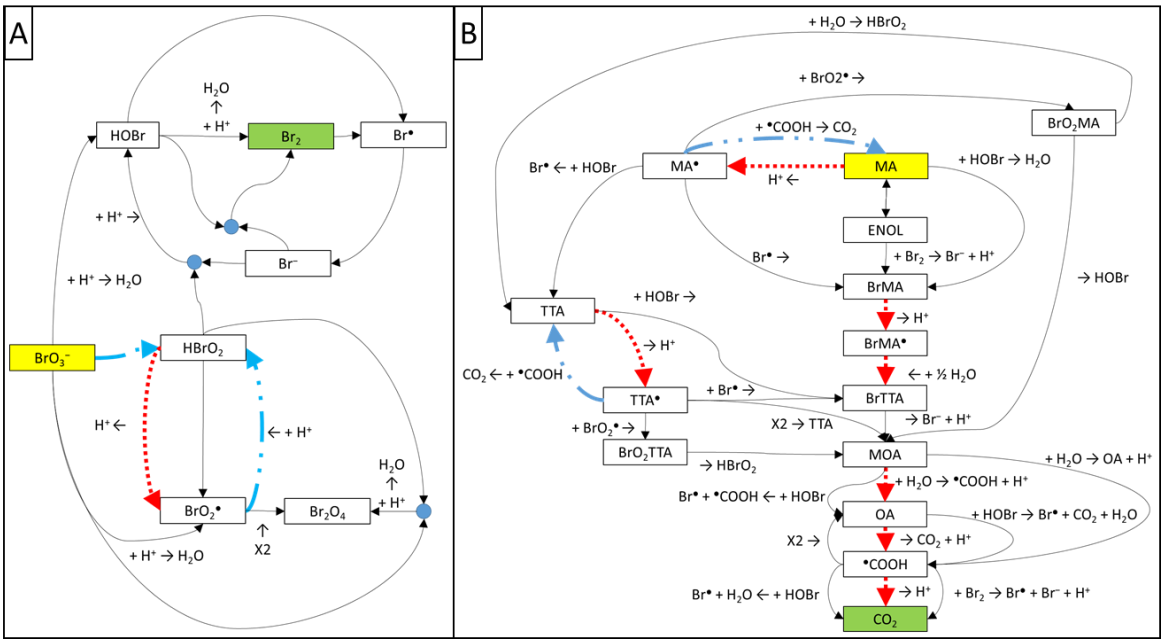

Figure 2.4 Illustration of MA BZ reactions based on 80 equation mechanisms [11]. BZ substrates shown in yellow and products removed from system shown in green. Red arrows denote reactions that reduce indicator while blue arrows denote reactions that oxidise indicator.

The processes are divided into Process A, B and C in the FKN mechanism, but are similar in the previously mentioned models. A simplified version of this reaction is shown in Figure 2.5 (B). In Process A, bromide has an initially high concentration and is consumed by acidified BrO_3^-, forming $HBrO_2$. When the bromide concentration is low enough, the system becomes unstable and the reaction switches to Process B. Now BrO_3^- switches to consuming $HBrO_2$, forming $BrO_2^\bullet$ free radicals. This oxidises the metal catalyst. After a delay, Process C starts, which reduces the catalyst back by consuming the organic component. This has the side effect of producing new bromide, which stops free radical production in Process B. This returns the solution to the state for Process A to start again by slowly consuming bromide and the cycle begins again [11, 54, 77, 82]. This corroborates with previous experimental evidence where electrodes were used to measure bromide and metal catalyst concentrations [74, 83, 84]. Diagrams of the reactions of MA BZ according to the 80-equation GTF mechanism are shown in Figure 2.4 (A) for the $NaBrO_3$ reaction and (B) for the reaction of the malonic acid. However, when the reaction is used with CHD instead of malonic acid, the CHD reaction proceeds as shown in Figure 2.5 (A), where it breaks down into benzoquinone which is soluble in oil and difficult to dissolve in water and 1,4-hydroquinone / 1,4-dihydroxybenzene which is easier to dissolve in water [71].

Changing the type of organic component, catalyst or compartmentalisation causes changes in the BZ behaviour. For the sake of brevity of this literature review, only the BZ catalyst, if a different organic component from MA is used, or if the effect is specific to BZ compartmentalised in gels is noted for Section 2.2. Less significant changes such as using HNO_3 for the H^+ source instead of H_2SO_4, using $KBrO_3$ instead of $NaBrO_3$ and the presence of a Br^- source such as KBr or NaBr are not noted. Changes in the concentrations of each component are also not noted as recipes differ between different studies [63].

BZ solutions tend to have an induction time when used with CHD (with ferroin) [71], but this is not present in free solutions of MA BZ used in ferroin [85]. However, if the MA BZ is used in gels (with ferroin) [64] or with other catalysts such as cerium [85], an induction phase exists. For cerium, this induction phase can take more than 20 minutes [11]. This is explained that for catalysts such as cerium, there is not enough energy released upon adding the catalyst to start the reaction initially. It is suggested that a certain concentration of bromomalonic acid is necessary to make the solution oscillatory [85].

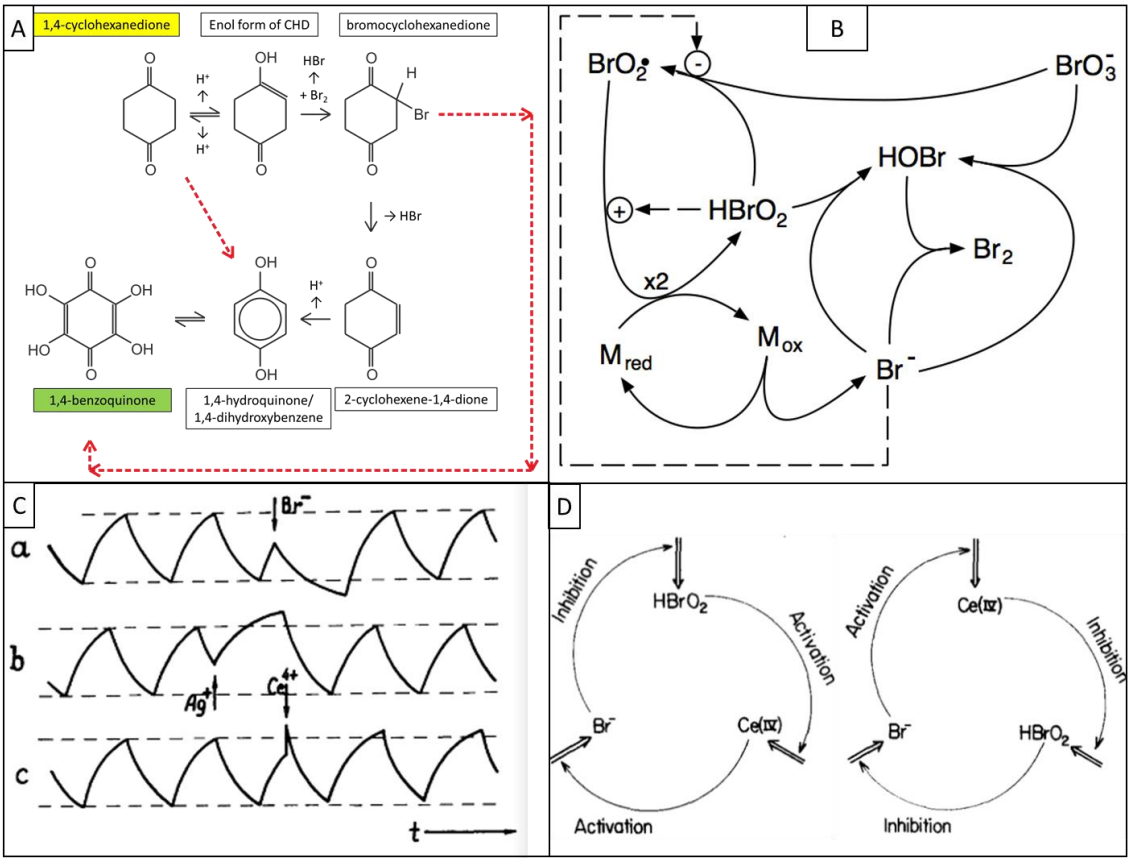

Figure 2.5 (A) Mechanism of decomposition of CHD in BZ solution. Red arrows denote reactions that reduce indicator solution. Based on [71]. (B) Simplified core scheme of BZ reaction. Reproduced from [86]. (C) Phase shifting of BZ solution by injecting bromide, silver and catalyst (cerium (IV)) ions into solution at different phases of the oscillation, where the "high" level is when the catalyst is oxidised. Reproduced from [87] and [13]. (D) Left shows the negative feedback loop where bromide acts as the inhibitor while hydrobromous acid acts as the initiator. Right shows the less likely positive feedback loop where catalyst acts as the inhibitor while bromide acts as the initiator, at conditions with low bromide. Reproduced from [54].

It is found that changing the concentration of H_2SO_4, $NaBrO_3$ and KBr, significantly different coupling behaviours are observed, from inhibitory to excitatory coupling (with ruthenium, but also seen with ferroin) [9, 88]. When acid concentration is increased, the induction time increases and the between waves is shorter (with ruthenium) [64], while wave front velocity increases (with ferroin) [75]. In one study, it is theorised that the wave speed is linked to both the concentration of acid and bromate. When acid concentration is increased the speed increases and the maximum wave speed also increases and only plateaus at very high total concentrations, or when the ratio of bromate is very high (with

cerium) [89]. When bromate concentration is increased, the induction time is increased, due to competition between bromination of malonic acid and oxidation of bromomalonic and malonic acid (with cerium) [81], and oscillation period reduced (with ruthenium) [64]. The wave speed also increases, but the maximum speed is limited when the acid concentration is limited (with cerium) [89]. Additionally, the oxidation magnitude of the catalyst is larger (with ruthenium) [65]. As malonic acid concentration is increased, the induction time is reduced (in gel with ruthenium) and the oscillation period at the start of the reaction is reduced (with ruthenium) [64] though the effect is not as large as that of bromate (with ruthenium) [65], and the period at the end of the lifetime is increased (with cerium) [79]. Increasing malonic acid concentration also decreases the oxidation magnitude of the catalyst (with ruthenium) [65]. As bromide concentration is increased, the rate for reaching the critical bromide concentration for induction reduces, so induction time increases (with cerium) [90]. This is explained with the previous models, where bromide is an inhibitor for the $HBrO_2$ autocatalytic cycle (Process B) (with ferroin) [91]. As the catalyst concentration increases, the accessibility of reactants increases, so the induction time is reduced (in gel with ruthenium) [64]. These intermediates can also be changed from activators to inhibitors and vice versa based on their initial concentrations as shown in Figure 2.5 (D).

Even when uniformly encapsulated in gels, the oscillation behaviour is changed in the case of ruthenium bipyridine ($Ru(bpy)_3$) catalysed BZ . It is observed that if BZ is encapsulated in microgel, the waveform of the oscillations is significantly affected by initial reactant concentrations. In free solution, the waveform does not change, but in microgels the time the catalyst stays oxidised increases, i.e. the wave peaks become wider as the concentration of acid or bromate is increased, and as the concentration of malonic acid is decreased [64]. This is possibly due to how the diffusion of substrates is limited in the gels, which plays a significant role in the oxidation and reduction of the catalyst. There is also a change in the period dependence on the initial substrate concentration [65]. The induction time increased compared to in free solutions and increases further as microgel cross-linking increases. This is possibly because the polymer cross-linking immobilised the catalyst molecules such that it is harder for reactants to interact with it, reducing its effective concentration. The oscillation period is also affected, where changes to the initial concentration of acid and bromate is found to have a smaller effect on the period

compared to when in free solution. Conversely, the initial malonic acid concentration has a larger effect on the frequency in microgel systems. This is speculated to be because process A has a shorter duration and process C longer, so bromate is the most effective reactant to use to control the oscillation period [64].

Other factors also affect the BZ reaction. For instance, wave velocity decreases as the temperature increases (with ferroin) [75]. Oxygen inhibition is studied and noted to only affect low cerium catalyst concentrations [80] or very shallow parts of BZ solutions (with ferroin) [92]. Stirring is observed not to have any effect in anaerobic conditions (with ferroin) [91]. However, it has an increased effect in reducing the induction time when the bromide concentration is high or bromate is low, because this decreases that rate at which bromide reaches its critical concentration for induction. There is also an increased effect for larger catalyst concentrations as this gives a larger fluctuation amplitude of critical concentration of intermediates while in nonequilibrium (with cerium) [90]. It is also observed that silver ions affect the solution as it lowers the bromide concentration, causing the critical concentration for induction to be reached faster (with cerium) [93]. Iodide ions (with cerium) [94], chloride ions and ethanol in concentrations of 0.07 M or greater can also be used to inhibit the system (with cerium) [74]. The oscillations are also affected by electrical and magnetic fields (with ferroin) [95, 96]. Additionally, light of 452 nm wavelength is known to inhibit propagation of waves in ruthenium-catalysed systems while 632.8 nm oxidises ferroin catalysed CHD systems [97]. Using a bathoferroinhexasulfonate catalyst causes oxidation waves to elongate the BZ droplet if placed on plexiglass substrate [98].

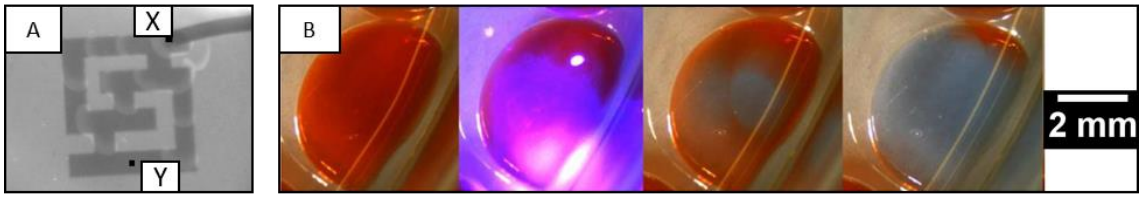

Figure 2.6 (A) Labyrinth shape projected using light on printed gel catalyst with initiation point by silver wire (top right and marked X) and waves moving to “output” point at Y. Reproduced from [8]. (B) A 402 nm wavelength laser light used to initiate wave in 5 mm diameter CHD droplet. Reproduced from [99].

These effects were exploited to control the BZ reaction. At first the BZ oscillations are disrupted by the addition of bromide, silver and oxidised catalyst ions. From these tests it is observed that bromide keeps the catalyst reduced, silver increases oxidation and the oxidised catalyst cerium disrupts the wave pattern. This method is used to shift the phase of the oscillation. The effect of these chemicals is shown in Figure 2.5 (C) (with cerium) [13]. This is expanded to couple two continuously stirred solutions in either an inhibitory or excitatory fashion (with cerium) [15]. Chloride ions and ethanol were used similarly as well (with cerium) [74]. A positively biased silver wire introduces silver ions to induce oscillations where it is connected, allowing control in both where the oscillations are induced and when using electrical signals (with ruthenium) [8]. A negative bias of -1.965 V is used to prevent the silver wire from initiating oscillations, then a pulse of +0.788 V is applied to stimulate them (with ferroin) [100]. Besides chemical methods, BZ were controlled with electric and magnetic fields to control where they are induced (with ferroin) [95, 96]. Finally, the ruthenium catalysed BZ was used with light of different wavelengths to induce or suppress oscillations [97]. Methods of controlling BZ using blue light projection and silver wire are shown in Figure 2.6.

Furthermore, coupling two BZ solutions has a potential of bringing even more unique behaviours. Using Oregonator and Brusselator simulations, the behaviours of how identical or non-identical BZ solutions couple can be estimated. In a two or more oscillator system, even if all are identical, “oscillation death” can occur. In this case, while all oscillators start at the same state, as time goes on the oscillators can eventually form an inhomogeneous steady state where all oscillators are in different states and remain in those states for the rest of the simulation (no catalyst specified) [101, 102].

When used in free aqueous solution in a petri dish, the profile of the wave at a specific time is that the wave front has a high amplitude while the oxidised parts behind the wave slowly reduce in amplitude as the solution becomes reduced again. The wave velocity is not significantly affected by the age of the solution, but the wave front amplitude and transmission increases as the solution ages. This is due to conversion of malonic acid into bromomalonic acid as well as the dissociation of ferroin in the acidic medium. This means that over time, the ferriin concentration also reduces and the ratio of ferroin to ferriin reduces [75]. Most traces of CHD BZ behaviour show that the amplitude of the oscillation reduces to zero if the solution is observed until it stops oscillating (with cerium) [103].

When observed in an unstirred batch reactor, it is observed that convection of the waves causes chaotic fluctuations in the wave frequency but also that it transitions from periodicity to chaos and back to periodicity. This effect is not observed in stirred batch reactors or containers with smaller volume (with cerium) [104].

Complex oscillations can be present due to the kinetic competition between the aromatic redox cycle and the redox of the catalyst. This causes the behaviour where the solution oscillates suddenly after some time in the reduced state and then stops. This cycle is repeated many times and is referred to as “bursting” oscillations. This is observed when phenol was added to a MA BZ system, and is hypothesised to be due to redox reactions of p-di-hydroxy-benzene and p-benzoquinone (with cerium) [105]. This complex behaviour is also observed in BZ solutions using both MA and CHD. These complex oscillations change in behaviour as the concentration of CHD is changed, where at lower and higher concentrations complex oscillations can be seen but at an intermediate concentration 2 mM CHD to 89 mM MA this is complex oscillation was not observed (with cerium) [103]. In acetylacetone with malonic acid BZ systems a significant transition can be observed as the solution changes between the reaction of one substrate with the other, where the solution turns colourless for a period of time before oscillating again (with manganese sulphate) [106]. In ascorbic acid with oxalic acid BZ systems, it is observed that when oxalic acid concentration is too low the oscillations stop, but oscillations are revived when enough oxalic acid is added (with cerium) [107].

These reaction mechanisms shows how future applications of the findings of this project can utilise combinations of these reaction control methods to produce unique behaviours even on the level of the reaction mechanism. It also gives insight into new chemicals that can be tested to interact with the complex reaction. This way, even without the compartmentalisation and structuring, complex behaviours and interactions can be formed.

2.3 Spontaneous patterns with BZ

Due of the mechanisms described previously, the BZ reaction forms unique patterns when left unstirred in a thin film solution with limited depth. This limited height and depth is important to ensure convection does not occur and 3D patterns do not form. The pattern generation mechanism is because the wave front consumes bromide as it travels forward, but once the solution is oxidised it produces a large amount of bromide stopping the oxidation process behind the wave. This also makes the region “refractory” as the high bromide stops any future oxidation until all the bromide is consumed. If another wave attempts to enter this refractory region, it is extinguished and the unique patterns from the wave interaction [108].

In free solutions, phase waves occur under a concentration gradient and trigger waves initiate in local sources. These waves them move away from the centre due to reaction-diffusion coupling [109]. These waves advance according to the Huygens principle as long as there are little curvature effects [19]. Waves generated at random locations travel outward from the original region and the original region eventually becomes reduced again. These are called circular trigger waves or “target” waves [18]. Waves that propagate continuously without a specific shape are called plane or planar waves [110, 111]. Spiral waves are also observed in free solution, where the centre tips of the spiral waves are observed to “meander” more if the bromate concentration increases. Existing waves can also spontaneously develop “turbulence”, which can break up existing waves and form new wave sources inside as shown in Figure 2.7 (A). This can happen due to delay in the inhibitor production [112]. This develops spontaneously from instability of the uniform state. Leading waves can also limit the speed of following waves as the region behind it is still in the refractory state and cannot oscillate [111]. It is possible to change the excitability of a ruthenium catalysed BZ system using pulses of light to “force” the oscillations. When the pulses are increased in frequency, more complex labyrinth patterns emerge. A lower frequency causes these complex patterns to break apart into larger localised structures over several hours, forming simpler and fewer shapes [113].

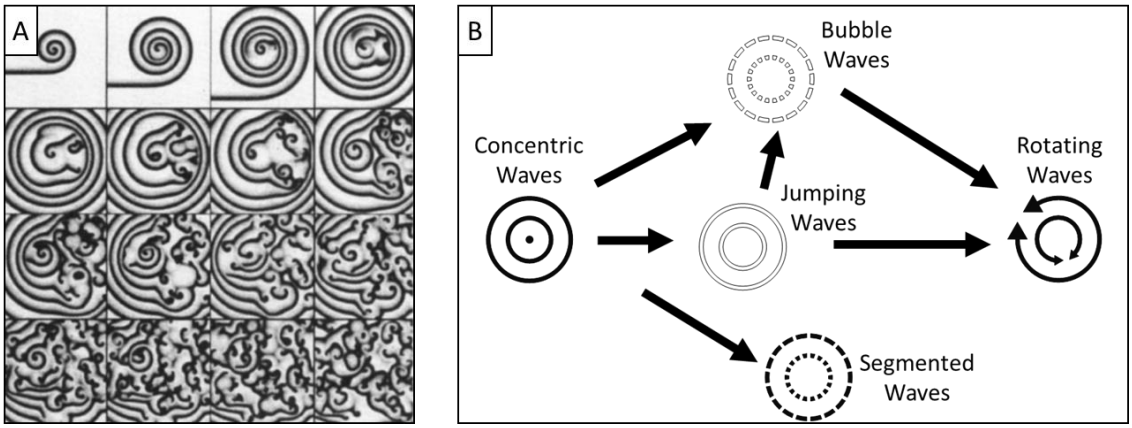

Figure 2.7 (A) Simulation of breakup of a spiral wave due to delay of inhibitor production. Reproduced from [112]. (B) Transformations of wave patterns in bathoferroin catalysed BZ AOT system: CWs, continuous trigger waves; SWs, segmented waves; JWs, jumping waves; BWs, bubble waves; and RWs, rotating waves. JW, BW, and RW are discontinuously propagating waves, while SW propagate smoothly. Reproduced from [18].

When these BZ solutions are mixed with oil via a phospholipid or surfactant, an emulsion of water in oil droplets is formed. A common emulsion system used in literature is the AOT (Aerosol OT) system using dioctyl sulfosuccinate sodium salt. The formation of droplets-in-oil is discussed in Section 2.6. When changing the ratio of BZ solution versus oil, the distance between droplets increases and the solution is subject to different reaction dynamics and new patterns can be formed. [110]. The different patterns formed from changing the water to oil ratio are shown in Figure 2.8. These patterns are never seen in normal free aqueous solutions and are observed to evolve over time based on the initial BZ reactant concentrations and temperature [18]. Examples of unique waves include localised structures like Turing patterns and oscillons, packet waves which are a pattern that moves as a whole, antispirals that move inward to the centre, accelerating waves which do not move at constant velocity, and segmented waves which are broken waves moving similarly to planar waves [110].

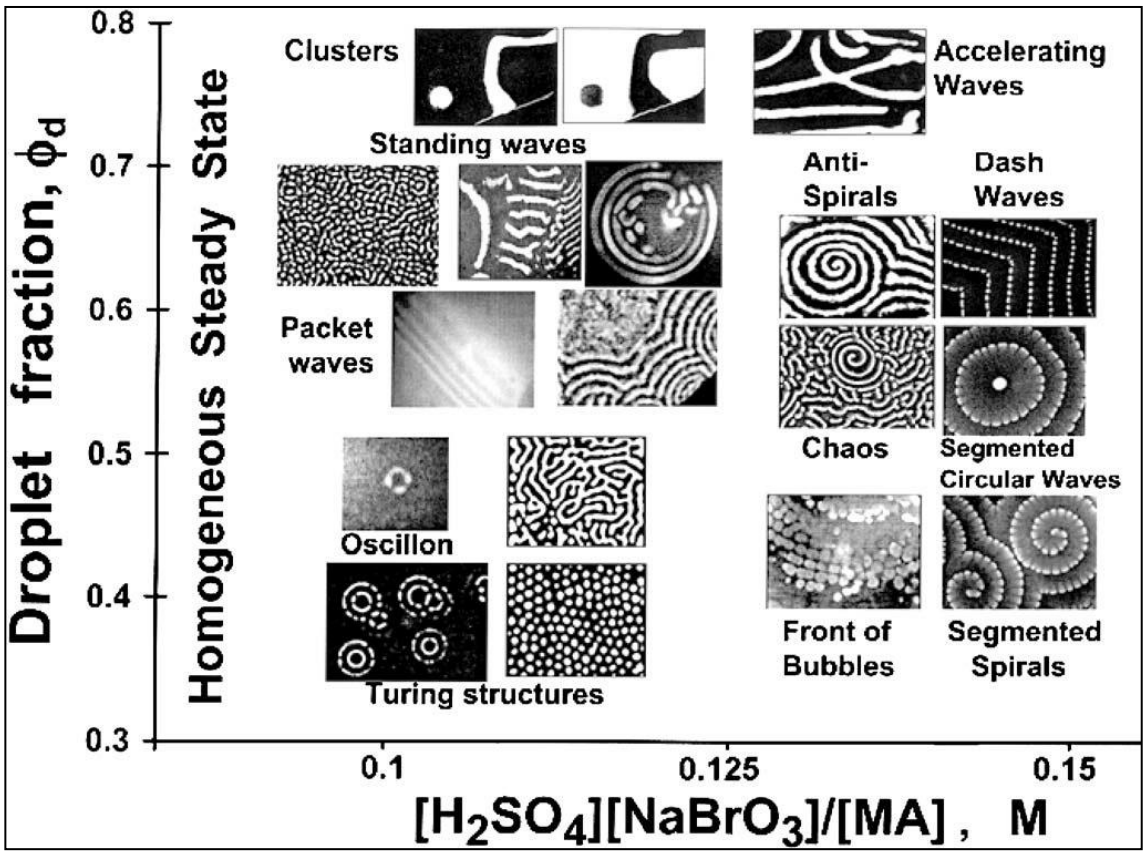

Figure 2.8 BZ-AOT system patterns formed by altering droplet fraction and the reaction rate of the BZ mixture. The reaction rate is controlled by the ratio of sulphuric acid and sodium bromate concentration to malonic acid concentration. Reproduced from [110].

Additionally, emulsion solutions also form discontinuous waves. These waves appear to "jump" when they propagate such that there is a region that is never oxidised between. These are divided into jumping waves, bubble waves and rotating waves. Jumping waves are standard circular waves which jump across gaps without oxidising the solution. Bubble waves are similar to continuously propagating segmented waves except that they also jump gaps, and appear as "bubbles" of small oxidised regions that are smaller than said gaps. Rotating waves have the oxidised fronts with a reduced section that circulate around the circumference of the circle, giving a rotating appearance. These patterns and the continuous segmented wave are observed to evolve from normal continuously propagating circular trigger waves over time. Bubble waves are more likely to evolve at room temperature while higher temperatures cause jumping waves to evolve into rotating waves. It must also be noted that all these patterns can coexist at the same time despite the same conditions [18]. These wave transformations are shown in Figure 2.7 (B).

Normally these waves are blue waves in a red solution, though it is possible to have red waves in a blue background if the malonic acid concentration is very low. As these “oxidising” and waves travel faster than “reducing” waves, new oscillations inside the reduced circle can catch up and oxidise the region again. This leads to even more complex behaviours as the reducing wave is still present and expanding while this occurs [114]. This behaviour is similar to “backfiring” behaviour [111].

When used with CHD even in free aqueous solution, additional effects on the circular waves are observed. Wave stacking behaviour was observed where waves are initiated from the centre but travel faster than the first wave front and so slow down and stack up closer together due to differences in the local excitation period. Hence, the frequency is low near the centre of oscillation and high further away. This was seen with very high acid and ferroin concentration and very low bromate and CHD concentrations. When the CHD concentration is increased, wave merging is observed where the first wave front extinguishes newer waves reaching it instead of allowing them to stack up, as the wave speed from the source is faster than the wave speed of the first wave front [115]. Similar behaviours were observed with CHD in glass capillary tubes [116]. Wave stacking behaviour is shown in Figure 2.9.

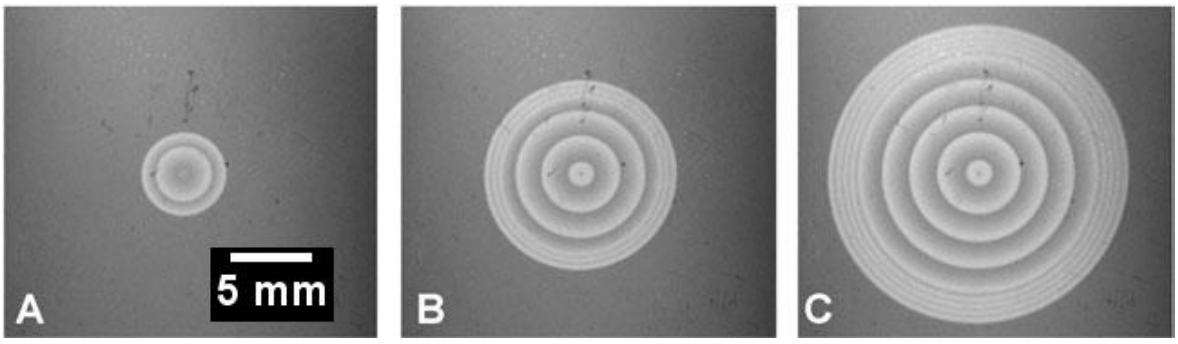

Figure 2.9 Wave “stacking” behaviour as the wave speed significantly decreases after a certain distance from the wave source due to discontinuous properties of the medium. Reproduced from [115].

2.4 BZ compartmentalisation in different mediums

BZ solutions can either be used as a continuous free aqueous solution, emulsion in oil or droplets in oil. Each has unique behaviours and considerations for compartmentalisation. When unstructured, BZ waves are generated at random locations and travel in random directions across the solution. However, it is found that when compartmentalised in 3D printed structures with varying depth, shallower parts of the solution are inhibited from generating and propagating waves. This is hypothesised to be due to oxygen inhibiting the shallower structures [117]. Additionally, when BZ waves confined in capillary tubes are allowed to interact, it is found that decreasing the aperture and tube width causes the waves to fail to propagate upon exiting. This is because restricting the connection reduces the diffusive dispersion of autocatalyst (Figure 2.10 (A)) [17]. Solutions can also be used under oil to reduce effects such as surface airflow. Using this method, experiments on the physical force of a BZ wave front were conducted [118]. When the BZ container is asymmetrical, it is found that wave propagation pattern and interactions produced are asymmetrical, showing that the container shape also affects the chemical dynamics [119]. BZ can also be compartmentalised inside gels, where some gels expand when the BZ solution oscillates and can be made to perform functions from the way the BZ oscillations propagate [120].

The waves in continuous free solution can also be restricted by using the solution without catalyst. Instead, the catalyst is compartmentalised inside a printed polymer shape, allowing the other substrates to be refreshed in a continuous flow reactor while restricting the waves to inside the printed polymer area (Figure 2.10 (B)) [19]. Some gel-polymers also increase in size at the regions with waves. This oscillatory increase in size is used for making gel structures than move in a specific way periodically as a robotic component [120-123]. If ruthenium catalyst is used, a projector can also be used to project shapes, where the bright regions suppress the formation of waves. This also allows the formation of sub-excitable regions, where designated regions are allowed to propagate waves but not generate them [8, 113, 124-127]. Using this method, Holley *et al.* designed “logic gate” structures where the interaction of waves generated from “inputs” changed whether waves are allowed to propagate into “output disks” Figure 2.11 (A) [20]. Besides changing where the waves can propagate, the membrane pattern also changes the shape of the wave front. This is shown when membranes are printed with a checkerboard array of

triangular cells, which caused hexagonal and diamond shaped fronts instead of rounded shapes [111].

When used as an emulsion in oil, the continuous free aqueous solution is mixed as many nanoliter volume droplets in a continuous oil phase, which causes slight changes in behaviour. It is observed that changing the ratio of BZ solution versus oil changes the sizes and spacing between individual droplets and also the wave behaviour [110]. Reducing the ratio of oil reduces the continuous oil phase, but does not affect the BZ droplet size, which is always between 2-3 nm in radius. However, as the oil phase is reduced the droplets are closer and can interact more easily [128]. Hence, if the oil ratio is too high, the BZ is does not oscillate, and this is calculated to be because some individual droplets do not contain enough catalyst needed for the reaction to continue [129]. In addition, there is an average of less than one molecule of catalyst per water droplet, so each droplet can be regarded as a single reactor where the mass exchange rate increases as the droplet size increases [110, 130]. The different behaviours possible are shown in Figure 2.8 and discussed in Section 2.3.

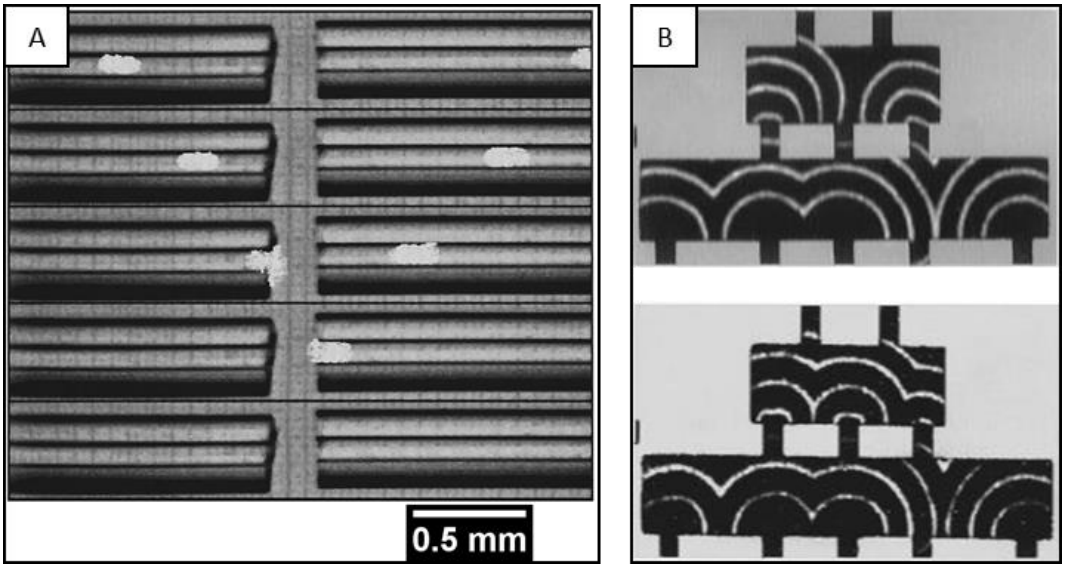

Figure 2.10 (A) Image sequence of waves travelling down two capillary tubes. When the waves meet, they interact and disappear. Reproduced from [17]. (B) Examples of XNOR-gate built from BZ without catalyst in agarose gel with polysulfone gel-immobilised catalyst printed on top as a logic gate. Top picture shows electrode inhibition of central gate preventing waves from travelling through. Bottom picture shows system with uninhibited central gate, changing the wave pattern. Image area is 4.2 cm^2 for each structure. Reproduced from [19].

BZ is also used as microliter-sized droplets in oil as opposed to in an emulsion of much smaller nanometre-sized droplets. Further information on the formation of droplets in oil can be found in Section 2.6. These larger droplets are usually placed in capillary tubes at a certain spacing to observe if their oscillations show coupling between droplets through the oil. It is observed that BZ droplets placed micrometres apart appear to couple and oscillate at a phase difference with adjacent droplets. When the spacing between each droplet is carefully set, it is observed that even these larger droplets can form Turing patterns. It is hypothesised that these droplets are coupled by the bromine generated as other components such as bromous acid and bromine dioxide travel a shorter distance in. These setups are shown in Figure 2.11 (B and C) [131, 132]. Besides the structuring the arrangement, changing the concentration of H_2SO_4, $NaBrO_3$ and KBr in the droplets also changes the coupling behaviours [88, 131]. When this coupling is optimised such that some droplets are constantly blue and others constantly red, it is found that the red droplets significantly increase in size due to its higher concentration, further increasing complexity of behaviour [132]. Other methods use droplets in oil where the droplets are placed in contact to form interdroplet interfaces. It is found that if this interface is disconnected the wave behaviour is significantly changed as waves can no longer propagate in that direction [2]. Gorecki *et al.* recently used a similar system of coupling microliter sized droplets, where it is discovered that larger sized droplets appear to act as wave initiators when placed in contact in an array with smaller droplets [133].

Recent progress in microliter-sized droplets includes using these droplets with two different oils to both constrain the shape of these droplet networks while also preventing these droplet networks from interacting. This is because the hexadecane oil and fluorocarbon oil wets the glass more effectively while being impermeable to $HBrO_2$. It is observed that the larger droplets had a significantly higher oscillation frequency and that oscillations disappear if the droplet size is too small. By pairing a large and small droplet, it is observed that the small droplets initially oscillate at a lower frequency but eventually synchronise in frequency with the large droplet. However, the rate and method of synchronisation for each array is different, with some arrays achieving synchronisation almost immediately while others have behaviour where some waves go through while others do not at different ratios [21].

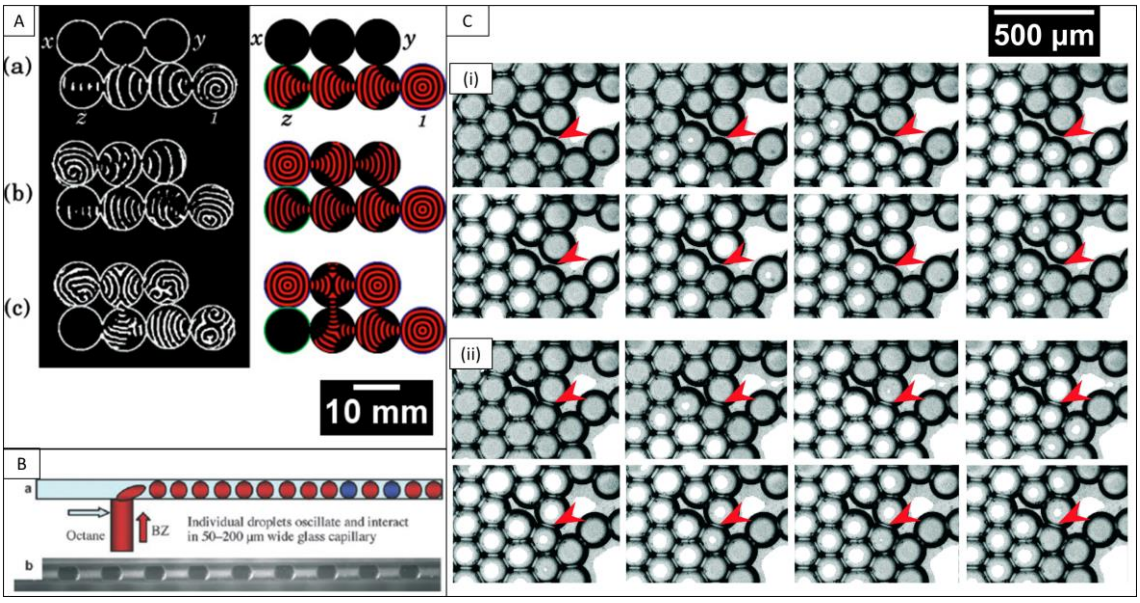

Figure 2.11 (A) Two input NAND-gate example using circular shaped structures. Left shows simulation of waves while right shows theoretical wave pattern. Inputs x and y must both be present to stop the output at z. Reproduced from [20]. (B) Schematic and photo of BZ droplets surrounded in octane oil arranged in a 1D array inside capillary tube to react. Capillary tube between 50-200 μm wide. Reproduced from [88]. (C) Droplets in oil showing transfer between membranes (read left to right). The red arrow shows the region where there is an oil gap in part (i) and close contact in part (ii). Part (i) shows no transfer of wave between region of red arrow and part (ii) shows a transfer which causes the wave pattern to be different. Droplets approximately 150 μm in diameter. Reproduced from [2].

100 micrometre sized droplets from BZ emulsions are also observed using shaped channels to contain the BZ droplets in arrays of specific shapes and controlling their oscillations with pulsed light. To form these complex shapes, PDMS was used to make channels just large enough to contain these BZ droplets and is impermeable to polar and charged species and permeable to non-polar species and gases. However, it is observed that the BZ droplets stop oscillating after some time, and this is speculated to be due to bromine gas build-up inside the PDMS. To solve this, silicon or silicon dioxide wafers etched with a profilometer are used as the new material to contain these droplets. These shapes are designed to be just large enough for a single BZ droplet to be placed inside, so the shape of the array is controlled. It is observed that optically isolated droplets placed directly touching each other can synchronise to be exactly out of phase, whereas droplets separated by non-oscillating BZ droplets appear to be unsynchronised. [134].

A microfluidic device was recently designed using two phases of different oils and an aqueous solution phase. This method of compartmentalisation is also interesting as it can form a large variety of array shapes by changing the ratio of hexadecane oil and BZ volume while surrounded by fluorocarbon oil. This changes the optimal arrangement of the droplet array inside the hexadecane shell, spontaneously forming different methods of connecting each droplet [135]. This method was tested with mixing BZ droplets in two droplet arrays with different sized droplets, showing that it is versatile in containing highly acidic redox oscillating solutions while allowing in-situ mixing of different volumes of each solution. However, the other possible complex array shapes are not yet tested with BZ [21].

Values of diffusion coefficient are reviewed to compare the effects of compartmentalised versus free solution to determine the extent this may be reduced for BZ components and intermediates. Compartmentalisation in gels causes the diffusion coefficient of water to be lowered to between 1 to 1.5 X 10^{-9} m^2/s. This is compared with a maximum value of 2.4 X 10^{-9} m^2/s for free diffusion of water and minimum value of 1.2 X 10^{-10} m^2/s in highly cross-linked hydrogel [136]. This is corroborated with chloride ions in agar gel, which had a diffusion coefficient of between 0.8 and 0.11 X 10^{-9} m^2/s compared with a maximum of 1.12 X 10^{-9} m^2/s in free solution [137]. In the case of alginate gel, the diffusion coefficient is only 10% less compared to in free solution [138], though another study reported a reduction of at least 24% [139]. The diffusion coefficients for compartmentalisation in emulsions is discussed in Section 2.6.3.

All these compartmentalisation techniques are interesting as arranging these droplets in defined geometries allows modelling bio-physical networks and pathways. Since these droplets are influenced by their initial conditions, using different coupling patterns also allows the phase shift to be tuned. Additionally, using different liquid phases such as oil and aqueous solutions causes different materials to diffuse and interact differently than in a homogeneous system, and gives great insight into long and short range communication between droplets. However, there is still a challenge in defining the location of signal producers in these complex networks, and semipermeable membranes are still not well understood so their interactions with different BZ messenger molecules is uncertain. Furthermore, all networks produced thus far are in 1D and 2D, though microfluidic networks has given great control in making these networks precisely and reproducibly. As such, there is great interest in furthering the study of BZ droplets in microfluidic networks

[10]. Utilising these bottom-up fabrication technologies at the microscale with BZ allows further understanding of dynamic and spatiotemporal effects, which is currently relatively primitive. This will hopefully lead to future developments in making nanoscale machinery that can utilise the periodic changes [140]

2.5 Processing BZ data

Earlier experiments with BZ measured oscillations using electrodes which detect the concentration of individual reactants. This formed graph plots where peaks can be seen when there is an oscillation [13]. Other experiments where the patterns or movement of the wave front in space showed image sequences showing its evolution over time [111] or with each type of wave shown as a representative image [18]. Images can also be enhanced by taking only the blue channel of the image, which gives a higher contrast between the blue wave and the red background. Conversely, using only the red channel gives a very low contrast such that only the droplet boundary and background lighting can be seen and waves are invisible [141]. This was then used to analyse BZ droplets that change in size as well as oscillate [142].

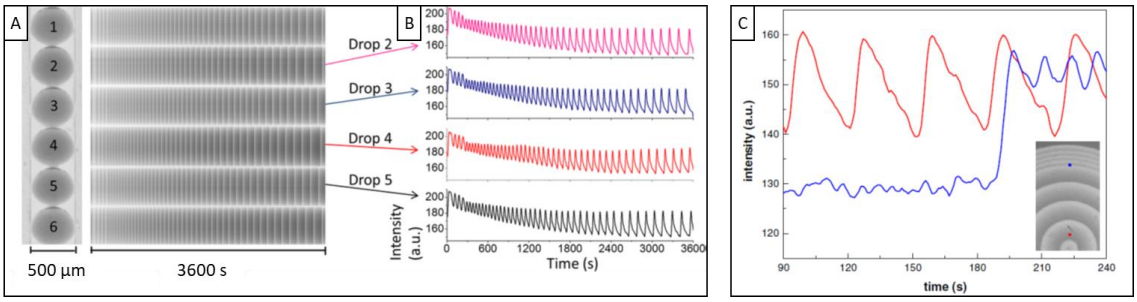

Figure 2.12 Example of (A) space-time plots formed from an array of droplets and (B) their pixel intensity measurements. Reproduced from [9]. (C) Example of wave stacking behaviour and measurement of pixel intensity measurements at only specified spatial locations. Reproduced from [115].

Most BZ data processing is performed by taking space-time plots of each droplet. These are formed by cutting an arbitrary width through the entire droplet for each frame in a video and arranging them together. When the droplet oscillates, a change in colour can be observed in the space-time plot. These colour changes can be measured as a graph whose peaks can be counted and measured for other parameters such as frequency. These can then be extrapolated into other data such as difference in frequency compared to a coupled droplet [9]. If the state, phase difference and synchronisation of droplet oscillations is important, it is also possible to show the time evolution different droplet states using these space-time plots. In one case, the space-time plot is annotated with different states showing how many oscillations have passed before one oscillation in a lower frequency droplet [21]. The phase between oscillations can be calculated and represented as a phase difference diagram, where the time is represented by the distance from the centre of a circle while the angle of a radius line shows the phase difference [134]. In a similar way to the space-time plot method, it is possible to measure the frequency of the oscillations in different parts of an image. Using the example of wave stacking phenomenon, the centre of the wave source has a lower frequency than a distance far outside, but because of the different reactivity, the waves further away start to “stack”, giving the appearance of a sudden high frequency wave after a long period without any oscillations [115]. Examples of the space-time plot are shown in Figure 2.12 (A and B) and for the wave stacking in Figure 2.12 (C).

As some coupling structures are complex, they are represented by a diagram which draws a line between coupled droplets. This is useful especially when droplets do not have an obvious oscillation pattern between droplets [134]. If the coupling is parallel to the observation direction (e.g. through the bottom of a flat surface) the patterns emerging from both sides of the recorded chambers can be combined in a single image with different colours. This can show if complex patterns are coupled in any way [16]. This can be expanded by using composite images with the waves at different times combined into a single image to show all the area covered at once. Furthermore, if the time when each wave appears is important, a colour gradient can be applied to show the elapsed time of the video when the wave reaches a certain region. Regions where the waves meet and annihilate can be marked out as well. This is particularly useful to determine the shortest and longest paths through a structured system [111].

2.6 Droplet in oil compartmentalisation

Droplet-in-oil compartmentalisation is the main method used in this project to compartmentalise droplets. This method uses the self-assembly of lipids or surfactants on the surface of droplets to form a barrier between the droplet and other droplets. When the droplets are pushed together to form an interface, these molecules prevent the droplets from fusing together and mixing while allowing the selective communication of chemical species. As these processes are very useful for coupling and compartmentalising substrates but affected by environmental conditions which disturb their self-assembly, some understanding of its mechanisms are required. Progress is being made in this field, with many new applications and greater scalability and control over the medium, which could be applied to the field of unconventional computing [7].

2.6.1 Surfactant self-assembly

Surfactants are molecules that change the surface tension of a solution, and can be made up of phospholipids or detergents. When aqueous droplets are placed inside a continuous oil phase, they are unable to mix and so a droplet in oil is formed. If surfactants are present in the system, they will self-assemble as a monolayer at the aqueous-oil interface. This is due to the molecular structure of these molecules, which contain a hydrophilic head and a hydrophobic tail section. This causes the hydrophilic heads to autonomously align to stay inside the aqueous solution and the hydrophobic tails to align inside the oil. The number of tails present, the length of the tails and the number of double-bonded carbon atoms present affect the stiffness of the membrane formed as these factors affect how densely packed the molecules can be. The length and number of tails also affects the permeability of the membrane. These surfactants also lower the surface tension of the water phase so that it is easier to produce and maintain small droplets in the oil phase [143]. Figure 2.13 (A) shows the structure of surfactants with different tail numbers and tail lengths.

When an aqueous droplet is placed in oil, the self-assembled structure is a monolayer where the hydrophilic head faces inside the aqueous droplet. This is known as a micelle. If it is an oil droplet in an aqueous solution however, the reverse arrangement is formed where the hydrophobic tails face inside the droplet. A vesicle is formed if an aqueous droplet is placed inside an aqueous solution, where two layers of lipid are arranged to

separate one aqueous solution from the other. The arrangement where two layers of lipid are formed is referred to as a lipid bilayer. Figure 2.13 (B) shows how these molecules self-assemble in oil versus in water and at the aqueous-oil interface forming a monolayer. Figure 2.13 (C) shows different self-assembled structures separating two aqueous phases where the opposite orientation will be formed for two oil phases. The reverse micelle in oil with the tails facing outward is the configuration used for this project. It is possible to mix the surfactants inside the aqueous droplets or the continuous oil phase, as both will allow the molecules to self-assemble at the interface between both phases. As living cells are also composed of phospholipid bilayers with aqueous solutions in the inside, these micelles and vesicles are often compared with cells [46, 144-146].

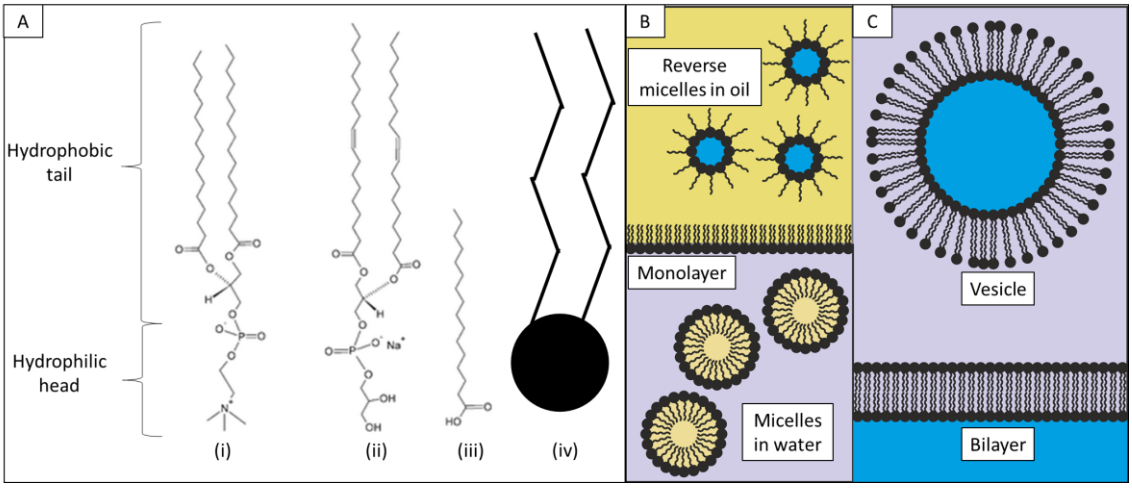

Figure 2.13 Molecular structure of different types of surfactants. Each has different lengths of their tails and (iii) only has one tail. (i) 1,2-Dipalmitoyl-sn-Glycero-3-Phosphocholine (DPPC), (ii) 1,2-Dioleoyl-sn-Glycero-3-[Phospho-rac-(1-glycerol)] (DOPG), (iii) palmitic acid (PA), (iv) simplified structure with two tails. (B) Micelles in oil where hydrophobic tails aligned outwards towards oil phase. Comparison with micelles in water is shown with opposite orientation where hydrophilic heads aligned outwards towards aqueous phase. Lipid monolayer formed at the aqueous-oil interface with hydrophobic tails aligned towards oil and hydrophilic heads aligned in water. (C) Vesicle and bilayer structures in water. Structures in oil aligned in opposite direction not shown. All structures can vary in size based on

It is possible for multiple layers of these structures to form on the droplet surface if the surfactant concentration is high. These are called multilamellar structures and can be prevented by using only the appropriate concentration of lipids in the solution. These results in lower efficiency of trapping large molecules and makes droplet sizes more difficult to control unless using microfluidic systems [147].

One form of self-assembled droplets used in literature is the Aerosol OT system (AOT) using dioctyl sulfosuccinate sodium salt. This forms an emulsion of micrometre sized droplets-in-oil with a fairly homogeneous droplet size. This is formed by adding using a specified ratio of aqueous solution versus oil and surfactant concentration and agitating the mixture. However, each droplet may have a different concentration of chemicals compared with the original aqueous solution due to how the droplets separate these chemicals of low concentration [110].

2.6.2 Interdroplet bilayers

When droplets are placed together for long enough, interdroplet bilayers can form at the interface. These bilayers are the result of pushing out all liquid of the external phase from between the surfactant layers of both droplets, forming a self-assembled structure of surfactant that allows communication between the separated solutions. These bilayers are a semipermeable interface and are useful for allowing chemical species to move and interact without mixing the droplets together.

Bayley *et al.* developed methods of connecting these droplets to form interdroplet bilayers. When these droplets are connected it is theorised that components dissolved inside the solutions can pass through the interface into other droplets. This allows the construction of mechanically stable bilayers and droplet networks which can be used for a variety of experiments with greater accuracy [144].

Usually aqueous droplets in oil are used, where the monolayer of lipid formed around it. When contacted with a second droplet, the oil between both is expelled and the monolayers self-assemble to form a bilayer at the interface. This is known as a droplet interface bilayer (DIB) or as an interdroplet bilayer [144]. This bilayer allows only certain small molecules to pass through such as water, while the membrane is not permeable to most types of larger molecules and ions [22, 46].

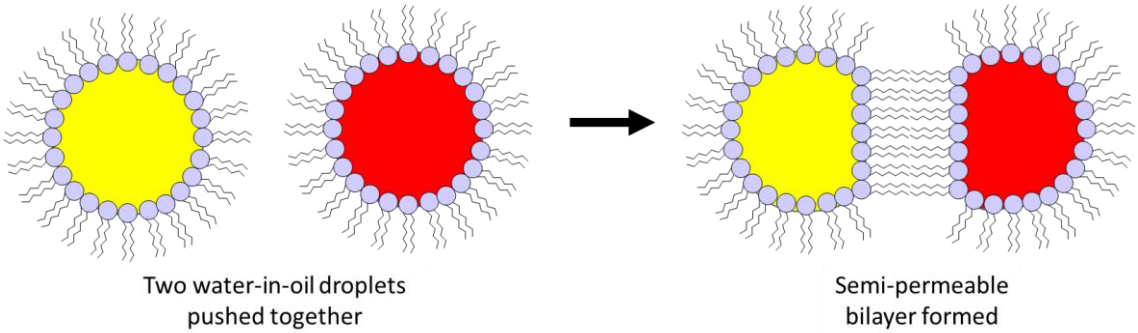

Figure 2.14 Droplets manipulated using electrodes on micromanipulators to push them closer together. Droplet interface forms bilayer when two droplets are pushed together. This bilayer and interface can form a connection through which components of the droplets can pass through. Reproduced based on [7] and [148].

When arrays containing many droplets are used in other studies, microliter sized droplets are formed by manually pipetting them into a continuous oil phase. These droplets are then manually manipulated using electrodes on micromanipulators to position them closer to each other while allowing electrical measurements to be taken from inside each droplet (Figure 2.14) [144]. The need for manual manipulation is one of the disadvantages of this system [22]. If nanoliter sized droplets are used, a microfluidic setup is used which pinches off small droplets using an oil-phase that is flowed faster. This allows droplets to be automatically formed and arranged using the flow of the continuous phase and the shape of the microfluidic setup's channels and traps. These traps function by balancing the hydrodynamic pressure between the oil inlet and outlet of the trap as well as the Laplace pressure of the droplet interface [149, 150].

However, it is found that microliter droplets are more suitable for experiments where visualisation of the droplet contents is important, and hence a millifluidic chip was previously developed for this project by King *et al.* which allows the accurate mixing and measurement of droplets of this scale. One advantage of this chip is that the design is 3D-printed and cast into polydimethysiloxane (PDMS), which gives good biocompatibility and is optically transparent. These droplets are then flowed into a capture chamber where they can be held in position for observations. This chip is 70 X 50 mm and uses channels that are 1.1 mm wide and 0.55 mm deep and a capture chamber that holds 2 mm wide droplets. This chip uses 40 mg/ml asolectin in hexadecane as the lipid in oil for its continuous phase and is capable of forming arrays of droplets up to 9 droplets long, each 2 µl in volume. This

array can then be maintained stable for up to 6 hours. Additionally, the T-junction of the design allows accurate mixing of two components of an aqueous solution. The aqueous inlets are capable of pushing out droplets of 0.7-6.0 µl in size. Electrodes can also be used in this chip for electrical measurements by punching the electrodes directly into the droplets in the capture chamber [22]. Images of the chip and its dimensions are shown in Figure 2.15.

This chip was improved upon by Carreras *et al.* by using smaller dimensions and a capture chamber design that allows two rows of droplets to be kept in position and coupled for observation. This allows larger arrays of smaller scale droplets to be produced with a lower lipid concentration. This design also incorporates wells for capturing droplets and forming more complex interdroplet interfaces while reducing stretching on the bilayer [151]. Other smaller microfluidic devices were also developed using a similar principle and smaller scale [150]. To further control droplet fusion, a chip is designed to purposely fuse small volume droplets using a microfluidic trap [152].

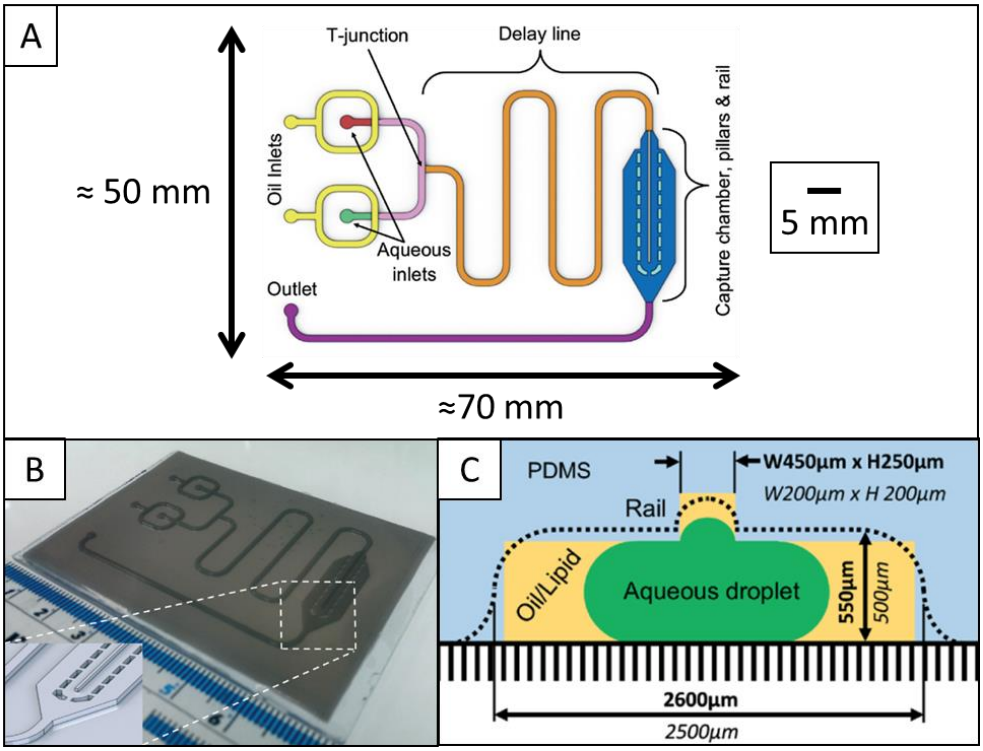

Figure 2.15 (A) Schematic of King *et al.*'s chip. Droplet arrays held in 2.5 mm wide space between pillars in capture chamber, channels are 1 mm wide and entire chip is 70 X 50 mm. (B) Photo of 3D printed master and capture chamber design (inset). (C) Scale and dimensions of the capture chamber and droplets produced. Reproduced from [22].

Due to the stability of such droplets, it is possible to produce 3D arrays by stacking such droplets on top of each other, which allows more complex interactions and patterns to be formed [153]. This can be used to produce even more elaborate structures to resemble tissues [145].

An additional consideration when fabricating new compartmentalisation techniques is that materials absorb oil and increase in size. Some work is done to determine materials which resist this, where THV is found to be a good replacement for PDMS [154]. There is little data on the effect of exposing acrylic (PMMA) to hexadecane, though when exposed to decane it is noted to have some swelling and softening [155].

2.6.3 Functional droplet networks

Biological cell membranes consist of a bilayer of lipid molecules. These cell membranes contain proteins, which act as channels for molecules and ions that would otherwise be unable to pass through these membranes (Figure 2.16). As such, by incorporating channel proteins such as α-hemolysin inside droplets used in droplet networks, it is possible to alter their permeability to certain ions and molecules. When used in conjunction with other droplets without channel proteins incorporated inside, a more complex network is produced where the chemical being tested can diffuse through some droplets and not others [144, 145, 153].

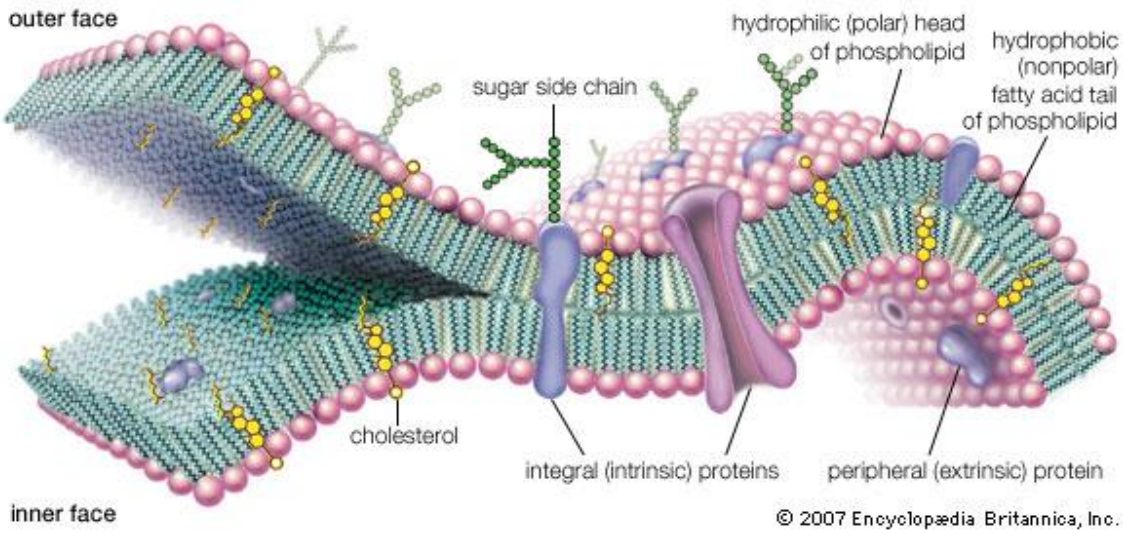

Figure 2.16 Schematic of cell membrane and several types of molecules present. Proteins incorporated into phospholipid bilayer can act as channels to allow otherwise impermeable substances to pass through the membrane. Reproduced from [156].

3D printing of droplets is utilised to precisely place droplets in a 3D network. Combining this with the ability to change the membrane permeability using α-hemolysin and contents of each droplet allowed complex droplet networks to be created with specific functions in each part. In one case, a 3D pyramid of droplets was assembled with only certain droplets allowing permeability of dye, forming a complex pattern [153]. In another case, a path was created of permeable droplets surrounded by impermeable droplets and driven using an electrical current to form a defined circuit [145]. As mentioned in Section 2.1 and Figure 2.2, individual droplets with different permeability can be used to concentrate specific reactions mimicking cells. These compartments can increase the reaction efficiency and yield and reduce interference by other products [46] and allows complex behaviours otherwise impossible if the droplets had uniform composition or permeability to all substances. Without control in compartmentalisation, these behaviours would be impossible in experimentation as well as in living cells [146].

For compartmentalisation in emulsions, the diffusion coefficient of water is reduced by 10 times to 2.29 X 10^{-10} m^2/s compared with 2.27 X 10^{-9} m^2/s for free diffusion in the same study [157]. These effects of compartmentalisation may not significantly affect the droplets in this project, as the distances involved are less than 0.1 mm at the droplet interfaces and the reaction-diffusion itself is mostly inside the aqueous droplets, which can be considered free solution. However, as the BZ reaction relies on very low concentrations of reaction intermediates and small changes in the initial conditions, the changes in diffusion coefficient may have a larger effect on the wave patterns, as shown in Figure 2.8.

Recent developments in the field of droplet compartmentalisation show these technologies being used to study a large variety of different chemical compositions and droplet topologies. These experiments would not be possible without the scalability and control provided by microfluidic techniques for controlling the droplet-in-oil mixtures and topologies as well as the semipermeable properties of droplet interfaces, which allow coupling of these droplets for a variety of applications [7].

Chapter 3 Methodology

3.1 Stock chemicals

2.5 M sulphuric acid (H_2SO_4) (Fluka Analytical) and 0.025 M 1,10-phenanthroline ferrous complex (ferroin) is obtained in solution and diluted further in other solutions when used. 99+% Sodium bromate ($NaBrO_3$) (Acros Organics), 99% acid (MA) (Sigma Aldrich), potassium bromide (KBr) (Fisher Scientific UK) and 98% 1,4-cyclohexanedione (CHD) (Sigma Aldrich) are obtained as powders and solutions are made by weighing out the mass of powder needed and adding 10 ml of deionised (DI) water measured using a measuring cylinder.

Asolectin from soybean (Sigma Aldrich) is obtained as a powder and is made into a solution by measuring the mass needed and diluting it with 99% hexadecane (Sigma Aldrich) measured using two 15 ml falcon tubes. These powders are weighed in 20 ml glass scintillation bottles and the solvents are added into the bottles. The bottles are shaken on a vortex mixer and then left closed at room temperature for some time to dissolve any remaining powder. The resulting solutions have a slightly larger volume compared to the intended volume, so this is measured and the real final concentrations are listed in Table 3.1.

Table 3.1 BZ component stock solutions and their actual final concentrations.

	H_2SO_4	**$NaBrO_3$**	**Malonic acid**	**Ferroin**	**CHD**	**KBr**	**Asolectin**
Molar mass (mg)	N/A	150.892	104.06	692.52	112.127	119.002	N/A
Conc. Intended (M)	2.5	2	2	0.025	1	1	40
Mass used (mg)	N/A	1508.92	1040.6	N/A	1121.27	595.01	800
Vol actual (ml)	2	5.32	5.6	N/A	10.8	N/A	21
Conc. Actual (M)	**2.50**	**1.88**	**1.79**	**0.025**	**0.93**	**1.00**	**38.10**

The asolectin in hexadecane oil is centrifuged at 6000 relative centrifugal force (RCF) for 15 minutes before each experiment. To recover excess oil, all visible aqueous droplets are removed and the oil is stored in falcon tubes. When reused, the oil is stored in the -16° freezer until needed, where it is allowed to melt at room temperature until all frozen oil is liquid. It is then shaken to obtain a more homogenous mixture of asolectin and then centrifuged to separate any possible small aqueous droplets. The CHD solution is also centrifuged at 6000 RCF for 15 minutes before each experiment to separate any undissolved powder.

The BZ components are mixed only when a recording is ready to be made. These solutions are mixed in the following order, first with DI water, then H_2SO_4, $NaBrO_3$, malonic acid and KBr. Once the yellow colour has disappeared, ferroin is added. CHD is added after waiting 5 minutes from the addition of ferroin. The KBr is added before the ferroin as yellow bromine is generated in the solution when it is added, which if reacted with ferroin results in dark precipitate that needs a longer time to disappear from the solution. CHD is added after ferroin as the solution needs a long incubation time if the MA BZ solution is not fully mixed first. A yellow precipitate is formed when CHD is added, which quickly dissolves and disappears. After the final component is added, the solution is gently swirled or a pipette tip is used to pump up and down to agitate and fully mix the solution. It must be noted that CHD solution is hay coloured when freshly mixed with some solid impurities. However, if these stock solutions are used over a long time the solution turns into a darker brown colour. For the purposes of this project the freshly mixed and older CHD solution is considered the same, with most experiments using hay coloured fresh solution.

The volumes for mixing the BZ solution of specific compositions are calculated from the stock concentrations and volumes added according to the order. The volume of DI water needed is calculated to top up the solution to the final intended volume. All MA BZ experiments use common concentrations of 0.5 M H_2SO_4, 0.47 M $NaBrO_3$, 0.18 M MA and 2 mM ferroin unless otherwise stated. The BZ composition to be used for MA BZ experiments is chosen based on feedback from Duncan Parker, a PhD student under Prof. George Attard. All MA-CHD BZ experiments use common concentrations of 0.5 M H_2SO_4, 0.28 M $NaBrO_3$, 0.09 M MA, 2 mM ferroin and 0.09 M CHD unless otherwise stated. A lookup table of the volumes needed to form 1 ml solution and the common concentration of each component in all experiments is shown in Table 3.2.

Table 3.2 Volume of stock solution needed to produce intended BZ concentration of 1 ml BZ solution. Remaining volume topped up with DI water calculated and added beforehand. Common concentrations of BZ components for all experiments also shown.

Order	Component and stock concentration	Concentration in BZ reaction mixture						Common conc.	
								MA BZ	MA-CHD BZ
1	H_2SO_4 (M)	0.1	0.2	0.3	0.4	0.5	0.6	**0.5**	**0.5**
	Volume from 2.5 M stock (µL)	40	80	120	160	200	240		
2	$NaBrO_3$ (M)	0.09	0.19	0.28	0.38	0.47	0.56	**0.47**	**0.28**
	Volume from 1.88 M stock (µL)	50	100	150	200	250	300		
3	Malonic acid (MA) (M)	0.09	0.18	0.27	0.36	0.45	0.54	**0.18**	**0.09**
	Volume from 1.79 M stock (µL)	50	100	150	200	250	300		
4	Ferroin (mM)	1	2	3	4	5	6	**2**	**2**
	Volume from 25 mM stock (µL)	40	80	120	160	200	240		
5	1,4-cyclohexanedione (CHD) (M)	0.09	0.19	0.28	0.37	0.46	0.56	**0**	**0.09**
	Volume from 0.93 M stock (µL)	100	200	300	400	500	600		

3.2 Image recording

All experiments are recorded using a Prosilica GX3300C CCD camera with a 3296 X 2472-pixel sensor chip (Allied Vision Technologies, Germany) on a calibrated flat overhead camera mount. The camera has a Helios 58 mm f2 lens 12 mm tube extension set at f/3.2 aperture and focused until the viewing area is in focus. The lighting of each experiment is from a MiniSun A4 LED Modern Ultra-Slim Art Craft Design LightPad providing lighting through the bottom of the experimental setup. External light sources are minimised using a curtain covering the observation area. AVT VIMBA (Allied Vision Technologies, Germany) is used to record the images at 0.4 frames per second in BMP format. The time stamps of each image are saved and then FIJI (Fiji is just ImageJ) (National Institute of Health, USA) is used to convert images to the compressed and lossless PNG format, which has a smaller file size, for storage. It is also used to process image sequences and convert them into an AVI file for initial analysis. The exposure time is set to be 25 ms and whitebalance to 2.49 for red and 1.10 for blue to remain consistent between experiments with this apparatus.

Experiments that need a closer zoom with smaller structures or in the millifluidic chips are recorded using a Prosilica GC2450C CCD camera with a 2448 X 2050-pixel sensor chip (Allied Vision Technologies, Germany) mounted inside a Stereozoom Discovery V8 microscope (Zeiss, Germany) at 0.15X magnification for a larger field of view. The same lighting setup is used as before. The AVT VIMBA software is used with the same procedure except the exposure time is set to be 15 ms and the whitebalance to 2.10 for red and 1.54 for blue.

3.3 PMMA laser cutting

Each design is made in CorelDRAW Graphics Suite (Corel Corporation, Ottawa, CA) software. Complex shapes are formed by overlapping shapes and “welding” them together to minimise the number of overlapping cuts and errors. Unconnected designs such as pillars are avoided as these cannot be held in place without multiple layers of PMMA. This limitation is overcome by using multi-layered designs as shown in Section 3.6.

An Epilog Mini 30W CO2 laser cutter (Epilog Laser, CO, USA) is used to cut acrylic (poly (methyl methacrylate)/PMMA) (TechSoft Ltd., Bodelwyddan, UK and Display Products Ltd., Norfolk, UK). The power and speed of the laser is optimised to create a hairline cut through the sheets. The laser is set to 1200 dots per inch (DPI) resolution, 5000 pulses per inch for

all cuts. 20% speed and 100% power is used to cut straight through 2 mm thick PMMA, 80% speed and 20% power is used to cut grooves for markings and 50% speed and 50% power is used to raster written characters. The speed is reduced and power increased appropriately for thicker PMMA pieces. The PMMA is placed on a flat piece of wet tissue during the cutting to prevent the laser from excessively heating the metal grid on which it rests and to dissipate excess heat from the surrounding plastic.

Each cut made by the laser cutter is measured to be 0.06 – 0.1 mm wider along each side of the cut due to the kerf of the laser. This is significantly smaller than for thicker pieces of PMMA and is fairly consistent depending on the geometry. As the difference is less than 10% of the intended geometry which is 2.5 mm at minimum, this difference is insignificant compared with the overall shape.

3.4 General PMMA wafer design

This project needs many repeats of the same experiment to be tested at the same time and these arrays all need to be kept under pressure to ensure the droplets are coupled. To achieve this, PMMA wafers with different slot designs for droplet arrays are used so for rapid prototyping of complex topologies. The petri dish is tilted at a fixed angle to allow the droplets to "fall" by gravity and apply pressure to any droplets that are coupled with it. This is achieved using the petri dish stand shown in Section 3.5.

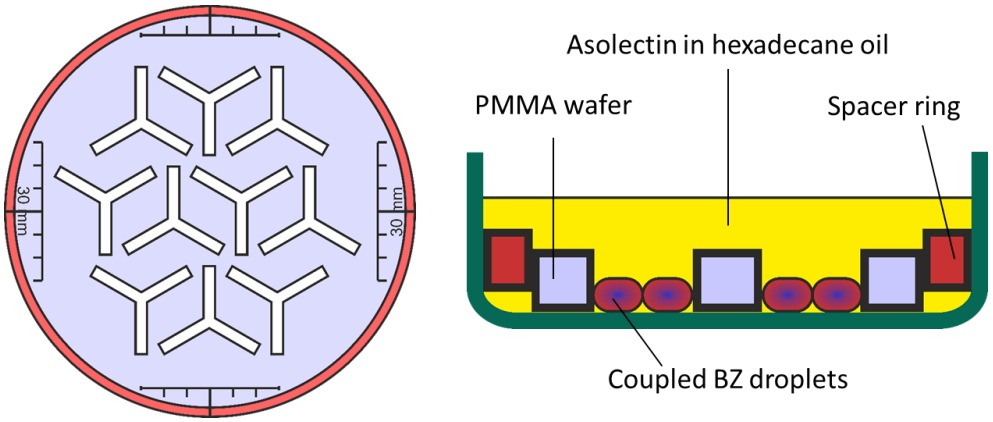

Figure 3.1 (Left) Example design of PMMA wafer and its spacer ring (marked in red). (Right) Schematic of the setup viewed from the side when the wafer is used in a petri dish under asolectin in hexadecane oil to shape droplet-in-oil arrays. The spacer ring is lifted off due to the curve of the petri dish glass but is able to keep the PMMA wafer centred as it sits flush with its edge.

Petri dish wafers made of PMMA are used as a way to structure the shape of each droplet array. These designs work as the PMMA sits flush against the glass and both the PMMA and glass surfaces are hydrophobic, so any space under the PMMA is filled with oil by capillary action. This oil prevents droplets from flowing underneath by capillary action into other parts of the design due to the larger contact angle of the water with glass versus the oil with glass, so oil preferentially stays in the small space under the PMMA wafer. This phenomenon is effective enough that any aqueous droplets present under the PMMA can even be pushed out into open parts of the design by the capillary action of the oil. Using the droplets under a layer of oil has the added benefit of reducing evaporation effects allowing small droplets to be observed for a significantly longer time and keeping the concentration of the components relatively consistent.

A typical wafer is shown in Figure 3.1. The bottom of the glass petri dish is not perfectly flat at the edges due to the curve of the glass. This means the PMMA wafer itself needs to be significantly smaller than 90 mm to avoid being lifted off the glass surface by the curve at the edge, but using a smaller wafer allows it to be set up off-centre and to be unintentionally moved during the experiment. To solve this, a spacer ring is fabricated alongside every PMMA wafer design to prevent excessive movement of the wafer itself and to keep the wafer precisely in the middle of the petri dish. Both the PMMA wafer and ring are fabricated using PMMA that is at least 2 mm in thickness. This thickness is necessary as lower thicknesses tested had wafers sliding under the ring. Grooves are lightly cut as a scale bar for calibration during recording. These scale bars are measured with a digital Vernier calliper and confirmed to be accurate within ±0.1 mm. The middle of these scale bars are positioned at the quadrants of the wafer edge so that they can be used to measure the alignment angle when placed on the petri dish stand. These lines are also extended to the edge of the wafer and spacer ring so that they overlap with the bottom layer of the petri dish stand for this purpose.

The width of each channel is designed to be 2.5 mm in width to mimic the width of the channel inside the millifluidic chip [22] to be used later. This allows observation of larger millimetre sized droplets where the channel width can only fit one droplet. Additionally, each channel design is made to be at least 2.5 mm distance away from each other as structural failure is more likely with smaller distances especially when washing with organic solvent. Each wafer is designed to contain many slots for repeats and droplet orientations.

Very complex shapes such as mazes are imported as curves and then the thickness of each line is set according to the required width of the channels. The curves are then converted into objects. This causes each line to be converted into rectangles that can be shaped and modified accordingly as in the standard procedure.

The wafer and less connected features are found to be warped after laser cutting from the heat and internal stresses of the material, so they cannot sit flat against the petri dish glass at all locations. If the wafer is found to be warped before use, each wafer is compressed at one tonne pressure and 80°C for at least 15 minutes. The heat is then switched off and the wafer is allowed to cool down under one tonne pressure for 10 more minutes before removing the wafer as it is found that releasing the pressure while hot allows the wafer to warp again. It is found that there is no significant change in wafer thickness from the compression and the wafer relatively flat after compression.

To form disconnected shapes such as pillars, multiple layers of PMMA are needed. A base layer of PMMA is used containing only alignment grooves, holes for alignment dowel pins and holes for the disconnected shapes to be set inside. The second layer contains the outline design with only connected shapes. A third piece using PMMA that is double the thickness is used to cut out the disconnected shapes, alignment dowels and spacer ring. The disconnected shapes and dowel pins are designed to be 0.5 mm wider than the intended design and their width at the top of the PMMA is significantly smaller than the bottom due to the kerf of the laser for thicker pieces. This methodology allows the pieces to be washed thoroughly then assembled for the experiment then disassembled for storage. This is used to fabricate the “fish” design shown in Figure 3.2.

Before use, each PMMA structure is wiped with blue roll with DI water followed by blue roll with propanol diluted with some DI water. It is then rinsed with DI water and a small amount of propanol then DI water again quickly. A clean blue roll is then used to wipe the PMMA and then the PMMA is blown with nitrogen gas to remove dust. This method is used because it is found that PMMA exposed to organic solvents tends to crack and break if exposed to pure organic solvent. The DI water also tends to leave very small droplets even after blowing with nitrogen gas. This forms emulsion droplets in the asolectin hexadecane oil.

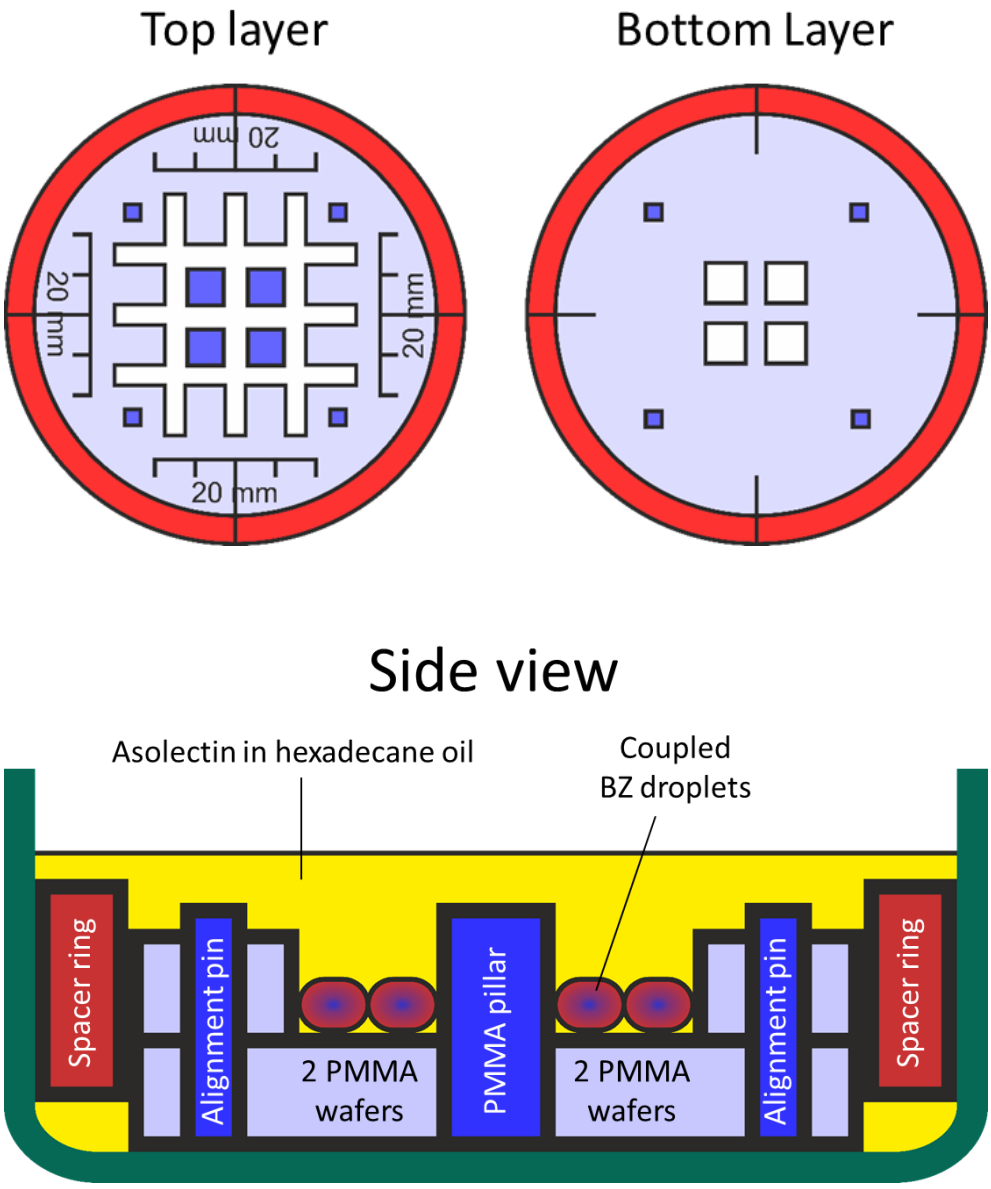

Figure 3.2 Schematic of two-layer "fish" design using a bottom layer of PMMA to hold pillars in position. Top view of both layers and side view shown.

The glass petri dish is wiped with blue roll soaked with DI water, then with propanol and then acetone. It is then rinsed with DI water, followed by propanol then acetone then propanol again. The petri dish is then dried with nitrogen gas. If the petri dish has never been used before, it is first silanised by exposing it to silane vapour. A drop of 97% Trichloro(1H,1H,2H,2H-perfluorooctyl)silane (Sigma Aldrich) is added onto a glass slide and placed alongside all the petri dishes to be exposed to silane vapour inside a plastic desiccating chamber. The air is sucked out and the setup left at low pressure for 30 minutes. The glass petri dishes are then washed as normal to remove any excess silane.

3.5 Petri dish stand

In order to keep the petri dish tilted in a consistent angle and position for recording, a petri dish stand is fabricated using sheets of laser cut PMMA. Multiple layers of sheets are cut and four 200 mg cylindrical steel weights are placed in cut slots in the corners for alignment and to prevent movement. A layer of degassed 10:1 ratio PDMS to curing agent is poured to cover the bottom surface to increase their friction and reduce abrasiveness.

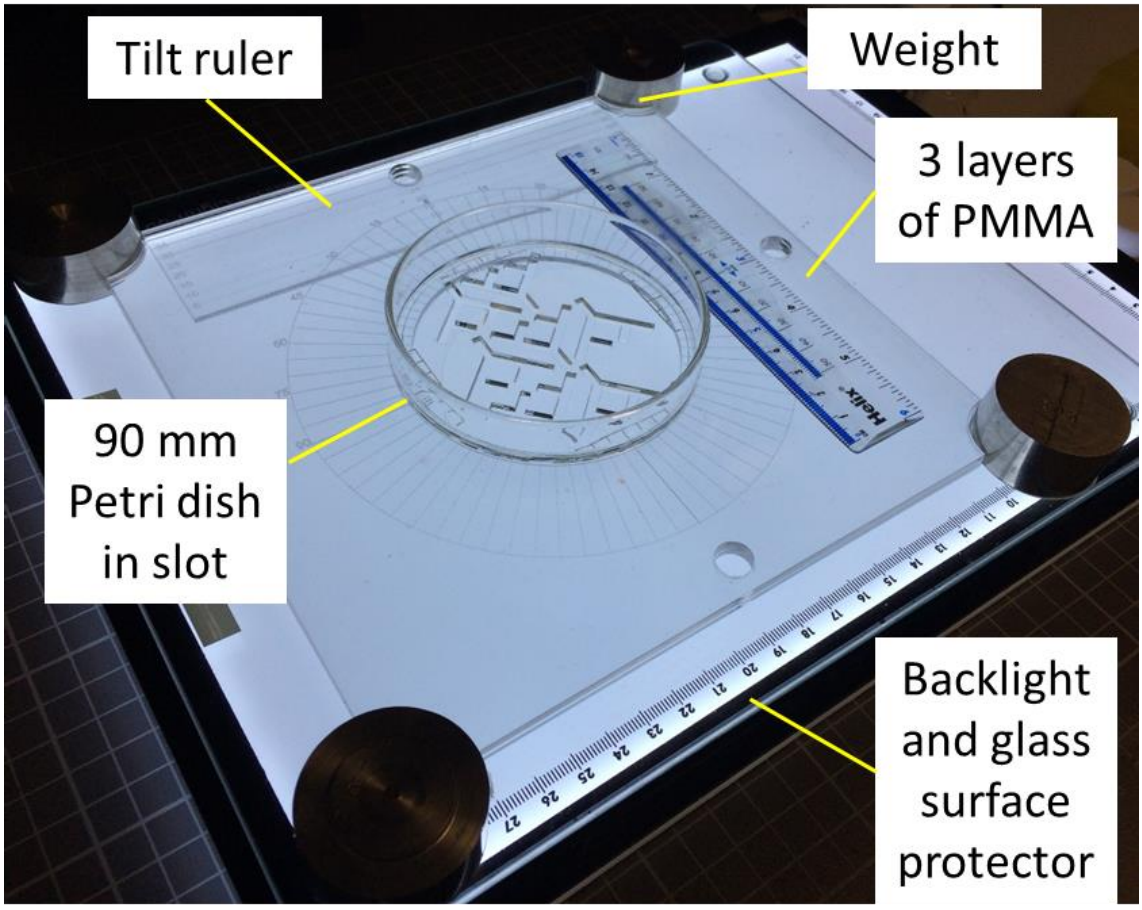

Figure 3.3 Photo of petri dish stand setup.

2 mm thick PMMA is used for each layer of the petri dish stand. These are cut according to the schematics in Appendix A. The hole at the bottom layer is 80 mm diameter, which is 10 mm smaller than the actual petri dish used. This produces a protruding groove where the petri dish is supported without obstructing the observation area in the middle. This bottom layer also has lightly cut grooves to as a protractor for measuring the angle of the PMMA wafer's design when placed in this stand. Above this layer are two pieces that are identical to the bottom layer except that it has no alignment grooves and the hole in the

middle is 90 mm wide, allowing the petri dish to sit precisely in the middle of the apparatus. This hole is still too large for the petri dish size as it is found that the petri dish has a smooth curve at the bottom, so the diameter is significantly smaller than 90 mm at the bottom and then curves outwards to be greater than 90 mm. Two layers are used so that the PMMA is thick enough to bypass the curve. A “tilt ruler” is cut using 2 mm thick PMMA and is sandwiched between the weights on one side of the PMMA setup. Lightly cut grooves mark the how far the ruler is inserted into the setup and allow it to be aligned precisely with the edges of the PMMA stand.

When measured, this ruler is approximately 1.73 mm thick due to the stock PMMA error. Additionally, the 3 layers of PMMA stacked together is measured to be approximately 5.5 mm thick, indicating each piece is 0.17 mm thinner than expected. This is due to the stock PMMA itself being slightly thinner and of different thickness between sheets and sheet parts.

The tilt of the PMMA stand is measured using a DWL 80E digital level (Digi-Pas) when the tilt ruler is inserted at 40 mm depth in the top edge. It is measured that the middle section where the petri dish is inserted is tilted at 0.5° on both the left and the right of the dish, but the top section is tilted at 0.7 to 0.8° on the top half and 0.2 to 0.3° at the bottom half. The middle section is consistent with the theoretical 0.52°, assuming the ruler is 2 mm thick as intended and no deformation is present.

3.6 Linear and non-linear arrays

Each experiment performed needs to compare the effect of the different BZ arrays and compositions while controlling for other factors. These factors include the orientation of the array with respect to the direction of gravity or the petri dish tilt, contact with the plastic versus oil, the composition of the droplets and the batch of chemicals used. To do this, each petri array is designed so that all arrays are aligned so that the main slots are upright at 0°, while some arrays are rotated 180° to account for the same array with a different direction of gravity and plastic contact location. Each petri wafer is also designed to have many repeats so that the same batch of BZ solution and oil can be observed for different configurations to determine if the wave behaviour is determined by the droplet and array composition and orientation or if the observations are due to random effects on

the droplet. In the case of this project, droplets are considered “coupled” once they have touched each other in the droplet array and can no longer move, as the interface formed when they touch should have only a small separating distance and hence should allow interdroplet communication.

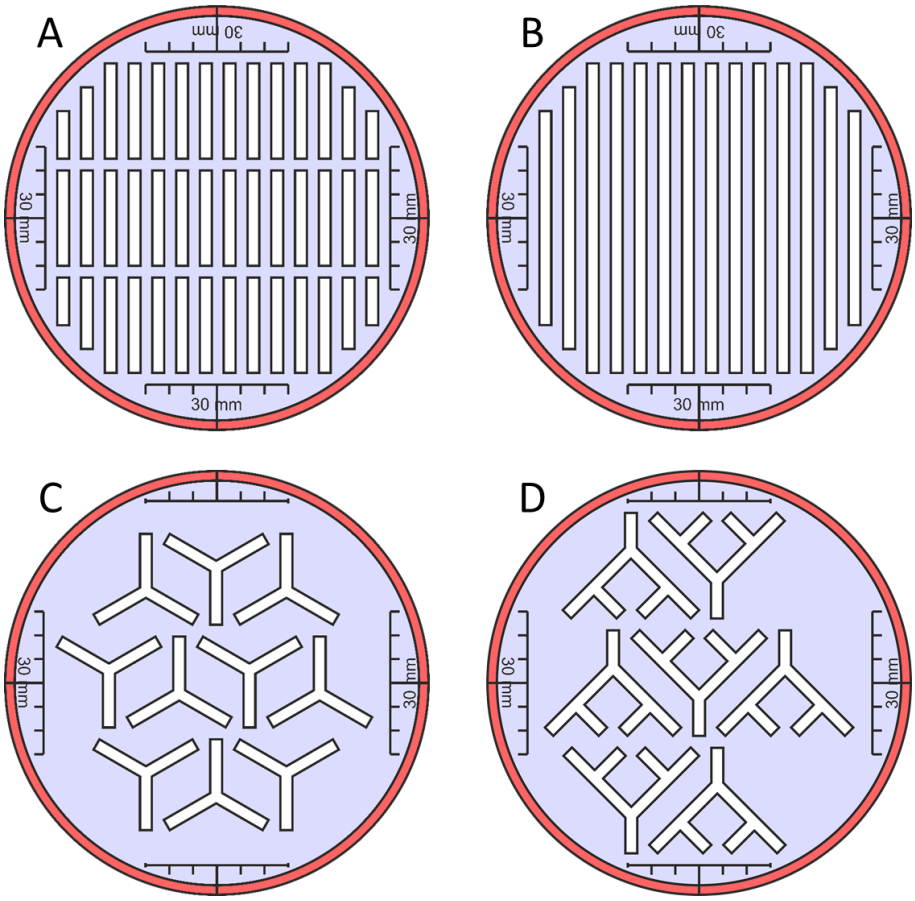

Figure 3.4 Different PMMA wafer designs. (A) Wafer for testing up to 42 arrays of different configurations for experiments needing many repeats. (B) Longer linear array for experiments where more than 20 droplets are needed. (C) Y-shaped array with only one meeting point. (D) Y-shaped array with many meeting points.

To characterise the behaviour of BZ droplets when coupled, linear arrays can be used to simplify the fabrication, set up and image processing of the experiment. The simple linear array design uses 2.5 mm slots that allow a single droplet to be placed on top of each other. This design uses multiple rows to allow up to 42 arrays to be observed during the same experiment (Figure 3.4 (A)). The slots are 20 mm in length to allow linear arrays of different length to be tested using the same array. The slots are parallel to the protractor marks at the quadrants of the wafer so that the wafer can be accurately rotated to different angles

to change the pressure of the linear arrays if necessary. This design is expanded to combine each row's slots into a single long row for the "long linear array" design (Figure 3.4 (B)).

BZ droplets also need to be coupled in non-linear arrays to determine if "splitting" the path of the array has effects on the wave behaviour. "Y-shaped" arrays are formed by welding linear arrays together at 120° angle. These arrays are arranged so that each array is oriented 180° from each other to test if the direction of the tilting of the petri dish and gravity affects the shape and stability of the arrays (Figure 3.4 (C)). This is expanded to form "multiple level Y-shaped" arrays, which have more meeting points and even more droplets in each array (Figure 3.4 (D)).

As it is proven that non-linear arrays are possible, the limits of this technique are tested using a complex maze array, which has paths that split many times at different angles. These paths do not merge with any other paths, as this would form freestanding structures unconnected to other sections of the plastic and are not stable. This simplifies the fabrication and set-up of the array and allows the stability and coupling to be tested, as the array angle changes throughout the wafer so the pressure from tilting the petri dish is not as consistent throughout the structure. The design is randomly generated from "http://www.mazegenerator.net" (JGB Service, 2017) such that the path splits and the length of the solution path is maximised. In these experiments, the BZ droplets used are all from the same stock to further simplify the set-up and analysis. A square design is tested at first to test if horizontally coupled droplets are feasible (Figure 3.5 (A)). A hexagonal maze is then tested for more complex coupling angles (Figure 3.5 (B)). Finally, a circular maze is tested where the array design area is maximised. The circular maze also tests the wave behaviour of a central region with a significantly larger number of droplets compared to all other paths (Figure 3.5 (C)).

As all the previous designs did not have any loop paths where the input can be used in a feedback mechanism, the "fish" structure from [158] is designed in PMMA (Figure 3.5 (D)). To simplify the design, fabrication, set-up and image processing steps, the design is simplified so that it is symmetrical with all paths leading to dead ends. Two pieces of PMMA are used with dowel pins to accommodate the central freestanding pillars as detailed in Section 3.4. The bottom piece consists of alignment holes for the dowel pins and slots for the freestanding pillars to be inserted. The top piece also has alignment holes and a large

hole in the middle for the channels. When assembled, the large hole is aligned with the four central pillars so that the channels between are enclosed. This design has six interconnected paths that provide feedback to each other. These feedback mechanisms further increase the complexity of the wave behaviour over time as the previous wave interact with itself as well as other wave sources in all the loops. This experiment also tests if the droplets behave in the same way when the bottom of the droplets are in contact with PMMA instead of glass, as it is uncertain if the hydrophobic and organic PMMA can disrupt the chemical reaction and coupling of the droplets. As in the maze, all droplets used in this design are from the same stock to simplify the set-up process and analysis.

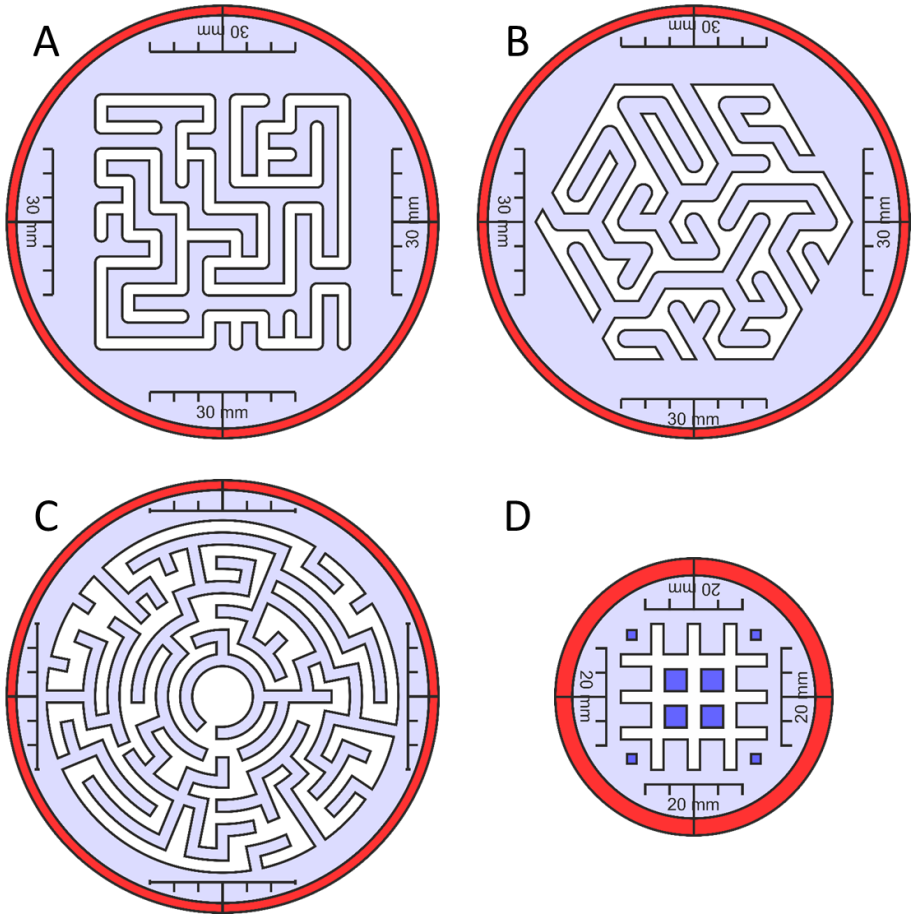

Figure 3.5 Non-linear array 2D designs with multiple meeting points. (A) Square maze design. (B) Hexagonal maze design. (C) Circular maze design. (D) Two-layer “Fish” design with many meeting points and feedback loops.

3.7 Experimental set-up

BZ solution is mixed in 20 ml glass scintillation bottles for large volumes of greater than 1 ml, but if the volume is very small such as 100 µl, the droplets are mixed on the surface of a clean 90 mm glass petri dish similar to that used for the experiment. There is a possibility that the asolectin lipid in the oil can slightly affect the BZ behaviour, but because the 38.1 mg/ml asolectin is would be equivalent to approximately 0.05 M, it is considered insignificant compared to the 0.1 M increments of each BZ component used.

The PMMA wafer and spacer ring are set inside the 90 mm glass petri dish. The petri dish is rotated so that the angle measurement lines of the scale bar are aligned with the protractor's on the petri dish stand. The BZ solution is then mixed as normal and the recording immediately started once the mixing is complete. 15 ml of centrifuged asolectin in hexadecane oil is added, ensuring there are no gaps or air bubbles under the PMMA. Air bubbles are removed by tapping on the surface of the PMMA until they are dislodged and float to the surface, ensuring the PMMA remains aligned.

BZ droplets are added into the oil using a 10 µl pipette. Usually 5 µl droplets are used to mimic their volume used in the millifluidic chip [22], though droplets of down to 0.5 µl size are possible. First, the fresh pipette tip is gently dipped in the petri dish oil before being used to extract BZ solution from the source. This ensures that the droplets formed are coated in a thin layer of oil, which prevents the droplet from "sliding" on the surface of the oil before fully entering. It is observed that when the pipette tip dipped in oil touches a small BZ droplet on a glass petri dish, the droplet quickly changes colour and slightly spreads out over the glass. This only happens if touched for the first time this way and does not occur for clean pipette tips.

The BZ droplets are pipetted out as a single droplet in the air above the oil and allowed to gently fall in and sink to the bottom. Care is taken not to immerse the droplet and pipette tip into the oil until ready as an emulsion is formed when the solution is pushed out. These droplets are pipetted above any arrays and allowed to slide down the slot before the next droplet is added. This is to allow the droplet time to build up a layer of phospholipid for its membrane surface and avoid disturbing already established arrays. If different types of droplets are used, droplets of the same type at the bottom of the arrays are pipetted first, followed by other types of bottom droplets. The process then repeats for the next droplet

in each array for each type. This is to minimise the time needed to pipette all the droplets into their positions and allow more time for the droplets to build up the phospholipid membrane.

In complex non-linear arrays, droplets are added until the entire array is filled with as little space for the oil as possible inside the array slot. This is to prevent the droplets from moving around during the experiment due to any small tilt in the petri dish. Extra droplets are added if any droplets fused in the array, as the fused droplet is observed to take up significantly less space, so the array may have enough space to move around after fusion.

3.8 Image processing

A FIJI (Fiji is just ImageJ) (National Institute of Health, USA) macro is used to cut images from each slot of PMMA wafer. Each cut is 15 pixels wide to allow for errors such as digital noise, gas bubbles, view blocking and misalignment to be minimised and smoothed. This macro functions by opening each frame of the recording and cutting slices from the middle of each slot in the PMMA wafer in fixed locations, which do not change once the recording has started. The top-left corner, rotation angle and X and Y-axis slot distances of the wafer design are used for calibrating the macro. The macro then copies each “Region of Interest” (ROI) and stores each slot’s image in the folder corresponding to its coordinates before repeating this for all slots.

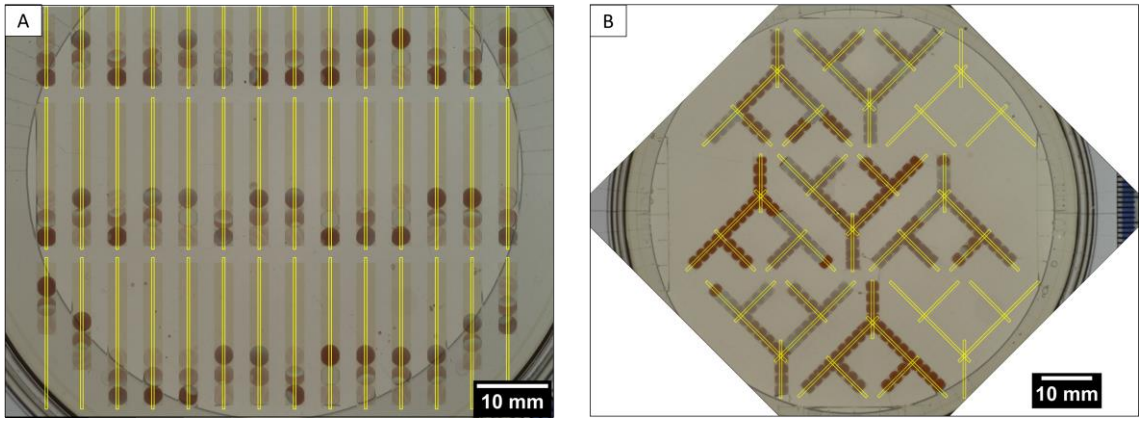

Figure 3.6 Automated cutting of 15-pixel wide slices from each slot of (A) 42-array PMMA wafer and (B) Y-shaped array with many meeting points. Image is rotated and all slices of the same orientation are cut for each individual arm of Y shape. Yellow rectangles mark regions cut out as individual images.

This cutting procedure is expanded for Y-shaped non-linear arrays, an algorithm is designed to use the top-left of the slot as before, but this coordinate is used to calculate the central meeting point of the array, which is used as the point of reference for all other meeting points and regions. Rotations are computationally expensive and increase the time of the algorithm, so to minimise the number of rotations performed, all cuts at a certain angle for the analysed frame are performed at the same time. The algorithm then cuts the upright regions as usual, and then rotates the entire image by 120° clockwise to cut each specific region of the Y shape at that angle. The algorithm then rotates it by 120° anticlockwise twice to cut the regions that are left. As the slot next to this shape is rotated 180°, the algorithm also alternates the point of reference to consider this. An additional variable is added so that the first array of each row can be rotated according to its orientation, as different rows may start with different orientations. Examples of cut slots are shown in Figure 3.6.

Another macro is then used to open each folder and stitch the images inside using the "Make Montage" function to form space-time plots, where the x-axis corresponds to time from left to right and the y-axis corresponds to the droplet location in the slot. Individual images are "Mean smoothed" by 15 pixels before the stitching process, meaning each horizontal row of pixels is averaged such that it is uniform in the x-axis. This smoothing removes defects in the cutting procedure, which may cut two or more waves travelling perpendicular to the cut direction, forming an artificial low intensity region in the middle of the same frame. This effect is shown in Figure 3.8. Each space-time plot is then saved corresponding to its slot coordinates and the process repeats for each folder. This procedure is shown in Figure 3.7.

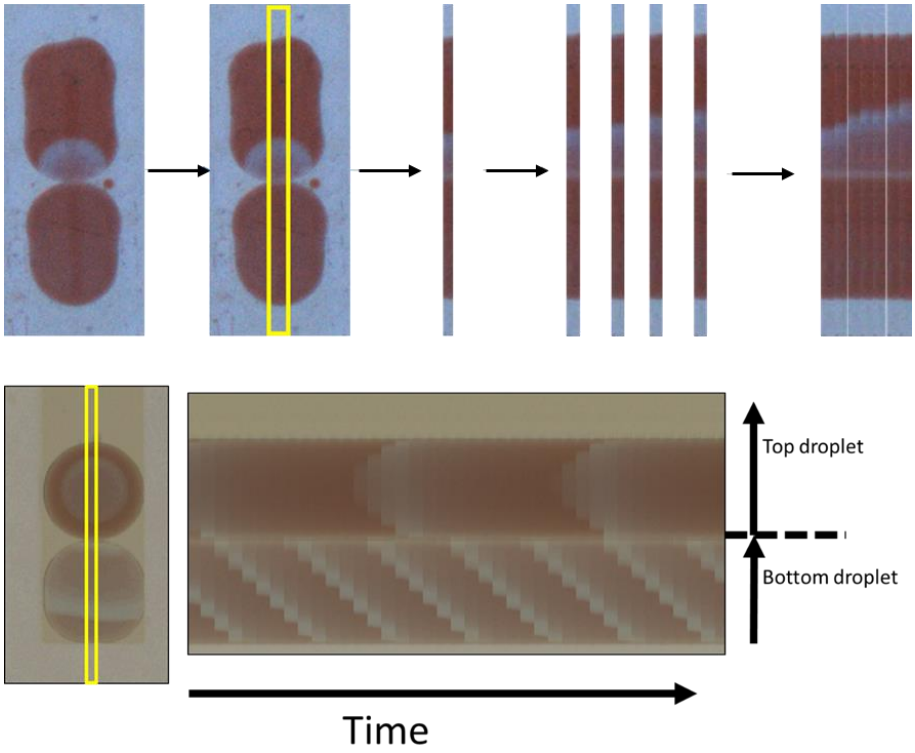

Figure 3.7 Steps for converting original image of droplets in droplet array into space-time plots. Example space-time plot shown underneath with significantly different wave frequency and direction of droplets. Droplets are 2.5 mm in diameter

A third macro opens each space-time plot and scans the entire width of the space-time plot in 5-pixel increments to form a pixel intensity plot. This macro first converts the space-time plot to show only the blue channel, which gives the highest contrast between the background of the droplet and the wave [141]. It then plots the mean brightness of all five pixels on that x-coordinate along the entire width of the space-time plot and saves it as a CSV file of the corresponding coordinate and then repeats this for the next five-pixel increment until the end of the image. This is so that the user can choose the location at which the measurement is taken as each location may have obstructions such as bubbles or the rounded corner of a droplet. This also allows measurement of different sections of the droplet (i.e. the top half or the bottom half) if other analyses need to be done. The droplets and their waves are also too small for 15-pixel increments without also picking up newer waves or a significant amount of red reduced region, which affects the pixel intensity measurements. In contrast, one-pixel increments are also not used as they are vulnerable to digital noise and other obstructions as mentioned before and cannot be smoothed.

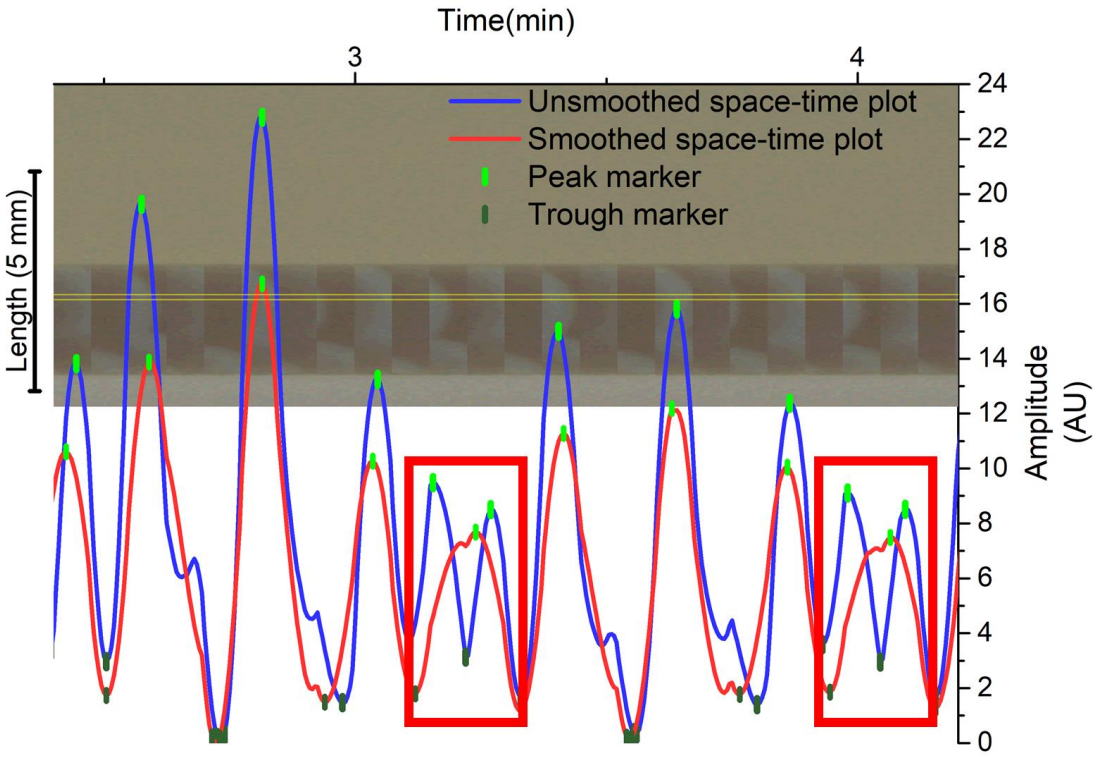

Figure 3.8 Graphs of space-time plots with each slice smoothed (red) and without smoothing (blue) with unsmoothed space-time plot image in the background for comparison. Unsmoothed plot has extra peaks due to the same wave appearing in half of a slice in the previous frame (highlighted with red boxes). Amplitude is measured in arbitrary units (AU) of pixel intensity. Peaks detected are marked in light green and troughs in dark green. Horizontal yellow lines on space-time plot mark where pixel intensity measurement was taken.

The resulting pixel intensity measurement values form a graph with periodic peaks where each wave is detected, where the y-axis corresponds to the pixel intensity measurement between 0 and 255 arbitrary units, where higher values are brighter, and the x-axis corresponds to time in the experiment. The blue oxidised state has a brighter appearance and hence higher intensity value whereas red reduced state has a darker appearance and hence lower intensity value. These graphs are not flat on the x-axis as there is a background pixel intensity from the red or blue colour of the droplet's background reduced state between waves, which varies depending on the droplet composition. This can also change due to background lighting conditions and camera settings, but these are kept constant during experiments.

The goal is to analyse the characteristics of these waves and their evolution over time using the pixel intensity graphs measured from the space-time plot. However, the characteristics of the periodic wave and the overall graph are unique between each droplet composition and each repeat experiment, so a consistent method of removing the noise and offsets must be developed. To do this, macros are developed as in Section 3.9.

3.9 Analysis of waves

The graphs obtained from the image processing steps in Section 3.8 are periodic graphs, where the "peaks" of these graphs are equivalent to the waves observed when the BZ droplet oscillates. Hence, the peaks characteristics are directly comparable to the wave characteristics as well. To study the BZ behaviour, these peak characteristics are analysed for patterns in their behaviour over time and in comparison to different BZ compositions.

Origin (OriginLab Corporation, MA, USA) is used to process each of these individual graphs and then analyse them using the built-in peak finding and statistics functions. The graphs are opened and aligned with the space-time plot itself for reference. When using the smoothing algorithms and filters, the smoothing windows chosen are within multiples of 15 pixels to ensure they are according to the number of frames, but are otherwise optimised to values that are manually chosen by adjusting the value until there is no noise or significant errors in the final processed graph, such losses of peaks and significant differences in peak height for too many peaks. This methodology is chosen instead of fixed values so that the final graphs and detected peaks that are as accurate as possible compared to the original. The window of the filters and functions used is defined as the total number of data points taken into account to get the value of that pixel in the x-axis. Half the number of data points are to the left of the analysed point, and the other half from the right. The graphs obtained from these processing steps are in arbitrary units (AU) of pixel intensity unless otherwise stated. The time is in pixels, which is converted to seconds using the frame rate of 2.5 seconds/frame and slice width of 15 pixels/frame.

For the purposes of this analysis, terminology is defined for each different characteristic analysed. The "pixel intensity" refers to the measured brightness of the pixel in the x-coordinate in arbitrary units (AU). This brightness value is the measured brightness of the BZ oscillation waves as well as its relative brightness (i.e. contrast) to the background or

reduced part of the BZ droplet. This background is defined as the “baseline”. The “lifetime” of the droplet is defined as the time between when the droplet starts oscillating until the time when it has stopped oscillating. This is assumed to be at the time when the final component of BZ is added to the stock solution because in the case of MA BZ the droplet starts oscillating once mixed. The “wave count” of the droplet is defined as the total number of oscillations observed up to that particular point in time. As the lifetime and frequency of the droplet is different for different compositions, this characteristic is not equivalent to the frequency of the oscillations. However, the gradient of this wave count graph can be used to determine the frequency at that point in time. The “total wave count” of the entire oscillation lifetime is determined by taking the final value of the wave count after the droplet has stopped oscillating.

It is also found that as time goes on BZ droplets undergo changes in behaviour, which can be seen both visually in the recorded video and in the graphs. These changes have similar characteristics between droplets of different composition and can be divided into distinct “phases” in the oscillation lifetime. The definition of a phase change is when a droplet has a significant change in wave characteristics compared to at least the previous 5 oscillations that is then continued for at least 5 oscillations after the change. This large change is defined to occur over approximately 5 oscillations. These phase changes typically show a significant change (doubling or halving) of amplitude or frequency. These “phases” are described in Chapter 4 and are divided into the “initial”, “middle” and “late” phases. The “initial” phase typically has a high frequency and low amplitude, while the “middle” phase has a low frequency and high amplitude and the “late” phase has a sudden increase in frequency and reduction in amplitude.

As a precaution to minimise the introduction of rounding and conversion errors, the processing steps of the graphs are done using arbitrary pixel units as in the raw measurements. These are only converted into their final units only when the final graphs and tables are to be presented. Another precaution is that any offsets to the time axis to calibrate the time of the droplets is also not done until the final graphs are to be presented to prevent errors in this offset from being carried over between processing steps.

First, the region where the original graph is measured is manually chosen to exclude regions with visual obstructions from gas bubbles or the pipetting step. This is the graph obtained

from the final output from Section 3.8, which is a measurement of the 5-pixel high region of the space-time plot, with peaks where bright waves are observed. This graph has step changes between each frame due to the smoothing of the space-time plot, random noise which causes fluctuations in the measurement between frames, and an offset from the x-axis due to the brightness of the background. This is filtered by the pixel intensity (y-axis) to remove any remaining disturbances. The window of this filter is manually selected to remove data points due to noise or visual obstructions that are too high or low in intensity. This is illustrated in Figure 3.9 (A) and (C).

The graph is first smoothed with the Savitzky-Golay filter [159] across 30 pixels to smooth the oscillations between two frames of the recording. This creates a local polynomial regression across each pixel, smoothing it while preserving the peak height and width. The resulting graph has step gradients and random noise smoothed. This makes it easier for the automatic peak finding function to detect peaks without mistakes. This is because the peak finding function works by finding places where the gradient changes from positive to negative and vice versa within the window specified. Large steps in gradient such as from noise can be mistaken as a peak and will need to be manually curated. The resulting graph is shown in Figure 3.9 (B).

A percentile filter is then used for both the zeroth and 100th percentile between a window of 180 to 14,400 pixels for both the original graph and the smoothed graph. The range for the window is usually between 630 and 2880 pixels for most droplets, but the large variation in BZ behaviour for different compositions causes the large total possible range. The window is adjusted according to the width of the peaks to be analysed to ensure these graphs are as close to the shape of the top and bottom of the graph as possible without any significant fluctuations inside each peak which can significantly affect the peak characteristics. The window of this filter is usually between one and two periods of the largest peak in size, but needs to be manually adjusted so that the graph continues to follow the shape of the troughs even when significant changes in droplet behaviours occur, such as in between different phases of the oscillation lifetime. This percentile filter selects all points in the window, arranges their values in ascending order and selects the value at the percentile selected as the new value for each point. The zeroth percentile gives a baseline for which the graph can be flattened on the x-axis. The 100% filter gives the original height

compared with the smoothed height. The resulting graph for the 0% filter is shown in Figure 3.9 (C) in red.

It is possible that the smoothed graph has become shorter or taller due to the smoothing process. To ensure that the peaks of the final graph are of the same height as in the original, the distance between the 0% and 100% filter graphs is taken for both the smoothed and unsmoothed graph for each x-coordinate. The ratio between these is then compared. By multiplying the ratio between the initial and smoothed height with the flattened graph, the height of the graph can be made more accurate to its original value. As the top of the peaks are further apart compared to the troughs, a larger window is usually used for the 100% filter to prevent the inaccuracies. As the 100% filter graphs are only used to compare the relative height of the original and smoothed graph, it is less susceptible to errors in the graph shape since the same shape is usually traced by the both graphs, with only differences in the total height. The final flattened graph is shown in Figure 3.9 (D).

The “Peak Analyser” function in Origin is then used to detect and numerically analyse each peak. This is done by selecting the window at which there are peaks present in the plot, then setting the baseline as $-1e^{-5}$ that moves the graph a very small amount above the zero line to allow for the base peaks and troughs to be detected without significant gaps. The peaks themselves are filtered according to 1% of the maximum height to detect smaller peaks and a local maximum of 15 pixels to correspond to one frame. Quantities such as the peak number, time, area amplitude, start time and end time can then be obtained. These can then be analysed for further derived quantities and graphs plotted. The output of this process is shown in Figure 3.9 (E).

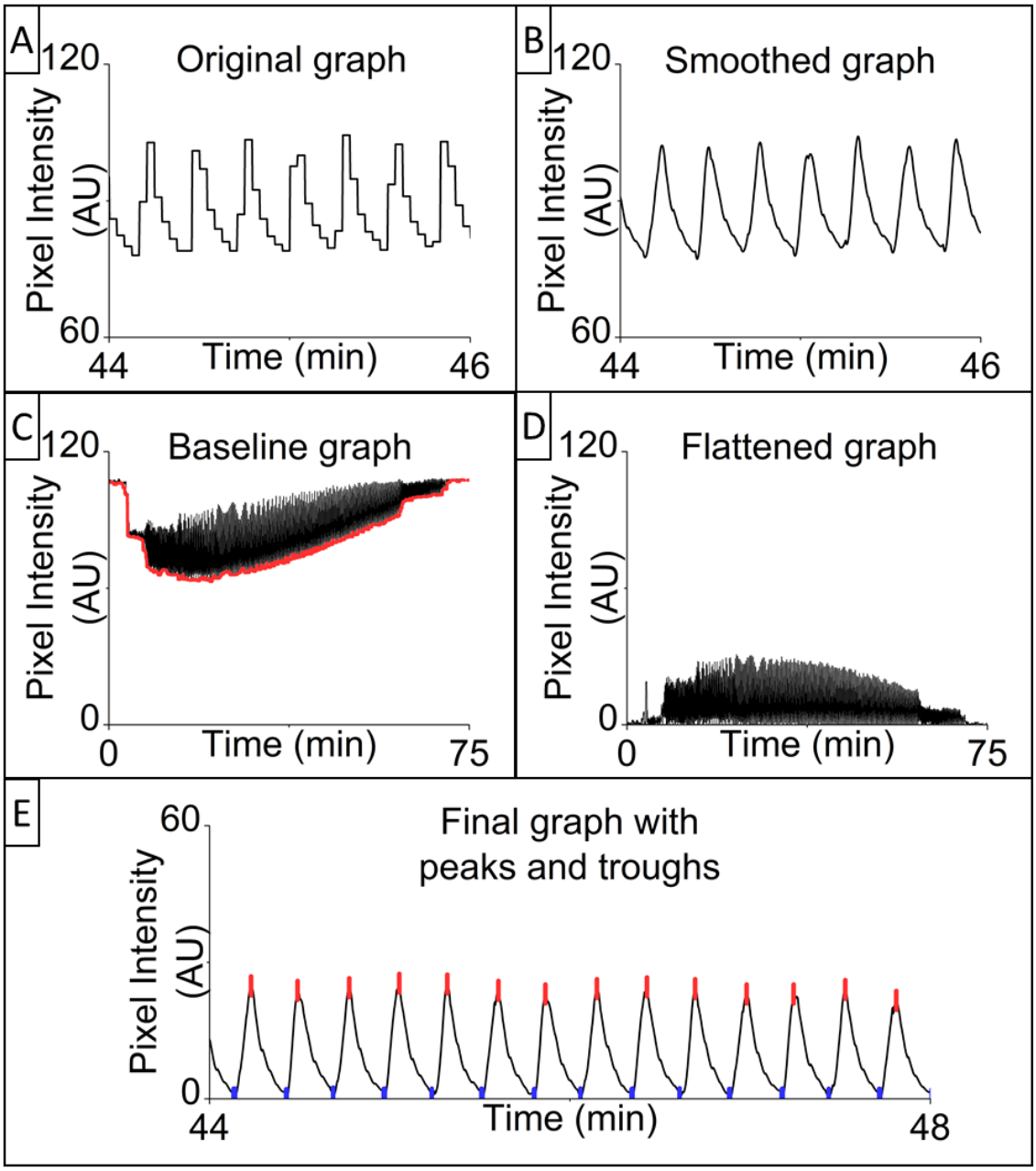

Figure 3.9 Processing steps for smoothing and flattening original pixel intensity graph and analysing peaks in Origin. All pixel intensities are measured in arbitrary units (AU). (A) The original unsmoothed graph from the measurement of the space-time plot. These have step changes between each frame, random noise and an offset. (B) Graph smoothed with Savitsky-Golay method, so noise and step changes are no longer present. (C) Baseline calculated using 0% percentile filter (marked in red), which selects the lowest value within the window specified. This is the value of the lowest trough. (D) Graph is flattened by subtracting the value of the baseline at each point. (E) Results of the peak finding function, where peaks are marked in red and troughs in blue.

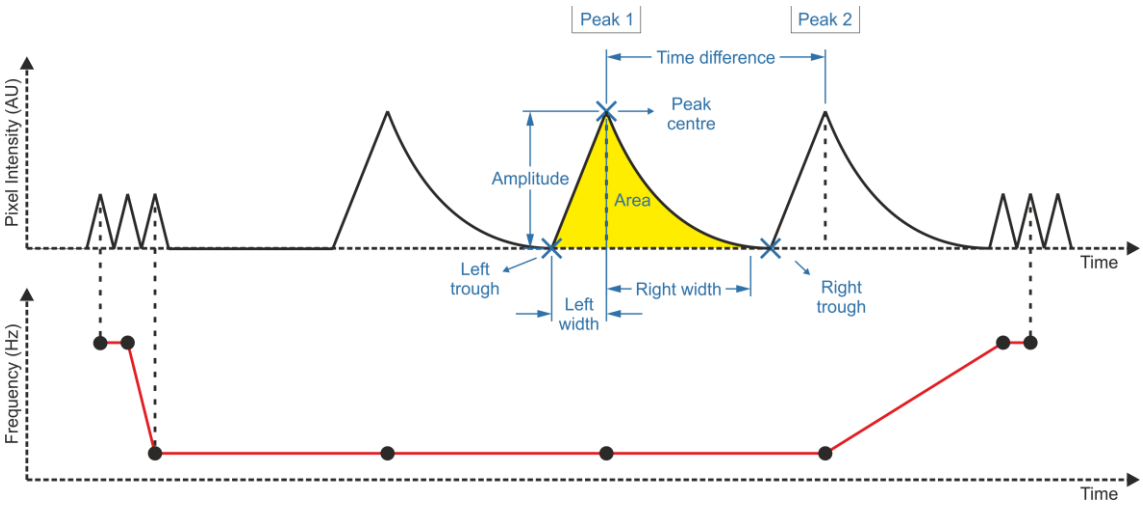

Figure 3.10 Diagram of peaks from pixel intensity measurements in arbitrary units, with wave characteristics defined and its accompanying frequency graph. The peak being analysed is labelled Peak 1 and its area measured is highlighted in yellow. The positions of the peak centre, left trough and right trough are marked as crosses and are used to calculate the different peak parameters. As the frequency is calculated as the time difference between the current analysed peak and the peak after, the final peak does not have a frequency value and changes in frequency are observed before they are observed in the pixel intensity graph.

The peak analyser's detection and analysis process is semi-automatic. It automatically detects peaks and analyses its characteristics, but extra peaks and missing peaks must be manually curated and the range of detection must be manually specified for each droplet. In the case of this project, it was decided to measure all possible peaks that can be detected in the space-time plot once the droplet has reached the bottom of the PMMA slot and the waves are visible in both the graph and space-time plot. This is done regardless of the time when the droplet has entered the oil and the length of the pipetting step.

While this is not ideal, it allows each droplet peak to be analysed blind without as much subjective input, as it is less likely that peaks are discarded for being in a different oscillatory phase and displaying different behaviour (as observed in Section 4.1 and 4.4), or due to other parts of the viewing area being disturbed at that time. This also saves time as the significant changes in phase or droplet state need to be observed and compared so they need to be analysed together in all cases for consistency and direct comparison. In tests using fixed start times of the analysis and of changing the smoothing parameters in Origin,

no significant differences in the wave characteristics and total wave count were found, as only the short initial phase of the droplet behaviour is affected.

The output of the peak analyser gives peak characteristic values for each individual peak, where the peak is formed due to the increase in pixel intensity (i.e. brightness) from that specific frame of the space-time plot caused by the oscillation of the BZ solution forming a wave. This directly correlates with the wave characteristics and allows the evolution of each characteristic over time to be analysed. The main wave characteristics analysed are the frequency, amplitude and area of each peak, as these showed significant changes over time and between droplets of different composition. These characteristics also change significantly during different phases of the oscillation lifetime as in Section 4.1 and 4.4, allowing the phase changes to be observed using these characteristics as well. The peaks and characteristics analysed are shown in Figure 3.10.

The frequency of the oscillations is calculated as the inverse of the time difference, which is the x-distance between the top of the peak being analysed to the top of the peak after, measured in Hz. This is the "frequency" at that particular point in time between two adjacent peaks, and allows the evolution of the frequency over the lifetime of the droplet to be monitored. As the frequency is calculated in this way, the actual time difference and frequency is for the time between the peak being analysed and the future peak, so changes in the frequency are observed in the frequency graph before changes in the real pixel intensity measurement. This method was initially chosen as offsetting the frequency value to a point between peaks would complicate the design of the macro, introduce rounding errors in the resulting graph plot and make direct comparisons between the peak values and the frequency more difficult for later analysis.

The amplitude is defined as the distance from the top of the peak to the x-axis, which is at the bottom trough and is measured in arbitrary units (AU) of pixel intensity. This value can be affected by the baseline obtained from the percentile filter, but this is assumed to be negligible compared with inaccuracies from other sources as it is typically an offset of less than 3 AU compared with the typical distance of approximately 15 to 45 AU between peak and trough. This amplitude value is the pixel intensity after the background pixel intensity of the baseline has been removed, so it is the contrast of the wave versus the background,

which is the difference in oxidation between the wave and the droplet background. This amplitude value is hypothesised to be correlated with the “power” of each oscillation.

The area is the sum of all amplitude values from each x-coordinate pixel in a detected peak from trough to trough. This is also measured in arbitrary units (AU), and is affected by the pixel intensity of each video frame of the recording in the peak, the number of pixels in the x-axis cut out in the image processing step used for each frame, the shape of the peaks and the baseline obtained from the percentile filter similarly to the amplitude. This value is directly proportional to the number of pixels for each frame cut out as slices for the space-time plot, but since this value is the same for all experiments and repeats the evolution and pattern of the area graphs can be compared directly with other values. This characteristic is analysed as this takes into account the oxidation level of the peak over the entire time the peak is present. The peak can have slightly different shapes because the rate of reduction of the BZ droplet is different at different times and with different BZ compositions. Also, as this area is the total amount of oxidation the BZ wave experiences over the time of the peak, it can be hypothesised to be correlated with the “energy” of the oscillation. This is in contrast with the “power” correlated with amplitude, as this is the total power over the entire time the peak is present.

Another characteristic that is analysed is the left and right width of the peak. These are the x-axis distances between the top of the peak and the left and right trough respectively, corresponding to the time measured in seconds. The right width corresponds to the time taken for the oxidised BZ droplet to return to the reduced state, which is the background intensity of the baseline. The left width corresponds to the time taken for the droplet change from the reduced state to the oxidised state. The right width graph typically shows a similar evolution as the graph for the time between peaks before it is converted into the frequency graph. The left width did not show significant change, possibly due to the low resolution from the low frame rate of the recording. A similar characteristic calculated by the peak finding function is the full width half amplitude, which is the left and right width measured from the top of the peak to the x-axis point at half of the amplitude instead of the trough. However, these characteristics also did not show significant changes over time. As the left width and full width half amplitude characteristics did not show significant changes over time, they are not analysed in this project. However, analysing these characteristics may be useful for future experiments with a higher recording framerate.

Once the analysis of individual droplets is completed, the statistical analysis is performed, where characteristics of repeats with the same composition are compared with other compositions. To do this, the behaviour of all the peaks must be simplified into single values for each BZ composition so that they can be compared. A file is created with the names of each analysed droplet added to a lookup table, and characteristics of each peak in every repeat of the same composition are compiled. This lookup table is used in the macro to copy data from the spreadsheet of the analysed droplet to its appropriate droplet composition so that further processes can be performed. The statistics function in Origin is then used for each characteristic.

The mean of all repeats is taken as the representative properties of all droplets of that composition and graphs can be plotted to observe trends in the changes. The median, or 2nd quartile, is computed as $(1-g)x_{(j)} + gx_{(j+1)}$, where j is the integer part, and g is the fractional part of equation $\frac{(n+1)}{2}$ and n is the number of samples. The mean between all repeats is calculated by getting the sum of all samples and dividing it by the number of samples.

Characteristics such as frequency, area and amplitude consist of hundreds of values from all oscillations and need to be simplified into a single representative value. To do this, the median of frequency, area and amplitude of each droplet is obtained so that any extreme spikes are not counted as typical properties. The median usually takes the most common peak behaviour, as it selects a value in the middle of an ordered list and all outliers or extreme values are at placed at either end of the list. This is more useful compared with the mean which takes all values into account so extreme values can significantly skew the final result. This median value is found using the statistics function of Origin and then used to represent that characteristic of all peaks detected in that experimental repeat.

The time of the first and last peak detected is compiled as well, which correspond to the first and last oscillation detected. The first oscillation can be taken as the time when the droplet stops being in the induction phase where there are no oscillations, and the last oscillation can be the total oscillation lifetime before the droplet has become exhausted. In the case of MA BZ droplets, the “lifetime” is defined as the total time from when the solutions are mixed until the droplets are exhausted, as the stock solutions start oscillating immediately after they are mixed, corroborating with [85]. In the case of MA-CHD BZ

droplet statistics, some droplets will have an induction time as the CHD ratio increases. In this case, the time of the first oscillation detected is also compiled as this shows when the BZ solution has finished the induction phase and started oscillating. The time between the first and last oscillation can then be taken as the lifetime of the droplet. The time of the last oscillation is still useful for MA-CHD BZ analysis as the time of the final oscillation can be made the same if the induction time is longer while having a shorter oscillation lifetime.

The total sum of the amplitude and area for all peaks in each repeat is also calculated during this statistical analysis. As the amplitude and area are hypothesised to be the “power” and “energy” of the waves, these values can be used to determine if low amplitude and area waves combine with a high total wave count to form a sum total that is determined by a specific BZ component.

These simplified characteristics are then plotted versus the concentration of the BZ component to be compared. As the spread between each repeat may be large, the mean of the repeats is also plotted on the same graph to visualise the effects. These statistics can then be used to compare between droplets in different contexts, such as droplets isolated as single droplets or droplets placed in an array. As the order of when the droplet is added into the oil and its position in the array is observed to have no significant effect on the characteristics, this is not presented in this thesis.

As each of the wave characteristics are directly tied to a peak in the original measurement, different characteristics can be plotted in the x and y-axis to compare their combined characteristics. This is useful to observe if a combination of characteristics can be attributed to different phases of the droplet behaviour. These graphs are plotted in three axes, with the different characteristics as the x and y-axes and time as the z-axis, which is presented as a colour map where red is for peaks earlier in the oscillation lifetime followed by green and then blue. Ratios of different characteristics such as amplitude and area can be plotted as well to determine if the area of a droplet changes despite having the same amplitude due to changes in the shape of each peak. Using a macro for representative values from the statistical analysis, several different combinations of these are plotted and analysed for patterns which can be attributed to changing a specific BZ component. Interesting patterns attributed to specific BZ components are then presented in Section 5.3.

Using these techniques, the characteristics of each peak of BZ droplets of different composition can be analysed and the representative values of each can be obtained. With this characterisation work, later experiments can be designed to use such oscillation behaviours to influence the droplets in arrays of droplets of different composition and topology.

Chapter 4 Droplet behaviour over time

A complexity of analysing BZ droplets is that their behaviour can evolve over time. This makes it more difficult to determine if any changes to the wave pattern or oscillation parameters later on are due to the independent evolution of the BZ reaction or due to effects from the droplet neighbours. Hence, it is important to analyse how these droplets evolve over time while having different compositions and to find common phases to classify its evolution.

The 42-array petri wafer design from Figure 3.4 (A) is used for these experiments as they allow observation of many droplet compositions at once in the same experimental conditions. It is assumed that there is no chemical communication between the 2.5 mm slots nor through the oil above due to the large distance between each slot and the plastic blocking different arrays. Using this wafer design allows the geometry and placement of these droplets to remain the same between each different experiment, which is exploited in the image processing macros to produce space-time plots and analyse them as explained in Section 3.8 and 3.9. Due to the large number of repeats and different compositions observed in the same conditions at the same time, this design allows the analysed wave characteristics to be compared and statistically analysed by comparing characteristics of different repeats and BZ compositions. This is done as described in Section 3.9 in Chapter 5 and Chapter 6.

At first, only visual inspection of common phases in the oscillation lifetime is performed to give insight into the natural evolution of the droplet appearance. These common phases are similar behaviours and appearances of the droplets and waves that are observed between droplets of different compositions at certain times in proportion to the droplet lifetime. Identifying such phases is important in understanding the evolution of the behaviour when droplets are isolated for later comparison with droplets in arrays. It is also useful for developing the methodology of the image processing and analysis explained in Section 3.8 and 3.9. This developed methodology is then used to numerically analyse each wave characteristic and their evolution for changes that are not directly observable as in Section 4.4.

4.1 Phase changes over time

Common phases that all droplets of different compositions go through is first visually identified. These phases have similar behaviour and appearance of the droplet and waves, even between different repeats and droplets of different composition. Even then, these can have slight differences in wave pattern, duration and other parameters. Identifying if all droplets can undergo similar changes will give insight to form a method of processing and analysing these waves.

When BZ droplets are added into the oil, the intensity of the ferroin colour is observed to slowly reduce with time until it becomes transparent. However, this effect is significantly faster for oscillating BZ droplets, though BZ droplets that have stopped oscillating in the red reduced state and oxidised blue BZ droplets that never oscillated also experience this gradual discolouration, but at a significantly slower rate. This discolouration is faster for droplets with higher H_2SO_4 or $NaBrO_3$ and slower with higher malonic acid concentration. These droplets discolour slower with higher ferroin concentration, but this could be because they also stop oscillating faster compared with lower concentration droplets.

When the droplets are first mixed and added into the oil, they have a higher blue intensity background and waves that have a low contrast. This is referred to as the “initial” phase as it exhibits a variety of wave patterns and behaviours that are not consistent between repeats in the same experiment and stock solution. While planar waves are possible, they usually exhibit low contrast or spiral wave patterns, where many wave sources can be present at the same time and oscillate at high frequency. After some time, these droplets “stabilise” to have a red background and waves with higher contrast, but the time taken and contrast of the red background versus the blue waves depends on the initial composition of the droplet. It is found that if the concentration of H_2SO_4 and $NaBrO_3$ is higher, this initial phase lasts longer. However, if the concentration of malonic acid, CHD or ferroin is higher, this initial phase is shorter and may have a smooth transition instead of a sudden drop in frequency and amplitude. This corroborates with the role of H_2SO_4 and $NaBrO_3$ in Process A and B, which is responsible for oxidising the catalyst whereas malonic acid and CHD reduce the catalyst [74]. It is hypothesised the ferroin has similar effects to the malonic acid and CHD as H_2SO_4 and $NaBrO_3$ are used in excess so having a greater amount of ferroin increases the activation energy needed to oxidise the entire droplet, so

the high rate from using excess H_2SO_4 and $NaBrO_3$ is reduced so the droplet can achieve a steady state faster. During this phase, the droplet forms waves that have a significantly lower contrast from the background and higher frequency. The wave speed is not significantly faster compared to after the droplet has stabilised, but the waves are significantly thinner and multiple waves can be seen in the droplet at the same time. The evolution of these behaviours is observed in Figure 4.1.

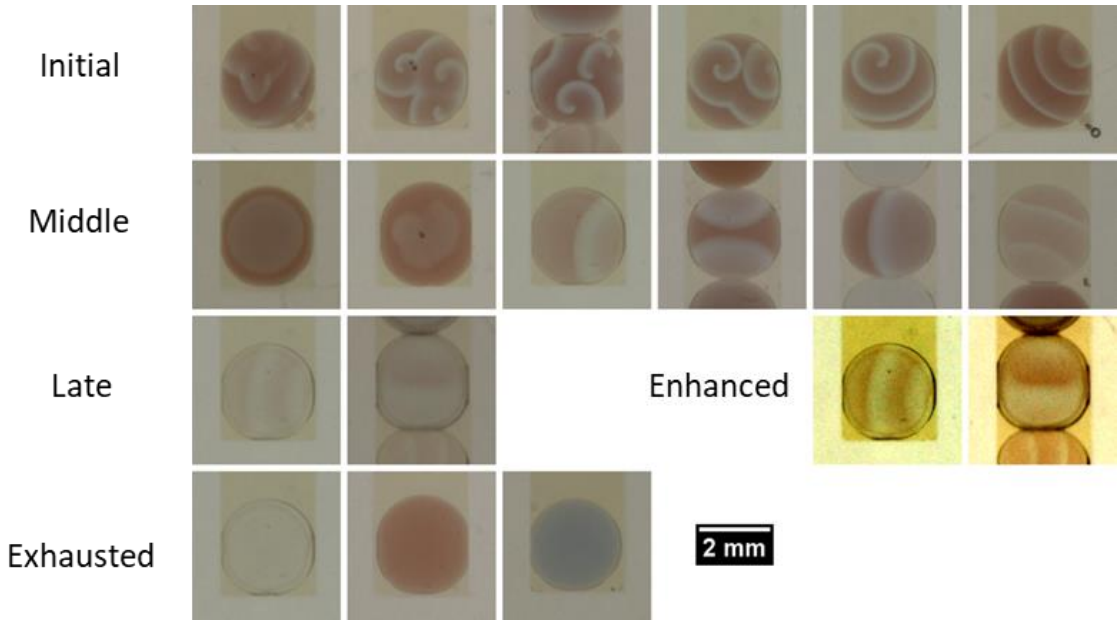

Figure 4.1 Different phases of droplet lifetime and the variety of wave patterns that can be formed. In the short "initial" phase, the droplet has high frequency, low contrast waves, and can have spiral shape or planar shape. The "middle" phase has waves with a lower frequency in the circular or planar shape. This phase is the longest phase with the most number of oscillations and is considered the normal behaviour of the droplet. As time goes on, the droplet turns more transparent and the contrast between the waves and background reduces. When the droplet has become almost transparent with low contrast waves it suddenly enters the short "late" phase, where the oscillation frequency increases significantly and wave contrast reduces even more. After this phase, the droplet enters the "exhausted" phase where no more oscillations are observed. In this phase, the droplet is usually transparent, but compositions with a higher malonic acid or CHD form red droplets while droplets with a higher ferroin content form blue droplets. Each droplet shown has different compositions of MA BZ, but within the ranges of concentration as shown in Table 3.2 on page 47.

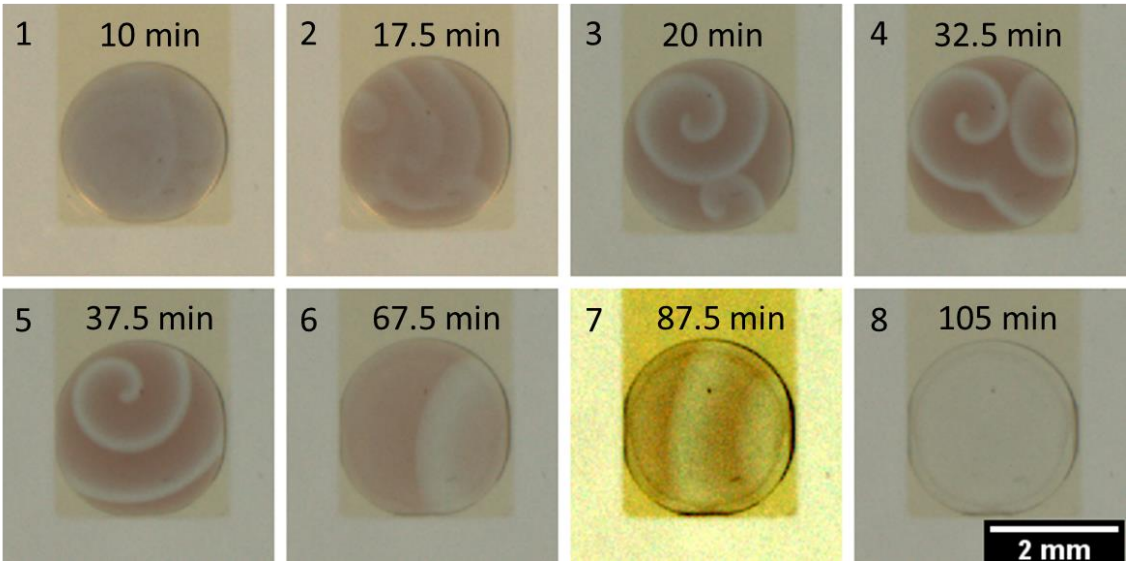

Figure 4.2 Images of different wave patterns in the same droplet at different arbitrary time steps. 1 and 2 show high frequency and low contrast waves where no distinct wave shapes or sources can be observed. 3 and 4 show the droplet with two spiral waves, one anticlockwise in the top-left and one clockwise in the bottom. The clockwise spiral centre moves anticlockwise along the droplet edge until the anticlockwise spiral extinguishes it. 5 shows the remaining anticlockwise spiral. 1-5 are all in the "initial" phase of the droplet. 6 is in the "middle" phase, and shows a planar wave after the spiral is extinguished and the source moved towards the PMMA wall. 7 shows high frequency planar waves in the "late" phase, with a higher oscillation frequency where two waves can be seen at the same time and just before the droplet stops oscillating (Contrast adjusted between 110 to 160 for visibility). 8 shows the "exhausted" phase droplet after it has turned transparent and stopped oscillating. Time measured from when stock mixed.

After this initial blue oxidised state, the droplet enters into a steady state where it oscillates with a lower frequency, referred to as the "middle" phase. This frequency gradually decreases as time goes on. Planar waves and circular waves are more common in this phase, and only one or sometimes two wave sources are present inside the droplet. If one wave source is "stronger" than another, it is possible for the waves from this source to "push back" where they interact until it eventually extinguishes the other wave source. This is the most common way for waves to "change direction", where a new wave source initiates and gradually pushes back the original wave source. In some droplets with lower $NaBrO_3$ concentration, it is possible for the "initial" phase to be skipped such that only the "middle" phase is observed. In other rare cases, the droplet does not stabilise and

continues to oscillate as in the high frequency “initial” phase until it is exhausted and stops oscillating.

After oscillating for some time, the oscillation frequency suddenly increases and the background red colour is reduced such that the contrast of the wave is significantly smaller. This phase is referred to as the “late” phase. The planar wave shape can also change in this phase to a “reverse” planar shape where the centre of the curve is on the opposite side to the wave source, towards the direction that the wave travels. This phase is easily visible as more than two waves from the source are present in the droplet at the same time. The droplet then oscillates with this higher frequency until it enters the “exhausted” phase.

When the droplet stops oscillating this phase is referred to as the “exhausted” phase. In this phase, the droplet no longer oscillates. Usually, the droplet is transparent in this phase. It is also possible for the droplet to stop oscillating as a reduced red state if there is a low concentration of $NaBrO_3$ relative to MA. Another possibility is for it to stop oscillating as an oxidised blue droplet if there is a high ferroin concentration. If this is these cases, the red and blue colour turns transparent over time. In one very rare case using 0.36 M malonic acid, self-oscillations are triggered after 2.5 hours in the reduced red state, similar to “revival” oscillations described in Section 7.1. Approximately 20 self-oscillations in the “late” phase are observed, until the droplet became transparent.

By identifying these common oscillation phases, it is possible to analyse the wave patterns and graph peaks to find further common behaviours and to understand the mechanisms of wave propagation through the droplet. Methods of compensating for background noise such as the droplet becoming more transparent can also be developed. While each droplet composition has differences in the phase duration and transition times, this is an important first step in characterising other derived parameters such as wave pattern, frequency, amplitude and wave pattern changes due to coupling. This knowledge also allows the effect of droplets interacting with neighbours to be more easily distinguished from these phase changes.

4.2 Evolution of wave patterns

The large size of the droplets also gives the opportunity to observe of how the wave patterns evolve over time in BZ droplets. Smaller size droplets are usually oxidised or reduced completely as the droplet size is smaller than the width of the wave. Characterising how these wave patterns evolve over time also gives the unique opportunity to determine if droplet neighbours can change the wave pattern behaviour.

Droplets with very high concentration of H_2SO_4 and $NaBrO_3$ initially have waves that have no distinct shape. In this case, parts of the droplet can be observed to oscillate, but the waves themselves are thin, close together and have no distinct shape. Eventually the droplet reaches the steady state such that normal waves can form.

Spiral wave patterns can be observed during the initial state in some high frequency droplets though this is not consistent and usually stabilises to lower frequency planar waves. However, other relatively rare droplets can sustain a high frequency spiral wave for the entire lifetime of the droplet, which is approximately 30 minutes. This is compared to the normal lifetime of 50 minutes if it had underwent normal oscillation phase changes. This implies that staying in the spiral shape initial phase with a higher frequency for a prolonged period can reduce the lifetime of the droplet. For these droplets, it is observed that the spiral wave can form in any part of the droplet, though spirals at a droplet edge are more common. Both clockwise and anticlockwise spirals are possible, where a clockwise spiral travels from the spiral centre towards the outside tip in a clockwise rotation and vice versa. Clockwise spirals have their centres travel in an anticlockwise direction, and vice versa for anticlockwise spirals. In one example of a 0.5 M H_2SO_4, 0.47 M $NaBrO_3$, 0.27 M malonic acid and 2 mM ferroin droplet at 25 minutes after mixing the stock, it is observed that the centre rotates slowly at first at 2°/min. At 40 minutes after mixing, the rotation speed increased to 9°/min. As the spiral rotates, it moves further from the middle of the droplet towards the droplet edge as well at 0.014 mm/min. This spiral pattern is shown in Figure 4.3.

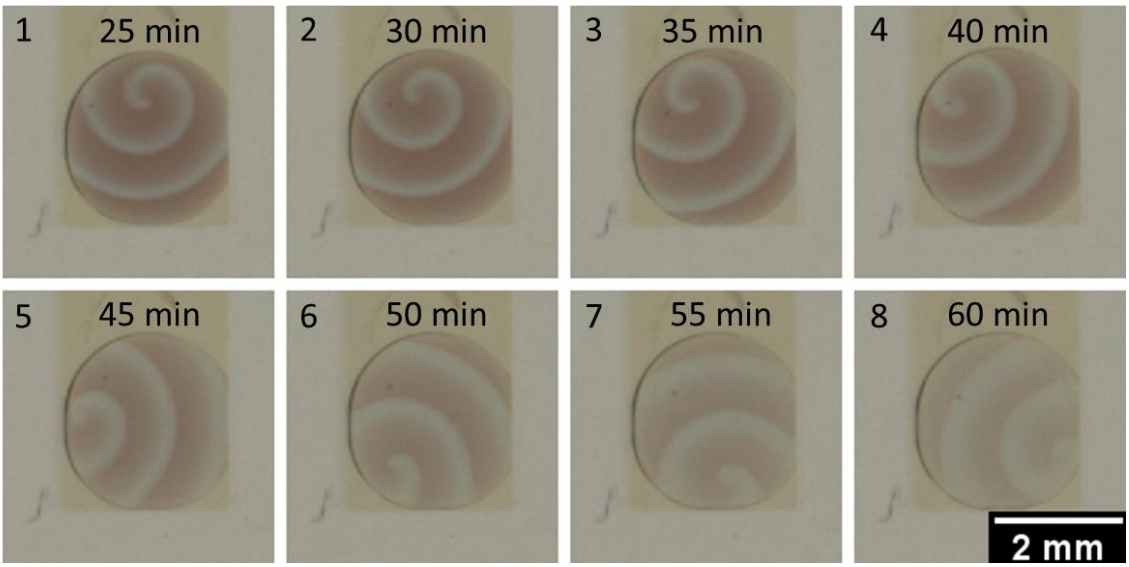

Figure 4.3 Example spiral pattern that did not become extinguished until the droplet has stopped oscillating. Droplet can also be observed to become more transparent over time. Spiral centre rotates about droplet edge and at a faster rate after 45 minutes. Time measured from when stock is mixed.

Multiple spiral patterns also possible. Usually these spirals quickly become extinguished by other high frequency waves interacting with it. When one clockwise and anticlockwise spiral remains for a long time, it is possible for their spiral centres to rotate along the edge of the droplet. These spiral centres eventually meet and one is extinguished while the other may remain. After all spirals are extinguished, the droplet remains refractory in the red reduced state for a short time then oscillates as normal with planar waves. When the spiral is extinguished, the first self-oscillation that occurs in the droplet is usually near the spiral centre. This corresponds to an abrupt reduction in wave frequency, though the frequency of the initial planar waves is still significantly higher. An example of an extinguished spiral wave evolving into a planar wave is shown in Figure 4.4.

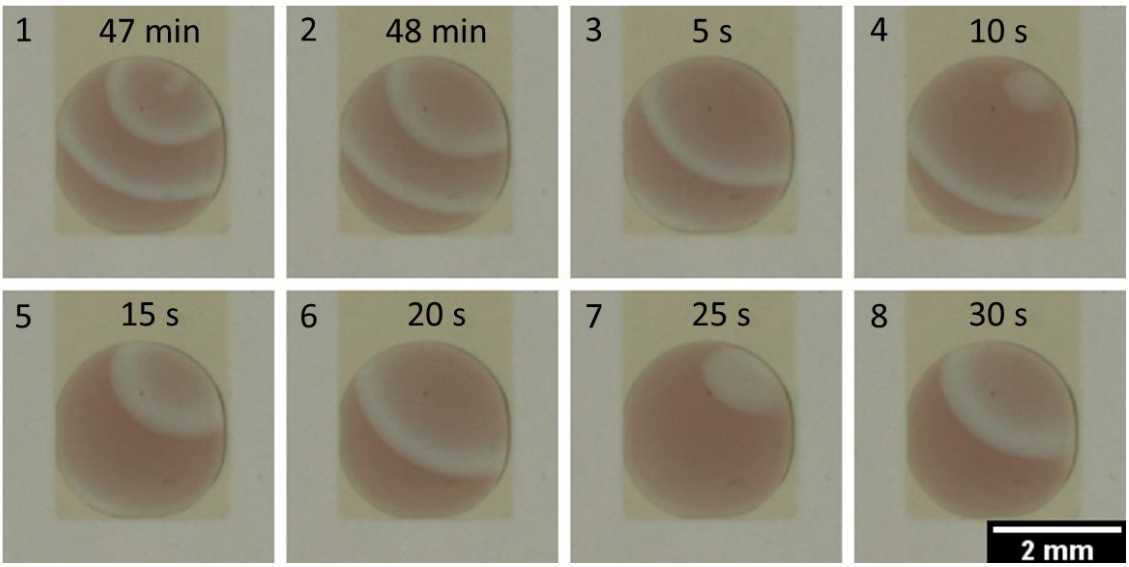

Figure 4.4 Spiral wave extinguished when spiral centre reaches droplet edge, then new planar wave self-oscillation starts at previous spiral centre location. Frequency reduces significantly from spiral to planar frequency. Time measured from when stock mixed, then from 48-minute mark.

Planar waves are the most common type of waves, where a wave forms on one edge of the droplet and spreads to other areas in a circular shape, with the centre in the direction of the wave source. Usually these waves form on the edge of a droplet in contact with either another droplet or the PMMA. When multiple wave fronts exist, they annihilate each other when they interact due to the refractory period of regions where a wave previously travelled through, such that only sections of the droplet that have not yet interacted with a wave can propagate the wave fronts. It is possible for the planar wave to change direction where a new wave is self-excited along its path faster than the initial wave front can reach it. Eventually, the new wave source initiates early enough before the initial wave front that it forms another planar wave that interacts and annihilates with the original. This new wave front then forms waves that gradually cover enough distance, pushing back the initial wave front until it reaches the source and extinguishes it, taking over as the main wave source inside this droplet. Waves formed tend to have a curve resembling a circular wave, but this curve becomes less pronounced as the wave travels further from the source. A “reverse” planar shape is also possible as shown in Figure 4.5. In this case, the centre of the circular wave front is on the opposite side to the wave source. These waves usually form in the high frequency state of the droplet just before the droplet is exhausted and stops oscillating. They otherwise behave similarly to normal planar waves.

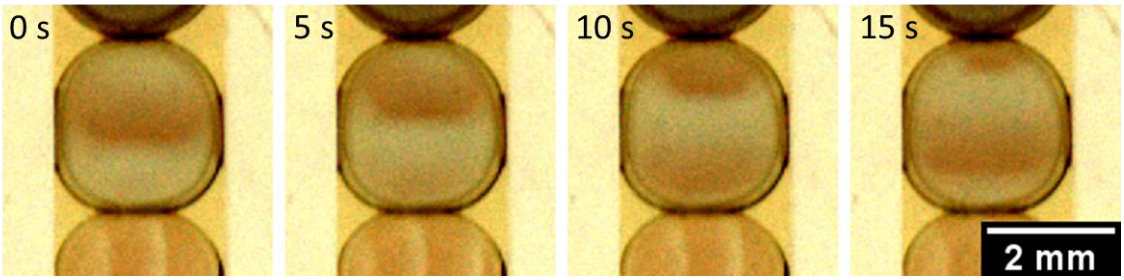

Figure 4.5 Example of “reverse” planar shape where wave is curved away from wave source. Contrast adjusted as 90 to 140 in ImageJ for visibility. First frame taken at 90 minutes after mixing BZ stock.

Circular waves can also be seen in these droplets. They are more common for droplets oscillating at a low frequency, where the wave centre is near the middle of the droplet. They behave similarly to planar waves, except that their centre is in the middle of the droplet so it can be observed that they propagate in all directions away from the source as seen in Figure 4.6 (A). The speed of the circular wave may not be uniform through all parts of the droplet, such that the circular shape is distorted as seen in Figure 4.6 (B). This is similar to how a part of the droplet can self-excite if the wave front takes too long to reach it, forming another wave source. This self-excitation forms another wave that joins with the circular wave front forming the distorted shape. Alternatively, parts of the droplet that are less excitable can slow down the circular wave front in that section. Usually it is observed that the circular wave takes on a shape similar to that of the droplet, such that an elongated droplet will also form circular waves elongated according to that shape. This effect is very small however, similar to that of the planar wave front following the shape of the droplet.

Gas bubbles do not have a significant effect on wave patterns except by separating parts of the droplet from each other when it becomes too large. Waves are not generated from and not prevented from propagating around these gas bubbles. Even when small gas bubbles form, float up and pop at a high frequency, there is no significant effect on the wave behaviour. However, if a very large gas bubble (approx. 1 mm diameter) forms and pops, the sudden and large displacement in volume can have a mixing effect that destroys wave patterns. The bubble can also become large enough that the entire droplet is moved instead of split apart due to the surface tension of the droplet. However, even after this case the droplet is observed to start oscillating again with almost no change in wave

behaviour except in the location of the wave source, which sometimes moves back to its original location relative to the droplet centre.

Due to the larger size of these droplets, spiral, planar and circular wave patterns are identified and observed. By analysing their wave behaviours, it can be shown that even in static conditions without coupling the wave pattern evolves over time. However, this evolution is random such that sometimes a wave source can start from the left, right or bottom of the droplet where the PMMA walls are and sometimes it and form a source from the middle.

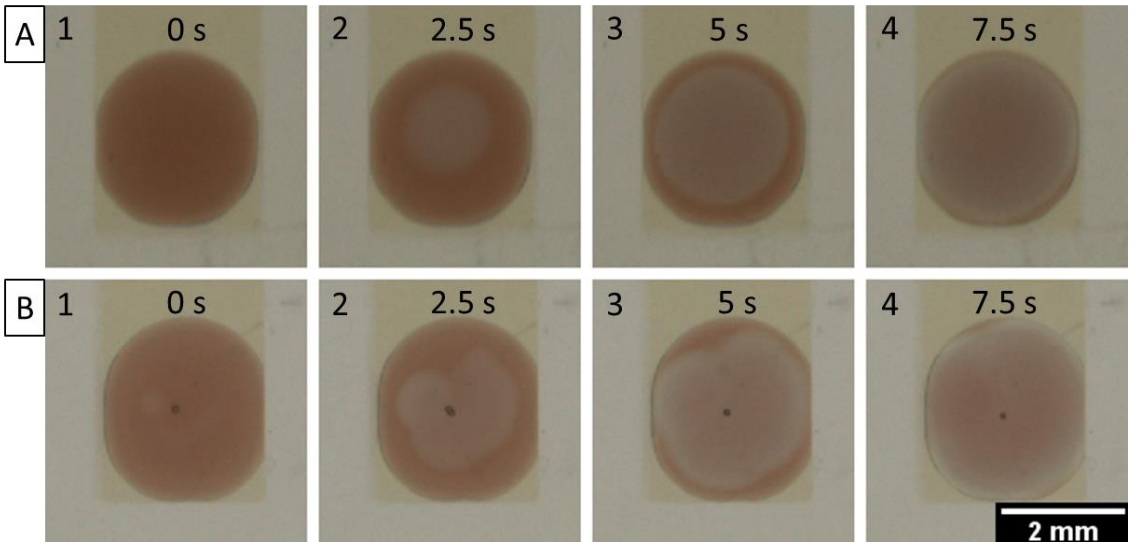

Figure 4.6 Circular wave from middle of droplet. Time measurement from 57 minutes after mixing BZ solution. (A) shows a more stable circular wave while (B) shows distorted circular wave in another droplet.

4.3 BZ droplet reactions when exhausted

Further information is needed to determine which BZ components are used up and which components have excess left over in their exhausted state. BZ droplets with 0.5 M H_2SO_4, 0.47 M $NaBrO_3$, 0.18 M malonic acid and 2 mM ferroin tested by leaving out components as well as adding new components to exhausted droplets. These experiments are carried out without asolectin as it is found that asolectin makes fusing droplets more difficult, so adding new components into existing exhausted droplets is more difficult.

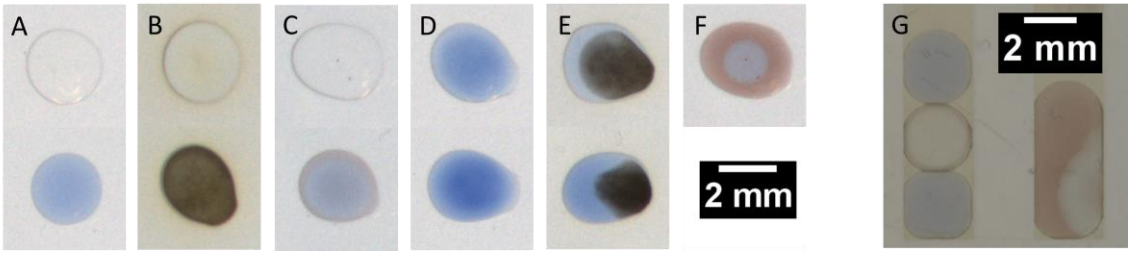

Figure 4.7 Observations when BZ components added to BZ solution exhausted overnight (Top) and fresh BZ solution without any malonic acid (Bottom). Both types of droplets are initially 5 µl and for both the same volume (at least 1 µl) of component is added to produce subsequent images. Exhausted BZ solution had initial composition of 0.5 M H_2SO_4, 0.47 M $NaBrO_3$, 0.18 M malonic acid and 2 mM ferroin and was left overnight. Freshly mixed solution had an identical composition except there was no malonic acid added. (A) Original droplet appearance. (B) Appearance 5 minutes after KBr added. Brown precipitate in top droplet has dissolved while brown precipitate in bottom droplet still present. Brown oil surrounding droplets is a bromine cloud inside the oil that has dissipated. (C) When malonic acid is added. (D) When ferroin is added. (E) 10 minutes after ferroin and KBr are added, slightly brown bromine cloud still visible and dark brown precipitate observed in both droplets despite longer time compared to (B). (F) When both ferroin and MA added, exhausted droplet starts oscillating again. Scale bar applies to A-F. (G) Comparison between blue droplets versus droplet oscillating to exhaustion in asolectin in hexadecane oil sandwiched between blue droplets. Both types of droplets have same composition as in A-F and photo is taken after 140 minutes. On the right is a still oscillating fused BZ droplet with the same composition except with 0.33 M H_2SO_4 and 0.12 M MA. Scale bar only applies to G.

When H_2SO_4 is left out of the BZ mixture, no oscillations are observed and the solution and droplet remains red in colour. This red colour slowly turns transparent over time, but over a very long time such as over several days. The loss of colour could be other factors such as light exposure, but it is significantly slower compared to oscillating BZ solutions. BZ solutions made without ferroin appear transparent and no oscillations can be observed due to the lack of coloured indicator.

If $NaBrO_3$ is left out of the mixture, the solution produced is does not oscillate and remains red in colour, but no significant colour loss was observed when this mixture was observed for a few hours. If malonic acid is left out of the mixture, the solution produced is in the blue oxidised state but does not oscillate. This blue colour reduces in intensity over time, but this is significantly slower than oscillating BZ droplets with the same concentration of all other components except with additional 0.18 M malonic acid. The oscillating droplets become fully transparent once exhausted while at the same time the blue droplets lacking malonic acid still have their blue colour. This effect is tested over at least 140 minutes in asolectin in hexadecane oil. A comparison of the colours can be seen in Figure 4.7 (G).

From these observations, it is hypothesised that the ferroin of the BZ droplets is being denatured significantly faster when BZ droplets are oscillating compared to ferroin that is left in the same acidic and oxidising BZ conditions but without oscillating. This is speculated to be because when the BZ is oscillating the malonic acid turns into intermediates that denature the ferroin. To test this hypothesis an experiment is conducted comparing the effect of adding KBr, ferroin and malonic acid in different combinations to BZ stock solution left overnight until exhausted and freshly mixed BZ solution without malonic acid. If the hypothesis is correct, adding ferroin to the exhausted droplet makes it identical to the freshly mixed one without malonic acid. Also, adding malonic acid to the exhausted droplet does not allow it to oscillate whereas adding it to the freshly mixed droplet causes oscillations. Adding KBr is also useful as it is known that adding KBr causes ferroin to form a precipitate and a BZ solution without malonic acid forms a yellow bromine cloud. These experiments are conducted in hexadecane oil without asolectin so that fresh component solution can be fused into the droplets more easily. The summary of this experiment is shown in Figure 4.7 (A to F) and Table 4.1.

The experiment is set up by filling hexadecane oil without any lipids inside a glass petri dish. Several of 5 µl droplets of BZ solution exhausted overnight are then pipetted into the oil and allowed to adsorb onto the glass surface. This is repeated in the same petri dish for BZ solution mixed without any malonic acid. Once the droplets are set up, 1 µl of stock solution in different combinations is pipetted into one droplet of each set and its reaction is observed. If more than one stock solution is pipetted into the droplet, 1 µl of each is still used as the pipette is not able to pipette solutions of any smaller volume. The stock solutions used are as described in Section 3.1, which are 1 M KBr, 0.025 M ferroin and 1.88 M $NaBrO_3$ and 1.79 M malonic acid. Initially, the exhausted BZ solution appears transparent with no oscillations and the BZ solution without malonic acid appears blue without any oscillations.

When ferroin is added, the red ferroin is observed to turn completely blue when mixed into the transparent droplet, but no oscillations are observed. BZ solutions mixed without any malonic acid are also observed to have a blue colour that has a higher blue intensity than the exhausted droplets. When KBr is added to both, a yellow cloud is formed that spreads from the droplet and a dark brown precipitate is formed.

In experiments where droplets with and without malonic acid were mixed and observed to oscillate until exhaustion, this blue colour is observed to slowly turn transparent over time, but lasts several hours longer than the ferroin colour in the oscillating droplet despite having the same initial concentration of H_2SO_4, $NaBrO_3$ and ferroin. This implies that the ferroin inside oscillating BZ droplets is being destroyed, causing the oscillating BZ droplets to turn transparent. It also implies this is not an effect of being inside the oil or the ferroin being exposed to the acidic or oxidising environment, but an effect of the BZ oscillations themselves.

If both ferroin and malonic acid are added to the same droplet, the droplet turns red and starts oscillating as a normal BZ droplet. This implies that both malonic acid and ferroin are used up in oscillating BZ droplets. As the droplets are blue when ferroin is added to exhausted droplets, it can be concluded that both H_2SO_4 and $NaBrO_3$ have a significant concentration left over at the end of the oscillation phase. BZ solutions without either component remains red, and when both malonic acid and ferroin are present, the droplet oscillates despite having a more diluted concentration of both components due to fusing

droplets containing both. When repeated with 1.5-hour-old droplets that have recently exhausted, oscillations can still be seen on a very faint red background that is much fainter compared to the fresh droplet and droplet with double initial ferroin concentration. This implies that even after exhaustion some ferroin is present, but in significantly smaller quantities than fresh solutions or even similarly aged solutions without malonic acid. This corroborates with the method used to "revive" exhausted BZ droplets [107], where the organic component, in this case malonic acid, is added to exhausted BZ solution so that further oscillations can be made.

If KBr is added to a transparent exhausted droplet, the droplet develops a brown precipitate when mixed and a yellow cloud is emitted from the aqueous droplet into the hexadecane oil outside. The brown precipitate formed slowly disappears and dissolves into the transparent solution. The yellow cloud reaches a maximum radial distance of approximately 4 mm from the source droplet and then stops. Due to the diffusion behaviour of this cloud, the intensity of the yellow cloud is lower the further away from the source droplet. The yellow cloud then slowly turns transparent over 30 minutes. When fresh BZ solutions are mixed without malonic acid and ferroin and KBr is added, the solution turns yellow without precipitate formation and forms a yellow cloud around droplets in hexadecane oil without asolectin. If this cloud touches droplets of potassium iodide (KI), the aqueous droplets are observed to turn yellow, whereas similar droplets of KBr, malonic acid and DI water remain transparent. If exposed to the yellow cloud for extended periods of time or in high cloud intensity, the yellow KI droplet turns darker yellow and starts to emit a purple cloud, which is consistent with the appearance of iodine. From these experiments, it can be concluded that the yellow cloud from addition of KBr is molecular bromine, Br_2.

If ferroin is added first forming a blue droplet, then KBr is added, an opaque, dark brown solid precipitate where the KBr is added. A cloud of bromine is also formed as in the previous experiment without adding ferroin, with no significant difference in the colour intensity of the bromine, its diffusion rate or the rate of intensity change when forming or dissipating. This effect is similar to when mixing BZ stock solutions where the solution turns yellow when KBr is first added. If ferroin is added before this colour disappears, a precipitate is also formed. If a separate blue BZ droplet or oscillating BZ is placed next to a bromine source, a dark brown precipitate is observed at the droplet circumference in

contact with the bromine. From these experiments, it can be concluded that the precipitate is formed due to ferroin reacting with the bromine gas. This also implies that exhausted transparent exhausted BZ droplets still have some ferroin remaining as they still form a small amount of precipitate when KBr is added.

In summary, these experiments conclude that for the standard MA BZ composition of 0.5 M H_2SO_4, 0.47 M $NaBrO_3$, 0.18 M malonic acid and 2 mM ferroin, both ferroin and malonic acid are denatured while there is leftover H_2SO_4 and $NaBrO_3$. This is corroborated by how droplets with higher malonic acid and less $NaBrO_3$ tend to be exhausted as red droplets while droplets with a higher ferroin concentration can be exhausted as blue droplets from Section 4.3.

Table 4.1 Summary of observations when BZ components are added to exhausted BZ droplets.

Added	Colour	Oscillate	Bromine	Precipitate
None	Transparent	✗	✗	✗
NaBrO3	Transparent	✗	✗	✗
Malonic acid (MA)	Transparent	✗	✗	✗
KBr	Yellow	✗	✓	✗
Ferroin	Blue	✗	✗	✗
MA + Ferroin	Red	✓	✗	✗
KBr + Ferroin	Brown precipitate (opaque) then blue	✗	✓	✓

4.4 Space-time plot analysis of phases

The changes in the frequency, contrast and direction of the waves can be seen in the space-time plots in Figure 3.7, where a large gradient of the line denotes that the wave is travelling at a high velocity, and the point closest to the left of the space-time plot is the starting point. When measuring the pixel intensity of the space-time plot along the time-axis, waves can be observed as a significant increase in pixel intensity at where the oxidation wave is detected. When the wave passes and the solution becomes reduced and red again, the pixel intensity drops. This pattern repeats for many oscillation cycles forming a graph with many peaks. The peaks properties can be analysed to determine wave properties. For instance, the distance between each peak denotes the period of the oscillation and hence the frequency, while the amplitude of the peak relative to the baseline shows the contrast between the blue wave and the red background. The shape of the peak shows the rate at which the droplet is oxidised and reduced, where a high gradient as the intensity increases or decreases indicates a high rate. The area under the graph shows the ratio of the size of the peaks taking into account these gradient measurements. Pixel intensity, amplitude and area measurements are measured in arbitrary units (AU).

It is observed that the rate of oxidation is significantly faster compared to the rate of reduction Figure 4.8. This is shown by the shape of the peaks where the peak increases to its maximum height very quickly within two frames, but then falls at first with a high rate then with a lower rate as time goes on in 6 frames. This is more visible in droplets with a low wave frequency, though this is possibly due to the low frame rate of the recording of the experiment, where the droplets are reduced too fast for the video to detect in high frequency droplets. It is also observed that high frequency droplets do not have as large of a drop in pixel intensity before the next oscillation starts, which is corroborated by the background having a significantly higher blue intensity.

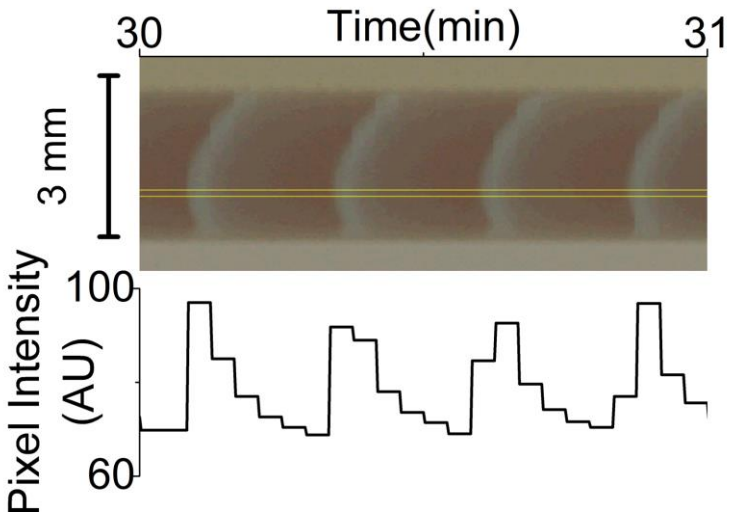

Figure 4.8 Pixel intensity measurement (in AU) and space-time plot. Left side of peak is much steeper compared to right side (1 or 2 steps compared with 5 steps). More visible for lower frequency droplets. Jagged edges due to Gaussian smoothing applied to each slice of measured space-time plot. Space-time plot used here is left unsmoothed for illustration. In this case, circular waves are observed as indicated by the start of the wave (left most part) is in the middle, and this spreads to the other edges (furthest right part). Yellow line highlights region where pixel intensity measurement taken and time calibrated to when stock solution is first mixed.

If the entire measured pixel intensity of the space-time plot is observed, it can be seen that the bottom baseline of the graph increases as time goes on Figure 4.9. This is due to the droplet becoming transparent over time. This also reduces the contrast of the waves in the droplet, as the difference between the oxidised wave and the reduced background is smaller, hence a smaller amplitude. This reduction in amplitude is reflected in the flattened graph. It is also interesting to note that when the droplet changes in state, the baseline graph also significantly changes, where the “initial” phase has a slightly higher baseline intensity than the “middle” phase’s minimum and the “late” phase has a significant spike in the intensity when it is reached. When the droplet is “exhausted” and transparent, the baseline reaches a maximum and stays at a constant flat reading until the end of the recording. For most graphs, the maximum baseline intensity is approximately 120 AU (Figure 4.10 (a)). Changes in the phases of the oscillation lifetime are characterised by sudden changes of amplitude and frequency of at least a factor of 1.5. These changes occur after a consistent behaviour of 5 oscillations or more, transitioning during less than 5 oscillations and persist for 5 oscillations or more, as previously stated in Section 3.9.

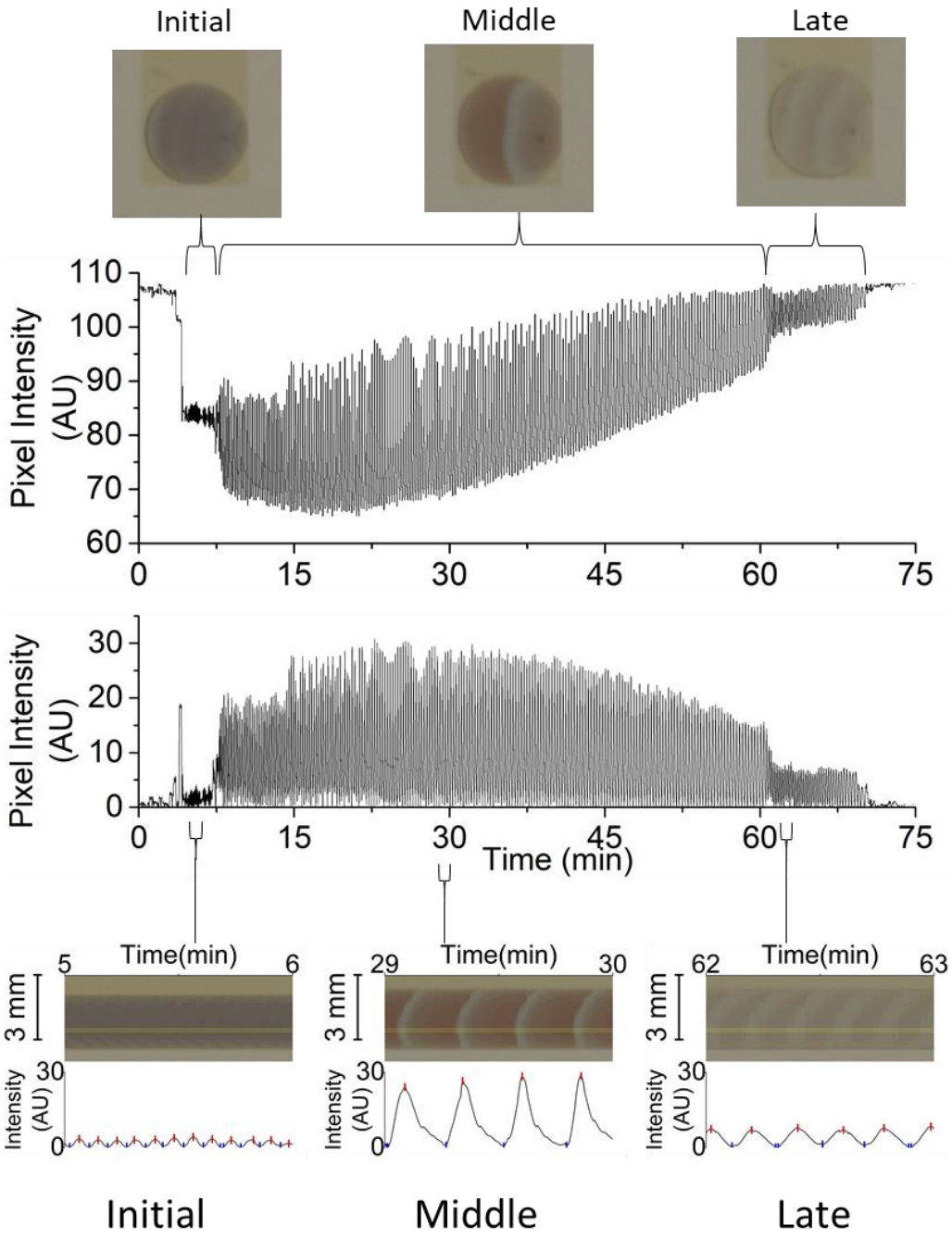

Figure 4.9 Example pictures of different phases in oscillation lifetime of the same droplet, its corresponding pixel intensity measurement of space-time plot, baseline corrected intensity and peaks analysed. All intensity measurements are in AU. The 5 µl Droplet contains [H_2SO_4] = 0.5 M, [$NaBrO_3$] = 0.38 M, [MA] = 0.18 M, [ferroin] = 2 mM inside one 2.5 mm slot. Time zero is when stock solution is mixed. Zoomed-in one minute sections with peaks (red) and troughs (blue) marked by peak finding algorithm are shown for the initial, middle and late phases, identified by sudden changes in frequency and amplitude by approximately a factor of 1.5 or more. Yellow lines on space-time plot images indicate where pixel intensity measurements were taken.

When the baseline graphs are compared between droplets of different lifetime Figure 4.10 (A), the baselines are observed to reach a maximum when the droplets have become transparent. It is also observed that droplets with a longer lifetime tend to have a lower minimum baseline compared with shorter lifetime droplets. Droplets that turn transparent have approximately the same final baseline, but droplets that remain reduced red tend to have a lower baseline and do not reach this, as is seen for 0.940 M $NaBrO_3$ droplets. The wave count graph shows the number of peaks counted so far at a certain time Figure 4.10 (B). This graph is useful as the number of peaks counted at a certain time point can be estimated. In addition, the gradient of the graph gives an indication of the frequency of the oscillations, where the steeper graph indicates a higher frequency. From this graph, the final total number of waves and the time this is reached can be determined and compared.

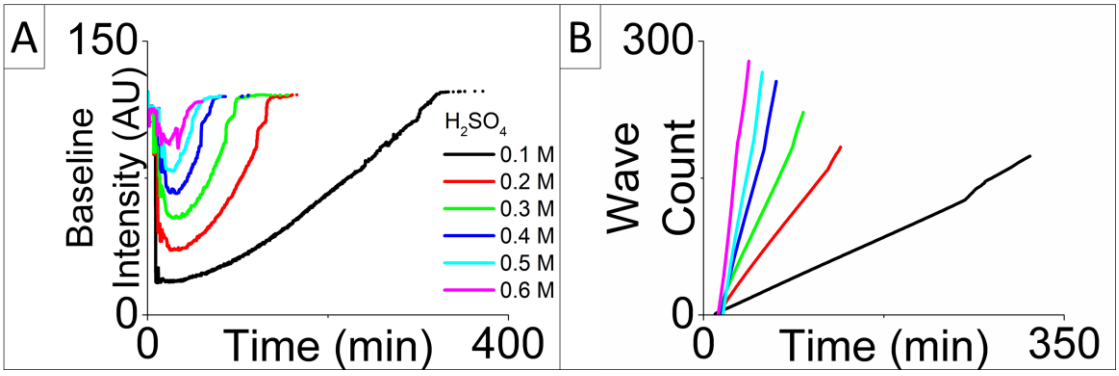

Figure 4.10 (A) Baseline graph (pixel intensity measured in AU) and (B) wave count graph for droplets of different lifetimes (0.1 M H_2SO_4 has the longest lifetime while 0.6 M H_2SO_4 has the shortest lifetime). The baseline graph traces the troughs of each graph. The wave count graph shows the total number of peaks observed up to that specific point in time, and its gradient can be used to obtain the frequency at that specific time. All the baseline graphs are observed to reach the same baseline amplitude of approximately 120 but at different times due to the different lifetimes of each droplet composition. Droplets are exhausted at different times ranging from 50 to over 360 minutes. The gradient for each wave count graph is different as a result, with larger gradients indicating a higher oscillation frequency. Graphs calibrated so zero minutes is when stock solutions mixed.

Graphs and space-time plots usually appear as in Figure 4.9, which is an example of a single 5 µl droplet in a 2.5 mm slot that contains [H2SO4] = 0.5 M, [NaBrO3] = 0.38 M, [MA] = 0.18 M, [ferroin] = 2 mM. In the graphs of each wave characteristic from this example in Figure 4.11, significant changes in wave characteristics can be seen between the initial phase (4.5-6.5 min), middle phase (60.5 to 70 min) and late phase (60.5 to 70 min).

During the "initial" phase when the droplet has a high frequency and low contrast waves, more stripes can be seen in the space-time plot and more peaks in the pixel intensity measurements. The amplitude and area of the peaks are significantly lower than in other states due to lower contrast of the waves. This is reflected in the baseline of the graph, which has a higher intensity. The distance between the peaks and width of the right side is also significantly smaller than in the rest of the lifetime, so the frequency is also much higher. After some time, the droplet enters the "middle" state, where some abrupt changes in the droplet and graph behaviour are observed. This abrupt change is where the frequency halves and the amplitude doubles and the new frequency and amplitude persists for more than 5 subsequent peaks with the change occurring over approximately 5 peaks.

When the "middle" phase is first reached, the baseline of the graph is almost at a minimum and the amplitude and area increases to its maximum, though this is not immediate, as some time is needed for consistent smooth high contrast waves from the new stabilised sources to be formed. The bottom baseline measurement shows that the droplet background is no longer as oxidised and bright blue as it was during the initial state. As time goes on, the frequency of the waves decreases, though this is more easily seen for long lifetime droplets. The amplitude and area of the peaks also decreases as the droplet becomes more transparent and the contrast decreases. After some time the droplet suddenly changes states into the "late" state. At this stage, the frequency suddenly increases again over approximately 5 peaks to 1.5 times the original and the amplitude also decreases by half. This change then persists for more than 5 peaks.

In the "late" phase, the frequency of oscillations suddenly increases and more than one wave can be observed in the droplet at the same time due to the increased frequency. The peak amplitude and area also become significantly smaller than previously. The droplet then oscillates at this higher frequency until it enters the "exhausted" state, where oscillations can no longer be seen in the graphs or space-time plot.

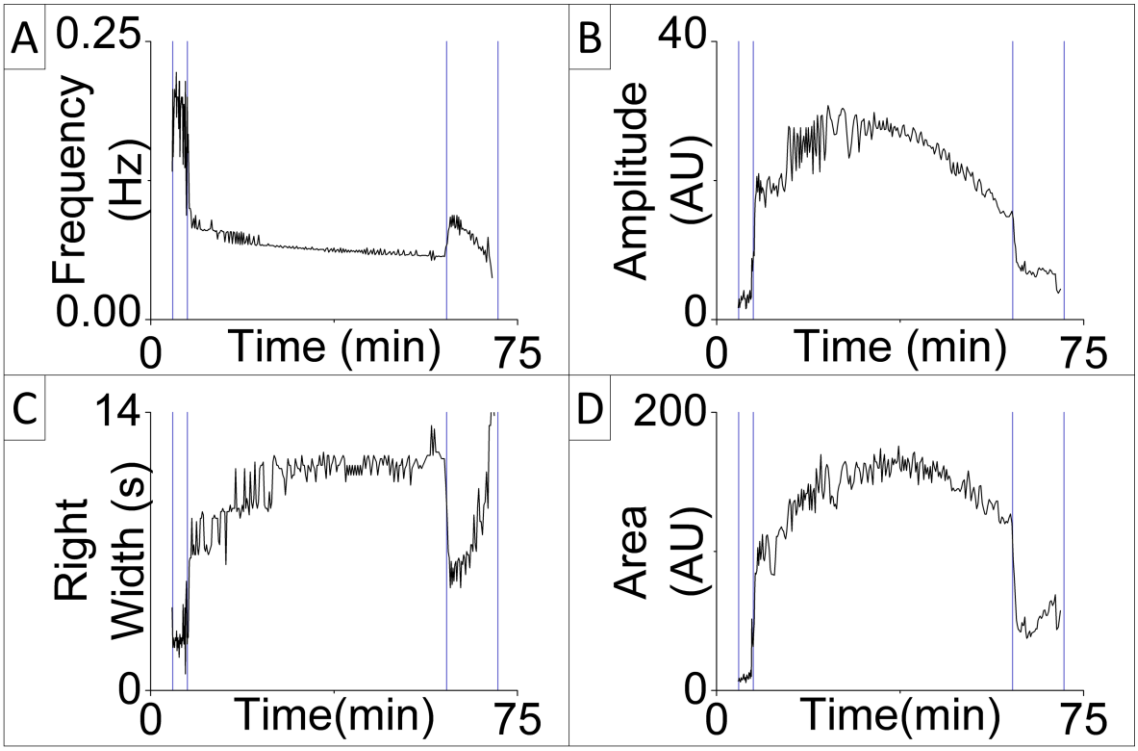

Figure 4.11 Peak analysis graphs of 5 µl droplet inside one 2.5 mm slot corresponding to Figure 4.9 that contains [H_2SO_4] = 0.5 M, [$NaBrO_3$] = 0.38 M, [MA] = 0.18 M, [ferroin] = 2 mM. Significant changes in wave characteristics observed during phase transitions marked by blue lines. Time zero is when BZ stock solution is mixed. (A) Frequency graph. (B) Amplitude (in AU), which is the height from the baseline (i.e. the trough) to the top of the peak. (C) Right width graph is the time taken between the maximum height of the peak to the right side trough. This is the time taken for the droplet to be reduced from blue to red after an oscillation and follows the reverse trend of frequency graph A. (D) Area (in AU) is the sum of pixel intensities for all x-coordinate values of the peak.

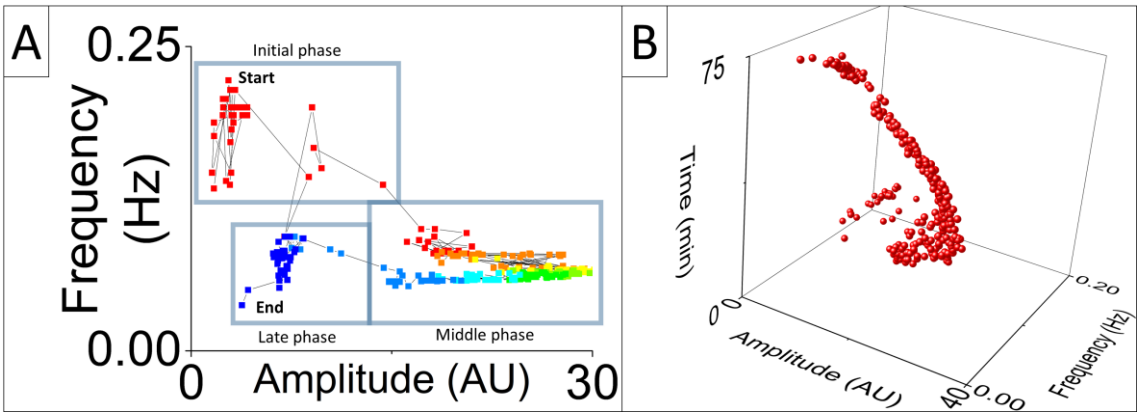

Figure 4.12 (A) Amplitude versus frequency graph for each analysed peak. Colour mapped to time where red is for earlier peaks followed by green then blue for peaks later in the oscillation lifetime. Peak data points cluster according to the different phases of the oscillation lifetime. The shape of the graph has a "reverse-C" shape, where the middle phase contains the most number of peaks while covering a small compact area. (B) Same graph in 3D plot with time as the Z-axis. With this perspective, the initial and late phases is observed to consist of a very small proportion of time compared with the middle phase.

The peaks are analysed as in Section 3.9 and the changes in the peak properties corresponds to the descriptions of each phase. Additional properties such as peak right width and area can also be taken and analysed and is shown in Figure 4.11 (C) and (D). The peak right width corresponds to the time from the maximum of one peak to the trough of the next peak. This time in seconds corresponds to the time taken for the droplet reduce from blue to red again after an oscillation. This is expected to correspond to the inverse of the frequency as the time for the left width is insignificant compared to the right width. The area is the sum of the pixel intensity measurements of all the x-coordinate frames in a peak, and is expected to increase proportionally to the amplitude. Both amplitude and area are measured in AU. However, if the peak increases in width it is possible for the area to increase even when the amplitude is decreased.

The right width and frequency graphs are the inverse of their trends, with deviations being insignificant. However, for the amplitude and area graphs, it is observed that the later part of the middle phase has the amplitude significantly reducing but the area does not reduce in the same proportion. There is also no significant change in the frequency or right width during this time compared with the change in amplitude. This implies that even though the

distance between each peak is approximately the same, the width of the peaks is increased. This allows the amplitude to drop significantly while still giving a relatively small drop in area and is corroborated by Figure 4.13 (A).

In order to visualise the way the frequency and amplitude change for each peak over the lifetime of the droplet, the amplitude versus frequency graph is plotted as in Figure 4.12 (A). This graph usually has a “reverse-C” shape and shows that the initial, middle and late phases can be differentiated as distinct clusters of data points if there is a significant change in behaviour when transitioning the phases. This is a common shape for most MA BZ droplets analysed. While the middle phase appears to cover a small area compared to the initial and late states, it has the greatest number of peaks and exists for the longest time, as seen in the 3D plot of this same graph with time as the Z-axis in Figure 4.12 (B).

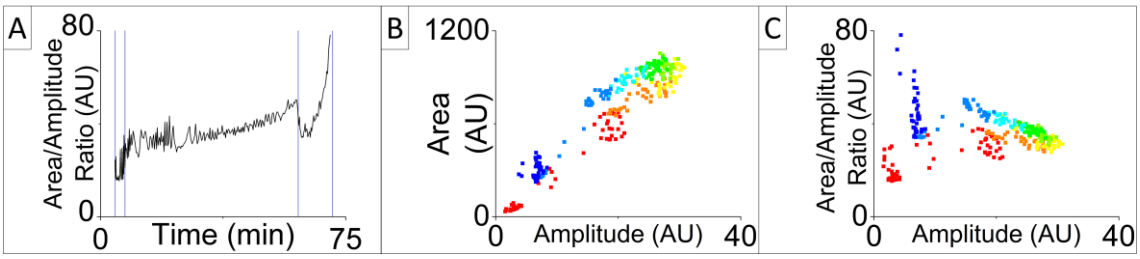

Figure 4.13 (A) Ratio of area per unit amplitude over time. Initial phase is from 4.5 to 7.5 minutes, middle phase is from 7.5 to 60.5 minutes and late phase is from 60.5 to 70 minutes. Large changes are observed in the ratio between phase changes (marked with blue lines) and a slight increase in the ratio is seen in the latter half of the middle phase. The late phase has an even larger increase as the peaks become smaller in amplitude but significantly wider in proportion. (B) Amplitude versus area graph. All points appear in almost a straight line for the first half of oscillation lifetime but in the second half, the area is slightly higher compared to the same amplitude. Peak data points cluster where bottom left red marks show initial phase peaks and blue shows late phase peaks in the same region. (C) Amplitude versus ratio of area to amplitude scatter plot showing significantly larger ratio as droplet approaches end of lifetime marked in blue. Scatter plots colour mapped where red is for earlier peaks and blue for later.

The proportion between the amplitude and area can also be taken to estimate the increase in the width of the peaks. If the peaks remain the same width, there should be no change in this proportion, whereas an increased width will show an increased ratio of area per unit amplitude. An area versus amplitude graph can also be plotted to show the change in proportion over time and if there is any clustering of the peaks. As shown in Figure 4.13 (A), this example has a slight increase in the area per unit amplitude over time at the end of the middle phase, with significant changes during the phase changes. When plotted in the amplitude versus area graph in Figure 4.13 (B), the cluster for the late phase is near the initial phase, but with a higher amplitude and area. In the scatter plot of amplitude versus area per unit amplitude in Figure 4.13 (C), it is clearer to see that the early part has similar value of amplitude per unit area but the latter half of the middle phase has an increasing area per unit amplitude.

The analysis shown here is only for one representative medium lifetime droplet where all phases are present. Other examples resemble the graphs in Figure 4.14 where phases such as the initial phase are missing or more difficult to differentiate. The amplitude graph in this case may be used to differentiate between the initial and late phases, but even then, the change is gradual over several peaks, though it appears to be sudden due to the time scale of the graph. The frequency graph also features a very gradual reduction in frequency over time, with no clear transition points between phases. The area and area per unit amplitude graph shows that the peak area does not scale proportionally to the reducing frequency, where the area remains almost the same despite a significant reduction in amplitude. This is reflected in the space-time plot, which shows that the region of solution stays oxidised for a longer period such that the peak becomes wider. Peaks are initially three frames wide with significantly lower intensity at the edges but towards the end of the middle phase the peaks increase to almost six frames wide.

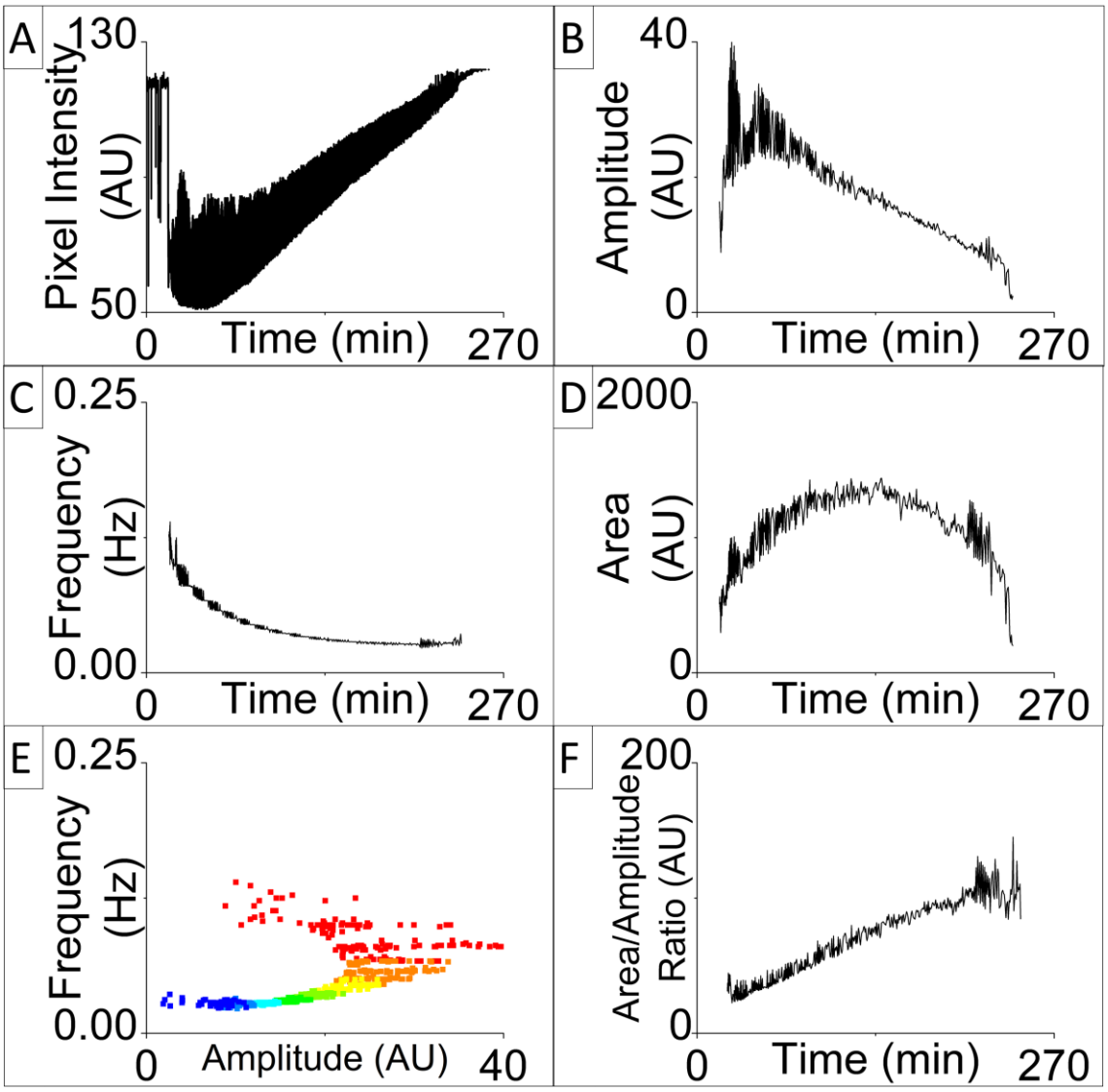

Figure 4.14 Example of a MA BZ droplet with long lifetime observed as a single droplet. No clear transitions in phase seen in all graphs. (A) Intensity graph where baseline of graph still increases over time until approximately 120 AU, but over a longer period of time and with more peaks. (B) Amplitude graph in AU shows similar curve after baseline correction where amplitude is at first lower then increases to a maximum, then slowly reduces as the droplet becomes more transparent. (C) Frequency graph calculated using the inverse of the time between each peak. Frequency gradually decreases over time. (D) Area graph in AU of each peak shows that the peak significantly increase in width as time goes on. (E) Amplitude versus frequency graph of each peak. Colour mapped where red is for earlier peaks and blue for later. Has a “reverse-C” shape as before. (F) Time versus ratio of area to amplitude graph shows that ratio is increasing over time. This means that the peaks are getting wider over time.

This analysis is carried out for as many droplets as possible in Chapter 5 to obtain statistical data for different compositions of droplets. By analysing these peak properties, significant patterns can be observed for the transition between phases in the oscillation lifetime. Less obvious observations can also be made using this graph's data that is difficult using the space-time plot alone. An example of this is the gradual decrease in amplitude and frequency of the waves during the middle phase. Extracting derived values such as area and right width can also show how the shape of each peak evolves over time. Additionally, by comparing different parameters such as amplitude versus area, further insight can be obtained for how the wave behaviour evolves over time.

Chapter 5 Droplet component characterisation

In order to determine the behaviour of BZ droplets in this system at this droplet size, the wave characteristics for each composition is analysed to determine the effect of changing the concentration of each BZ chemical component. In this analysis, only single droplets are observed in separate plastic slots. To do this more efficiently, the PMMA wafer design in Figure 3.4 (A) with many linear slots is used. This allows up to 42 arrays to be observed simultaneously. The slots are longer than necessary leading to fewer arrays, but this allows 1D arrays with larger numbers of droplets to be observed with the same setup later. For organisation purposes, the slots are named “row number – column number”.

It is assumed there is no communication between the plastic slots as the distance between them is too large at 2.5 mm and there is no direct contact between the droplets. The waves of each droplet are analysed only once they have touched the bottom of the plastic slot and they are visible in the space-time plot to have distinct waves. While some waves are lost in the initial and late phase, this is necessary as the oscillations are high in frequency and have too low a contrast to distinguish waves. It is also assumed that all the solutions have started oscillating once the final components of each mixture have been added, but that the first waves that are analysed are those observed after they have stopped moving in the oil. This may miss some waves in the stock solution and while it is sliding down the slot, but it is assumed all droplets experience this effect equally so it should not affect the final comparisons of each wave. Most droplets are added into the setup according to the order of mixing in an attempt to minimise such effects, though some droplets are added at different times to randomise the sample.

All droplets contain [H_2SO_4] = 0.5 M, [$NaBrO_3$] = 0.47 M, [malonic acid] = 0.18 M, [ferroin] = 2 mM unless otherwise stated. The variable component’s concentration is chosen to cover a range that is reasonably observable for at least 30 minutes, so concentrations that are too low or too high are not used. The increment between each concentration change is kept consistent and at least five different concentrations are observed. One stock solution of each concentration in the range is made and each PMMA slot contains a single droplet of different concentrations. Each concentration is added at the same time, such that each column increments the concentration by one stock solution for easier

organisation. Additional droplets of certain concentrations are added in extra pre-defined slots at the end of this setup step to observe if the time taken to add these droplets has a significant effect on the overall behaviour. The droplet behaviour is recorded until all droplets have stopped oscillating for at least 20 minutes for droplets that are completely transparent with no apparent changes on visual inspection and up to 3 hours for droplets that still have a red colour.

The droplet behaviour is analysed as in Section 3.8 and 3.9. The phase of the droplet as it evolves over time is observed. These changes in phase are compared to the graphs to correlate with any significant changes in wave characteristics. The inverse of the time between each peak is used to determine the wave frequency. The time between a wave peak and the wave trough is used to determine the refractory period. Scatter graphs of area versus frequency and amplitude versus frequency are plotted to observe any population distributions for different droplets and droplet states.

5.1 Effect of varying BZ components

The effect of varying each BZ components is investigated so that the wave behaviour between single droplets and droplets in arrays of different number of droplets to be compared. The methodology uses the results from analysis in Section 4.4 and uses it for statistical analysis as described in Section 3.9. This data also gives insight into how these concentrations can be varied to control the behaviour of BZ droplets for use in future applications in coupled arrays. Controlling behaviours such as droplet lifetime and oscillation frequency are important for future use as it gives insight into the limitations of how long the droplets can be used and potential effects on other droplets coupled with them.

Graphs of the changes in behaviour are shown in Figure 5.1 and a summary of these results is in Table 5.1. The number of samples for each graph are H_2SO_4 = 7, $NaBrO_3$ = 7, malonic acid = 4 and ferroin = 4. All droplets contain [H_2SO_4] = 0.5 M, [$NaBrO_3$] = 0.47 M, [malonic acid] = 0.18 M, [ferroin] = 2 mM unless otherwise stated. Each experiment only varies one component so that their individual effects can be compared between many repeats in the same experimental conditions. Wave characteristics such as the time of each oscillation, the total wave count (total number of oscillations), frequency, amplitude and area are

analysed. All waves from all states that can be detected are characterised so that the median behaviour can be represented, where the different number and duration of waves in each phase can be accounted for. These characteristics are then collected for each repeat of that droplet composition and the mean of each characteristic is obtained. The behaviour as the concentration is changed for each different component is then compared.

When these droplet parameters are arranged according to the order of which droplets entered the oil, no clear pattern can be observed in the changes of the wave characteristics. This shows that even though there is at least 30 seconds of difference between the addition of the first droplet and the last droplet in the petri dish for different repeats of the same composition, there is no significant difference in their wave behaviour. In addition, when the malonic acid samples were reprocessed to omit the initial and late phases of the oscillating phase so that only the lower frequency middle phase is analysed, only a small difference in the wave characteristics is observed. The largest difference is in the frequency and total wave count characteristics. Repeats with a higher frequency than the mean changed to have frequencies near the mean value. This is because the initial high frequency phase was omitted using this method, and these samples had a unusually long initial phases as they did not revert from the spiral wave pattern to the “normal” planar wave pattern for much of their lifetime. The total wave count is reduced from omitting the initial and late phases. The lifetime is reduced by a few minutes due to omitting the high frequency late oscillation phase, but the pattern and values did not change significantly, as only 5 minutes were omitted out of the total lifetime of at least 50 minutes. The largest difference omitted was 10 minutes out of a total lifetime of 154 minutes. These show that while it is not perfect to process all waves from all oscillatory phases and to use the stock mixing time as the reference time to quantify the lifetime, it is still more accurate and less dependent on interpretation compared to omitting wave observations.

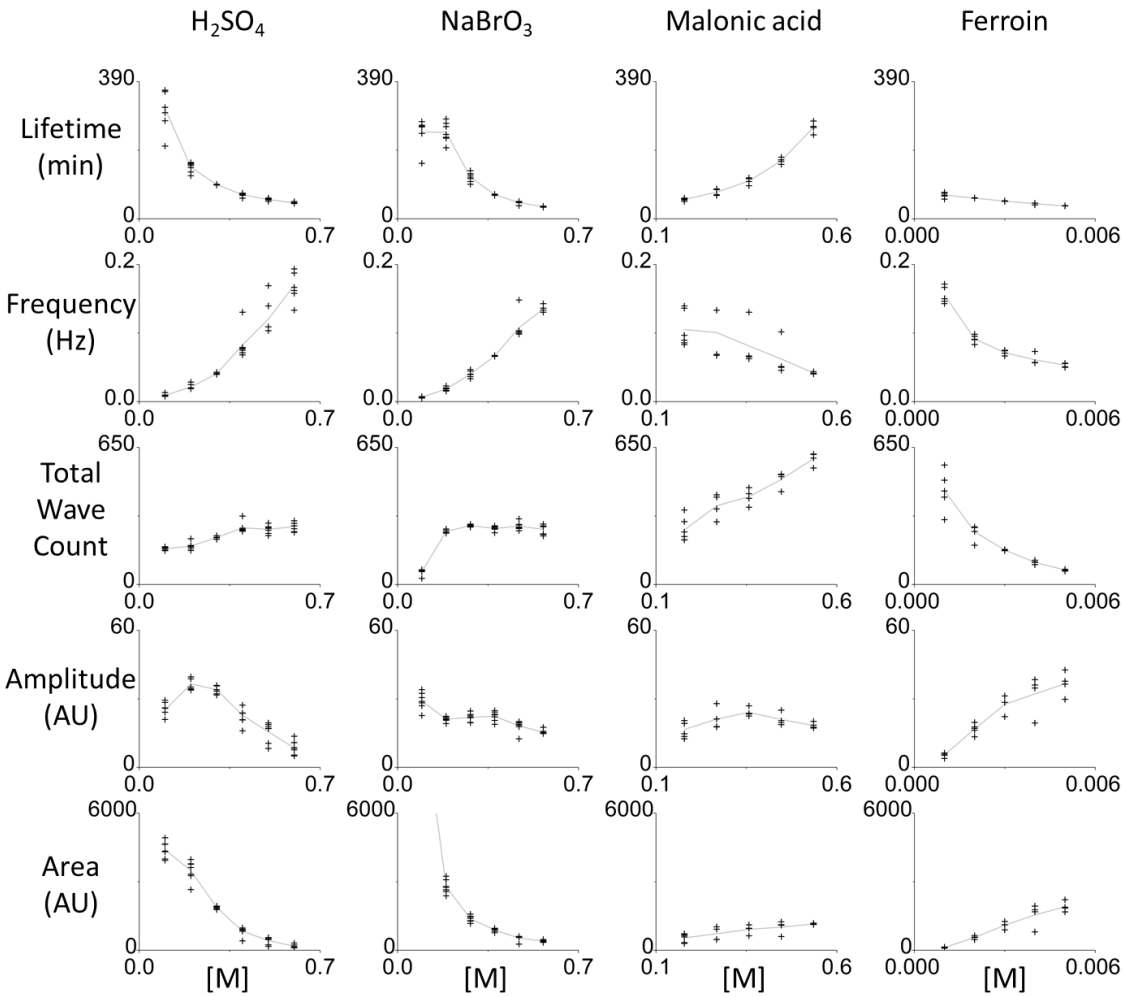

Figure 5.1 Graphs showing wave characteristics of MA BZ droplets when each component is varied and droplet behaviour is observed until no more oscillations can be seen. All droplets contain [H_2SO_4] = 0.5 M, [$NaBrO_3$] = 0.47 M, [malonic acid] = 0.18 M, [ferroin] = 2 mM unless otherwise stated. The number of samples for each graph are H_2SO_4 = 7, $NaBrO_3$ = 7, malonic acid = 4 and ferroin = 4. The area for 0.09 M $NaBrO_3$ is out of bounds, with a mean of 10816 AU and range between 7957 and 13778 AU.

As H_2SO_4 is increased, the lifetime significantly reduces while the frequency significantly increases. However, the total wave count has only a small increase (compared to increasing other components) while this is the case, indicating that the loss of lifetime is compensated by an increase in frequency. The amplitude and area of the waves is observed to decrease as the concentrations are increased, indicating that the background of the droplets is more blue at higher concentrations so that the contrast with the waves is not as high. However, when the concentration of H_2SO_4 is reduced to 0.1 M, the amplitude is observed to be

smaller compared with 0.2 M. In the recordings, the waves are observed to be less blue compared with the red background and thinner compared with 0.2 M H_2SO_4 droplets. This is hypothesised to be because the H_2SO_4 concentration is low enough as to be a limiting factor when below 0.2 M.

When $NaBrO_3$ is increased, the lifetime is increased while the frequency is reduced as in the case of H_2SO_4. However, total wave count again stays approximately the same above 0.19 M $NaBrO_3$, indicating that the decreased lifetime is compensated by the increased frequency to form a similar total wave count. As in the case of H_2SO_4, the amplitude and area are observed to decrease as the concentration increases. However, the gradient of the amplitude and area is significantly smaller compared with H_2SO_4, indicating that the increase in the blue background is not as significant. However, at 0.09 M $NaBrO_3$, the trend for the droplet characteristics is different compared to the other concentrations. The lifetime is similar to droplets with 0.19 M while the total wave count is significantly lower than for other concentrations. In addition, the area under the peaks is significantly higher than the increase in amplitude observed. It is also higher than all other droplets with a mean of 10816 AU. At this concentration, the droplets are observed to become exhausted and stop oscillating as red droplets, while at other concentrations they stop oscillating as transparent droplets. Even though these droplets have no waves, the red colour is observed to become more transparent over time, eventually becoming fully transparent between 9 to 21 hours of after the BZ solutions are mixed. From both these observations, is hypothesised that this very large change in behaviour is because this concentration of $NaBrO_3$ is significantly lower than the malonic acid concentration of 0.18 M. Hence, the $NaBrO_3$ concentration becomes the limiting factor and the lifetime can no longer increase even with the significantly lower oscillation frequency.

Increasing malonic acid concentration has the opposite effect of increasing H_2SO_4 and $NaBrO_3$ concentration. This time, increasing the concentration also increases the lifetime and total wave count. The frequency is observed to reduce, but at a lower rate than when changing the concentration of other components and not enough to compensate so that the total wave count still increases significantly. The amplitude is observed to be similar for all concentrations while the area is observed to increase slightly. This observation is interesting as it shows that the wave characteristics themselves do not significantly change while the lifetime and total wave count significantly increase. The change in frequency can

potentially be attributed to how these wave characteristics are obtained from the median of many waves. This is because as the droplet oscillates, frequency reduces over time. Therefore, if the droplet has a long lifetime with significantly larger number of waves, the median frequency would be lower even if the droplet starts with the same initial frequency, as the median wave would have had more time to reduce in frequency before eventually turning transparent. One method of compensating for this is by using only the frequency at the early part of the low frequency oscillation phase, but this would no longer be representative of the overall behaviour of the oscillations and was not used. Significant outliers are present in the frequency graph as four droplets had long initial phases and did not achieve the middle phase where it has a lower frequency. These droplets are observed to be exhausted slightly faster than other repeats, with only the area being reduced compared to other repeats. Other wave characteristics are not affected in these cases.

As ferroin increases, frequency and total wave count reduces significantly while the lifetime slightly reduces. The amplitude and area are also observed to increase significantly when the concentration is increased, indicating a higher contrast of the blue wave compared with the red background. As the shorter lifetime is no longer compensated by an increased frequency, the total wave count is also significantly reduced. Unique to the other components, this means that it is possible to have droplets with a short lifetime, low frequency as well as small total wave count by varying ferroin. While the difference in lifetime is relatively smaller compared to changing other chemical components.

Important observations for array experiments is that both H_2SO_4 and $NaBrO_3$ have similar changes in behaviour as they are increased, where they both reduce the lifetime and increase the frequency significantly with little effect on the total wave count. Malonic acid causes the opposite effect, where increasing it causes a significant increase in lifetime and total wave count when increased with relatively smaller effects on other wave characteristics. Ferroin has a unique effect than all other components, where increasing its concentration decreases its lifetime, frequency and total wave count at the same time. All these characteristics are useful for applications in arrays, where changing different parameters in different ways can give different effects to coupled neighbours.

5.2 Effect of limiting $NaBrO_3$ and MA concentration

Further tests are performed in order to determine if using different concentrations of $NaBrO_3$ and MA can significantly change the oscillation behaviour of BZ droplets. This is because these components may act as limiting factors for other components when changed too significantly due to their function in oxidising and reducing the droplet rather than as the catalyst for the reaction. To test this, an experiment is performed to compare the effect of varying MA concentration while $NaBrO_3$ is halved and varying the ferroin concentration while MA is doubled. For a better comparison, both experiments were performed at the same time as the experiments with normal concentrations of $NaBrO_3$ and MA.

The experiment with increasing MA at 0.24 M $NaBrO_3$ concentration, which is half of the previously investigated concentration, showed significant changes to the BZ oscillation behaviour as shown in Figure 5.2 (A). This experiment shows characteristics consistent with the previous experiment for reducing $NaBrO_3$, such as increased lifetime, reduced frequency, similar total wave count, larger amplitude and larger area. In the previous experiment where the MA concentration is not increased too much above the concentration of $NaBrO_3$, the behaviours were consistent where lifetime and total wave count would increase while frequency slightly decreases. However, when $NaBrO_3$ is limited, the lifetime and total wave count is observed to decrease as MA is increased. The amplitude and area are also observed to decrease slightly with increased MA concentration while the frequency is almost constant. There is a significant change in the trend between 0.18 M MA and 0.27 M MA. It is speculated that this is because the malonic acid is significantly higher in concentration than the $NaBrO_3$ when increased above this point, and so the $NaBrO_3$ is limited and increasing the MA further no longer causes the same trends in wave characteristics. This corroborates with the previous experiment in Figure 5.1, when the $NaBrO_3$ concentration is 0.09 M, which is significantly lower than the MA concentration of 0.18 M. In this experiment the trend for wave characteristics also significantly changes, showing that $NaBrO_3$ is limited at this concentration.

When MA is doubled from the previous investigation to 0.36 M $NaBrO_3$, there is almost no change in the trends for all wave characteristics while ferroin is varied. These results are summarised in Figure 5.2 (B). The most significant difference is that the lifetime is approximately doubled and the total wave count is doubled for lower ferroin

concentrations. Additionally, the frequency is slightly reduced while the amplitude and area are slightly increased. It is interesting to note that at higher concentrations the total wave count is similar for both MA concentrations while the trend for all the other wave characteristics continues similarly. This result is significant as it shows that as long as the other components are not limited, the range of ferroin used can still have significant effect on the wave

An experiment was performed with H_2SO_4 with half $NaBrO_3$ concentration (0.24 M) as well, but the behaviours were only visually inspected due to time constraints. It is observed that the behaviours are similar to the previous experiments with 0.47 M $NaBrO_3$ that the frequency is decreased for samples with half $NaBrO_3$ and all droplets became exhausted as transparent droplets. Only 0.1 M H_2SO_4 with half $NaBrO_3$ concentration became exhausted as a red droplet. This droplet slowly became transparent over time. Out of four samples observed, one droplet started having revival oscillations just before it was fully transparent, which caused it to become fully exhausted as a transparent droplet. This is similar in behaviour to droplets of 0.09 M $NaBrO_3$ and droplets of 0.24 M $NaBrO_3$ with higher MA concentration.

From these experiments, it can be concluded that the range at which different components can be varied is limited but still large enough to cause significant changes to the oscillation behaviour. The ratio of $NaBrO_3$ and MA is important to consider as it causes significant changes in the trends of the wave behaviour when one has a higher concentration. Hence, in other experiments where the concentrations are varied care is taken to ensure that the $NaBrO_3$ concentration is always higher than that of the MA concentration.

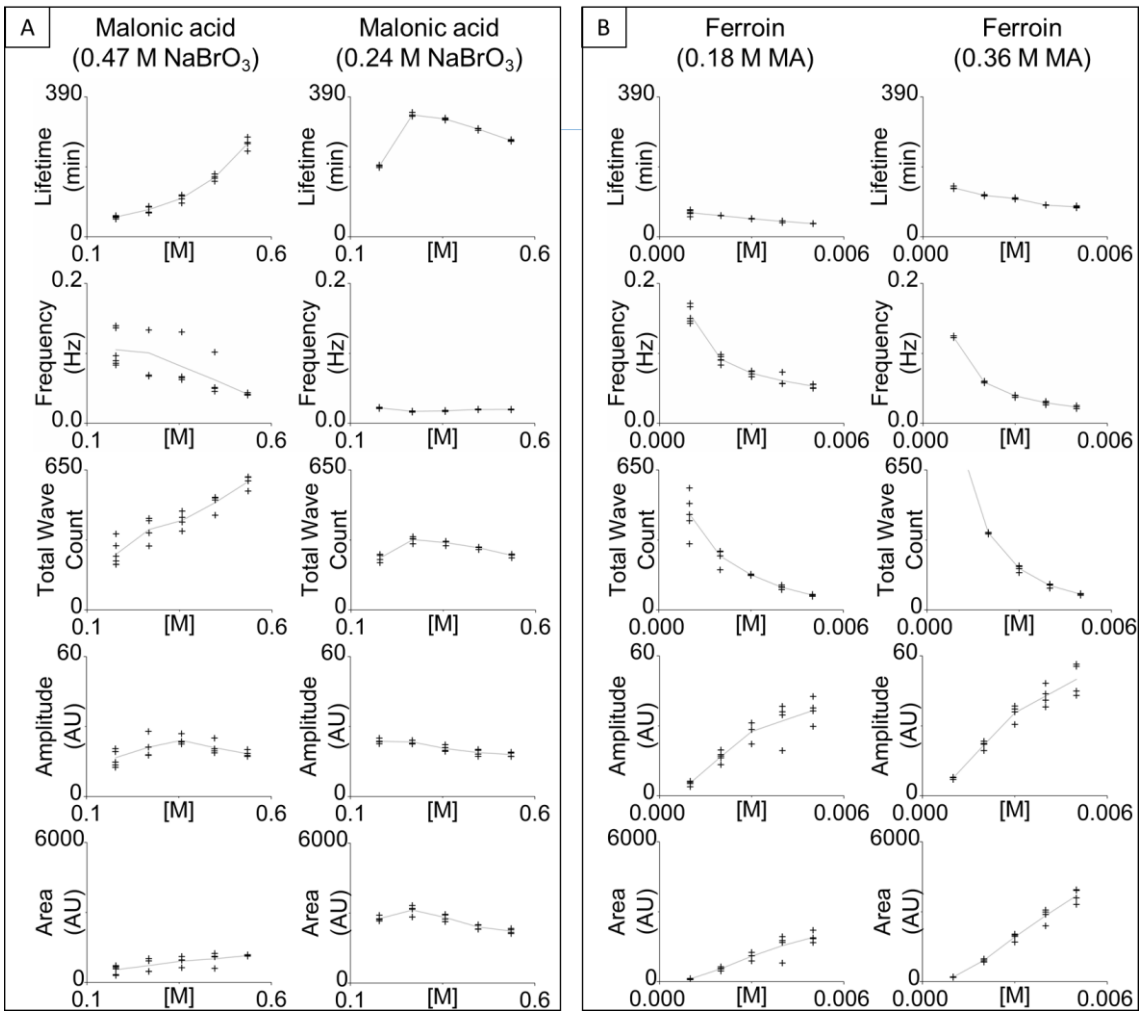

Figure 5.2 Graphs showing wave characteristics of MA BZ droplets when $NaBrO_3$ is halved and MA is doubled. All droplets contain [H2SO4] = 0.5 M, [NaBrO3] = 0.47 M, [malonic acid] = 0.18 M, [ferroin] = 2 mM unless otherwise stated. (A) Graphs comparing increasing malonic acid when $NaBrO_3$ is halved. A significant difference in droplet behaviour is observed, where oscillation properties are reduce above 0.27 M MA for 0.24 M $NaBrO_3$. A change in the trend is also observed between 0.18 M MA and 0.27 M MA in this case, where the lifetime and total wave count can increases but after 0.27 MA, it starts decreasing as MA is increased. (B) Graphs comparing increasing ferroin when MA is doubled. All droplet characteristic patterns are almost the same. Lifetime is doubled while total wave count is significantly increased for lower ferroin concentrations. Frequency is slightly reduced while amplitude and area are slightly increased. The total wave count for 0.36 M MA 1 mM ferroin is out of bounds, with a mean of 803 waves. N = 4 for each case, except for 0.18 M MA 1 mM and 2 mM ferroin where N = 5 and 0.47 M NaBrO3 0.18 M MA where N = 6.

5.3 Relationships between different wave characteristics

Besides comparing the wave analysis with respect to time and chemical concentrations, it is also possible to compare their effect with respect to other wave characteristics. When droplets of different compositions are compared, some trends can be observed that are not observed when reducing the data into simpler statistics as in Section 5.1 and 5.2.

When comparing the baseline and wave count (at the specific time) of droplets as in Figure 5.3, it is observed that besides becoming transparent at different times the background of the droplet reduces at a similar rate at first until it reaches a minimum point. Each baseline then increases according to the lifetime of the oscillations, where the shorter lifetime having the steeper gradient. In each experiment, the droplets have a similar baseline pixel intensity when the droplet has become transparent. The value is not exactly the same for each experiment but it is usually at approximately 120 AU. The $NaBrO_3$ droplets can be observed in (A) and (B) to have a similar final wave count (equivalent to "total wave count" for the whole lifetime) despite having very different gradients and lifetimes. In contrast, the H_2SO_4 wave count graph from Figure 4.10 has a slightly higher wave count for droplets with higher frequency and H_2SO_4 concentration, which corroborates with the statistical data. The MA graphs in (C) and (D) on the other hand show that the graphs become transparent at different times, but have a very similar frequency such that all the wave count graphs overlap. To compensate, the wave count graphs extend further for longer lifetimes at the same gradient to have a larger final wave count. This graph also shows a change in decrease in gradient as time goes on, which explains why the statistics for higher malonic acid with a longer lifetime show a lower frequency despite a similar initial frequency. In comparison, graphs (B) and (D) have too short of a lifetime for this to be observed. For the ferroin experiment in (E) and (F), the baseline when it has become transparent is lower as higher concentration droplets can become exhausted as blue droplets, so it is not completely transparent. In the wave count graph, the droplets with a higher frequency have a steeper gradient and all corroborate with the statistical data. Additionally, despite having significantly different gradients, the graphs with a lower gradient are found to be significantly shorter in lifetime, so they have an even lower final wave count despite having a low frequency.

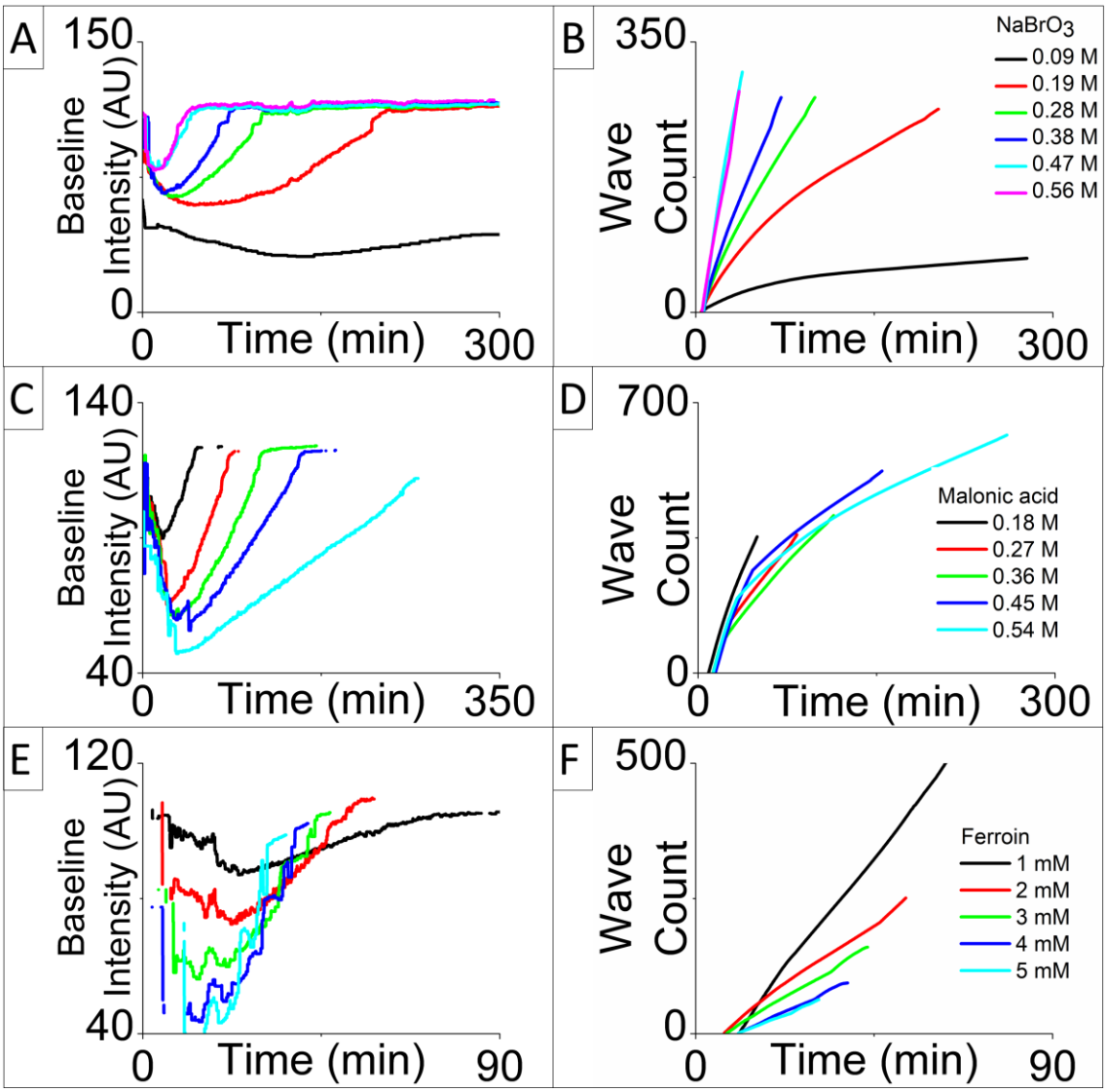

Figure 5.3 Baseline intensity (pixel intensity measured in AU) and Wave count graphs over time. The time when baseline intensity reaches its maximum value is the time when the droplet becomes transparent. The gradient of the baseline is steeper for shorter lifetime droplets. The gradient of the wave count graph is steeper as the frequency increases. (A) Baseline intensity graph for different $NaBrO_3$ concentrations. $NaBrO_3$ has a shorter lifetime as the concentration is increased. (B) Wave count of $NaBrO_3$ shows that all concentrations of $NaBrO_3$ has approximately the same final wave count except for 0.09 M $NaBrO_3$, corroborating with statistical data. (C) Baseline intensity for MA is also shows that higher MA droplets become transparent and exhausted later. (D) Wave count graph shows that higher MA droplets have greater number of waves if the MA concentration is higher. Gradients also show that the frequency for each is approximately the same. (E) Baseline graph for ferroin shows that lower ferroin concentrations lasts longer. (F) Wave count graph shows that lower concentration ferroin has higher frequency while still having a longer lifetime and larger final wave count.

When comparing the scatter plots using different combinations of wave characteristics, some patterns in behaviour can also be observed as in Figure 5.4. When the Amplitude versus frequency graph of H_2SO_4 or ferroin are plotted for each different concentration as in (A), both have the common pattern when the higher frequency composition has a low amplitude and vice versa. All these plots fall into a curve such that they are unable to have an increased amplitude and increased frequency at the same time with only a small amount of overlap. For $NaBrO_3$ in (B), this pattern is not observed, as instead the amplitude of all the concentrations is almost the same but with significantly different frequency. Instead, the entire graph is shifted upwards in the frequency axis as the concentration is increased. The graphs also reduced in frequency range, such that graphs of lower concentration droplets appear compressed in the y-axis. In comparison in (C), the amplitude versus frequency graph for droplets with different MA is significantly different, where all the concentrations overlap. When the graph in (C) is colour mapped according to the peak count as in (D), it is observed that the peaks all occupy similar positions depending on the time the peak is formed relative to the total lifetime of the droplet. This is observed by how all the peaks in colour mapped in red and blue are in approximately the same positions for all the different concentrations marked with different symbols.

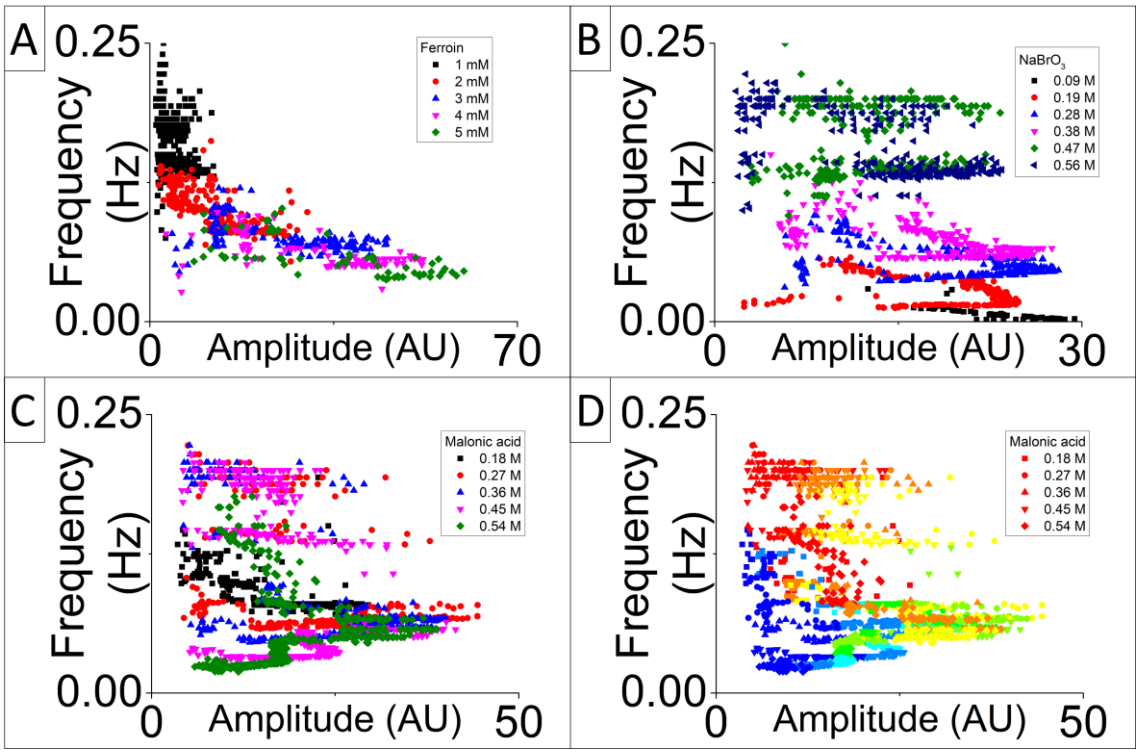

Figure 5.4 Frequency versus amplitude graphs of droplets of different composition. Droplets of different composition are plotted with different symbols and colours. (A) Graph for ferroin shows that as the concentration increases, frequency of the droplet reduces and the amplitude increases. A similar graph is observed for H_2SO_4, except that the frequency reduces as the concentration is decreased. (B) Graph for $NaBrO_3$ shows that as the concentration is reduced the entire plot is shifted downwards with relatively little overlap. The graph can also be seen to be compressed in the y-direction as it covers a smaller frequency range. (C) Graph for MA shows that there is almost no difference in the plots as the concentration increases, with all the plots overlapping despite each droplet having different lifetimes and total wave counts. (D) Colour mapped version of C. Colour map shows earlier peaks as red and later peaks as blue. All overlapping graphs have a similar shape and cover approximately the same area showing that oscillations at the same proportion of lifetime have approximately the same behaviour. Only 0.18 M MA has a slightly compressed shape, but this may be due to the significantly shorter lifetime.

When the statistical data is plotted using different peak parameters as well, other patterns emerge. In the graph of total wave count versus sum of area in Figure 5.5 (A), it is observed that the sum is not proportional to the number of waves counted. The values for all graphs should be similar if all the peaks had the same area under the graph, which implies that the shapes of the peaks is different for different droplet compositions. For example, droplets with varying ferroin can have significantly different total wave counts, but the sum of the area of all peaks remains approximately the same for that malonic acid concentration. The $NaBrO_3$ shows that even though the total wave count has reduced for 0.09 M $NaBrO_3$, the sum of the area has still significantly increased, indicating that the peaks are significantly wider. This droplet composition is exhausted as red droplets. Droplets with a lower H_2SO_4 and $NaBrO_3$ tend to have a significantly higher sum of area for the same total wave count. For increasing malonic acid, increasing the total wave count also increases the sum of the area proportionally. This is also reflected in the amplitude versus area graph in Figure 5.5 (B), where the droplets with low H_2SO_4 and $NaBrO_3$ have a significantly larger area for the same amplitude, while changing malonic acid or ferroin concentration increases the amplitude and area proportionally. It can also be observed that for the ferroin droplet graphs overlap, except that the graph with higher MA is extrapolated further into higher amplitude and area.

In the amplitude versus frequency graph in Figure 5.5 (C), droplets with lower H_2SO_4 and $NaBrO_3$ form a cluster with low frequency for a medium amplitude. This shows that despite having the same amplitude as other droplets, the frequency is significantly lower even compared to droplets with a larger amplitude. In comparison, the area versus frequency graph in Figure 5.5 (D), which is expected to be the same shape if the area and amplitude were directly proportional shows no significant outlier, with all droplet compositions in a curve where higher frequency droplets have a smaller area. As all the points in this graph fall into a curve with almost no outlier despite the significantly different wave characteristics and droplet compositions, it can be speculated that there may be trade-off in oscillation characteristics to maintain this shape for all droplet compositions.

Further analysis of such data can yield insight into the relationship between different wave characteristics. This in turn can be applied to understand the mechanism of droplet oscillations for future applications. From this data, it can be confirmed that decreasing the H_2SO_4 and $NaBrO_3$ concentrations cam have an effect on the shape of the peaks detected for each BZ oscillation.

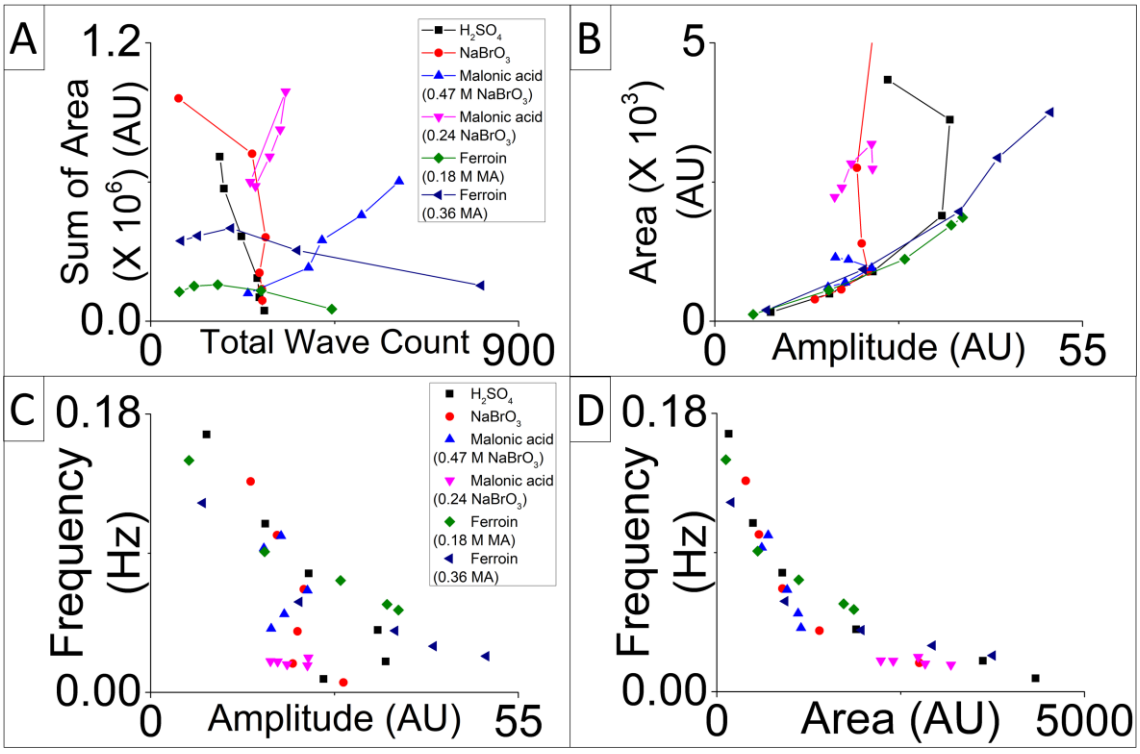

Figure 5.5 Graphs of relationships between different peak parameters from summarised statistical data of multiple repeats of the same droplet composition. (A) Graph of total wave count versus sum of area shows that for the same total wave count a significantly higher sum of area can be achieved, even though this is should be a proportional increase if the peaks are the same shape. (B) Graph of Amplitude versus area shows that for the same amplitude, some droplets have a significantly different area. The area for 0.09 M $NaBrO_3$ is out of bounds, with a mean of 10816 AU. (C) Graph of amplitude versus frequency shows that droplets with lower H_2SO_4 and $NaBrO_3$ form a cluster of significantly lower frequency for the same amplitude. This implies that even though the graphs are the same height, the frequency is significantly lower than other droplet compositions. (D) Graph of area versus frequency shows that all compositions fall into a common curve where higher frequency droplets have a smaller area and vice versa. However, the cluster for lower H_2SO_4 and $NaBrO_3$ in C is not observed here. This implies that the wave shapes are not the same despite having the same amplitude.

In summary, the characterisation of single droplets of different compositions has yielded trends in the oscillation behaviour and wave characteristics when each component is changed. This can be used in the other experiments to both design droplet arrays with specific properties in specific locations in the topology. It can also be used to compare any changes in the droplet behaviour between droplets in arrays and single droplets to determine if there are any significant changes in the wave characteristics due to droplet communication. A summary of the droplet behaviours for different compositions is shown in Table 5.1.

Table 5.1 Summary of changing component concentrations and their effects on wave characteristics. Characteristics that increase are marked in blue, while those that decrease are marked in orange and those that stay the same are left white.

Increasing Concentration	Lifetime	Total Wave Count	Frequency	Amplitude	Area
H2SO4	↓	↑/≈	↑	↓	↓
NaBrO3	↓	≈	↑	↓	↓
Malonic acid	↑	↑	↓/≈	≈	↑/≈
Malonic acid (Half NaBrO3)	↓	≈	≈	↓	↓
Ferroin	↓/≈	↓	↓	↑	↑
Ferroin (Double MA)	↓/≈	↓	↓	↑	↑

Chapter 6 Droplet behaviour in arrays

Droplets in future systems will need to be placed in coupled arrays allowing communication so that their behaviours can be changed and manipulated based on their topology and the composition of neighbouring droplet compositions. Using the data obtained from Chapter 4 and 5, it is now possible to compare the behaviour of these droplets when coupled with other droplets versus their behaviour as single uncoupled droplets. As before, the same PMMA wafer design in Figure 3.4 (A) with many linear slots is used. This allows up to 42 arrays to be observed simultaneously and gives the same conditions as the single droplet characterisation done previously so a direct comparison can be made. As before, it is assumed that there is no communication between the plastic slots either through the PMMA or the oil above the arrays due to the large distance. First, the stability of the arrays of droplets of different compositions is analysed, followed by the wave patterns of coupled droplets and the statistical analysis of the wave characteristics.

6.1 Stability of droplet arrays

A practical unconventional computing setup needs different coupled droplets to for different functions and behaviours and these arrays need to survive for a long enough time for the computation to be completed. Due to this necessity, it is important to determine the stability of droplet arrays containing coupled droplets of different composition. To do this, the number of interfaces in the experiment are counted, taking note how many interfaces are between droplets of the same composition. The number of fusions after 1 hour and after the entire experimental time are compared while comparing with the number of fusions between droplets of the same composition. Most fusions occur a short time after the filling procedure long before 1-hour observation time, where the number of fusions after this 1-hour observation time not significantly higher despite being observed for between 5 to 8 hours. Usually these remaining arrays even survive until the next day. For the purposes of the analysis, the final survival rate after 5 to 8 hours is taken into account and the survival rate of droplets of the same composition is disregarded to exaggerate the instability of the arrays.

All experiments are conducted alongside at least one or two repeats where all droplets in the array are of the same composition to confirm that the stability is affected by the composition of the droplet rather than the conditions of the asolectin in hexadecane oil, PMMA wafer or petri dish glass. Usually none of these droplets of the same concentration is observed to fuse. Only one experiment using varied ferroin concentration had droplets of the same concentration fusing, but even then the survival rate for both droplets of different and the same concentration was similar at 85%.

When droplets of identical composition are placed together, the survival rate is very high, with no fusions or only one fusion. Droplets with significantly different malonic acid concentration, which is 0.1 M difference between droplets, also have high survival rates at 84%, while droplets with 0.2 M difference has a 77% survival rate. Droplets with different ferroin concentrations of 0.002 M difference have a similar 85 to 99% survival rate. Droplets with a 0.2 M difference in $NaBrO_3$ had a survival rate of 79%. Droplets with 0.1 M difference in $NaBrO_3$ has a survival rate of 100% in a plate with 56 interfaces though this experiment was only observed for 1 hour and most droplets had stopped oscillating by then. H_2SO_4 has the lowest survival rate with differences of 0.2 M at approximately 50% survival rate. One experiment reused a PMMA in oil setup by removing all the previous droplets and adding new arrays. These conditions caused the setup to be more hydrophilic than normal, but the survival rate was still over 85% for both droplets of the same and different concentrations. This shows that even when used in imperfect conditions BZ droplets are quite stable.

Non-oscillating droplets are also tested. Droplets with no H_2SO_4 are observed to all undergo fusion with their coupled droplets, even though droplets with no malonic acid in the same array mostly remained intact. In a separate experiment with droplets containing no malonic acid, 91% of the interfaces remained intact despite having the same difference in concentration as that of the no H_2SO_4 droplets and in addition to a 0.1 M difference in $NaBrO_3$. Droplets containing no ferroin has only a 19% survival rate despite the smaller difference in concentration compared to those of droplets without MA. In addition, when droplets of uninitiated pure CHD BZ were tested, only 27% of the interfaces survived, though this experiment used both a 0.1 M difference in $NaBrO_3$ and 0.2 M difference between CHD and malonic acid concentration, which is similar to the experiment with non-oscillating droplets containing no malonic acid.

From these results, it is concluded that the concentration differences in $NaBrO_3$, malonic acid and ferroin all have little effect on the stability of the arrays. It is also significant to note that droplets with no malonic acid with an oxidised blue state are still very stable despite the large difference in concentration and lack of oscillations. However, droplets with significantly lower oscillation frequency or oxidising agents such as H_2SO_4 and $NaBrO_3$ also have a higher chance of fusion compared to others. Ferroin also appears to significantly affect the stability of the droplets, as droplets without ferroin but containing all other components are much less stable. Pure CHD droplets are also less stable when coupled with droplets of pure malonic acid, despite being in the uninitiated oxidised blue state, though this could be due to other factors. A summary of the survival percentages is shown in Table 6.1.

Table 6.1 Survival percentage range of droplet interfaces when concentration of one species is changed. Only interfaces between 0.1 and 0.3 M droplets for H_2SO_4 and between 0.09 and 0.28 M $NaBrO_3$ were assessed as these interfaces experienced the worst case for droplets of different H_2SO_4 and NaBrO3 coupled in arrays and while the interface with the higher concentration droplets were stable.

Interface Type	**0.1 and 0.3 M H_2SO_4**	**0.09 and 0.28 M $NaBrO_3$**	**MA**	**Ferroin**	**No H_2SO_4**	**No MA**	**No ferroin**	**Pure CHD**
Total interfaces	40	39	84	84	40	38	42	41
Broken interfaces after 2.5 hours	29	15	5	0	40	3	33	29
Interfaces survived (%)	**27**	**61**	**77**	**100**	**0**	**92**	**19**	**27**

6.2 Wave pattern behaviour

The wave behaviour of the single droplets is then compared with droplets played in arrays. It is observed that waves in pure MA BZ droplet arrays do not propagate through the droplet interface to interact with waves on the other side consistently. When analysing the video, space-time plot and analysing the numerical data, no consistent phase difference can be observed, where droplets go in and out of phase similar to uncoupled droplets. However, it is observed that the wave pattern in these droplets can be influenced by having BZ droplets of different lifetime coupled to them.

When first placed in an array, wave sources start from random locations in each droplet even between repeats. When first coupled, a new wave source forms from the interfaces of each droplet or existing wave sources move towards the interface. Waves from the interface propagate and meet with waves from other sources, where the meeting point is slowly pushed back until all other wave sources are extinguished. This effect has been observed over 10 different experiments with different array compositions and positions. This is pattern is shown in Figure 6.1 (A). While the wave pattern can evolve such that PMMA walls can form wave sources, this is the most common pattern for droplets coupled with other droplets of similar or longer lifetime. As the neighbouring coupled droplet becomes exhausted, the wave source at the interface becomes weaker so the wave source can move towards the middle of the droplet or the PMMA wall, as seen in Figure 6.1 (B). This was observed for droplets of different composition and for two identical droplets with 0.3 M H_2SO_4, 0.45 M $NaBrO_3$, 0.35 M MA, 60 mM KBr and 1.7 mM ferroin. In most cases where two droplets of identical composition are coupled, this usually does not happen and instead they have waves from the interface until exhaustion.

If a freshly mixed droplet of the same composition is added to the top of the array, the newly formed interface above the original droplets forms a wave source that becomes dominant over other sources. However, only droplets directly coupled to the fresh droplet are affected, and other droplets in the array continue with their original behaviour with waves sources in the middle or the PMMA wall. This is shown in Figure 6.1 (C). It is hypothesised that the wave source forms at the interfaces when the droplets are still freshly mixed, but this wave source disappears as the droplet becomes exhausted. This experiment is repeated in the millifluidic chip in Chapter 8 with similar results.

When similar setups were observed in longer droplets of a larger volume, the same observations are observed. These droplets had formed due to fusion of two initially different droplets, but some repeats with the same topology and composition were observed. Waves start from interfaces with droplets of a longer lifetime and from other sources if the interface is with a nearly exhausted droplet. If a fresh droplet is placed on top of a larger fused droplet of the same composition, a new wave source starts at the interface with the fresh droplet that extinguishes other wave sources.

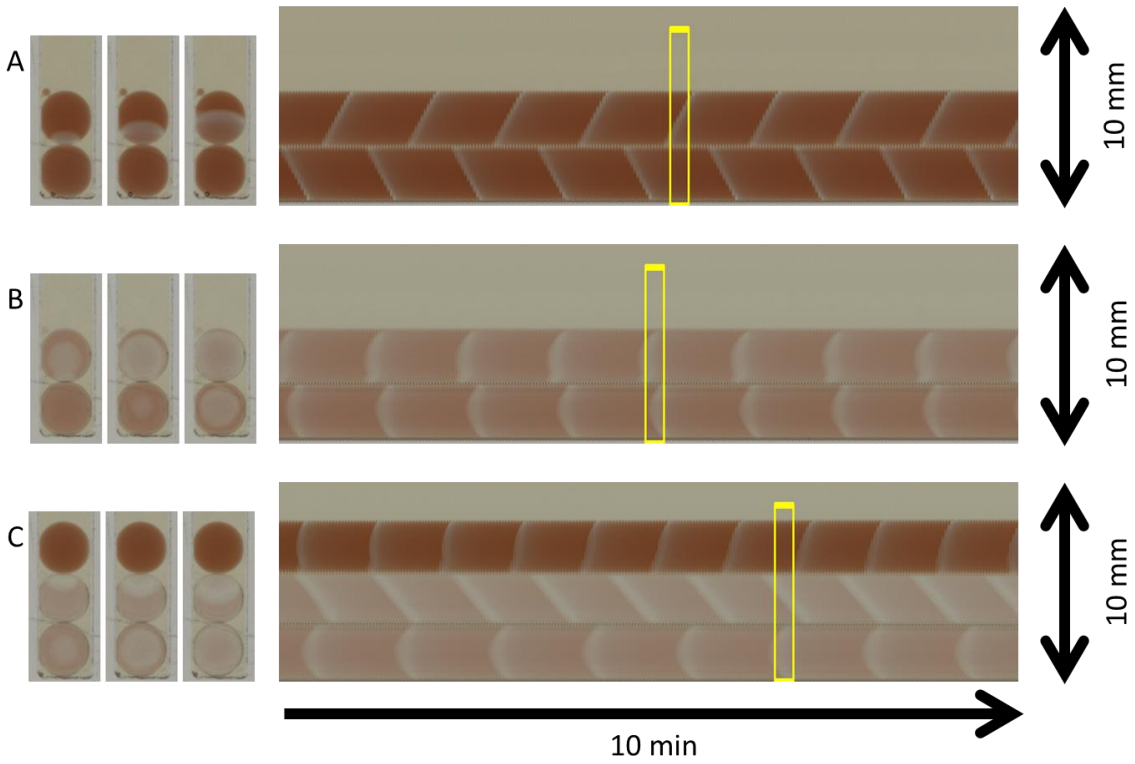

Figure 6.1 Wave pattern evolution of MA BZ droplets of identical composition in 2-droplet array and with fresh droplet of the same composition added on top. Wave sources are at droplet interfaces, until droplets are nearly exhausted. All photos taken at 5-second intervals. All droplets are 2.5 mm diameter. Yellow rectangles mark locations of images on space-time plots. All droplets have 0.3 M H_2SO_4, 0.45 M $NaBrO_3$, 0.35 M MA, 60 mM KBr and 1.7 mM ferroin. (A) Droplets have waves from interface 60 minutes after solution mixed. (B) 180 minutes after solutions mixed, droplets almost exhausted and wave source moves towards middle of droplet. Droplet red colour is also more transparent as it approaches the exhausted state over time. (C) 220 minutes after droplets mixed, fresh droplet of identical composition added on top, causing wave source to move to interface with fresh droplet. Bottom droplet not affected and still has wave from middle of droplet.

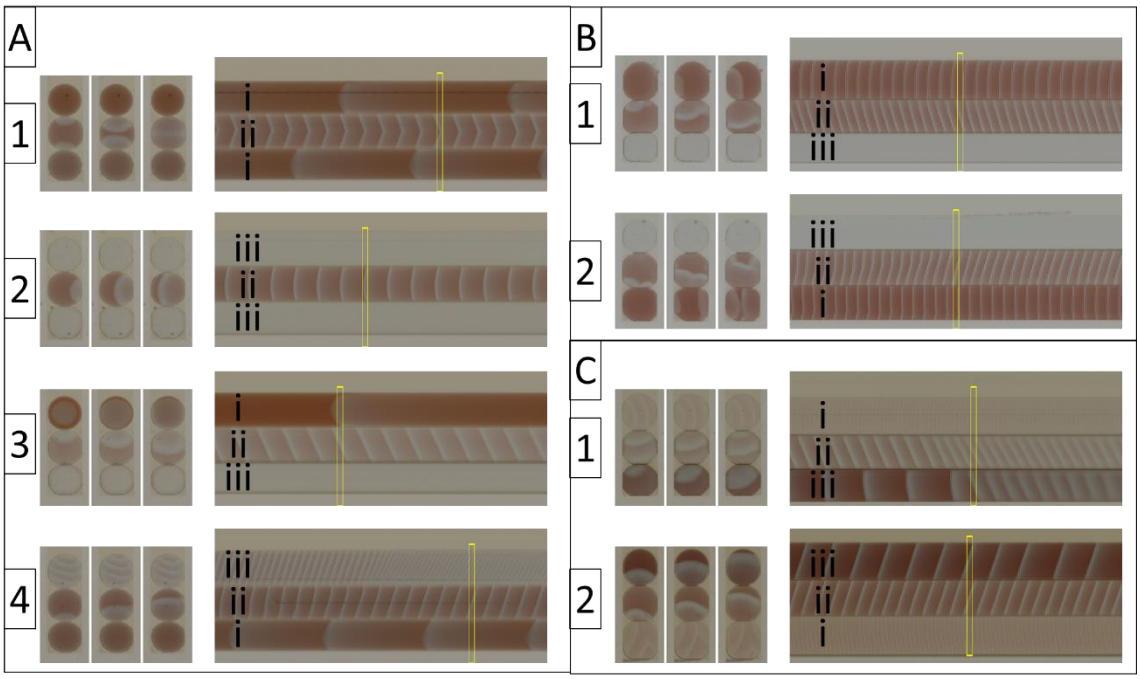

Figure 6.2 Photos of arrays with droplets of the same composition except one component is varied. Each space-time plot denotes a 10-minute period in the x-axis and 10 mm distance in the y-axis. Yellow rectangles mark times where photos taken. Each photo is taken at 5-second intervals and each droplet is 2.5 mm in diameter. Long lifetime droplets are denoted with (i), while intermediate lifetime "sensor" droplets are denoted with (ii) and short lifetime droplets are denoted with (iii). "Sensor" droplets are always sandwiched between neighbours of different composition. Waves observed to start from droplets with longer lifetime (droplet (i)) in all examples. (i) droplets usually do not have waves starting at the interface while (iii) droplets usually do have waves starting from interface. All droplets contain 0.5 M H2SO4, 0.47 M NaBrO3, 0.18 M MA and 2 mM ferroin unless otherwise stated. (A) Arrays with only NaBrO3 concentration varied. Additional cases where "sensor" droplet is coupled with two (i) droplets and two (iii) droplets are tested. In case where only (iii) droplets are present, the waves start from the PMMA wall instead. NaBrO3 concentration in (i) = 0.09 M, (ii) = 0.28 M and (iii) = 0.47 M. (A1) taken at 60 minutes after solutions mixed and (A2) from 75 minutes. (A3) taken at 120 minutes to show that frequency of oscillations reduces over time and (A4) at 43 minutes to show (iii) droplet with a higher frequency as it transitions from the middle to late phase before exhausting. (B) Arrays with only MA concentration varied. MA concentration in (i) = 0.18 M, (ii) = 0.36 M and (iii) = 0.54 M. Images taken at 60 minutes. (C) Arrays with only ferroin concentration varied. Droplets contain 0.36 M MA. Ferroin concentration in (i) = 1 mM, (ii) = 3 mM and (iii) = 5 mM. (C1) taken at 83 minutes to show late phase droplets and (C2) at 60 minutes.

To test this hypothesis, droplets of significantly different lifetime are coupled with a sandwiched droplet with intermediate lifetime and the wave pattern evolution is observed. If this hypothesis is true, when one of the neighbours has stopped oscillating, the remaining interface will act as the wave source. As this middle sandwiched droplet detects if its neighbour is still oscillating and has its wave pattern respond accordingly, this droplet is referred to as the "sensor" droplet. A schematic of this is shown in Figure 1.1 and example results in Figure 6.2. To confirm that this effect is not due to a difference in frequency or concentration differences causing osmotic effects, experiments are performed by sandwiching droplets of intermediate concentration between droplets of different H_2SO_4, $NaBrO_3$, malonic acid and ferroin concentrations. Increasing the H_2SO_4 and $NaBrO_3$ increases the oscillation frequency and reduces the lifetime. In comparison, increasing malonic acid increases the lifetime and reduces the frequency while ferroin decreases the frequency and lifetime as the concentration is increased. Readings of the wave direction are usually taken at 85 to 90 minutes after the solution is mixed so that wave patterns have had time to evolve and extinguish other wave sources.

Experiments with different H_2SO_4 concentration were performed, but the droplet arrays are not very stable with as mentioned in Table 6.1, with only a 27% survival rate, where only 11 of 42 arrays survived intact. However, the droplet behaviour was almost the same as with $NaBrO_3$, where waves started at interfaces with droplets with lower H_2SO_4 concentration, which had lower frequency and longer lifetime. Only 2 arrays coupled with only short lifetime droplets also had waves from the exhausted droplet as well as the PMMA wall, giving this an 82% rate. However, it can also be observed from the fused droplets, which had a concentration of 0.2 M H_2SO_4 that even fused droplets coupled with long lifetime and short lifetime droplets exhibited this behaviour. When coupled to a long lifetime droplet, waves started from the interface. Fused droplets coupled with short lifetime droplets had waves starting from the PMMA wall or from the middle of the droplet instead despite having the same orientation and same composition.

When tested with different $NaBrO_3$, it is observed that it is much more likely that the interface with the droplet with lower $NaBrO_3$, which has longer lifetime and lower frequency act as the wave source and extinguish other wave sources, with 26 out of 26 surviving arrays displaying this behaviour. Interfaces with droplets with higher $NaBrO_3$ that oscillated at high frequency, but have been exhausted, did not start waves from their

interfaces, where the “sensor” droplet preferred to form waves from the PMMA wall or other interfaces. This same effect is also observed in all droplets that have fused due to the instability, where droplets containing an overall $NaBrO_3$ concentration of 0.38 M $NaBrO_3$ and double the volume. These droplets form waves from the interface when coupled with 0.09 M $NaBrO_3$ droplets but form waves from the PMMA wall of from the middle of the droplet when coupled with 0.47 M $NaBrO_3$ droplets. This experiment eliminates that interfaces with droplets with higher concentration and frequency do not act as preferred wave sources.

The interface with droplets of higher malonic acid tended to act as wave initiators, where the coupled droplets are still oscillating after the others have stopped. These droplets have a significantly longer lifetime, higher salt concentration and a slightly lower oscillation frequency for waves. This effect is observed at approximately 80 minutes after mixing, which is 30 minutes after the low malonic acid droplets have become exhausted and stopped oscillating. Out of 42 arrays, 36 arrays exhibited this behaviour, three arrays had wave sources that were slightly offset from the interface with the longer lifetime droplet, one array had a spiral wave that did not stabilise and two arrays had waves from other sources. This is a rate of 86%. This corroborates the $NaBrO_3$ experiment that interfaces droplets with a higher frequency do not act as wave sources, as these have a slightly lower frequency. However, it contradicts the conclusion regarding salt concentration, where the interface with droplets of lower salt concentration act as a wave source in the $NaBrO_3$ experiment. Hence, this experiment eliminates that salt concentration as having any effect and raises the possibility that lower oscillation frequency causes the interface to act as preferred wave sources.

When tested with ferroin, it is found that interfaces with droplets with lower ferroin behave as the preferred interface for waves. These lower ferroin droplets tend to have a less intense red colour of reduced background, low contrast of waves and a very high frequency, similar to the high $NaBrO_3$ droplets. This shows that interfaces with droplets with a lower frequency, darker red background with larger wave peak contrast do not necessarily tend to act as the wave source. Instead, lower ferroin droplets have a significantly longer lifetime instead. Of 42 arrays tested, 4 had spiral waves and did not evolve to have waves from the interface, 2 had waves from other wave sources and 1 had waves from both the PMMA wall and the interface with the longer lifetime droplet. 8

droplets also had waves from the PMMA wall until 60 minutes after the solutions are mixed, after which they all had waves from the interface with the longer lifetime droplet. This gives 35 arrays that had the interface with the longer lifetime droplet as the wave source, which is an 83% rate. This eliminates higher red colour intensity, lower frequency and higher amplitude and width waves as the source of this phenomenon.

Additional experiments with 4-droplet arrays with varying ferroin concentration and with two sensor droplets were attempted, but did not have conclusive results. It was expected that as there were two sensor droplets of identical composition and lifetime, waves would start from the interface of those sensor droplets if only short lifetime droplets were coupled to either end of the array. Of 42 arrays tested, 1 array had fusion event, 11 arrays had waves from other sources, 8 arrays had spiral waves inside the sensor droplet that never evolved into planar waves 5 had waves from the interface with the long lifetime droplet while also having waves from the PMMA wall. In comparison, only 17 arrays had waves from only the interface with longer lifetime droplets, for a 40% rate. It must be noted that most of these arrays with both sensor droplets having waves from the longer lifetime droplet were coupled with only long lifetime droplets of 1 mM ferroin, whereas many of the droplets with waves from the interface with shorter lifetime droplets were coupled with the shorter lifetime 5 mM ferroin droplets. This implies that the difference in lifetime between the 3 mM ferroin sensor droplets and the 5 mM ferroin droplets is not enough for the wave source at the interface with the 3 mM droplet to become the dominant wave source.

It is important to note that while the shorter lifetime droplets usually have waves from the interface, the long lifetime droplets usually have waves that start from other parts of the droplet such as from the PMMA wall or from the middle of the droplet. The exception to this is in the case of the ferroin experiment, where the higher frequency longer lifetime droplets had waves starting from the interface at first, but which moved to the PMMA wall as the sandwiched sensor droplet became exhausted. In comparison, the low frequency short lifetime droplets had waves from the PMMA walls at first, but had waves from the interface as the droplets became exhausted, though droplets placed at the top of the array were more likely to have waves from the interface. This may imply that the effect of the droplet interface acting as a wave source may not be strong enough to influence droplets with a longer lifetime or too low a frequency.

There is also the possibility that the higher blue intensity of the oxidised background due to having more oxidising species is the reason for the interface of the coupled droplet acting as the preferred wave initiator, rather than the oscillation lifetime of the droplet itself. It is also possible that interfaces with the lower $NaBrO_3$ concentration and larger malonic acid droplets acts as a wave source as it releases less bromine or other inhibiting species, where $NaBrO_3$ produces more bromine while malonic acid absorbs it. This effect is tested by coupling blue oxidised non-oscillating droplets containing no malonic acid and 0.24 M $NaBrO_3$. To increase the lifetime of the sensor droplet, 0.31 M MA instead of the normal 0.18 M MA. In theory, if this preference in wave sources is due to the higher blue intensity of the oxidised droplet, the interface connected to the non-oscillating droplet should be preferred as a wave source. When both interfaces are coupled with non-oscillating droplets, the preferred wave source is at random, either from one of the interfaces, the PMMA wall or even the centre of the droplet. However, when an oscillating droplet is coupled at one interface, this interface acts as the preferred wave source and extinguishes wave sources at the interface with the non-oscillating droplet. In this case, of the 10 arrays tested where the sensor droplet is only paired with non-oscillating blue droplets, 8 arrays had waves from the middle of the droplet 25 minutes after the solutions are mixed for 80% rate. Of the 32 other arrays paired with the oscillating droplets, 4 had spiral waves in the coupled droplets, yet the sensor droplet still had waves from the interface with the oscillating droplet and one had waves from the non-oscillating blue droplet. In comparison, 27 had waves from interfaces with the oscillating droplets, for an 84% rate. These sensor

droplets had waves from the middle of the droplet after 60 minutes, but this is reasonable as the droplets used in both the sensor droplet and coupled oscillating droplet had a total lifetime of 90 minutes from mixing, so after 60 minutes the remaining oscillating droplet would be nearly in the exhausted phase.

Due to problems with stability mentioned in Section 6.1, experiments of droplets with different H_2SO_4, without any H_2SO_4, without ferroin and with pure uninitiated CHD BZ did not produce conclusive results about wave coupling behaviour. A summary of the previous results and the conclusions about the properties of coupled droplet that affect the wave source is shown in Table 6.2.

Table 6.2 Summary of experimental results and property of droplet neighbour where wave source formed at interface. Arrays counted 85 to 90 minutes after solutions mixed.

Experiment/ Wave starts from interface with	**H_2SO_4**	**$NaBrO_3$**	**Malonic acid**	**Ferroin**	**Blue non-oscillating droplet**
Concentration	Lower	Lower	Higher	Lower	Higher
Frequency	Lower	Lower	Lower	Higher	Higher (oscillating)
Total Wave count	Lower	Lower	Higher	Higher	Higher
Red background / wave peak contrast	Higher	Higher	Higher	Lower	Higher
Oxidising species ratio	Lower	Lower	Lower	Higher (less ferroin)	Lower
Lifetime	Higher	Higher	Higher	Higher	Higher
Number of arrays from interface longer lifetime droplet	9	26	36	35	27
Number of arrays from other wave sources or with spiral waves	2	0	6	7	5
Percentage from interface with longer lifetime droplet (%)	**81**	**100**	**86**	**83**	**84**

6.3 Oscillation characteristics compared with single droplets

When droplets are coupled, waves did not appear to propagate through the interface or maintain a specific phase difference. The phase difference is observed to change as time goes on similar to uncoupled droplets. Only consistent changes in wave pattern behaviour were observed as in Section 6.2. To determine if there are less obvious effects on the wave properties, statistical analysis is performed on the wave characteristics as described in Section 3.8, 3.9, and 5.3 to compare their wave characteristics with those observed as single droplet. Statistics analysis of H_2SO_4 droplets is not performed, as the droplet arrays were not stable enough to provide enough repeats, as mentioned in Section 6.1.

It is observed in Figure 6.3 that the lifetime, frequency, total wave count, amplitude and area characteristics are similar to those of the uncoupled single droplets. This indicates that for this composition of MA BZ in this asolectin in hexadecane system, the communication between the droplets is not enough to affect the wave characteristics. It also shows that the effect of BZ components leeching into the oil is not significantly different even while coupling the droplets with other aqueous BZ droplets, which should block some surface area exposed to the oil.

When these graphs were plotted with respect to their position in the array, whether it is at the top next to oil or at the bottom next to a PMMA wall, droplets at the bottom near the PMMA wall have slightly longer lifetime and larger total wave count. This is despite the droplets being from the same stock and the lifetime being calculated from the stock mixing time. This may imply that the lifetime is longer if the droplets are pipetted into the oil earlier. In this case, droplets at the bottom of the array were added approximately 10 minutes earlier than droplets of the same composition at the top of the array. However, even with this slight skewing, the trends between the droplets and the differences between the values are very small compared to the error and compared to changing the droplet composition.

This section concludes that while the wave pattern of the droplets has significant changes due to coupling with droplets of different composition, there is no significant quantitative difference in the wave behaviour. There is also no significant interaction between waves of different droplets as the waves are unable to propagate through the interface into other droplets for interaction, while using the current range of pure malonic acid BZ droplet compositions.

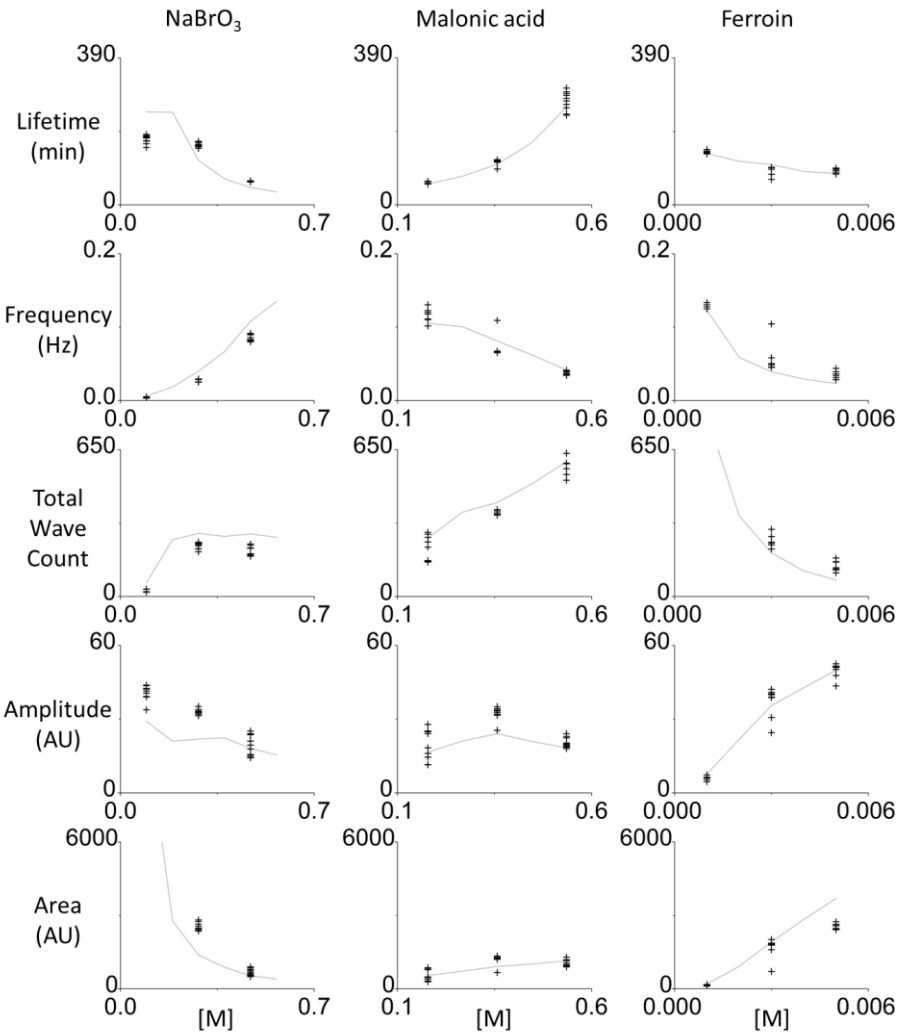

Figure 6.3 Graphs for three droplet arrays where only a single BZ component is varied of different wave characteristics versus concentration when while others are kept constant. The grey line shows the mean of all repeats for single droplet experiments for comparison. The $NaBrO_3$ experiment was prematurely stopped before the long lifetime (0.09 M) $NaBrO_3$ droplets had become exhausted, so the data points for "lifetime" are lower than the data of the single droplet experiments and should be ignored, but are included for context. This does not significantly affect the total wave count (or other graphs) as the droplets have a very low frequency at this stage, so any lost waves do not significantly affect the median statistics. Even so, there is no significant change in the trends of all of the droplets observed, though the points are slightly offset from the mean of the single droplet experiments. The $NaBrO_3$ area graph is out of bounds with a mean of 22501 for multiple droplets and 10816 for single droplets. The total wave count graph of ferroin is out of bounds with a mean of 936 for multiple droplets and 803 for single droplets. N = 12 for $NaBrO_3$ graph, 10 for MA graph and 8 for ferroin graphs.

6.4 Effect of coupling with H_2O_2 droplets

As waves in MA BZ are unable to propagate through the interface, it is interesting to test if coupling these droplets with other chemicals is able to exhibit a change in the droplet behaviour. H_2O_2 is able to move through the interfaces of droplets formed in the asolectin in hexadecane system and is chosen for this purpose. This is corroborated by results in literature [46] and Appendix B, which show that H_2O_2 can move through droplet interfaces while larger molecules cannot.

MA BZ droplets used contain 0.5 M H2SO4, 0.47 M NaBrO3, 0.36 M Malonic acid and 2 mM ferroin to have a high frequency and longer observation time. When pure 9.8 M (30%) and 4.9 M (15%) H_2O_2 droplets are coupled with MA BZ droplets, it is found that it has very low stability and always fuses with the coupled BZ droplet even when diluted. However, when 9.8 M H_2O_2 is mixed into the same BZ solution in a 1:1 volume ratio, the mixed 4.9 M H_2O_2 and MA BZ droplet formed is stable in the array for several hours, though still relatively less stable compared with normal BZ droplets. When coupled with a MA BZ droplet, it is found that the waves in the BZ droplet stop propagating where it is coupled with the H_2O_2 BZ droplet. A zone where the propagation is not possible expands from the interface, eventually pushing the wave source of the BZ droplet further away. Eventually, the zone covers the entire BZ droplet and no more oscillations are observed. Additionally, when it reaches the interface to the next droplet, the region expands through that interface as well. This shows that this effect is able to propagate through interfaces through all droplets in the array. This is shown in Figure 6.4.

This shows that H_2O_2 is usable as a method of stopping BZ wave propagations permanently, but takes a significant amount of time for the inhibition zone to expand and propagate through interfaces. The fact that this inhibition zone can expand through droplet interfaces even in MA BZ shows that the droplet interface still allows chemical communication. It also shows that H_2O_2 droplets are stable when mixed with BZ droplets, but are very unstable when used as pure H_2O_2 droplets even when diluted to the same concentration.

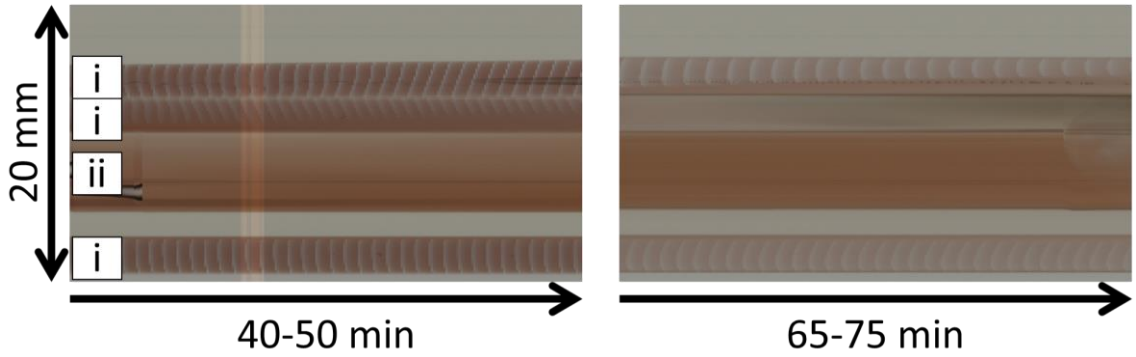

Figure 6.4 Inhibition zone expanding from H_2O_2 droplet. Droplets marked as (i) are 5 µl MA BZ droplets of the standard composition. (ii) is a H_2O_2 droplet fused with an MA BZ droplet. The waves in the droplet coupled with the H_2O_2 droplet are observed to propagate a shorter distance until the whole droplet stops oscillating. After 65 min, the droplet coupled above it also has a zone of inhibition that expands from the interface. The control droplet at the bottom is not coupled with any H_2O_2 droplets and does not experience this effect.

6.5 Effect of exposure to bromine gas under oil

From the literature review, Li *et al.* [160] confirmed that molecular bromine behaves as an inhibitor to the BZ reaction as it promotes the reduction process of the reaction. This was used in other literature such as in [134] and [131] to control the BZ oscillation behaviour and is noted down in review papers such as [10]. Bromine can be produced in situ by mixing H_2SO_4, $NaBrO_3$ and KBr using a half-solution of H_2SO_4, and another half-solution containing $NaBrO_3$ and KBr. The H_2SO_4 is separated from $NaBrO_3$ to prevent it from activating the $NaBrO_3$. The composition of the half-solutions is shown in Table 6.3. The reaction is shown in the following equation:

$$5\ KBr\ (aq) + 3\ H_2SO_4\ (aq) + NaBrO_3\ (aq) \rightarrow$$
$$3\ Br_2\ (g) + 3\ K_2SO_4\ /\ Na_2SO_4\ (aq) + 3\ H_2O\ (l) \quad (1)$$

Table 6.3 Half-solutions of bromine-generating solution. Solution split into two parts and mixed in situ to prevent bromine generation outside of oil.

Half-mixture	Chemical Stock Solution	Volume (µl)	Concentration in complete mixture of 1:1 volume ratio (mM)
A	2.5 M sulphuric acid (H_2SO_4)	120	**692**
A	Deionised water (H_2O)	313.3	**-**
B	1.5 M sodium bromate ($NaBrO_3$)	66.7	**176**
B	1.0 M potassium bromide (KBr)	500	**882**

The droplets are tested by adding the droplets of unmixed half-solution in between a group of 10 µl MA BZ droplets with standard concentrations except with 0.08 M H_2SO_4 as shown in Figure 6.5. The BZ solution contains a reduced amount of H_2SO_4, as it is found that the effects of the bromine are significantly stronger compared to when used in the normal concentration of H_2SO_4. When the BZ droplets are exposed to bromine gas under oil, a dark precipitate is observed which forms on the interface between the aqueous BZ droplet and the bromine oil. This precipitate slowly dissolves back into the aqueous droplet over time until it is no longer observed. Wave sources inside the BZ droplet are also observed to move closer to the bromine source. In comparison, none of these changes is observed in droplets that have not been exposed to bromine. It is hypothesised that the precipitate formed is due to the reaction with ferroin in the droplet. This is because this precipitate is also observed if KBr is added to the BZ mixture when ferroin is present. If ferroin is not present, the yellow bromine gas is observed in the solution, and if ferroin is added, the precipitate is formed. In comparison, if KBr is not added or the yellow bromine is allowed to dissipate before adding the ferroin, this precipitate is not formed.

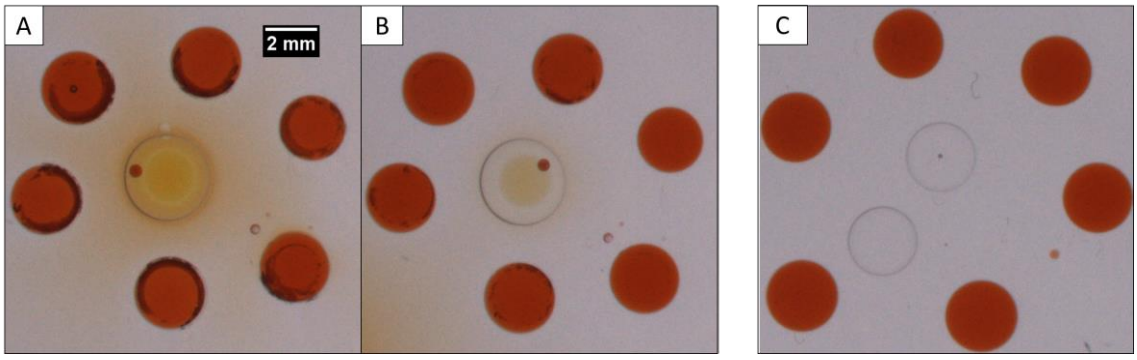

Figure 6.5 Droplets of MA BZ with 0.08 M H_2SO_4. A bromine-generating solution is mixed under oil in the middle of these droplets, forming yellow bromine gas that forms the precipitate. (A) Droplets 10 minutes after mixing bromine. (B) Same droplets 30 minutes after mixing bromine showing that precipitate has dissolved. (C) Control experiment with only unmixed bromine-generating half-solutions without any precipitate.

When BZ droplets with 0.3 M H_2SO_4 are exposed to bromine, the wave source moves from the middle of the droplet towards the source of bromine for approximately 5 oscillations, as seen in Figure 6.6. The effect of bromine is weak, where only droplets placed less than 1 mm away from the bromine source had an effect on the wave pattern. Of 6 droplets tested, only 3 were close enough to have an effect. The precipitate is observed as in the previous experiment still forms, but has a significantly smaller area than in Figure 6.5. Attempts are made to couple bromine-generating droplets in asolectin in hexadecane oil, but bromine has an even shorter range due to reactions with asolectin, which form a dark brown precipitate. These droplets are also very unstable, and tend to fuse once in contact with oscillating MA BZ droplets.

This concludes that bromine can be generated in situ under oil to cause a significant affect to BZ droplets with low H_2SO_4. However, these effects cannot be achieved in asolectin in hexadecane oil as the bromine reacts with the hexadecane to both limit the range of bromine propagation and destabilise the droplet arrays when coupled. This means that bromine gas cannot be feasibly used to control BZ in the current droplet-in-oil setup.

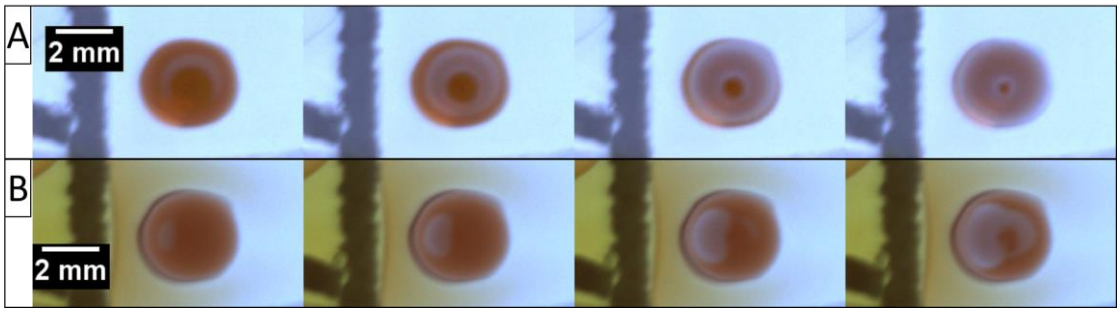

Figure 6.6 Change in wave pattern when 10 µl MA BZ droplets with 0.3 M exposed to yellow bromine gas from droplets held in fibreglass. Images taken at 2-second intervals. (A) Before exposure, wave source is in middle of droplet. (B) After exposure, wave source moved towards bromine source. Dark brown precipitate also observed at oil interface on bromine side.

This chapter concludes that MA BZ droplets have been tested in coupled droplet arrays. These droplets are able to form wave sources from the droplet interface, which stops acting as a wave source when the MA BZ neighbour is exhausted. This causes a significant effect on the wave pattern, which changes its wave source to any interfaces with MA BZ droplets that are still oscillating. By using droplets of different composition, it was also ascertained that factors such as the oscillation frequency, amplitude and osmotic pressure were not the cause of these effects. When the wave characteristics were analysed, there was no significant effect on the trends of the wave characteristics from using the droplets in arrays compared to the observations of single droplets. By testing these droplets with H_2O_2, it was confirmed that chemical communication through the droplet interface is occurring, and that the MA BZ composition itself is the reason why waves are unable to propagate through the interface. Tests with bromine showed that there is a small effect on the BZ wave pattern, but that this is not significant compared to other factors and requires a very large concentration and close distance to be significant. It also showed that bromine is not compatible for use in this droplet-in-oil system. Hence, to study BZ wave behaviour that can propagate through droplet interfaces in this system, a new composition of BZ must be used.

Chapter 7 MA-CHD BZ droplet behaviour

MA-CHD BZ droplets combine the advantage of both MA and CHD BZ, where the mixture allows a relatively short induction time compared to the hours needed by CHD BZ while having waves that can propagate through the droplet interface. This allows larger and more complex networks to be studied and tested using this droplet-in-oil system and gives more interesting observations as to the effects of these complex topologies. The same PMMA wafer design in Figure 3.4 (A) with many linear slots is used. This allows up to 42 arrays to be observed simultaneously and gives the same conditions as the MA BZ characterisation done previously so a direct comparison can be made. As before, it is assumed that there is no communication between the plastic slots either through the PMMA or the oil above the arrays due to the large distance. The wave pattern and characteristics are analysed as described in Section 3.8 and 3.9, similar to analysis done in Chapter 4, 5 and 6. The effect of using different compositions of MA-CHD BZ is then tested by characterising droplets with different ratio of CHD to MA and ferroin concentration. As wave propagation through the interface is now possible, these droplets are then tested in longer arrays and non-linear arrays with meeting points between different linear sections, culminating in tests with complex maze arrays. The “fish” design with loops that can allow waves to feed back into the same path to affect new waves is also tested. The fabrication of these designs is discussed in Section 3.6 and shown in Figure 3.5. As these arrays are difficult to analyse, a modified procedure of using stitched space-time plots is used to observe the wave pattern. Initial work using computer vision techniques to isolate wave fronts from the background and track and analyse their paths is also done. Finally, initiator droplets of higher frequency are tested to as future devices will need to use droplets of different compositions to manipulate the wave pattern behaviour of the arrays for computation.

7.1 Differences in evolution of droplet behaviour

MA-CHD BZ droplets have unique phases that are not present in MA BZ droplets either in single droplets or in arrays. Some phases resemble those in CHD BZ droplets, allowing unique behaviours in arrays to be explored and applied for future designed arrays. An important distinction is that MA-CHD BZ droplets are able to propagate waves through the interface particularly during the middle phase, allowing waves to pass through multiple droplets to interact while having the advantage of MA BZ droplets, which reliably start oscillating without as long of an induction phase. Because of these important advantages, the characterisation and application of MA-CHD BZ droplets is pursued.

When MA-CHD BZ droplets are first mixed, there is an "induction" phase [11, 85, 103] where no waves are observed and the droplet remains in the blue oxidised state for several minutes. This is not observed in MA BZ droplets. This induction phase is present in droplets with a high ratio of CHD but becomes significantly shorter as the ratio of CHD is reduced, as detailed in Section 7.3. While the 50% CHD MA-CHD droplets could oscillate immediately upon mixing with low amplitude high frequency waves, droplets that have 60% and above of CHD ratio needed 102 to 158 minutes after mixing the stock for oscillations to start. This is a significant increase in time the compared with the 50% CHD droplets. However, it is still significantly shorter than the 5 hours needed for pure CHD BZ solution to start oscillating in the bottle with no guarantee of a long period of oscillations after that. It is also more reliable as it can still oscillate even if freshly mixed droplets can be placed in the oil before the stock solution has started oscillating. In contrast, pure CHD BZ droplets can sometimes never oscillate if placed in the oil in the induction phase or even in the middle phase when the background is in the reduced red state with oscillations in the bottle.

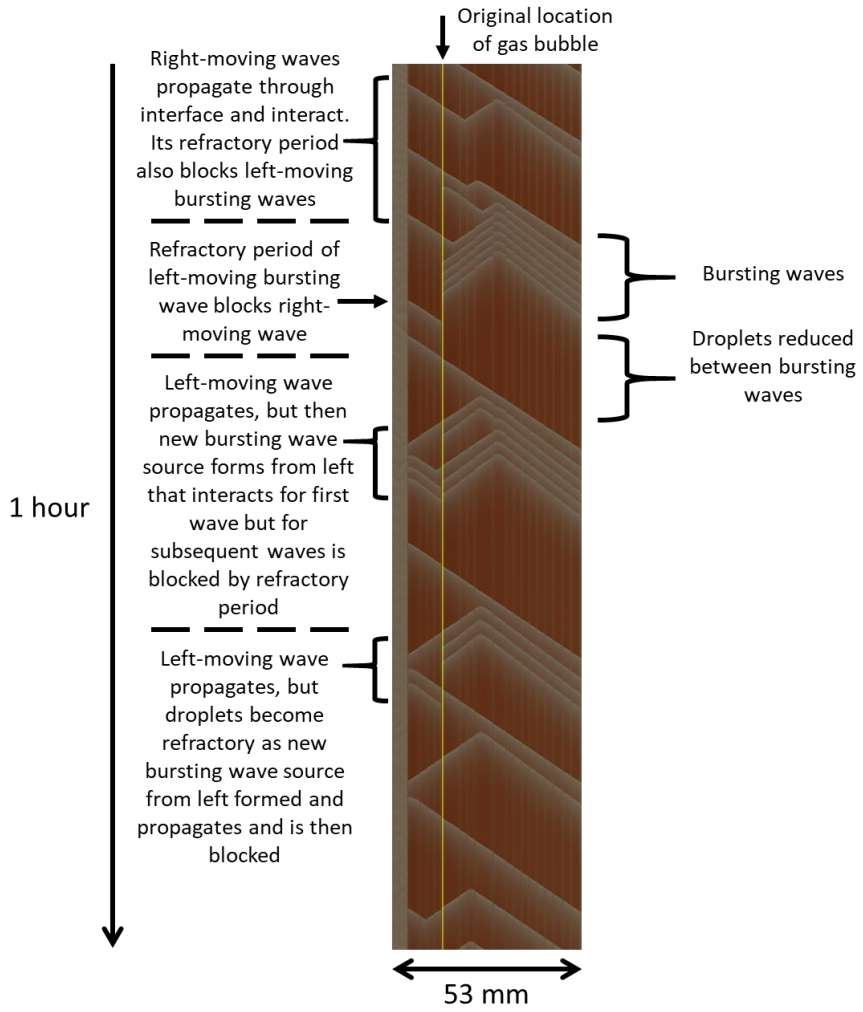

Figure 7.1 Bursting oscillations causing complex behaviours in a 20-droplet array of 5 µl each. Space-time plot rotated 90° clockwise compared with others in thesis. Space-time plot starts at approximately 2.5 hours after stock solution is mixed and gravity acts towards the left side. Five of these droplets are droplets larger than 5 µl due to fusion and are distributed between the bottom and middle of the array. Droplets are observed to stay in the reduced state for a significantly long time and then be self-excited to form higher frequency waves. This process repeats over several cycles, with each "bursting" source occurring after different amounts of time in the reduced state. Waves are more likely to be blocked from propagating through at the sixth droplet from the bottom of the array (marked in yellow) due to a gas bubble that previously separated it from the rest of the array. This bubble had already disappeared 1 hour before the time depicted. Waves do not propagate to or from the left-most droplet as it is still in the initial phase. All droplets use the base composition of 50% CHD MA-CHD BZ. The oil is darker in appearance as it was previously exposed to MA-CHD BZ to test if oil can be recycled while still allowing such behaviours.

It is observed that increasing $NaBrO_3$ increases this induction time and increasing malonic acid, CHD or ferroin decreases this time. However, if the CHD concentration is increased, it is observed that the droplets oscillate for a shorter time and become exhausted as red droplets, or just turn red and never oscillate at all. In comparison, if the MA concentration is increased while keeping CHD at 0.09 M, the droplets will oscillate as normal MA BZ droplets with no waves propagating through interfaces. The duration of this induction phase varies significantly between experiments and repeats on the same dish despite having the same composition and experimental conditions. The ferroin concentration is also observed to affect the length of the induction phase, and is discussed in Section 7.4.

After the induction phase, waves are observed on the blue background, which evolve into high frequency waves of a variety of shapes such as spirals and planar waves. This is the transition to the “initial” phase and it behaves similar to the initial phase in MA BZ droplets. The droplet then undergoes the “initial”, “middle”, “late” and “exhausted” phases similar to MA BZ droplets. As in the induction phase, these phases also vary in duration between experiments and repeats on the same dish, despite having the same composition and setup procedures. In arrays, the middle phase has waves that pass directly through the droplet interface, whereas waves in other phases do not. Besides that, the wave patterns observed in each of these phases is similar to that of MA BZ except that the width of the wave is slightly larger. In the middle oscillating phase though, the width of the planar waves is significantly larger such that the entire wave is large enough to cover the entire droplet, which is approximately 2.5 mm in diameter. Additionally, as the frequency is much lower and the background significantly darker red, the oxidised blue droplet takes more time to be reduced to its original red colour.

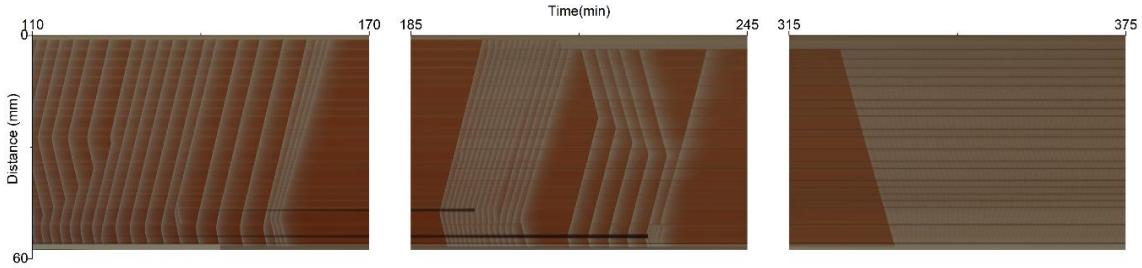

Figure 7.2 Revival oscillations of 21-droplet array. Time measured from when BZ stocks mixed. Droplets all remain reduced for a long time and then start oscillating again. Waves observed to travel directly through droplet interfaces during these stages, except in the case of top droplet after it entered late phase prematurely at 210 minutes. Left image shows “middle” phase droplets suddenly having high frequency “bursting” oscillations and then stopping in the red reduced state. Middle image shows “revived” oscillations where high frequency oscillations suddenly form, and then stop as the droplets enter the red reduced state again. Final image shows droplet entering “late” phase triggered after a final “middle” phase self-oscillation from the top of the array travels through the entire array. Time starts from when stock solution is mixed. Black lines at bottom of space-time plot are gas bubbles that expand and then float to the surface and pop after becoming large enough. In this case, the gas bubbles are large enough and adsorbed onto the glass such that they displaced the large fused droplet without splitting it. All droplets use the base composition of 50% CHD MA-CHD BZ. Oil appears darker in appearance as it was previously exposed to MA-CHD BZ.

MA-CHD droplets can also experience complex oscillatory behaviour such as those resembling “bursting” oscillations [103] and “revival” oscillations [161, 162] between the “middle” and “late” phases. Bursting oscillations occur when multiple waves are self-excited followed by a period of where no waves are observed and then followed by another set of bursting oscillations repeatedly. This is shown in Figure 7.1. Revival oscillations occur where after a long period in the reduced phase, oscillations in the array start again, as shown in Figure 7.2. There is an overlap between these phenomena because the bursting oscillations are the same as revival oscillations where the reduced period and revival oscillation period is a much shorter and where the remaining lifetime of the droplets is enough that this process can repeat over several cycles. So far, this behaviour is observed only in arrays of longer than three droplets, where smaller arrays tend to have long periods

staying in the reduced red state and then a single oscillation that transitions it into the late phase.

BZ droplets containing CHD also emit a “black cloud” while in asolectin oil after it has stopped oscillating. If CHD BZ is left in the hexadecane without asolectin, the oil turns from transparent to yellow instead. These colours remain even after a long time and repeatedly freezing, melting and centrifuging the oil. If the aqueous MA-CHD BZ solution is stored in a glass bottle overnight, a black precipitate is observed on the inner surface of the lid indicating that this product can evaporate into the air above the aqueous solution. This precipitate is difficult to dissolve in water, but soluble in acetone. Experiments in oil previously exposed to MA-CHD BZ show that this has no significant effect on the droplet behaviour compared with the variability of MA-CHD BZ droplets even from the same stock, setup procedure and in the same petri dish.

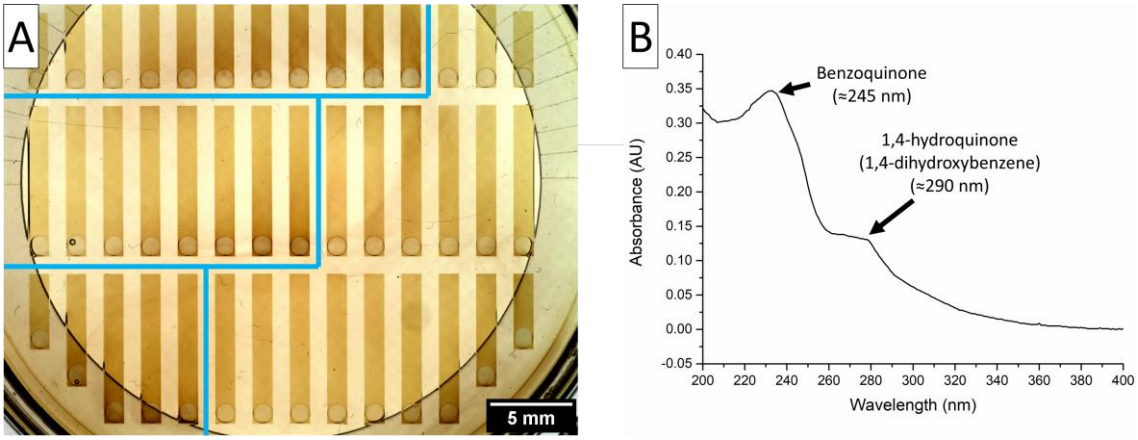

Figure 7.3 (A) Array of MA-CHD BZ droplets with increasing percentage of CHD under asolectin in hexadecane oil. Droplets arranged from 0% CHD to 100% CHD MA-CHD BZ droplets in 10% increments from left to right, then repeated again for the next column and from the left side of the next row. Oil above droplet is darker as the percentage of CHD is increased. Image taken 9 hours 20 minutes after BZ stock mixed. Contrast adjusted in ImageJ between 80 and 140 for visibility and lines in blue indicate when a new repeat from 0% CHD begins. (B) UV-Vis results of yellow pure hexadecane exposed to CHD BZ overnight diluted to 1:2000 (v/v). Annotations show theoretical peaks wavelengths. Measurements are of similar shape to theoretical measurements, but all wavelengths are shifted to the left by 10 nm.

UV-Vis measurements are performed on pure hexadecane and asolectin in hexadecane oil exposed to CHD BZ. These solutions are diluted to 1:2000 (v/v) using pure hexadecane before measurement. The absorbance graph for pure hexadecane forms peaks at 235 and 280 nm for both samples as in Figure 7.3, which is 10 nm from the expected peaks at 245 nm for benzoquinone and 290 nm for hydroquinone. This offset may be due to error from the UV spectrophotometer itself however. Fresh hexadecane, unexposed asolectin in hexadecane oil and oil exposed to only malonic acid BZ did not produce similar peaks. The asolectin in hexadecane oil only formed a peak at 280 nm, with only a slight bump in gradient at 235 nm. From UV-Vis spectrophotometry data, it is hypothesised that this is benzoquinone and 1,4-hydroquinone that has reacted with the asolectin in the hexadecane [103, 163, 164]. This corroborates with the mechanism of the CHD BZ reaction based on literature [71].

MA-CHD BZ also experiences a significantly larger drop in frequency in the middle phase of the oscillations. This makes the number of peaks in the middle phase to be significantly smaller. The middle phase is also a shorter period relative to the full oscillation time compared with MA BZ, so the window for observing wave interactions may not be as large. Droplets typically also still have a high contrast of waves on a red background while having this behaviour.

Besides this, the MA-CHD BZ also has significant variation in behaviour even between repeats in the same experiment, using the same stock solution and experimental conditions. Some droplets become exhausted up to 1 hour before other droplets in the same array and other droplets transition from the initial to the middle phase 1 hour after others. These considerations make characterising the behaviour using the graph observations significantly more difficult.

With these observations, the complexity of characterising MA-CHD BZ can be considered and methods of overcoming them can be compared. These considerations needed to be taken into account for experiments in arrays in Section 7.5 as the behaviour can significantly diverge between repeats and changing the droplet composition too much can prevent oscillations from initiating.

7.2 Space-time plot analysis of wave characteristics

There are significant differences in the graphs between MA BZ and MA-CHD BZ that may affect the peak analysis methods employed and the statistical methods employed. This is due to the differences in phase behaviour observed in Section 7.1. It is also unclear if the MA-CHD droplets are “switching oscillatory modes” between the MA and CHD oscillatory behaviours so this graph analysis can help show if there is any significant changes in wave behaviour which may not be detectable in the video recording.

An example of MA-CHD BZ behaviour in arrays is shown in Figure 7.4, though with significant differences in the length of the middle phase, especially in single droplets. In comparison, 0% to 40% CHD ratio droplets tend to have graphs resembling MA BZ droplets as in Section 4.4. The measured pixel intensity graph has a different shape compared with the MA BZ graph, where the baseline is observed to reduce as the frequency reduces during the middle phase before suddenly increasing again as it transitions to the late phase. This is because the background of the droplet becomes darker red. Initial, middle and late phases are visible in the frequency graph, with a very significant drop in frequency even compared to MA BZ graphs. The area significantly increases with a relatively small increase in amplitude. This is because the peak becomes wider towards the end of the middle phase. Amplitude versus frequency graph shows that the “reverse-C” shape is no longer formed as in MA BZ. Instead, a very high amplitude low frequency region is formed due to the low frequency oscillations in the later part of the middle phase. Colour mapped where red is for earlier peaks and blue for later. The initial and late phases also show separated clusters represented by the red and blue regions respectively. Graph of time versus the ratio of area to amplitude shows that while the initial increase in width of the peak is relatively small for the smaller gradient at first, in the middle phase the gradient suddenly significantly increases. This means that for a smaller increase in amplitude the area increases more.

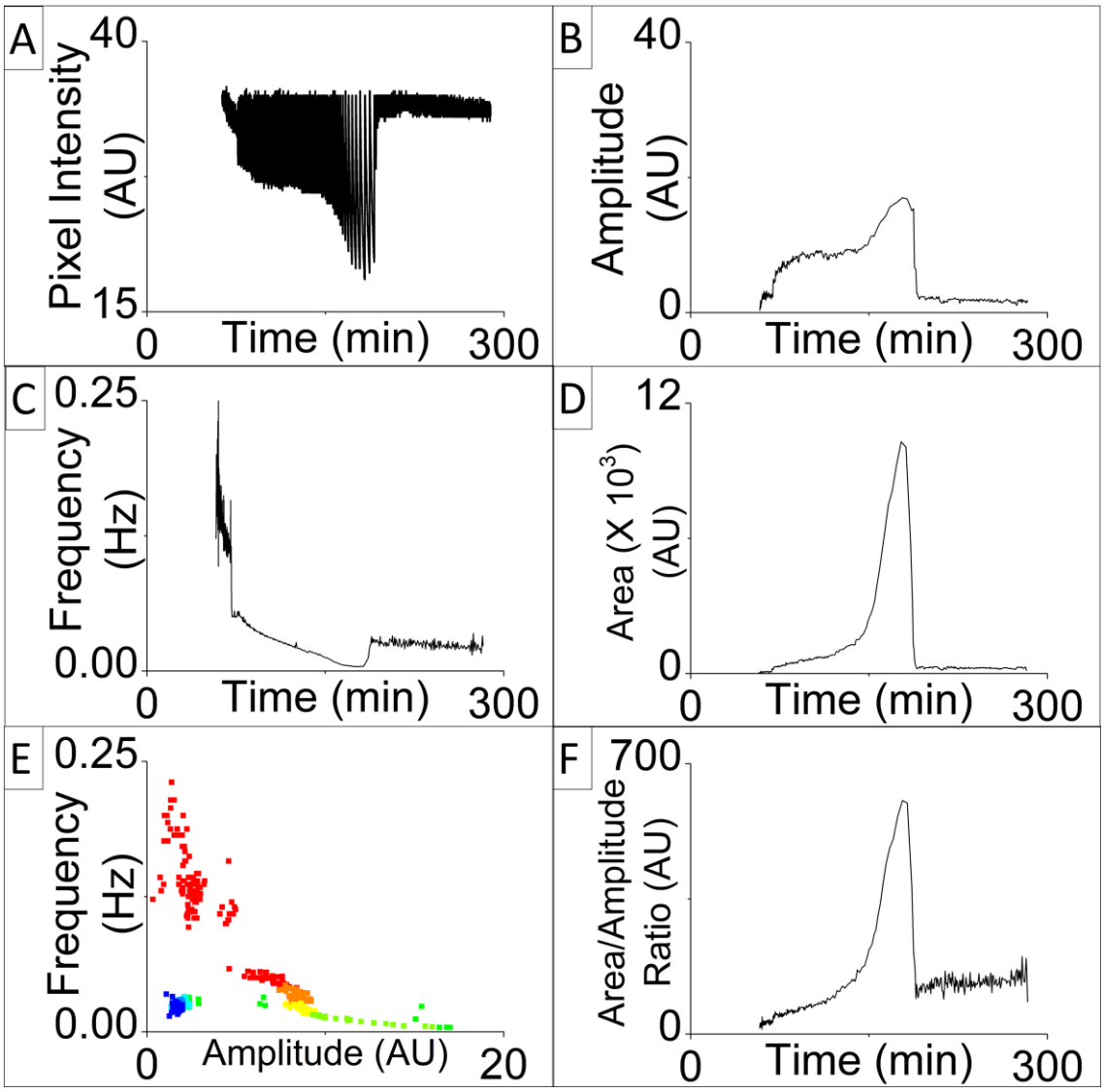

Figure 7.4 Graphs of 50% CHD MA-CHD droplet in the middle of a three-droplet array in oil previously exposed to MA-CHD BZ. This example is chosen as it has a very long and easily identified middle phase compared to other samples. Time measured from when BZ stocks mixed. (A) Measured pixel intensity from space-time plot. (B) Amplitude over time. (C) Frequency over time. (D) Area over time. (E) Amplitude versus frequency graph. Colour mapped where red is for earlier peaks followed by green then blue for later peaks. (F) Ratio of area to amplitude over time.

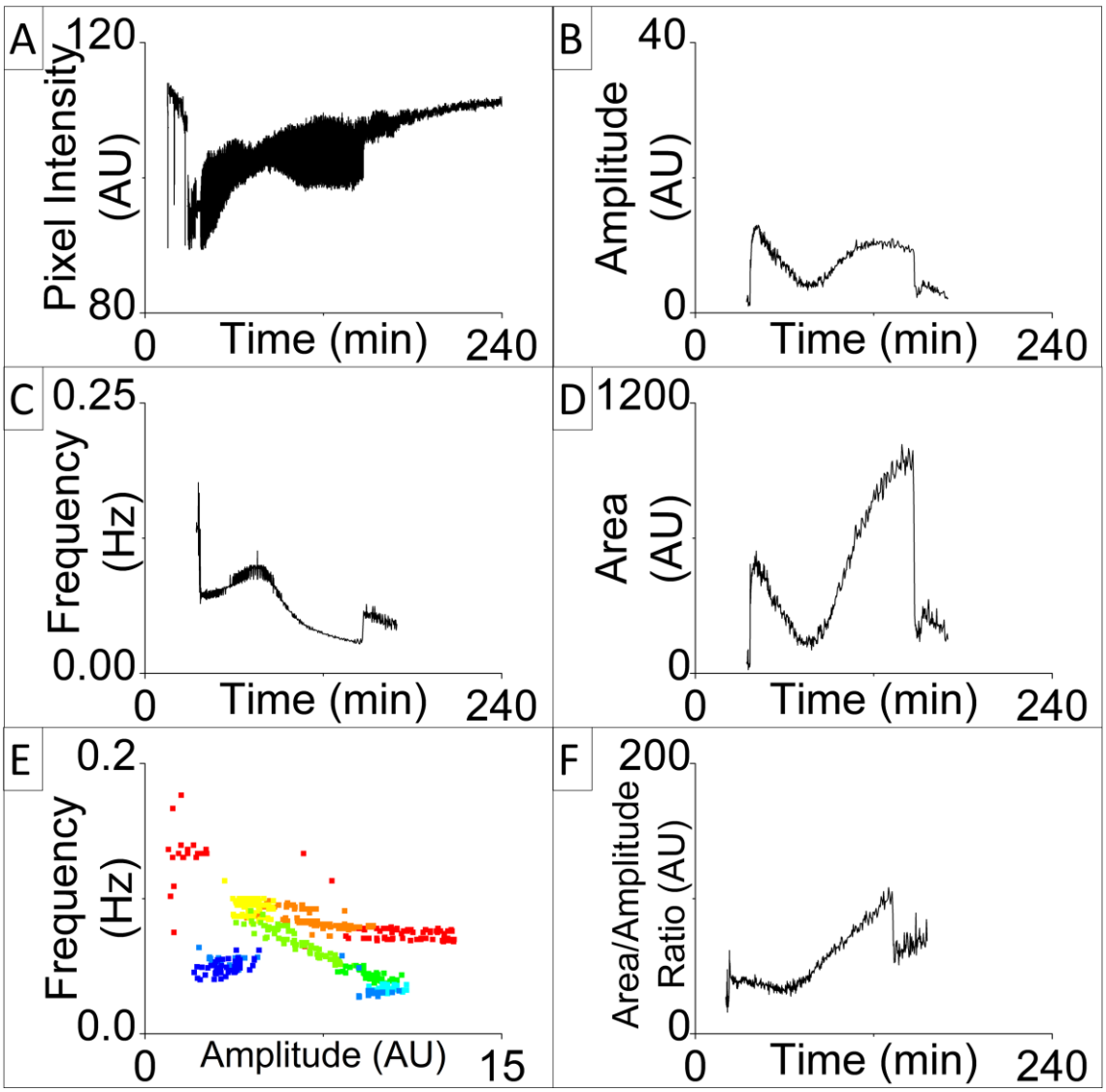

Figure 7.5 Graphs of wave characteristics for 50% CHD ratio MA-CHD BZ as a single isolated droplet in fresh oil. Time measured from when BZ stock solutions mixed. (A) Measured pixel intensity from space-time plot. (B) Amplitude graph over time. (C) Frequency over time. (D) Area over time. (E) Amplitude versus frequency graph. Colour mapped so that red is for earlier peaks followed by green then blue for later peaks. (F) Ratio of area to amplitude over time.

In the single droplet experiment, droplets with 50% CHD ratio have a unique graph shape compared to both higher and lower CHD ratios, as shown in Figure 7.5. This is similar to the transition in BZ behaviour when it changes modes between different BZ substrates as seen in [106]. These graphs resemble both the behaviour of MA BZ and MA-CHD BZ graphs, but it is only observed in the single droplet experiment and not in arrays. The baseline of the graph in the middle phase is observed to increase at first similar to MA BZ droplets, but then suddenly reduce in pixel intensity in the middle phase. Amplitude of peaks shows a

gradual reduction in amplitude followed by an increase, reflecting MA BZ in the earlier part and MA-CHD BZ in the later part of the middle phase. Frequency of peaks shows a sudden reduction from the initial phase but then an increase followed by a gradual decrease in the middle phase. The change in direction for the graph corresponds to the change in the baseline direction as well. The frequency then increases suddenly as in other graphs when transitioning to the late phase. Graph of area under the peaks shows that for the latter half of the middle phase the area increase is significantly greater than in the earlier part of the middle phase, even though the increase in amplitude is smaller. This shows that the width of the peaks is increasing significantly more in the latter half of the middle phase, as confirmed by the graph of ratio between area and amplitude. Amplitude versus frequency graph shows a C-shape between the initial and late phases in blue and red. This shape shows that the frequency decreases over time while showing a decrease followed by increase of amplitude, reflecting what is observed in the middle phase. Colour mapped where red is for earlier peaks and blue for later. The initial and late phases also show separated clusters represented by the red and blue regions respectively.

With the peak analysis, it is concluded that the behaviour of MA-CHD BZ is significantly different compared to MA BZ while retaining some common characteristics. Both types of BZ still have initial, middle and late phases in their oscillation lifetime with common wave characteristics such as higher frequency and smaller amplitude. It also highlighted that there is significant variation between repeats of the same droplet composition in the same experiment, which may not be easy to compensate for in experiments using MA-CHD BZ in arrays.

7.3 Effect of changing ratio of MA to CHD

Due to the significantly different wave evolution behaviour where there are a greater number of peaks in the initial and late phases compared to the middle phase, the methodology for making the statistics of frequency, amplitude and area are not as reliable, where the median may be from the other phases instead of the middle phase. To keep the methodology consistent, the same methodology is used as in Chapter 5 and 6. The difference is in the calculation of the "lifetime" graph, where in previous chapters it corresponds to the "oscillation stop" graph. The oscillation period is calculated as the period between the first and last oscillation detected, which is also shown. The statistics processed using only oscillations from the middle phase is shown for comparison. In the case of 50% CHD droplets that exhibit the transition behaviour where the early part of the middle phase behaves the same as MA BZ, the middle statistics only account for the peaks after the baseline starts dropping in the second half of the middle phase. Both sets of graphs are shown in Figure 7.6 (A).

The oscillation stop time corresponds to the time when the final oscillation is observed, which is when the droplets are exhausted, become transparent and start forming the black cloud. This graph comparable to the lifetime graphs for MA BZ, as MA BZ oscillates from the time of mixing until the time of the final oscillation. It is observed that for the normal processing method, a trend is found where increasing CHD ratios cause the droplets to be exhausted later. The gradient of the graph is significantly increased above 40% CHD ratio as well. This time is shorter for the alternative processing method as the late phase oscillations are not counted.

The "time of first oscillation" graph is the time when the first peak is detected corresponds to the time where the droplets are in the induction phase. Droplets of 50% CHD and lower start oscillating immediately while 60% CHD droplets only start oscillating approximately 1 hour after mixing the solutions. This induction time increases as the CHD ratio is increased. With the alternative processing method, this time is significantly longer starting from the 50% CHD droplets as the first half of the middle phase is not counted since they behave similarly to MA BZ and is omitted.

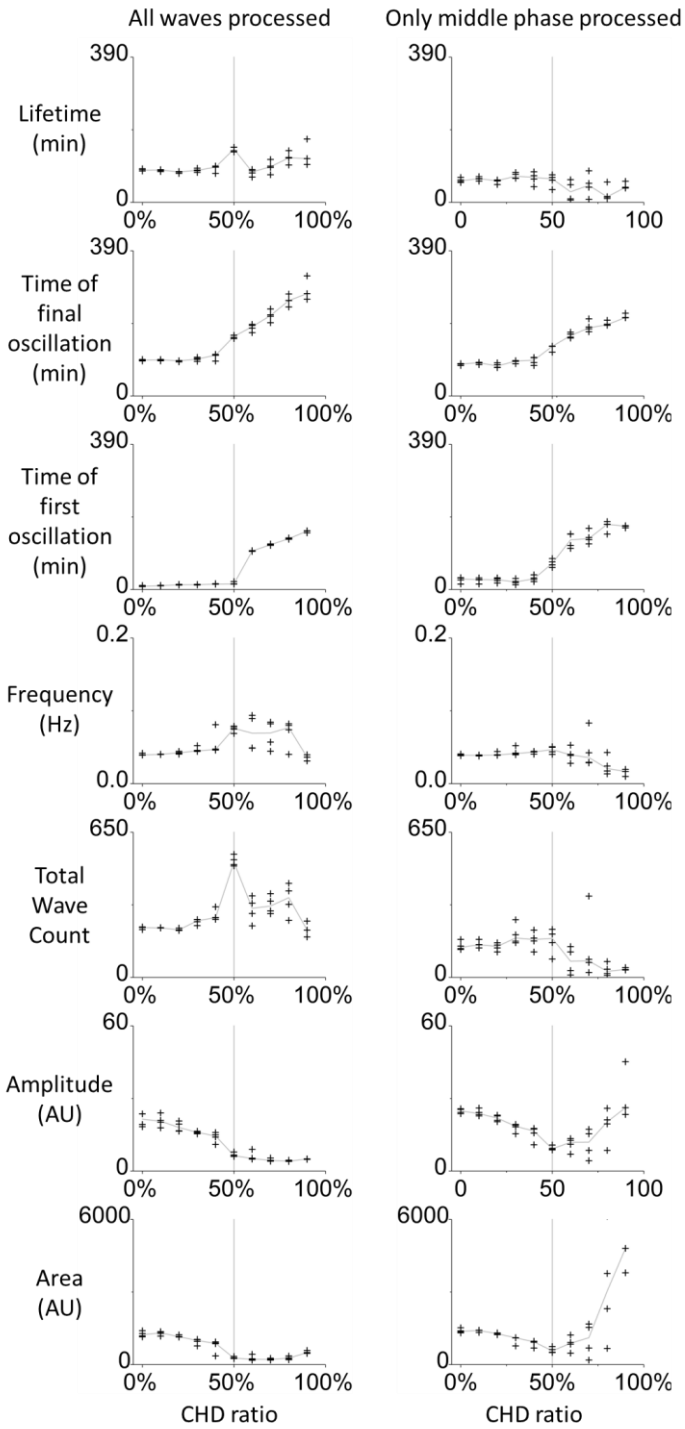

Figure 7.6 Statistics graphs of MA-CHD droplets as the ratio of CHD is increased. Grey line indicates mean of all repeats. The vertical line indicates repeats of 50% CHD droplets. Time zero is when stock solutions are mixed. The “time of first oscillation” can be correlated with the induction time. The “time of final oscillation” is the time from when the BZ is mixed to when the droplet is exhausted. The “lifetime” in this case is this “time of final oscillation” subtracted by the “time of first oscillation” to get the actual length of time when the BZ is oscillating.

The “lifetime” graph corresponds to the time between the first and last oscillation, and represents the actual lifetime of the oscillations once the induction time is removed. It is observed that as the ratio of CHD to MA increases, the time when the droplets stop oscillating and turns transparent also increases. However, because the time until the first oscillation is detected also increases, the resulting oscillatory period is shown to be almost the same between all ratios of CHD to MA. However, because 50% CHD MA-CHD BZ droplets do not have a large induction phase compared to even the 60% CHD droplets, the oscillation period is significantly higher for 50% droplets compared to all others. This is reflected in the first oscillation observed for 60% CHD BZ droplets, which is approximately 1 hour after the solutions have been mixed. In comparison, the 50% CHD droplets have their first oscillation detected at approximately the same time as the pure MA BZ droplets, i.e. the 0% CHD droplets. However, in the alternative processing method, it is observed that the oscillation time for all the droplets is almost the same, with even shorter periods observed for higher CHD ratios.

The frequency graph shows that droplets with a higher CHD ratio have a significantly larger variation in frequency when the CHD ratio is above 60%. 50% CHD droplets also have a significantly higher median frequency than droplets with less CHD due to the higher frequency at the start of the middle phase where it behaves similarly to MA BZ. Droplets with higher CHD concentration have a much larger variation of frequency due to the differences in the length of the low frequency middle phase but is generally higher on visual inspection due to the larger number and longer duration of the initial and late phases. When the initial and late phases are excluded from the statistics, the frequency is observed to drop above 50% CHD ratio.

Due to the longer lifetime of 50% CHD droplets, it has a significantly larger number of waves compared to ratios above and below 50% CHD. Ratios of CHD below 50% have approximately the same total wave count, but ratios above 50% CHD have a larger variation due to the differences in the length of the middle phase. As only the middle phase waves are known to propagate through droplet interfaces (as shown in Section 7.1), the wave number of other phases is not relevant and can be excluded from these statistics, so a second processing procedure is carried out counting only the waves in the middle phase. When only the middle phase is counted, the total wave count is observed to drop significantly at ratios higher than 50%.

The amplitude of the waves is observed to decrease as the ratio of CHD is increased, where at 50% the amplitude drops significantly. This is due to the large number and long duration of initial and late phase waves. If these are excluded, the amplitude is at a minimum at 50% CHD ratio, and starts increasing as only the waves where the droplet has a very low frequency and red background are counted. Similar to the amplitude graph, the area graph also shows a sudden drop at 50% CHD ratio, but which increases slightly as the CHD ratio increases. A similar trend is observed if only the middle phase is analysed, but with a much larger increase in area as the peaks with a large width in the middle phase are chosen.

As MA-CHD BZ is used due to its ability to propagate waves through all interfaces in the array, some tests with BZ droplets of different ratios in arrays is also conducted in oil previously exposed to CHD BZ. These droplets behave similarly as in single droplets, except the middle phase appears to be longer than in single droplets. Tests of different ratios of CHD in arrays of identical droplets show that there is no significant difference in the stability of the droplets, where both high and low CHD ratios fuse at similar rate of approximately 10 of 42 arrays fused, which is a 76% survival rate. Similar results are obtained when these arrays are coupled with 0% CHD droplets, where out of 32 arrays of droplets observed, 6 arrays experienced fusion of these droplets for an 81% survival rate.

It is also observed that even droplets with only 20% CHD ratio are able to form waves that propagate through the droplet interface. However, if coupled with a 0% CHD droplet, it takes a much longer time for waves to propagate through the interface. Droplets with 40% and 50% CHD ratio are observed to have waves that propagate through that interface at the same time as the interfaces between two MA-CHD BZ droplets. In addition, 0% CHD droplets do not exhibit wave propagations through the interface for most of its lifetime. It must also be noted that the interface between the 0 and 50% CHD droplet allow waves to propagate in both directions. Figure 7.7 (A) shows waves propagating through interfaces only with droplets of MA-CHD BZ while 0% CHD ratio droplets do not propagate waves through the interface.

It is also observed that 0% CHD ratio droplets tend to stop oscillating approximately 45 to 60 minutes earlier than MA-CHD BZ droplets, even when coupled with other CHD ratios. Additionally, when all sandwiched droplets are MA-CHD BZ droplets and only one 0% CHD droplet is coupled at one end, it is observed that at first the MA-CHD BZ droplets act as the

wave source. As the droplets reach the latter half of the middle phase, the frequency drops significantly and the 0% CHD droplet acts as the wave source. This is because MA BZ droplets have a more consistent frequency instead of the large drop experienced by MA-CHD BZ. This is shown in Figure 7.7 (B), where the frequency graphs of all droplets also reflect this.

Another test using 50% CHD ratio droplets with different age of CHD BZ solution is also conducted, where the original CHD BZ stock is allowed to react for between 0 to 6 hours before being mixed with fresh MA BZ solution. In this experiment, 6 repeats of each age of CHD BZ were observed. 13 of 18 arrays older than 3 hours experienced fusion while 3 of 24 arrays of 3 hours or newer experienced fusion, indicating lower stability for older CHD used. Older CHD droplets have droplets with a darker red background sooner. If the CHD BZ used was 1 to 3 hours old, waves propagate through interfaces at approximately 50 minutes after the solutions are mixed, while fresh solutions need approximately 70 minutes to transition from the initial phase. In comparison, CHD BZ that is older than 3 hours old needs approximately 80 minutes before waves can propagate through the interface reliably, even though none has a significant initial phase. The frequency of the oscillations also becomes lower as the age of the CHD BZ used increases. It is also observed that all these solutions stop oscillating as transparent droplets at approximately the same time despite the significant differences in CHD BZ age. The lower oscillation frequency and longer time until waves propagate through interfaces means that using CHD BZ that is older than 3 hours forms significantly fewer waves that propagate through the entire array.

These statistics show that significant variations in behaviour are present even between repeats of the same composition when above 50% CHD ratio. It also shows that the middle phase has an inconsistent period above 50%, leading to significantly differences in total wave counts and oscillation lifetimes. As a result, 50% CHD ratio is chosen for all future experiments to take advantage of the fast induction time, consistent wave behaviour, longer oscillation period and larger total wave count while ensuring that the CHD behaviour is still observed. These experiments also showed that using aged CHD BZ solution does not offer significant advantages compared with using freshly mixed solution. From these conclusions, subsequent experiments used freshly mixed 50% MA-CHD BZ solutions.

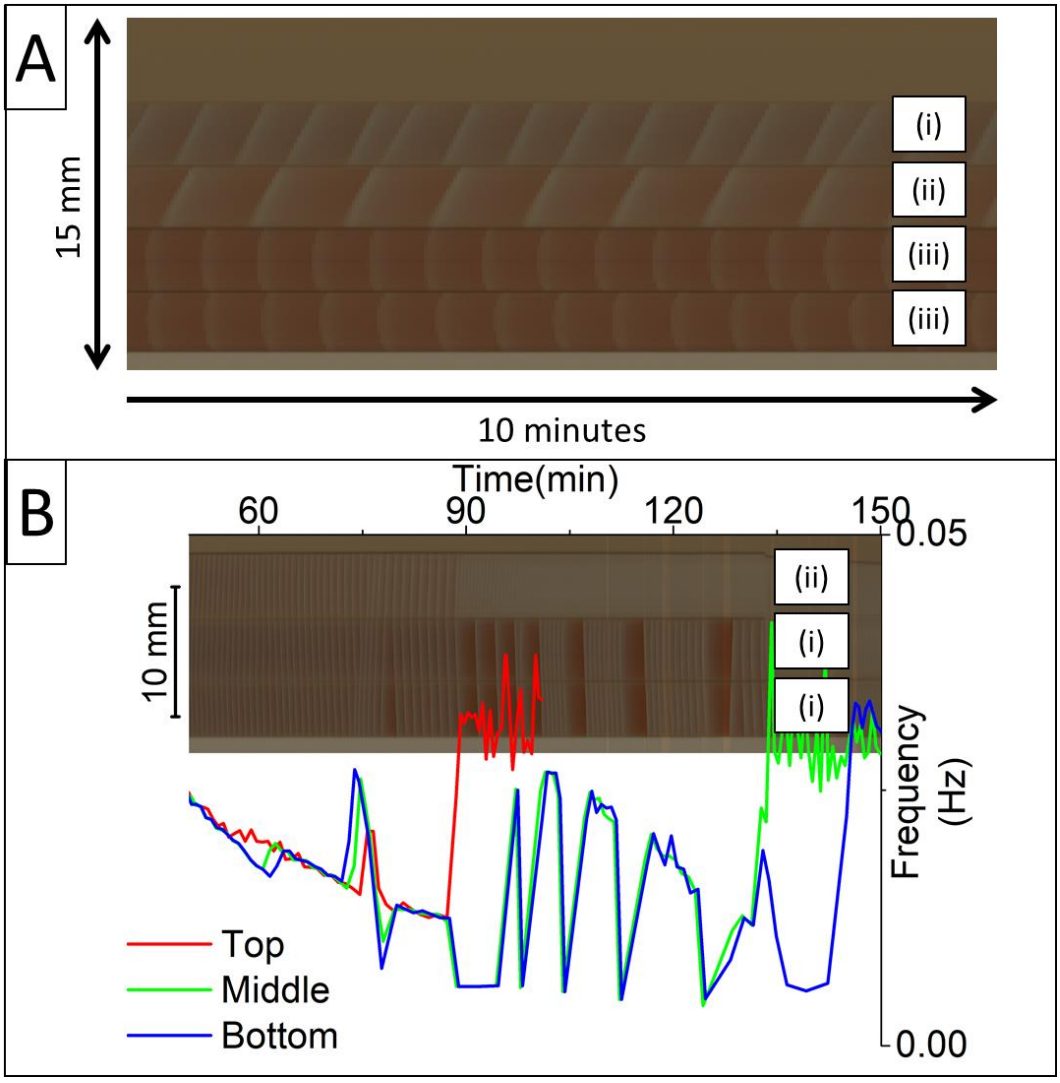

Figure 7.7 Space-time plots of 0% CHD ratio MA-CHD coupled with 50% CHD droplets. Droplets labelled (i) are 50% ratio CHD droplets, (ii) are 0% CHD and (iii) are 0% CHD ratio with longer lifetime and higher frequency. Waves are observed to pass through interfaces with droplets labelled (i). (A) Array with 50% CHD droplet on top of 0% CHD droplets. 0% CHD droplets (ii) and (iii) show no wave propagation through interfaces. Only interface with droplet (i) shows propagation, which results in spikes of frequency. Space-time plot taken 2 hours after solutions mixed. (B) Array with 0% CHD droplet on top of 50% CHD droplets. Droplets all observed to couple even in graphs of frequency, which shows all droplets with equal frequency. Red graph of (ii) droplet tends to act as wave source, with a higher frequency than the other graphs, though a spike at 75 minutes from blue graph of bottom droplet shows when bottom droplet acted as wave source for 6 oscillations. Droplet (ii) becomes exhausted earlier than other droplets and they are observed to go into bursting oscillation behaviour after that. After 90-minute mark (i) droplets have large fluctuations in frequency together during bursting period. Oil is darker in appearance as it was previously exposed to MA-CHD BZ.

7.4 Effect of changing ferroin concentration

As changing the $NaBrO_3$, MA and CHD concentrations causes the droplet to become unable to oscillate and changing H_2SO_4 causes the arrays to be too unstable, ferroin is the only viable component that can be changed to change the oscillation behaviour. These behaviours are characterised in 3-droplet arrays of 50% CHD MA-CHD BZ to ensure more consistent behaviours compared to when tested in single droplets. The experiment is performed in oil previously exposed to MA-CHD BZ and had waves propagating through most interfaces. These statistics are also performed in the same method as in MA BZ, where peaks from all phases are analysed so that they can be directly compared. Only the middle droplet of each array is analysed to save time as waves in MA-CHD BZ can propagate through the interface so they will share similar characteristics. These graphs and the MA BZ graphs are shown together for comparison in Figure 7.8.

All the droplets are observed to stop oscillating at approximately the same time despite having different wave behaviours. The time of the first oscillation detected corresponds to the induction time of the droplet. This is observed to decrease as the ferroin concentration increases. The 2 mM droplets are observed to have a significant induction time compared to the previous experiment as well, despite having the same composition. This may be an effect of using this composition in oil previously exposed to MA-CHD BZ, though no other wave characteristics appear to be affected even when compared to experiments in fresh oil.

When the actual lifetime of the oscillation period is compared, the trends between both are completely the opposite, where the oscillation lifetime increases as the ferroin concentration is increased in MA-CHD BZ while it is observed to decrease in MA BZ. The change in frequency is also not as large as in MA BZ, though it is still observed to decrease as ferroin concentration is increased. The total wave count of the oscillations is observed to increase as the ferroin concentration is increased instead of decrease as in the case of MA BZ. The amplitude and area of the peaks is also observed to increase with increasing ferroin concentration, but with a much smaller gradient than in MA BZ.

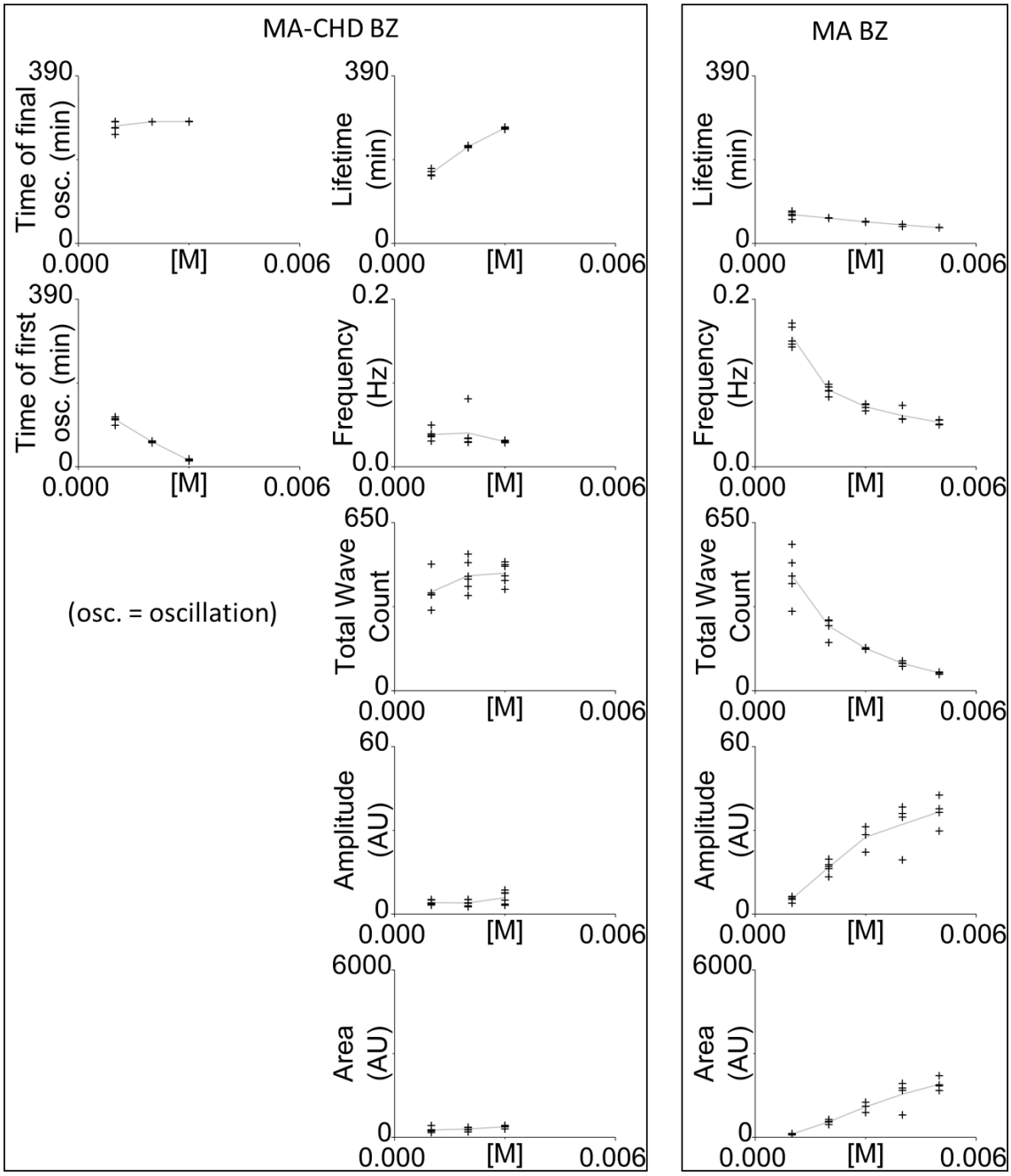

Figure 7.8 Effect of changing ferroin concentration in MA-CHD BZ compared with MA BZ. Grey lines indicate the mean of all repeats. N = 6 for MA-CHD BZ samples and N = 4 for MA BZ samples except for 1 mM and 2 mM where N = 5. The “time of first oscillation” can be correlated with the induction time. The “time of final oscillation” is the time from when the BZ is mixed to when the droplet is exhausted. The “lifetime” in the MA-CHD BZ case is this “time of final oscillation” subtracted by the “time of first oscillation” to get the actual length of time when the BZ is oscillating.

As each droplet starts oscillating in the middle phase at different times, it can also be observed visually that the frequency of each droplet composition at a particular time since mixing the stock solutions is different, where the frequency of the droplets with lower ferroin is significantly higher than droplets with higher ferroin concentrations. Concurrent experiments where droplets with different ferroin concentrations paired together showed that there is a higher probability that waves start from droplets with a lower ferroin concentration in the array when the droplets enter the middle phase.

This experiment shows that changing the ferroin concentration is a viable method of changing the wave behaviour of MA-CHD BZ while still forming stable arrays with waves that can propagate through the interface. The differences in wave characteristics is not as large as in the MA BZ, but still show that droplets with a higher ferroin concentration have a lower frequency. Combined with the longer time needed for droplets of lower ferroin to start oscillating, droplets mixed and placed in the array at the same time can have significantly different frequency. These conclusions led to subsequent experiments with initiator droplets using MA-CHD BZ with lower ferroin concentrations.

In addition, it is observed that using 1 mM ferroin is not viable as it has a significantly longer initiation time and stops oscillating at the same time as other droplets while being difficult to see due to the low contrast. Hence, higher ferroin concentrations may be needed both to increase the differences in frequency and to ensure that waves can propagate through the interfaces for a long enough observation time. To allow a large enough difference of ferroin concentration and large enough contrast for observation, subsequent experiments used 4 mM ferroin. This allows both 2 and 3 mM droplets to be tested as initiator droplets in case the range is not large enough.

7.5 MA-CHD BZ droplets in long non-linear arrays

MA-CHD BZ droplets need to be used in longer and more complex arrays if used in future applications for unconventional computing. Hence, it is necessary to test if the waves are still able to propagate through interfaces and if the arrays can remain stable for such longer arrays. Unique behaviours due to the geometry of the array can also be observed. Most droplets used in these experiments are 4 mM ferroin 50% CHD MA-CHD BZ droplets, though droplets with lower ferroin concentrations exhibit the same behaviours.

This is first tested by using 2 mM ferroin 50% CHD MA-CHD BZ droplets of the same composition in the long linear array design in Figure 3.4 (B). This allows linear arrays of 20 droplets to be observed, and tests if long arrays are stable with waves propagating through the interface. Several droplets in all repeats fused during the first 30 minutes while the petri dish is being filled, but after that, all droplets were stable for at least 4 hours with no fusions. A photo of this setup is shown in Figure 1.2. Each repeat had different wave sources with some being from fused or unfused droplets and some from above or below, and can change over time. Droplets towards the bottom of the array are slightly flattened compared to droplets above due to the force of gravity. This is shown in Figure 7.9 (A). Waves are observed to propagate through all interfaces, except through droplets separated due to gas bubbles or droplets in the initial or late phase and droplets. For these interfaces, they must remain connected and undisturbed for at least 2 hours before it is able to propagate waves. This is shown in Figure 7.9 (B). This shows that using longer arrays is viable. This shows that even when using droplets of lower ferroin, it is possible to produce these long arrays with relatively short induction time and with waves able to propagate through all interfaces after the 30 minute initial phase.

For better performance of MA-CHD BZ droplets in larger non-linear arrays with initiator droplets, the concentration of ferroin for all droplets in these non-linear array experiments is increased to 4 mM, with other components kept constant. This also reduced the time the droplets stayed in the initial phase and these droplets are never observed in the induction phase, allowing wave propagation through the interface to occur with a shorter time delay from when droplets are first placed in contact. This also gives better performance when using droplets of lower ferroin as initiator droplets as explained in Section 7.6.

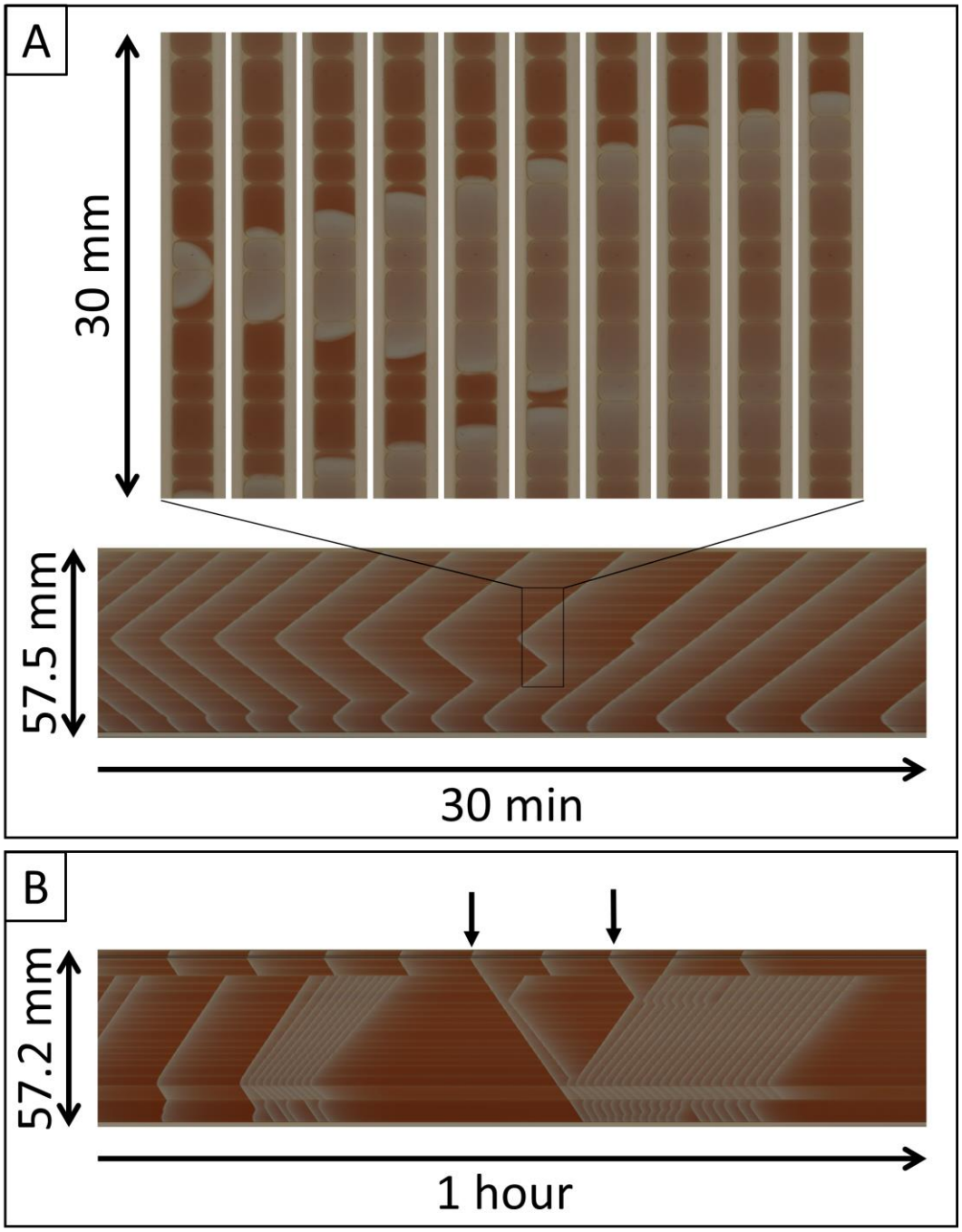

Figure 7.9 (A) Sequence of photos taken at 5-second intervals (top) and space-time plot (bottom) of long droplet array containing 20 droplets. Seven of these droplets are larger as they have fused while droplets are added to the array. The top of the array is on the right, with gravitational force applied towards the left. Waves observed to propagate through all interfaces. Droplets on the left slightly flattened compared to droplets on the right due to pressure from droplets above. (B) 19-droplet repeat where top three droplets separated by gas bubble initially then reconnected. Black arrows show where waves managed to propagate through interface, but that propagation is not consistent even though gas bubble had disappeared approximately 90 minutes before. All droplets in this case have 2 mM ferroin.

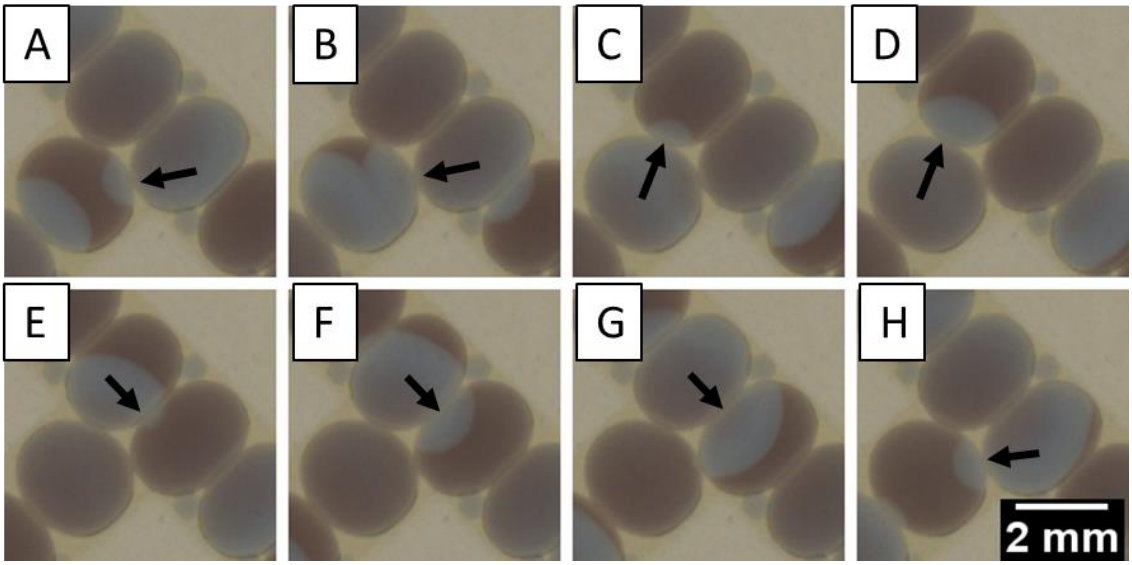

Figure 7.10 Wave behaviour at meeting point between three identical droplets. Droplets excite each other forming a “spiral” pattern with its centre about the meeting point. Images taken at 5-second intervals. Annotated black arrows show wave propagation through interface. Cycle repeats after final image. Droplets use 4 mM ferroin in this case.

When 4 mM ferroin 50% CHD MA-CHD BZ droplets of the same composition are placed in Y-shaped non-linear arrays as in Figure 3.4 (C) and (D), it is observed that waves can propagate from one arm and spread to other arms in the Y-shape. This shows that the wave propagation is not limited by the concentration of intermediate at this composition when used to split into more than one coupled droplet. Due to the meeting point of the Y-shaped array, it is observed that the droplets all couple amongst each other and one droplet that oscillates can excite the other two at the same time. However, if there one of these droplets is in the refractory period, a unique wave pattern can emerge where the three droplets excite each other continuously, forming a “spiral” pattern about this meeting point. This is shown in Figure 7.10.

At the start of the experiment, droplets that are less than 0.5 mm diameter have a slightly higher probability of acting as a wave source compared with other larger droplets in the array. However, it is usually extinguished after approximately one hour by other wave sources from other larger droplets of identical composition. If these smaller droplets are sandwiched between two larger droplets, it is possible to separate them so that the smaller droplet acts as the connecting bridge.

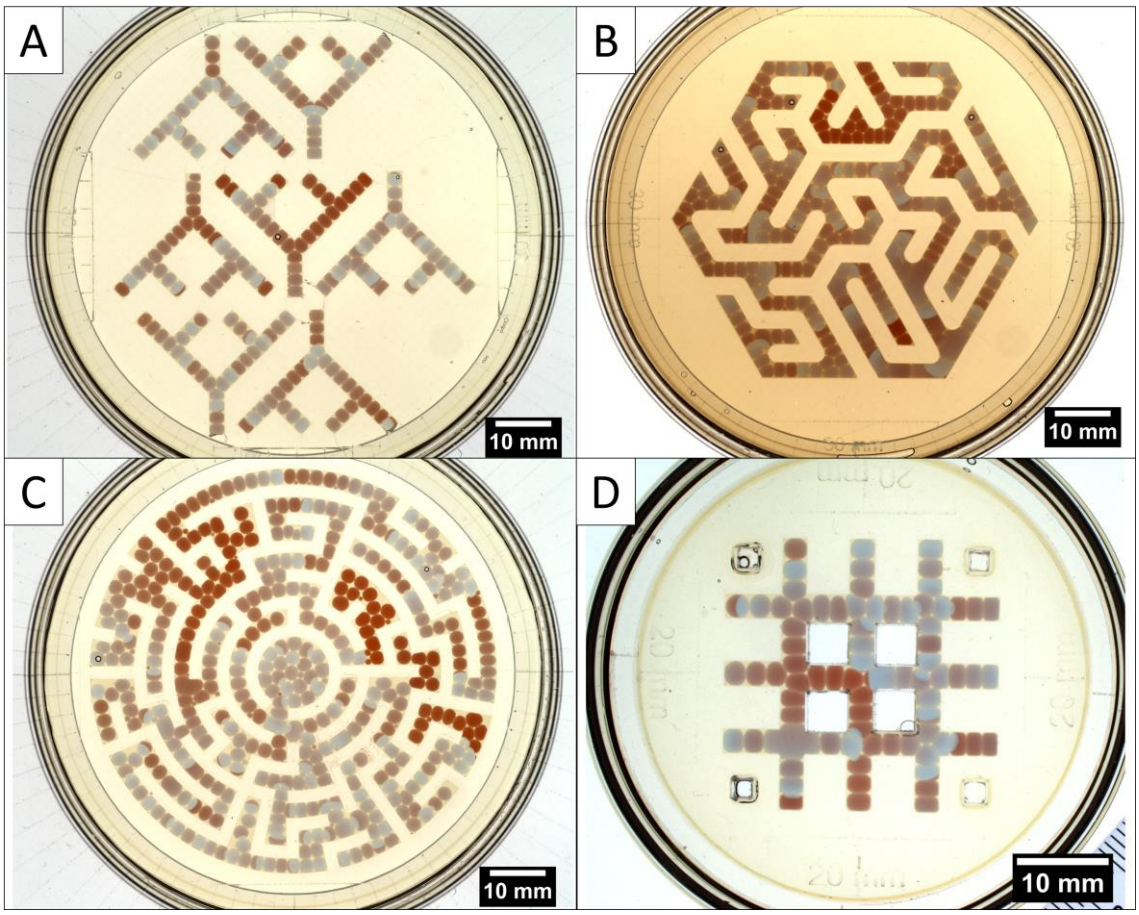

Figure 7.11 Complex designs with BZ waves propagating through most interfaces. (A) Y-shaped arrays with many meeting points. (B) Hexagonal maze array using oil previously exposed to MA-CHD BZ, which causes the darker oil colour. Fusions here due to moving PMMA wafer while filling. (C) Circular maze array with 399 droplets, of which 376 remain unfused for 94% survival rate. (D) “Fish” design with multiple meeting points that feed back into itself. Consists of 82 droplets of which 7 fused for 91% survival rate. All petri dishes are 90 mm diameter except (D) which is 60 mm. All images contrast enhanced using histogram. All droplets use 4 mM ferroin in these cases.

When these 4 mM ferroin MA-CHD BZ droplets are used in even larger arrays with more complex patterns as in Figure 3.5 and 7.11, it is observed that the waves still propagate through all interfaces as before. Droplets are again stable for at least 4 hours after initial fusions during the first 30 minutes when the petri dish is filled. In the case of the circular maze in Figure 7.11 (C), an array of 399 droplets was formed where 376 remained unfused, giving a 94% survival rate.

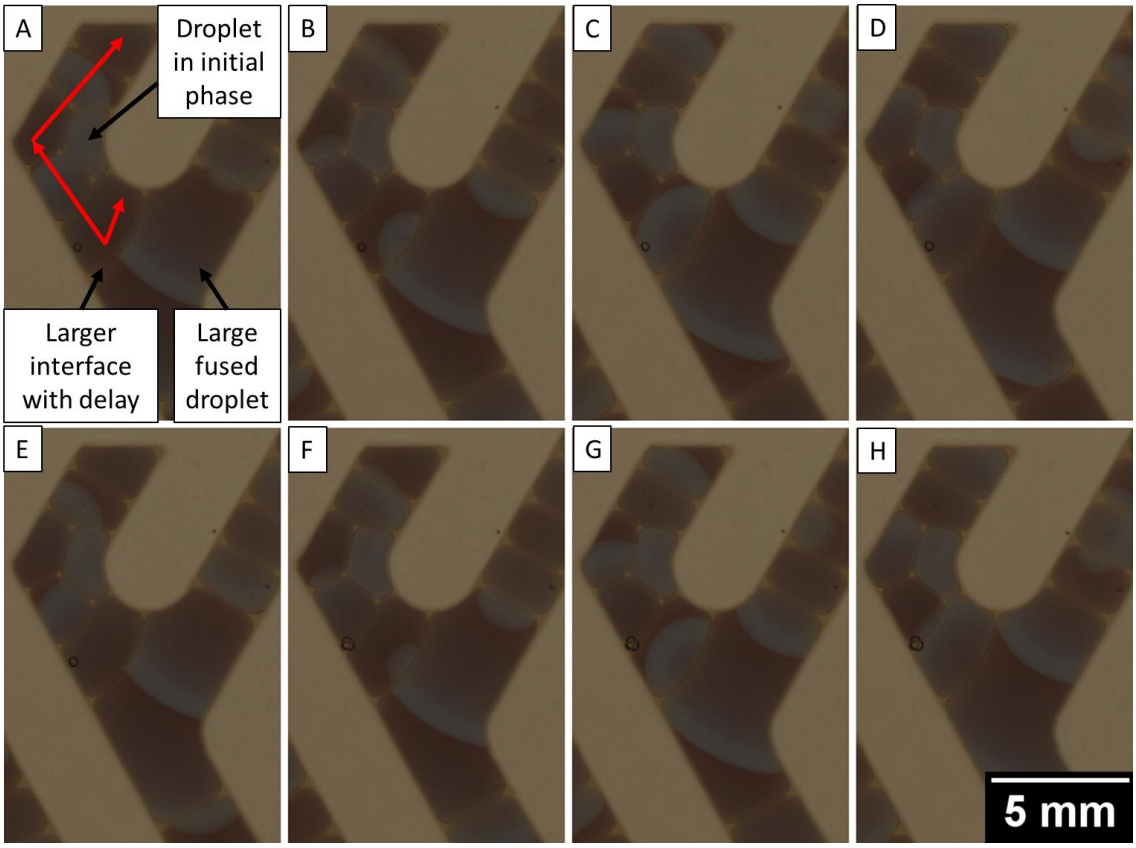

Figure 7.12 Section of hexagonal maze with larger interface with fused droplet and droplet in initial phase blocking alternate, shorter path. Wave has touched interface but did not propagate through interface due to refractory period. Wave only propagated after some time at the location further along the path. Wave touched droplet in initial phase but did not propagate through the other side even though path is shorter. Arrows in red show propagation path of wave to propagate to other parts of larger interface and avoid droplet in initial phase. Images taken at 10-second intervals. Droplets use 4 mM ferroin. Oil was previously exposed to MA-CHD BZ, causing the darker oil appearance

If the angle of the interface is obtuse compared with the angle of propagation, a delay in the propagation can be observed, where even though the wave has touched the interface, the refractory period of the droplet prevents the wave from initiating until later when it has moved to another part of the same interface. Droplets can also block certain paths of the array while in the initial phase. These paths are blocked until the droplet has entered the middle phase and is able to propagate waves as normal. Both cases are shown in Figure 7.12. Similar problems were encountered in the experiment with the square maze array in Figure 3.5 (B), where one PMMA arm from the design was not flattened enough and became dislodged from the glass surface as the experiment went on. This caused the

droplets supported by that arm to fall underneath the design. Waves were still observed to propagate, through the new interfaces formed, but were unable to do so at first similar to the array separated disrupted by CO_2 gas bubbles previously.

To analyse the more complex homogeneous arrays, attempts are made to use space-time plots of each linear path that are stitched together. For example in Figure 7.13, in the "fish" design the arrays are able to feed back into the original path and are non-linear. The sections A, B, C and D correspond to their respective linear paths and they are stitched together to form the loop in the space-time plot. The stitched space-time plot shows that the wave speed is significantly different at the stitched locations due to the wave changing direction to enter the path. In addition, it is possible to see how the wave initiates itself on the other side of the space-time plot. In this case, a wave travels anticlockwise about the path continuously exciting itself. Other paths were excited by this wave, and so formed a wave source in the middle of the stitched sections instead. A lot of information is lost using this method, such as how the waves initiate waves in three other paths at the same time. This shows the difficulty of using space-time plots to analyse non-linear designs such as this.

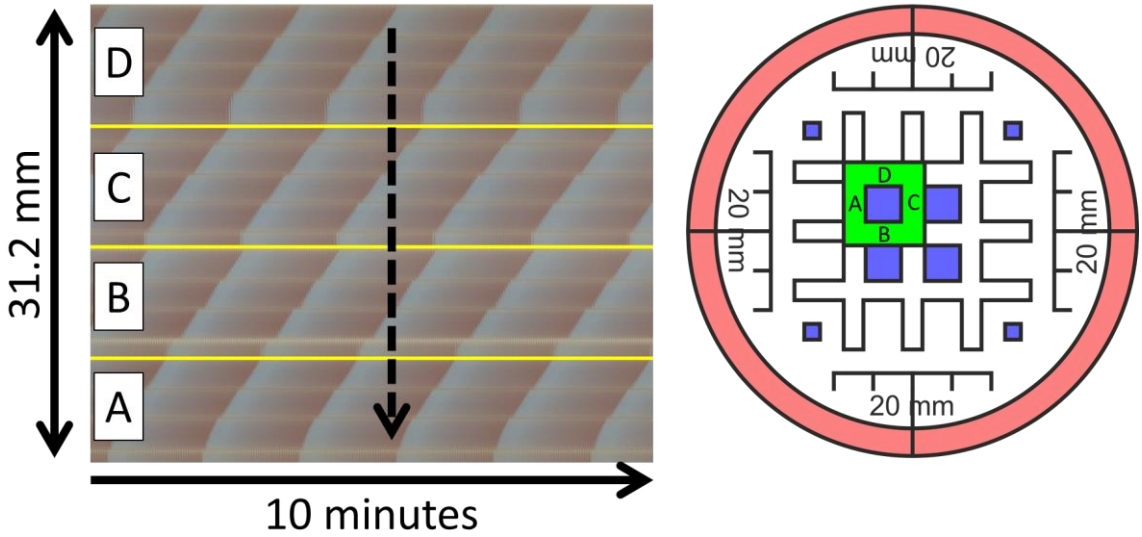

Figure 7.13 Stitched space-time plot and section highlighted section in "Fish" design. Space-time plot taken 150 minutes after solutions mixed. Sections in space-time plot labelled according path in schematic on right. Yellow lines indicate where space-time plots are stitched together. Black dotted line shows how wave from (D) feeds back into (A) to form a wave moving in anticlockwise direction. Droplets use 4 mM ferroin.

Initial work is done in order to analyse non-linear droplets using the circular maze design using more advanced computer vision techniques. First, waves are isolated from the background by taking two consecutive images and subtracting one image from the other. This leaves only the moving waves and removes the background. The resulting image sequence is then fed into the "TrackMate" function in ImageJ, setting the size of the particles as the size of each droplet in pixels. This optical flow algorithm uses computer vision to identify moving objects in a series of images and tracks their path. This function also evaluates the brightness of each wave tracked and their velocity. Example results are shown in Figure 7.14. As shown in (A), the total intensity of each path is significantly higher for the red path on the right and yellow one on top. These droplets were added at different times and from the same stock, so this could show the variability of the droplets and the effect of being coupled in different topologies. Most evaluated settings show colour maps similar to (A). The result (B) shows the standard deviation of the velocity, which can be correlated with the range of velocity in these paths. It can be observed that the paths in the central circle have a large variation of velocity, possibly because droplets here behave as a spiral wave that self-excites due to the many interfaces formed. The path lengths of each wave could not be analysed using this method as the function does not recognise the edges of droplets, information on droplet interfaces is discarded using this processing method, and the waves in each frame are counted as the same wave following a path.

By initial visual inspection, towards the end of the recording the path length increases as there are fewer wave sources that form waves to stop the propagation of existing waves. One path from the middle of the maze to the dead end in the middle-top arm extends for 40 droplets, where initially the waves only propagate approximately 5 droplets before being stopped by another wave source and at the end it propagates through all 40 droplets to the dead end.

This section concludes that it is non-trivial to analyse non-linear arrays of MA-CHD droplets, but that the new techniques explored can provide very interesting insight into the behaviour and evolution of the waves given enough computing resources. This section also shows that even when using the same composition of droplet in a complex array, a wide variety of behaviours can be observed.

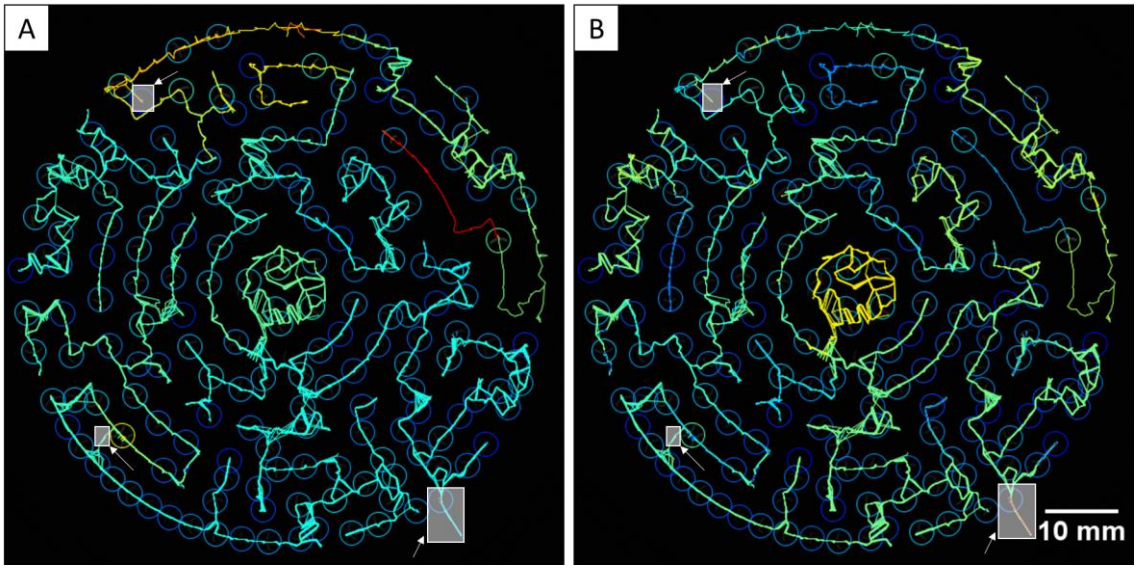

Figure 7.14 Two different settings for the optical flow parameters shown. Circles indicate waves identified and lines indicate their paths. Colours mapped where red is for high values and blue for low values. (A) Tracks show the Total intensity of the path, with higher intensity as red and lower as blue. (B) Tracks show the standard deviation of the velocity of the paths. This shows the amount of change the velocity of each path experiences throughout the evaluated image sequence. There are three instances of gas bubbles detected and their paths shown on the top-left, bottom-left and bottom-right of each image. These are highlighted in white squares with arrows.

7.6 MA-CHD BZ arrays with lower ferroin droplets to initiate waves

Initial work has been done to couple these complex arrays with initiator droplets to control the source of the waves. To do this, arrays with 50% CHD droplets are coupled with droplets of lower ferroin concentration. This droplet has a slightly higher frequency than the rest of the array and is able to generate waves to extinguish other wave sources that also appear.

To evaluate if they are effective, the video and space-time plots are analysed to determine where the wave source and direction of the waves for each array are. Each array can have differences in behaviour, which may disturb the wave propagation such as random droplets being in the refractory period and self-oscillations from other parts of the array, the general trend of the wave source, and direction for the entire lifetime after entering the middle phase is taken into account. If the wave pattern 60 to 120 minutes after the arrays are set up is only from initiator droplets after a long period with no other wave sources that propagate for a long distance or last for a significantly long time, these are counted as

arrays with waves from the initiator droplet only. If a significant number of waves start from other sources or if the waves from the initiator droplet are either blocked by droplets in the initial phase or interfaces which do not propagate waves, these are counted as arrays with waves from other sources. Statistics are then simplified to whether arrays can be said to have a steady state wave pattern from the initiator droplet or not. From the different experiments performed, a mean probability of 69% is obtained, excluding the experiment where the initiator droplet is placed in the middle of the 7-droplet array where 100% of arrays had wave sources only from the initiator droplet. These results are shown in Table 7.1.

These droplets are first tested in linear arrays that are seven droplets long, where the initiator droplet used a ferroin concentration of 2 mM while other droplets in the array used a concentration of 3 mM. First, the droplets are placed in the middle of the array such that there are three droplets on either side. This is then tested by placing the droplets at either end of the seven-droplet array to test the effective range of these droplets. The analysis of these arrays is non-trivial, as new wave sources sometimes form that become extinguished by waves from the initiator droplet. In addition, sometimes droplets in the red reduced state can fail to propagate waves, possibly because it is in the refractory period at that time. However, in all cases, the initiator droplet is observed to form wave sources with a higher frequency that can propagate at least into its immediate neighbour.

Table 7.1 Number of arrays where wave source is an initiator droplet versus from other parts of the array. Wave sources observed 60 to 120 minutes after arrays set up.

Array type tested/ Number of arrays with waves	**Linear 7 droplets (Middle)**	**Linear 7 droplets (Top or Bottom)**	**Simple Y**	**Multiple-Y (1 initiator)**	**Multiple-Y (2 initiator)**	**Multiple-Y (3 initiator)**
Only from initiator	12	16	4	5	6	3
From other sources	0	8	6	2	1	2
Probability of waves only from initiator (%)	100	67	40	71	86	60

From this experiment, a new droplet state is also observed, referred to as the "over-excited" state. This state is shown in Figure 7.15. In this state, the droplet with higher ferroin is excited by the waves from the initiator droplet and achieves the same frequency and wave contrast as the initiator droplet despite having the same droplet composition as the rest of the array. However, these waves are unable to pass through the other interface to the other droplets in the array. These droplets usually stabilise together with the initiator droplets to have a lower frequency after some time, where all waves are observed to propagate through all arrays reliably. It is also possible for droplets in the over-excited state to become exhausted faster than the rest of the array due to its higher frequency. It is interesting to note that droplets placed in the bottom of the array and fused droplets with higher ferroin concentration are not likely to form "over-excited" coupled droplets. In addition, this phenomenon was not observed in the previous experiment where more than one droplet was coupled to the initiator droplet. This may mean that coupling more than one droplet to the initiator droplet may help to reduce the excitation by the initiator droplet.

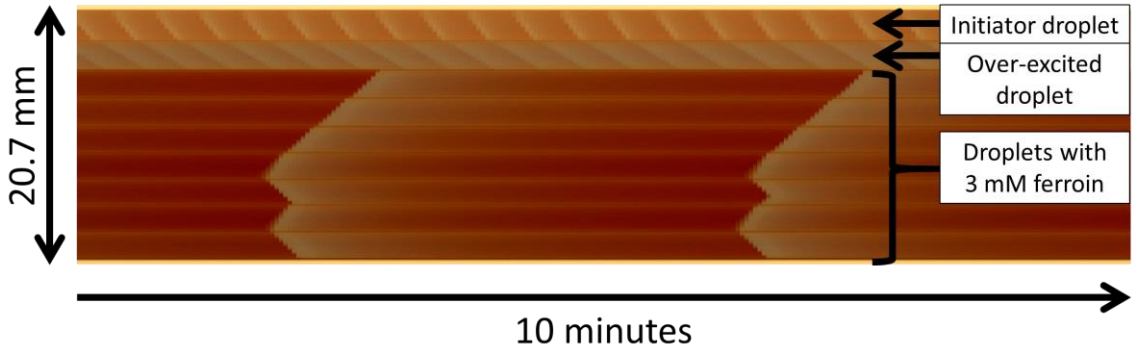

Figure 7.15 Droplet in "over-excited" state coupled with initiator droplet. Over-excited droplet is identical to other droplets in array but is fully coupled to initiator droplet and has the same frequency and wave contrast, but waves cannot propagate to the rest of array. Contrast histogram set between 20 and 90 for visibility. Initiator droplet uses 3 mM ferroin while all other droplets use 4 mM ferroin. In this case, oil used was previously exposed to MA-CHD BZ in a previous experiment, causing the darker oil appearance.

To prevent the “over-excited” state and increase the likelihood that waves can propagate through all interfaces, the ferroin concentration is increased to 3 mM ferroin for the initiator droplets and 4 mM for other droplets. The initial choice using 2 mM and 4 mM droplets usually formed over-excited droplets, and is not viable. Initiator droplets are then tested in the Y-shaped arrays as in Figure 3.5 (A) and (B). Due to the larger number of droplets in each array, it is much harder for the initiator droplet to overcome the self-oscillations that can randomly form in any other droplet. These arrays are analysed by stitching the space-time plots of each arm together and observing the oscillations are synchronised. As each arm is coupled to two others at the same time, the space-time plots are reoriented so that the meeting point is always at the bottom of the space-time plot, and the top shows the dead-end of each array where initiator droplets are usually placed. This way, arrays in all arms can be compared at the same time.

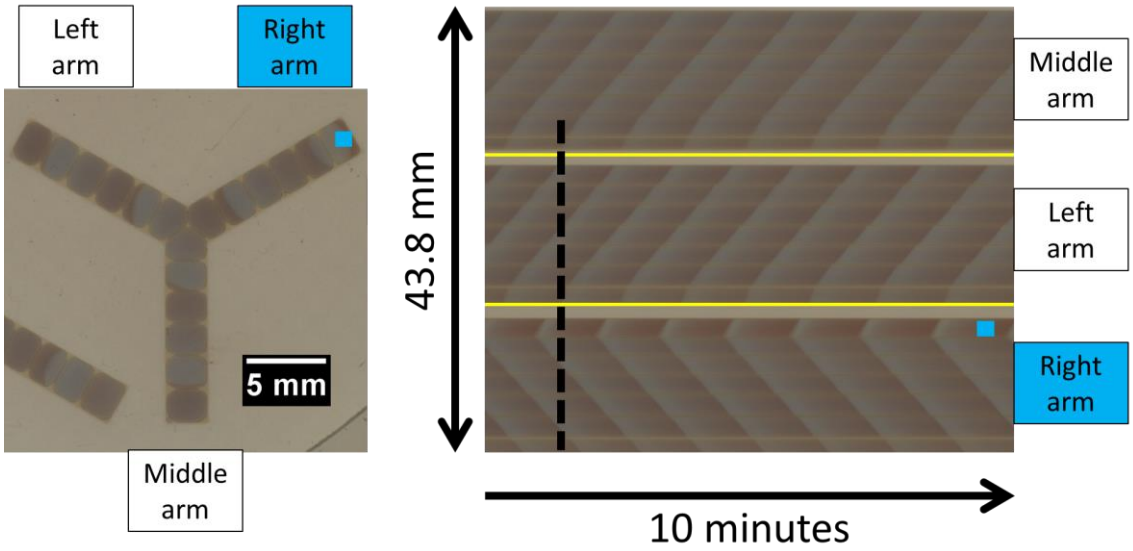

Figure 7.16 Photo and space-time plot of Y-shaped array with only one meeting point. Blue square in right arm indicates initiator droplet location. Right arm space-time plot has wave move from top to bottom while others have from bottom to top, indicating that waves initiated from right arm. Dotted line shows wave initiated at right arm propagates into other arms. Space-time plot and photo taken 2 hours after solutions mixed. Blue squares mark arms with initiator droplets and their locations. All space-time plots oriented so that dead-end of array is on top and meeting point is at the bottom. Initiator droplet uses 3 mM ferroin while all other droplets use 4 mM ferroin.

In the simple Y-shaped arrays with only one meeting point, it is observed that 7 out of the 10 arrays observed had a steady state with waves starting from the initiator droplet and propagating through to all other arms of the arrays through the meeting point. This is significant as there are 18 droplets in each array, so the initiator droplet has a 12.6 times higher chance of acting as a wave source than the other droplets in the same array. However, many take a long time to reach a steady state, with some having waves from other sources up until the final 30 minutes of the droplet lifetime out of 2 hours. Sometimes the initiator droplets would stay in the initial state for a long time and fail to form waves that propagate through the interface. The three interconnected droplets at the meeting point can also form a high frequency wave source that extinguishes waves from the initiator droplet and becomes the dominant wave. Additionally, small droplets can act as a wave source when the array is first formed, which can set the initial wave pattern to be from the region of the small droplet. This is less likely to be a problem for the whole lifetime, as small droplets tend to reduce in frequency and have their wave source extinguished by other sources. To analyse the space-time plots, the space-time plot of each arm is oriented so that the dead-end of the arm where initiator droplets are placed is at the top while the meeting point is at the bottom. An example of a space-time plot is shown in Figure 7.16.

For the Y-shaped array with many meeting points, initiator droplets are only added into one of the 4 connected arms and never in the middle arm. Different combinations of one, two, three and four initiator droplets are used in each array to observe if there are any distinguishing features in the resulting wave pattern. When only one initiator droplet is used, that initiator droplet extinguishes other random wave sources and propagates waves throughout the rest of the array. An example is shown in Figure 7.17. As before, the initiator droplet needs time in order to propagate waves throughout the array to extinguish other wave sources.

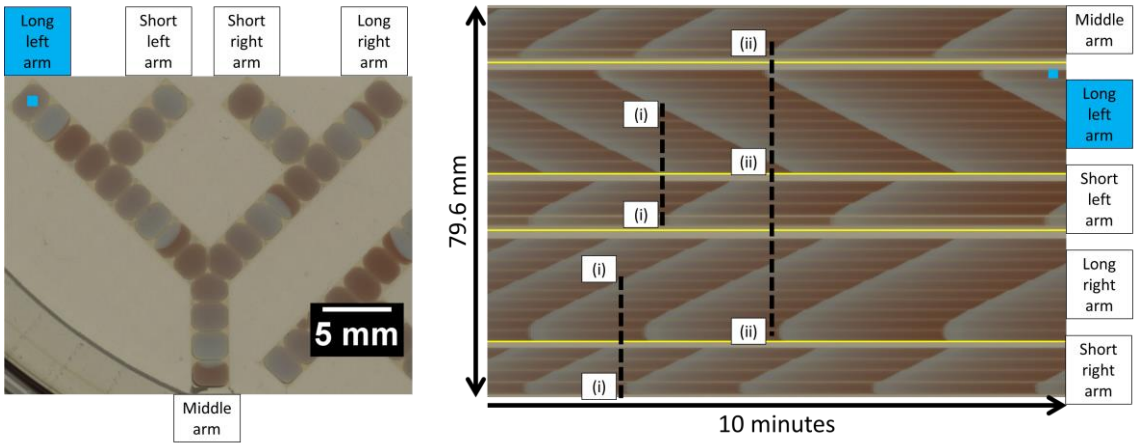

Figure 7.17 Photo and space-time plot of Y-shaped array with many meeting points with only one initiator droplet. All space-time plots oriented so that dead-end of array is on top and meeting point is at the bottom. Waves propagate from top to bottom of long left arm space-time plot but from bottom to top for all others. This indicates that long left arm acts as the wave source. Wave from initiator droplet also observed to propagate into all other arms through meeting points. (i) Waves that propagate from long arm into their respective short arms from the meeting point. (ii) Waves that propagate to meeting point between long arms and middle arm of array. Blue squares mark arms with initiator droplets and their locations. Space-time plot taken 2 hours after solutions mixed. Initiator droplet uses 3 mM ferroin while all other droplets use 4 mM ferroin.

It is observed that there is no significant difference between using only one initiator droplet versus many, as a random initiator droplet would form waves that propagate through most of the array. The dominant initiator droplet can randomly change as the wave pattern evolves, but usually the same droplet remains dominant for the majority of the lifetime. However, it is possible to see that the initiator droplets have a higher frequency and can initiate waves that propagate into their immediate neighbours, though the distance of propagation is random and is usually stopped after a short distance by waves from the dominant initiator droplet. This is shown in Figure 7.18.

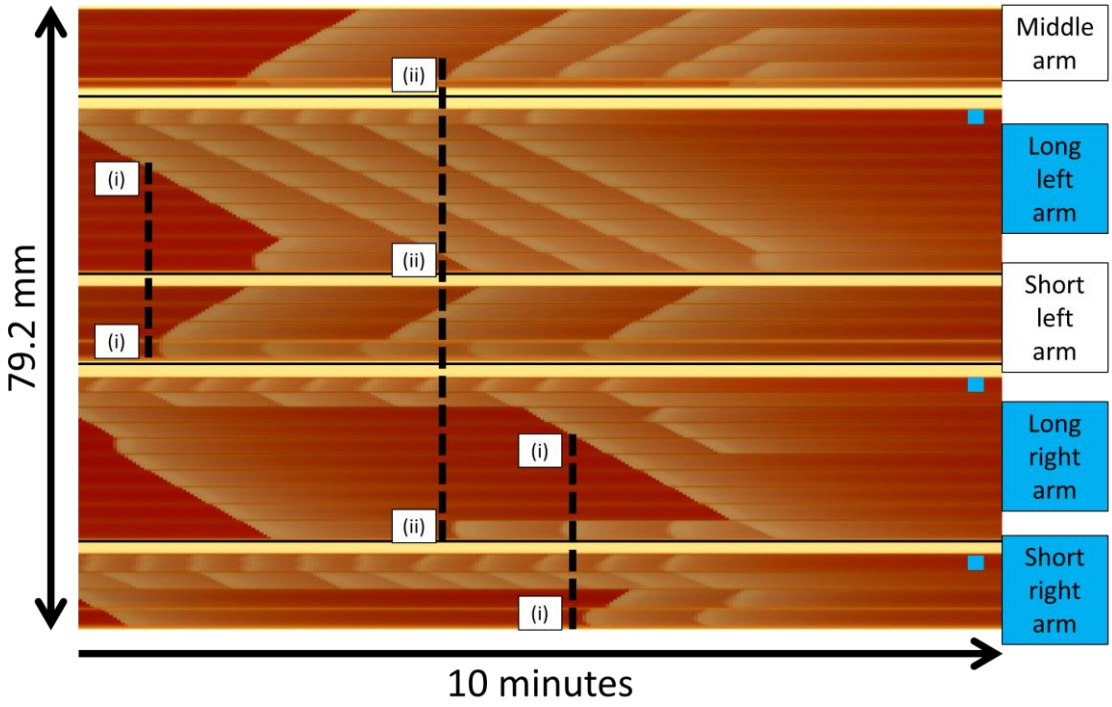

Figure 7.18 Space-time plot of Y-shaped array with many meeting points and 3 initiator droplets. All space-time plots oriented so that dead-end of array is on top and meeting point is at the bottom. Higher frequency of initiator and its coupled droplet observed with not all waves propagating. Waves propagate from top to bottom in blue marked arms, indicating that waves initiated from initiator droplet. (i) Waves that propagate from long arm into their respective short arms from the meeting point. (ii) Waves that propagate to meeting point between long arms and middle arm of array. Blue squares mark arms with initiator droplets and their locations. Space-time plot taken 2 hours after solutions mixed. Contrast histogram set between 20 and 90 for visibility. Initiator droplets use 3 mM ferroin while all other droplets use 4 mM ferroin. In this case, oil used was previously exposed to MA-CHD BZ in a previous experiment, causing the darker oil appearance.

Additional experiments were also performed using initiator droplets of 0.5 M H_2SO_4 and 0.47 M $NaBrO_3$ of 1 µl each. These droplets are the same composition as blue MA BZ droplets without MA and ferroin. It is hypothesised to produce the oxidising free radicals needed to turn the ferroin from red to blue. These droplets are stable when coupled to the array when used in such small volumes. When these droplets are coupled with MA-CHD BZ arrays that have stopped oscillating as red droplets, a single wave is initiated at the interface that travels through the entire array. However, subsequent waves initiated from this point are of a high frequency and do not propagate waves through the interface. These

droplets resemble the “over-excited” droplets described previously. If the initiator droplets fuse with the MA-CHD BZ droplet, the BZ droplet turns blue and no longer oscillates.

With these experiments, the initial work in developing initiator droplets is completed. It can be observed that the low ferroin droplets has a high probability of acting as the wave source even though all other droplets in the array of up to 28 droplets has a chance of forming a wave source. The initiator droplet is also observed to be able to extinguish wave sources formed from small droplets and from the self-exciting meeting points in these arrays, overcoming some of the natural behaviours of BZ arrays due to the topology. However, they are not yet fully reliable with approximately 70% of repeats forming wave sources at the initiator droplets.

This concludes the progress of characterising and using MA-CHD BZ droplets in structured arrays in the asolectin in hexadecane droplet-in-oil system. This mixture is observed to produce waves that propagate through most interfaces in the array while having a short induction time compared with CHD BZ. Large, non-linear arrays of up to 399 droplets were also formed and kept stable for the 4-hour observation period. Initiator droplets using droplets of lower ferroin were tested and evaluated. Initial work using advanced computer vision techniques and using stitched space-time plots were performed and is able to detect changes in wave characteristics based on the topology of the array as well as the presence of initiator droplets. With this, future studies can be performed to combine BZ droplets of different composition to test designs of greater complexity for unconventional computing applications.

Chapter 8 Millifluidic chip

8.1 Chip modifications for BZ compatibility

The process of making BZ arrays of different composition and topology needs to be scaled up and made more repeatable for future applications, which may need even larger arrays arranged to designs that are even more complex. Microfluidic techniques allow droplets to be mixed in situ with high repeatability and throughput and with the possibility of automating the procedure.

For this purpose, the millifluidic chip used in [22] is modified for use with BZ solutions. The advantage of this system is that it is able to mix droplets of 2 to 5 µl in situ efficiently and accurately. The “delay line” ensures that each droplet is mixed homogenously ensure that wave sources are not formed due to BZ components being concentrated at certain regions. The droplet capture chamber is also large enough to fit large droplets to allow their wave patterns to be observed. Additionally, the height of the droplet is constrained, so droplets or large and small volumes will have the same height and interface area. As the design uses oil pressure to keep the array in place instead of gravity, it is also possible to apply different pressures to the array to increase or decrease the interface contact area as well as to stop the array from moving around. This also has the effect of replenishing the asolectin in hexadecane oil surrounding the array to keep the concentration constant and to reduce any contaminants escaping from the droplets into the oil. The combination of oil pressure and constrained array of the capture chamber also allows the chip to be moved without disturbing the array inside. Using PDMS and polymer masters for moulding instead of glass or steel capillary tubes also allows the chip to be replaced regularly to prevent excessive contamination. This also allows future modifications to the design to be made.

One disadvantage of using a microfluidic system is that it is not as effective at dealing with CO_2 gas bubble formation from the BZ mixture. In the previous PMMA system, gas bubbles tend to float to the surface and disappear without significantly disturbing the droplet array, but this is not possible in a closed microfluidic system. This is because while PDMS is gas permeable, CO_2 is still not removed fast enough to prevent bubble formation. To remove unwanted droplets or gas bubbles it is also necessary to flush out the entire existing array.

Another challenge of using BZ droplets on chip is that BZ solutions cannot be used in syringes while fully mixed. This is due to CO_2 gas bubble formation and because the BZ solution will become exhausted if fully mixed and allowed to oscillate. This means that components must be separated into at least two half-solutions without these separated solutions denaturing while making sure that the resulting BZ solution can still oscillate when they are mixed together. Bromine formation is also a concern in the chip as fully mixed BZ with KBr added forms precipitate that must dissolve and may disrupt the oscillation behaviour. The PDMS can also absorb and remove the bromine due to its gas permeability, which may also cause the droplet to become non-oscillatory. To maintain the advantages while reducing the disadvantages, the following modifications were performed. It must also be noted that these disadvantages also allow unique observations in the microfluidic chip that cannot be done in the PMMA arrays, such as the effect of coupling CO_2 bubbles.

Defects the 3D-printed PDMS master will affect any moulded chips that are produced. This can be avoided by periodically changing to use new masters. To allow new PDMS moulding masters to be fabricated more often and at cheaper cost, polyurethane masters are used. The cured polyurethane is then used as the master for PDMS chips as in [165]. This is done by producing a PDMS chip from the original 3D-printed master. This PDMS is used as a reverse mould for the polyurethane by pouring uncured polyurethane mixed with curing agent into it. The poured mixture is degassed in a desiccator to remove any gas bubbles in the features and then left overnight to cure. The cured polyurethane is then used in the same procedure as the original as the replacement for the 3D-printed master. This way it the polyurethane master can be replaced when it is damaged and the 3D-printed master can be preserved. Polyurethane masters melt if placed at 80°C, so any PDMS chips made using these new masters are first cured at 60°C for at least two hours. The PDMS is then cut and removed from the master and cured one more time at 80°C for at least one hour to it ensure it is fully cured. The PDMS is placed with the features facing on a clean glass slide surface to prevent contamination while in the oven. This PDMS can then be bonded to a clean glass slide in the normal procedure by exposing the bonding surfaces to 30 seconds of oxygen plasma, bonding it, and then placing it in the 80°C oven for at least 1 hour for the surface to return to its original uncharged state.

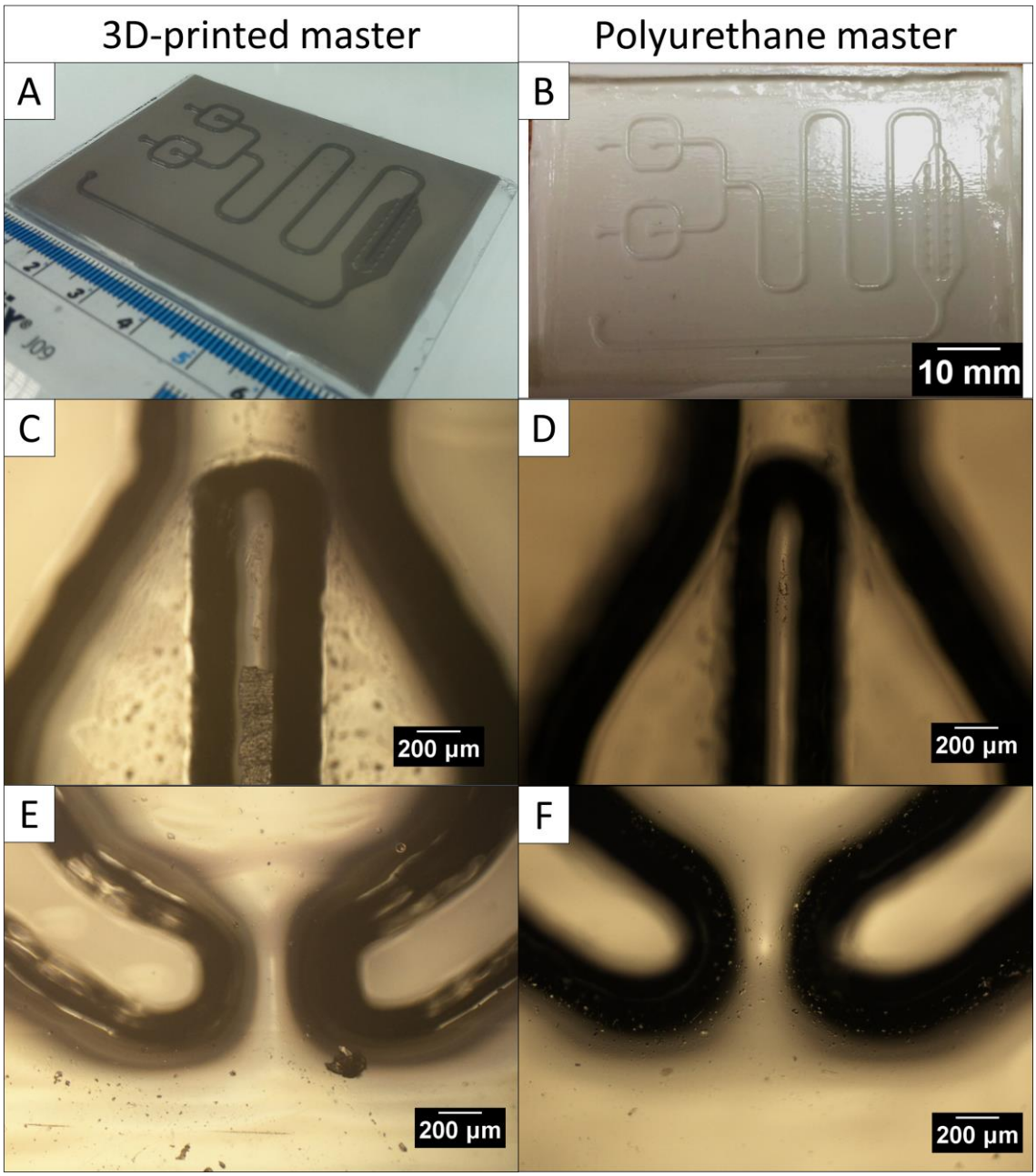

Figure 8.1 Comparison between 3D-printed master and polyurethane master and their resulting unused PDMS chips features viewed in a Nikon Eclipse LV100 microscope under 5X magnification in the dark field with lighting from bottom. PDMS chip photos show that 3D-printed master has defects from wear and tear but smaller sized gaps for channels and features compared with chip from the polyurethane master. (A) 3D-printed master is relatively smooth. (B) Polyurethane master with rougher surface where there are no features. (C) and (D) show the top of the capture chamber of PDMS chip. (E) and (F) show the pillar gap at the bottom of the capture chamber of PDMS chip.

These polyurethane masters and their PDMS moulds were checked under a Nikon Eclipse LV100 microscope at 5 times magnification under both bright and dark field and lighting from the top and bottom, but no significant differences in the shape of the structures is observed. The old 3D-printed master's PDMS chip was rougher and had more defects than the one made with the polyurethane master as the result of damage from wear and tear from repeated use. However, the gaps for features and channels made using the polyurethane master were significantly smaller. Large features such as the channel from the delay line was approximately 100-200 µm larger compared with the PDMS from the polyurethane master. Small features such as the rail and pillar gap of at the bottom of the capture chamber was approximately 30 to 50 µm larger for the 3D-printed master. In addition, where there are no features the polyurethane master's surface is rougher compared with the original 3D-printed master. Despite this, the PDMS chip is bonded to the glass slide without leaks and the droplet mixing and array performance was not significantly affected. Images comparing the 3D-printed master and subsequent PDMS chip features are shown in Figure 8.1.

BZ droplets of this size tend to form CO_2 gas bubbles when observed inside a closed system such as microfluidic chips. In order to overcome this, the ratio of PDMS to curing agent used is changed from 10:1 to 20:1 mass ratio. This causes the PDMS made to be softer and up to three times more permeable to gas [166]. In addition, before each use the PDMS is placed in a desiccator at low pressure for at least 5 minutes to remove any gas already absorbed inside the large volume of polymer. This is to reduce the chance of initial gas bubble nucleation when the BZ droplet is mixed in the chip. As the PDMS used is much softer than the standard, the biopsy punches used to form inlet and outlet holes must be larger, so 2 mm biopsy punches are used instead of the 1.5 mm ones from the original paper. An additional curing step at 80°C is also needed as the 20:1 PDMS ratio is not fully cured at 60°C.

The asolectin in hexadecane oil used is 38.1 mg/ml instead of the 20 mg/ml used in the original paper to maximise the amount of lipid in the oil so that the lipid membrane around the droplets forms more easily. This increases the stability of the droplet array as each droplet does not need as much time for the lipid membrane to cover the entire surface. To ensure the maximum amount of asolectin is present, the oil is not filtered or centrifuged. However, it is recommended to centrifuge the oil to remove any large contaminants to the asolectin in hexadecane oil for future experiments.

The BZ solution to be used is split into two half-solutions that are added through both aqueous inlets in the original chip design. This makes sure that the oscillations can be started at the precise moment when it is needed and that CO_2 gas bubbles do not form and disrupt the chip. With guidance from Philip King, the BZ components are split as shown in

Table 8.1. H_2SO_4 and malonic acid are placed in one half-solution so that all acidic components can be kept away from the other components. $NaBrO_3$ and KBr are kept in the other separate half-solution to isolate all possible sources of bromine. Ferroin is kept in both solutions to ensure that the ratio of the half-solutions can be changed without changing the final concentration of ferroin. KBr is used in this case to observe if BZ solutions that are mixed with added KBr can dissolve the precipitate formed and oscillate while inside the PDMS chip. This is important for future experiments where KBr may need to be added to BZ solutions to regulate their behaviour. MA-CHD BZ solutions are not used yet in this setup. This is because it is difficult for these droplets to oscillate without first mixing the full MA BZ solution before adding the CHD. This makes it more complicated to separate into only two half-solutions. The final BZ composition for the droplets in all ratios is significantly different from the droplets used in the PMMA array. In the 1:1 ratio droplets, the malonic acid concentration is higher while the final H_2SO_4 is lower and KBr is present. The $NaBrO_3$ and ferroin concentration is approximately the same. This should result in oscillations of a lower frequency as well as a longer droplet lifetime.

Table 8.1 Tables of half-solutions of BZ used for the chip. Different ratios are mixed by changing the volume of half-solution released from the aqueous inlets.

Order	Half-solution A	Volume	Conc.	Final concentration in ratio		
				1:1	3:2	2:3
1	2.5 M sulphuric acid (H_2SO_4)	300 µl	595 mM	298 mM	357 mM	238 mM
2	1.0 M malonic acid	875 µl	694 mM	347 mM	417 mM	278 mM
3	25 mM ferroin	85 µl	1.7 mM	1.7 mM	1.7 mM	1.7 mM

Order	Half-solution B	Volume	Conc.	Final concentration in ratio		
				1:1	3:2	2:3
1	Deionised water (H_2O)	255 µl	-	-	-	-
2	1.5 M sodium bromate ($NaBrO_3$)	750 µl	907 mM	454 mM	363 mM	544 mM
3	1.0 M potassium bromide (KBr)	150 µl	121 mM	60 mM	48 mM	73 mM
4	25 mM ferroin	85 µl	1.7 mM	1.7 mM	1.7 mM	1.7 mM

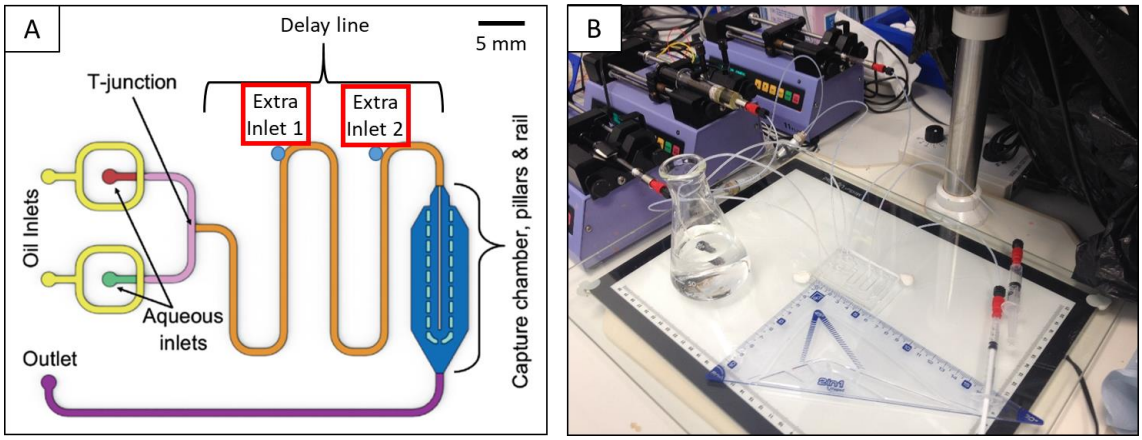

Figure 8.2 (A) Schematic of modified millifluidic chip with modified extra syringe inputs highlighted. Droplet arrays held in 2.5 mm wide space between pillars in capture chamber, channels are 1 mm wide and entire chip is 70 X 50 mm. Original image reproduced from [22]. (B) Photo of setup under Stereozoom microscope and on light source with syringe pumps, syringes and drain connected.

To remove bubbles and unwanted droplets from the system without flushing the capture chamber, extra outlets are added into the delay line of the design. These outlets are connected to plastic syringes and can be manually used to remove material from the oil flow. This also allows the oil flow in the capture chamber to be reversed if necessary. Besides this, these outlets can also be used to input a third type of aqueous droplet for mixing or other uses in the millifluidic chip, as both original inlets of the chip are already used for mixing the BZ half-solutions. This is shown in Figure 8.2.

As a result of these modifications the rate at which arrays can be formed without fusion and disruption from unwanted droplets and gas bubbles is improved. Though bubble formation is still possible with these modifications, the CO_2 gas bubble formation is reduced enough that more arrays can be formed without disruption. Greater control over the array formation and types of droplets that can be mixed is also achieved due to these modifications. This enables the procedure for using this setup with BZ solutions to be developed.

8.2 Chip operation for setting up droplet arrays

The chip is operated and controlled in the same way as in the original paper [22]. The aqueous and oil flows can be changed according to the experimental conditions to prevent droplet fusion but usually use the same settings. The oil inlets are connected to the same oil syringe and can be controlled using the off-chip solenoid valves (LFE series PFE 2-way Micro Inert Valves (The Lee Company, CT, USA)). However, no other valves are used in these experiments, so the aqueous inlets, extra inlets and outlet are all kept from entering the chip by the oil pressure. The oil and aqueous syringe flow is controlled by "Harvard Apparatus 11 Plus" syringe pumps.

The ratio of half-solution A and B are controlled by releasing a measured volume using at 10 µl/min while the oil flow is switched off. Each part is then separated from the main syringe solutions at the inlets by restarting the 20 µl/min oil flow to form droplets. The oil valves are rapidly switched off and on (pulsed) as both droplets meet at the T-junction to mix them. As the droplets mix, a dark precipitate forms consistent with when KBr is added to BZ solution. The droplet is then released into the delay line, which has a serpentine shape to agitate and homogenously mix the droplet. Mixed droplets of 5 µl are used as in the PMMA arrays. The mixing procedures are shown in Figure 8.3.

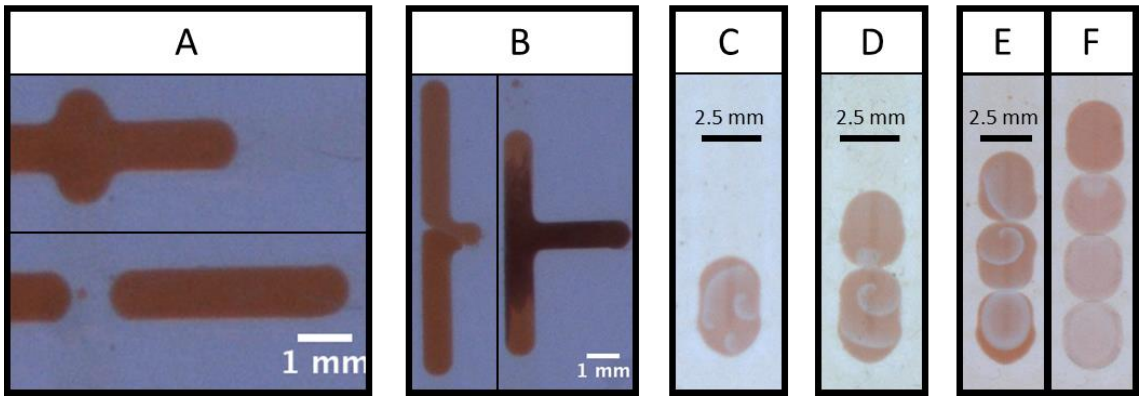

Figure 8.3 (A) Sequence of preparing accurate volume of solution from syringe and separating from syringe solution for mixing by pulsing oil valves. (B) Sequence of mixing two prepared solutions by pulsing oil valves. Dark colour forms upon mixing. (C) Example one-droplet array. (D) Example two-droplet array. (E) Example three-droplet array. (F) The same three droplet array as (G) but with a freshly mixed droplet placed on top after 1 hour to form a four droplet array. Width of droplets in arrays is approximately 2.5 mm. Each droplet is 5 µl.

Each droplet is mixed and then allowed to flow at 20 µl/min oil flow until it reaches the capture chamber. 20-200 µl/min flow is then applied to push the droplet to the bottom of the capture chamber. This flow rate is varied to prevent excessive pressure that can fuse droplets already present inside the capture chamber. The flow is then reset to 20 µl/min and the next droplet is mixed. When all droplets are inside the capture chamber, the oil flow is kept at 20 µl/min to maintain the pressure on the droplets and prevent backflow from the drain. If the droplets no longer appear rounded at the top of the array and appear to have too much pressure, the oil pressure is reduced to a minimum of 5 µl/min to reduce the chance of droplets fusion.

The oil syringe can be refilled by stopping the flow, closing both oil inlet valves then removing the syringe from the luer lock. The syringe is then refilled as normal. When the syringe is reconnected, the valves are reopened and the flow is resumed as before. The flow is observed to ensure no gas bubbles have been introduced, and any that are introduced are removed by first slightly increasing the flow of the oil and then sucking out the bubble using the extra drain syringes at the extra inlets. This must be done carefully as it is observed that suction from these syringes is likely to fuse droplet arrays in the capture chamber.

The oil flow rate of 20 µl/min is chosen in order to maintain the oil pressure for a longer period without the need to refill the oil syringe. A higher flow rate can be used to increase the pressure on the droplets, but it is observed that at least 50 to 100 µl/min needs to be used to form a flattened interface. This increases the chance of droplet fusion and can flush the array out of the capture chamber. Using such a high flow rate also shortens the time before the oil syringe needs to be refilled.

The recording is started before the mixing step and continued for at least 1 hour after the droplets have reached the bottom of the capture chamber. This allows the mixing step to be recorded and the behaviour of the BZ from when it is first mixed until it has formed a consistent wave pattern to be observed. When mixing arrays of droplets, each droplet is allowed to reach the bottom of the capture chamber before the next one is mixed. This is to prevent the droplets from moving while in contact inside the capture chamber, which may increase the probability of fusion. The array is also formed as quickly as possible to reduce the age difference between droplets. Due to this procedure, droplets have up to 5

minutes delay between each other. It is assumed that the half-solutions do not denature in any way inside the syringes, though the acidic half-solution A is observed to become more transparent after it is kept in the syringe for more than 5 hours.

The extra inlets are usually used as drains by sucking out solution from the oil flow as they pass near the inlet. Care is taken to reduce the force and flow of this process as excessive suction pulls oil and drain solution from the chip outlet. This process can also fuse droplets already present in the capture chamber. Removed aqueous droplets must also be sucked a long distance into the syringe as they can be released back into the flow as aqueous solutions are more dense than oil and tend to sink. Gas bubbles do not have this problem and tend to block any flow from the extra drain syringe into the chip.

When using the extra inlets for mixing additional types of aqueous solutions, this third solution is pushed out manually and the volume of the droplet is estimated based on the length of the droplet released. If the droplet needs to be mixed to another half-solution, the droplet is gently released into the middle of the other droplet without splitting it. The syringe is then gently pulled to suck in the droplet, causing the droplets to fuse. The third solution is then gently pushed out until the length of the droplet is approximately at the volume required. Then, the oil flow is resumed and the droplet is allowed to separate from the syringe inlet. As this process contaminates the solution in the syringe, it is usually not used. This process can be improved in the future using additional syringe pumps, using glass syringes and by redesigning the chip so that the extra inlets are connected in the same way as the other aqueous inlets.

These procedures are used in subsequent experiments where BZ droplets are observed as arrays of up to four droplets in the capture chamber for up to four hours. In some experiments, a fresh droplet is mixed while an older existing array is present and added to the top of this array. This tests the chip's ability to keep the array stable while the new droplet is mixed with fluctuating oil flow. This is also to observe the effect of a droplet with longer remaining lifetime on other nearly exhausted droplets in the array inside the chip. An experiment with bromine-generating droplets is also attempted in the chip to test its compatibility, since bromine could not be used in the asolectin in hexadecane system due to asolectin absorbing the bromine as well as the tendency for the droplets to fuse when forming an interface.

8.3 Observations of BZ arrays on chip

When placed in the chip, the droplet is significantly flatter as it is height constrained due to the z-axis thickness of the channel so it covers more surface area compared to droplets in the PMMA arrays. Droplet arrays formed this way are still able to fuse within the first hour of the experiment, but after this period, the arrays are stable and can survive for up to six hours. An array of eight droplets of dye of 2 µl each was previously observed to remain stable for eight hours. As in the PMMA arrays, MA BZ droplets are observed to oscillate in the same behaviour and the same phases as mentioned in Chapters 4 and 6. However, waves formed in this system are unlikely to be from the walls of the capture chamber and usually forms at the interfaces or the centre of the droplet. This is very useful as it can isolate whether waves start from the walls for PMMA due to PMMA acting as a BZ substrate or if this is due to the natural evolution of the BZ wave pattern. These droplets are observed to oscillate for similar lifetime as those in the PMMA arrays, of approximately 5.5 hours, after which it becomes exhausted and stops oscillating as transparent droplets. As before, several varieties of wave patterns can be observed when they are first mixed such as multiple spiral shapes, single spirals and low contrast waves where many wave sources and directions are observed. This then reaches a steady state to form planar and circular waves as it reaches the middle phase. Droplets are observed to oscillate with a lower frequency and with a longer lifetime of 5.5 hours as expected and is similar to when these droplets of the same composition were tested in PMMA arrays in Section 6.2.

When placed in arrays of two and three droplets, the waves form at the droplet interfaces as in previous sections. The waves are unable to propagate through the interface to interact, so both droplets oscillate independently and occasionally go in and out of phase. Hence, when coupled there is a significant change in wave pattern but not in other wave characteristics. When three droplets are coupled, both interfaces in the sandwiched middle droplet act as wave sources but eventually one source extinguishes the wave source at the other and becomes the only wave source. It is random if the top or bottom wave source remains.

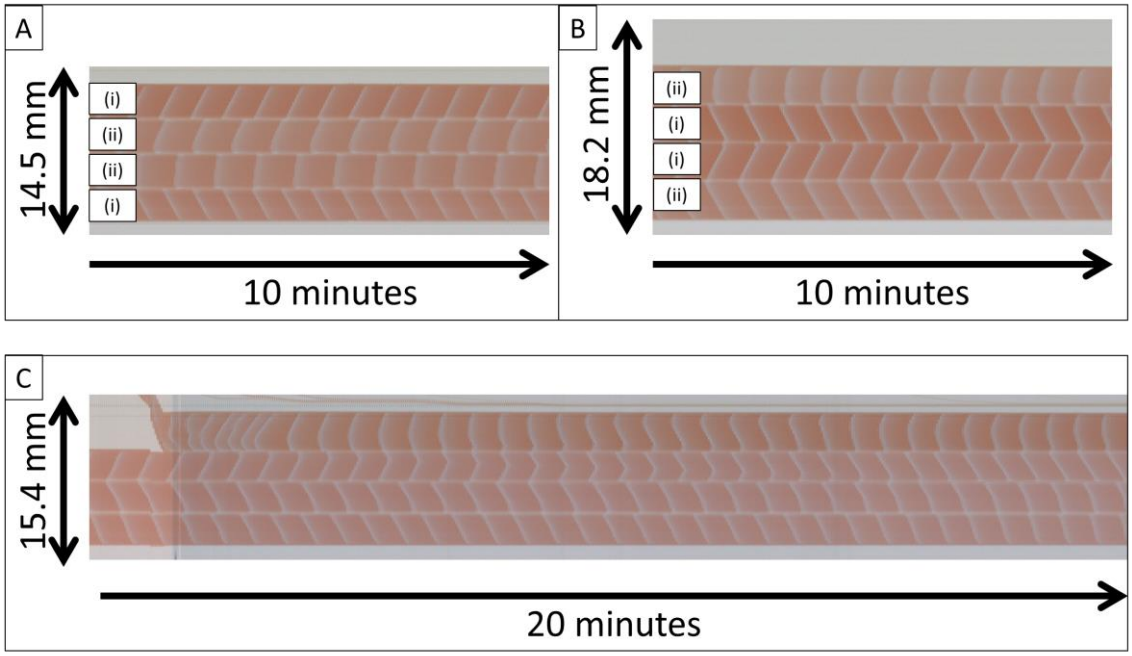

Figure 8.4 Space-time plots of droplets of different composition on chip. Droplets marked (i) are 1:1 droplets while droplets marked (ii) are 3:1 droplets. All droplets are 4 µl. (A) 3:1 droplets sandwiched between 1:1 droplets. Plot taken after approximately 30 minutes. (B) 1:1 droplets sandwiched between 3:1 droplets. 1:1 droplets form wave sources from interfaces with 3:1 droplets. Plot taken after approximately 30 minutes. (C) 1:1 droplets in a 1 hour old 3-droplet array that has a fresh 1:1 droplet added on top. New wave source from new interface with fresh droplet formed which extinguishes wave source from interface with older droplet in array. Other droplets in array are not affected by this. Plot taken after approximately 1 hour.

Limited tests are performed droplets of different ratio and only visually analysed. It is observed that the frequency of the oscillations is similar to the droplets of 1:1 ratio despite the differences in composition. Droplets of 3:1 ratio have a similar frequency to 1:1 droplets despite the difference in composition. They also tend to have circular waves from the middle of the droplet even when coupled, though they also form waves from the droplet interface. Droplets of 1:3 ratio tend to also have a similar frequency but tend to form wave sources at the interfaces with other droplets. These ratios were chosen to exaggerate the difference in ratio of half solutions. These patterns were also observed when repeated in arrays of 5 µl droplets in PMMA arrays, but only limited experiments were performed.

Using the chip, a fresh droplet can be mixed in situ to be placed on top of an existing array without destabilising and fusing the existing droplets. This is useful as older arrays change in pattern after oscillating for at least one hour. After this time, the wave source at the interface forming planar waves moves to the middle of the droplet to form circular waves. When a fresh droplet is mixed and placed on the top of this array, the same response is observed as in the PMMA arrays, which is that a new wave source is formed at the droplet interface between the old droplet and the freshly mixed droplet. This new wave source forms waves that extinguish the existing wave source from the middle of the droplet, changing the direction and shape of the waves. As before, only the droplet directly coupled to the fresh droplet forms this behaviour and other older droplets do not. If two fresh droplets are placed on top of this old array, the two fresh droplets form waves from the interface between both fresh droplets, while in the directly coupled old droplet forms a source from the new interface with the fresh droplets. The waves in these cases do not directly propagate through the interface to interact similar to all other cases with pure malonic acid droplets. This experiment was repeated using 5 µl droplet arrays in the PMMA array setup and were found to behave similarly in Section 6.2.

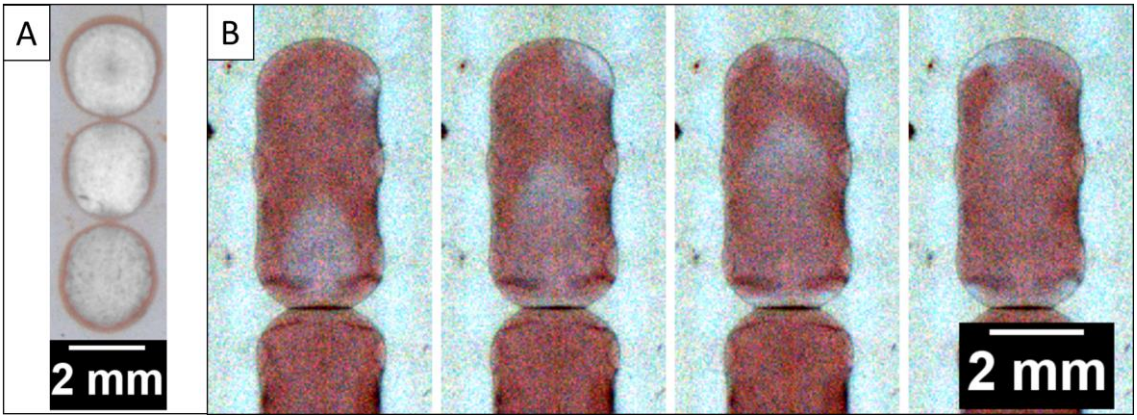

Figure 8.5 BZ droplet arrays zoomed in under microscope with different wave behaviour at droplet-oil interface. (A) Image of several waves combined using "maximum" function of image calculator. White regions show where waves propagated. Red regions observed at boundary of droplet indicating that waves never propagated through these regions even over several oscillations. Images taken after approximately 30 minutes for oscillations over 16 minutes or 400 frames. (B) Separate wave formed along aqueous-oil interface on top of array, which does not interact or propagate into the middle of the droplet. This is later observed for droplet below. Images taken after approximately 5 hours at 5-second increments.

The droplet arrays in the chips are also quite stable as it is well constrained in height inside the capture chamber and has a constant pressure from the oil flow. This is taken advantage of by moving the chip once the array is set up to zoom in on the droplet. This enabled behaviours that have a low contrast and are too small to see to be more closely examined. It is observed that for all BZ droplets in the chip, there is a red reduced region at the aqueous-oil interface where waves do not propagate. In comparison, the droplet interface has a wave that forms and propagates at the edge of the droplet with no red reduced region seen. This effect is observed for the aqueous-oil interface for all droplets in the array, though this largest where the droplets are directly exposed to oil at the top and bottom of the capture chamber. This effect is shown in Figure 8.5 (A).

One rare observation is that some droplets form separate wave patterns at this aqueous-oil interface, where previously no waves are able to propagate. This is shown in Figure 8.5 (B). This behaviour usually occurs after a long time of observation when the droplet is almost at the late or exhausted phases. In this case, the centre of the droplet oscillates as normal with either planar or circular waves, but these waves stop before reaching the aqueous-oil interface. A separate wave self-oscillates at the droplet edge, which travels around the droplet centre through the aqueous-oil interface, never interacting with the waves in the centre of the droplet, which separately oscillates while this is happening. When the droplet is almost exhausted this wave may evolve into “reverse” waves that start from the droplet edge and move towards the middle. It is hypothesised that this behaviour is due to the asolectin in hexadecane oil’s flow interacting with the BZ droplet, as this is usually first observed for droplets in the millifluidic chip at the top of the array where the shear from the oil flow is greatest. This is followed by the bottom of the array near the outlet of the capture chamber.

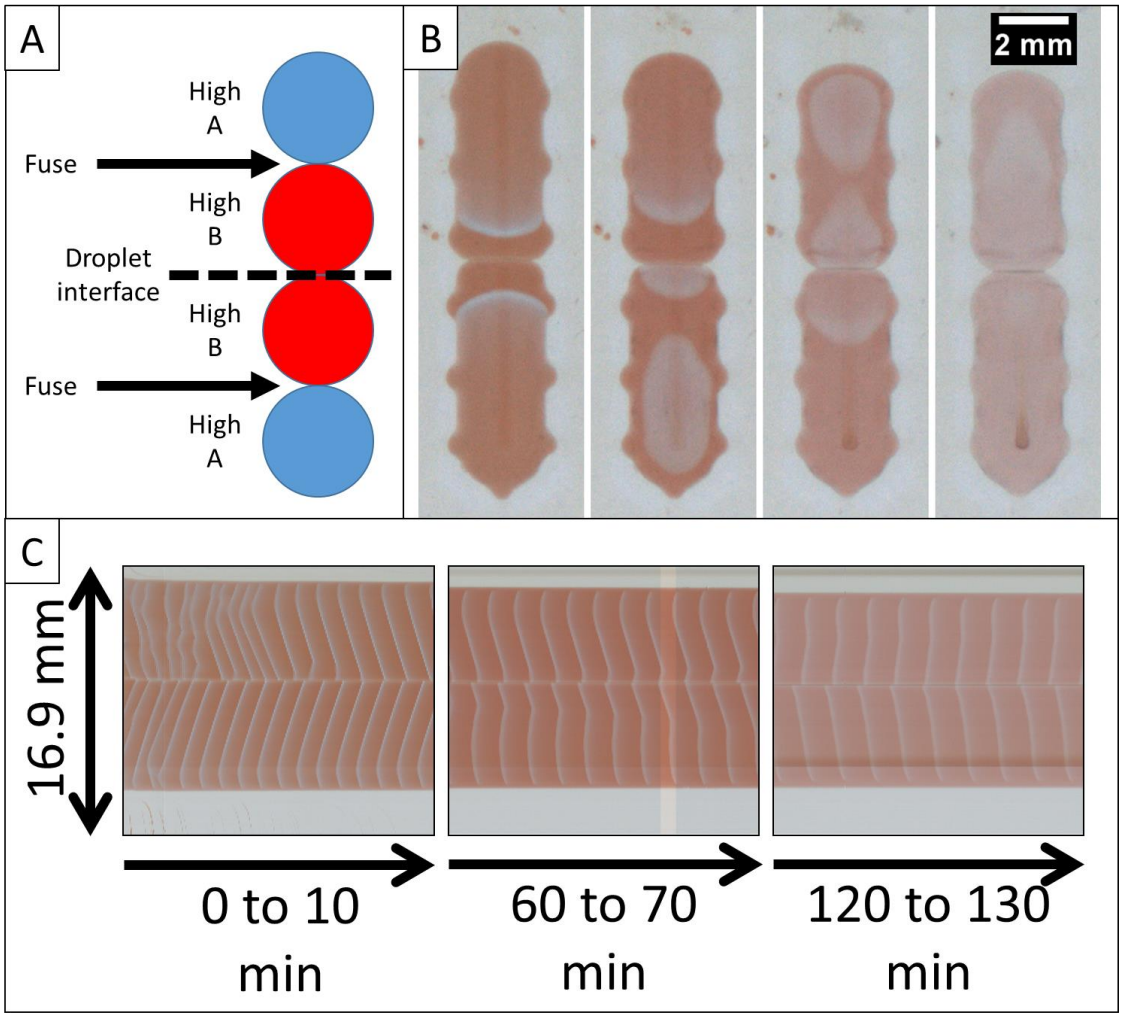

Figure 8.6 Droplets purposely fused at specific locations to form inhomogenously mixed droplet and a droplet interface in the middle. (A) Schematic of initial compositions of droplets with higher half-solution ratio of A or B and location of fusion and droplet interface. (B) Wave pattern evolution of inhomogenously mixed droplets taken at approximately 20, 65, 140 and 235 minutes. Inhomogenously mixed droplet has waves from initial positions of droplets high in ratio of half-solution A at first, but droplet interface later forms a wave source that eventually extinguishes initial wave sources. (C) Space-time plots showing evolution of wave direction as it changes from waves at the edges of the droplets to have a wave source from the droplet interface.

To take advantage of the array stability and control of the oil flow and droplet position, an experiment is performed to fuse droplets of significantly different composition purposely while maintaining a droplet interface bilayer in the middle of the array. This produces droplets that are mixed homogenously as they were fused while in the capture chamber instead of in the delay line where the droplets are allowed to mix homogenously in the flow. To do this, a droplet of with higher part A half-solution and hence higher ratio of H_2SO_4 and malonic acid is used with droplets with higher part B half-solution containing higher ratio of inhibitor KBr. The droplets with higher part A tend to form wave sources due to the significantly higher H_2SO_4 and lower KBr. The array is arranged such that those with higher part A are placed at the top and bottom of the array sandwiching droplets with higher part B. The bottom half of the array is mixed in quick succession. After reaching the bottom of the capture chamber, these droplets are fused by sucking out oil from one of the extra syringes in the delay line. The top half of the array is then made in quick succession and allowed to flow until they are at the top of the capture chamber. The top half is fused in the same way, taking care not to disturb the fused droplet already present. The fused top droplet is then allowed to slowly flow into place and form a droplet interface bilayer with the first, bottom fused droplet.

As the middle of the array contains more KBr inhibitor and less H_2SO_4, it is less likely to act as the wave source even though a bilayer is present. Instead, the top and bottom of the array act as a wave source forming circular waves from where the high part A droplet used to be. As the droplet stabilises, the bilayer forms a wave source whose waves interact with the other wave sources. The waves from the bilayer propagate further until it extinguishes the wave sources from the droplets with high ratio of half-solution A, forming the normal wave behaviour where waves start from the droplet interface bilayer. As time goes on the wave source from the bilayer becomes weaker and eventually the wave source moves to the middle of each droplet. This experiment is shown in Figure 8.6.

Especially for the unmodified chips with 10:1 PDMS ratio, small gas bubbles are observed to quickly grow in size and start displacing the aqueous droplet. These bubbles do not affect the wave behaviour and only act as a “wall” which prevents waves from travelling through that region. Usually the wave splits into all paths around the bubble, which then meets and interacts on the other side of the bubble. However, the wave sometimes disappears while travelling through the path on one side of the bubble, so when the other wave is able to

propagate and feed back through this other path using the bubble as its centre of rotation and then returns to its original source. This extinguishes the source and causes the wave to act as a “spiral” behaviour with its centre at the gas bubble. This wave then travels around the bubble at a higher frequency than originally as the wave is able to excite itself as it moves around the loop. Bubbles that form above or between droplets do not influence the wave behaviour even at the interface, and only act as physical walls that separate or displace droplets in the array. If the movement of the bubble is significantly violent as to cause turbulence in the droplet, the existing waves can be “stirred” and disrupted.

When tested with bromine gas producing droplets, it is found that these droplets are unstable when coupled with other droplets in the array despite the increased stability of arrays in the capture chamber. Compared to experiments in petri dishes, the bromine also still has a significantly smaller range despite the lower exposure area to asolectin in hexadecane oil, and no effect is observed in the droplet arrays placed close to these bromine source droplets. It is hypothesised that the bromine is diffusing into the surrounding gas permeable PDMS. This is due to the slight brown colour observed where the bromine droplet first mixed. When an iodine-producing droplet is used instead, a significantly darker colour is observed in the PDMS of the surrounding channels where it is mixed and where it has travelled through. This colour persists even after washing with both oil and DI water, and spreads throughout the PDMS chip beyond the initial channels after several days. Figure 8.7 (A) shows an experiment where a bromine-generating droplet sandwiched between two KI droplets. Bromine generated in capture chamber turns KI droplets yellow due to displacement of iodine by bromine, which is yellow in aqueous solution. The colour change is observed closest to the bromine-generating droplet first and slowly spreads through the entire droplet. Figure 8.7 (B) shows the effect of bromine and iodine exposure to the PDMS of the chip. Chip has a yellow colour especially in the channels. Extra inlet 2 until the outlet has the highest colour intensity as bromine and iodine is generated starting at that inlet.

This section concludes that BZ droplets are mixed in situ and observed for up to four hours inside the millifluidic chip. The chip is demonstrated to have good stability of the array in the capture chamber, control over the proportion of half-solution mixed, the oil flow pressure and position of droplets in the array. This allowed experiments to be performed where droplets are mixed at specific mixing times without disturbing the existing array, for

the array to be moved for a zoomed in view of the array and for specific droplets in the array to be fused while maintaining a droplet interface bilayer at a specific location. These experiments gave observations of the effect of a fresh droplet on top of an array, the wave behaviour at the aqueous-oil interface and the evolution of wave behaviour if a wave source is formed in another part of the droplet while a droplet interface bilayer is present. Observations of BZ droplets forming interfaces with growing CO_2 gas bubbles are also made possible because the capture chamber is enclosed. Future applications with more sophisticated chip designs, pumps and valves can allow the process to be automated to form droplet array topologies of greater complexity and mixtures with high repeatability.

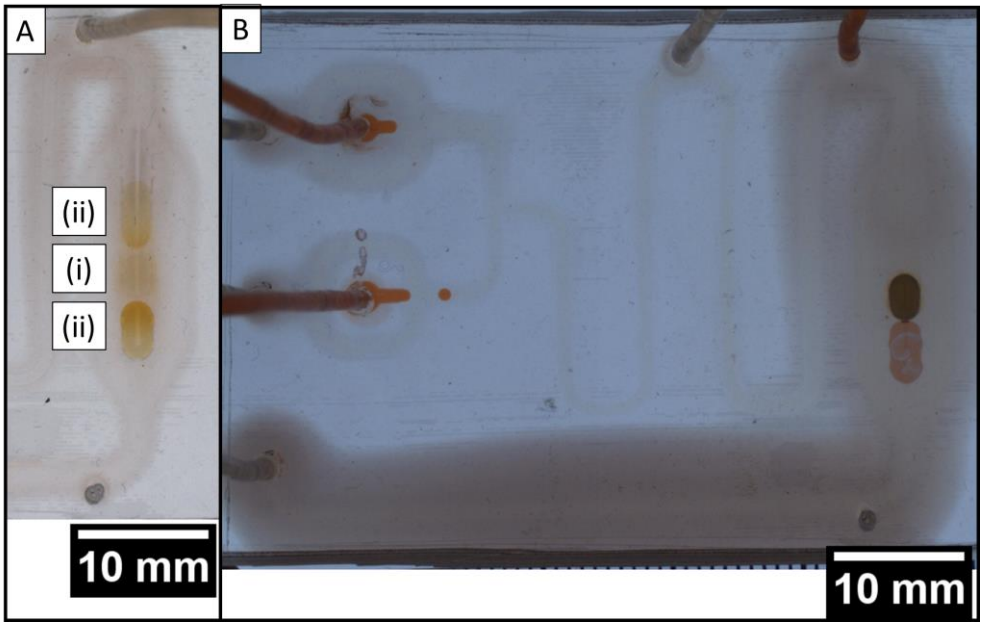

Figure 8.7 Image sequence of bromine-generating droplets on chip and the absorption of bromine and iodine into the PDMS. (A) Bromine-generating droplet marked as (i) sandwiched between KI droplets marked as (ii). KI droplets turn yellow starting from nearest location to bromine-generating droplet. At this stage (i) is almost transparent and the surrounding oil has little colour from bromine due to PDMS absorption. (ii) is not coloured as deeply as in previous experiments in petri dishes despite similar volume and concentrations used due to loss of bromine as well. (B) Chip exposed to both bromine and iodine shows absorption of in PDMS. Colour especially dark starting from extra inlet 2 where bromine-generating droplets initiated. Droplets are 2.5 mm wide in all images.

Chapter 9 Conclusion

In this project, compartmentalisation of the BZ reaction medium in linear and more complex droplet-in-oil arrays was realised and coupling between droplet compartments was comprehensively evaluated. This work will contribute to the eventual goal of using droplet-in-oil networks for unconventional computing. In the continuous effort to develop new substrates and components to make computing more efficient in different applications, this work provides insight into the possibilities of structuring and controlling the BZ reaction in these droplet-in-oil networks to inspire future applications. It also shows the versatility of the droplet-in-oil system in changing the physical scale to accommodate smaller and larger devices as well as scalability in production, as it can take advantage of existing micro and nanofabrication techniques. The achievements are summarised as follows:

1. BZ droplets confirmed to oscillate and are stable in arrays in this environment and can be observed and analysed over a long time without evaporation effects.
2. Using droplets of larger size than literature allows wave patterns to be analysed.
3. Different phases in oscillation lifetime analysed. These phases are common to droplets of different compositions.
4. Effects of changing individual BZ components on the wave characteristics are statistically analysed in single isolated droplets and can be applied to control characteristics for applications in experiments.
5. Effects of coupling BZ are characterised. Droplets of different compositions are stable in arrays when coupled despite differences in concentration. Wave pattern significantly affected by droplet neighbour's lifetime, but no wave propagation through interfaces is observed. Also, no significant effect on wave characteristics observed from coupling with different neighbours.
6. Developed MA-CHD BZ composition to form droplets with waves that consistently propagate through interfaces and with significantly shorter induction time than pure CHD BZ.
7. MA-CHD BZ droplets tested in large arrays with junctions confirms this method is stable even in large arrays and shows unique behaviours caused by topology.

8. Initial work on using droplets of other compositions to control BZ behaviour is done, which is made possible due to droplet-in-oil structure as opposed to homogeneous free solution.
9. Initial work on testing BZ in millifluidic PDMS chips for future automation showed BZ can be mixed on chip, positioned in stable arrays and oscillate with similar behaviours as in oil structured with PMMA.

By using the droplet-in-oil technique, the properties of individual droplets placed in specific positions can be preserved unlike in continuous systems, which fully mix all the components into a homogeneous solution. Droplets could also be observed for much longer periods without the need for stirrers and other apparatus that may disrupt the observations. As the droplets are under oil, evaporation of the aqueous solution is prevented so the droplet composition and behaviours are not disturbed. This allowed these droplets to be observed over several hours until they were exhausted. By combining this with the rapid prototyping of complex array designs using the laser cutting technique, a high volume of repeatable experiments can be performed over long periods. This in turn allowed different topologies and arrays using different droplets at different locations to be tested. When combined with automated image processing macros, the large number of repeat experiments also allowed some statistical analysis of their data. These macros conveniently simplified the images into space-time plots, which could be converted into pixel intensity graphs for analysis.

Observing droplets of millimetre scale gave insight into the variety of wave patterns that can be found as well as its changes over time. This is in contrast to smaller micrometre scale droplets, which usually only have an oxidised or reduced state with no observable patterns inside the droplet itself. Additionally, observing the time evolution of the wave patterns showed that droplets of different composition predictably change between different phases in the oscillation lifetime with distinct wave behaviours. These behaviours were numerically analysed and graphed to show that the characteristics of each wave measurement change over time as well. It is observed that droplets undergo an initial phase, which can form higher frequency waves with a variety of patterns including spiral waves. These then stabilise into the middle phase, where the droplets stay in a lower frequency behaviour that gradually decreases in frequency over time. The droplets then enter a late phase where they suddenly have a significantly higher wave frequency, but this

also slowly reduces over time. Eventually the droplet enters the exhausted phase where it stops oscillating and waves are no longer seen. During this entire process, the red reduced background of the droplet slowly becomes more transparent so the contrast of the wave reduces. These properties are all reflected in the graphs of each wave characteristic over time in Section 4.4, which showed relationships that were not apparent without this additional processing such as how the area under the peaks increased over the oscillation lifetime.

The wave patterns are also evaluated during these observations. Spiral waves are observed to form both clockwise and anticlockwise varieties, whose centres "meander" in the opposite direction of the wave patterns. Spiral patterns suddenly "disappear" when the droplet enters the middle phase, and it is observed that the first planar waves formed in this state have their wave source near the original spiral wave source as well. In addition, the planar waves initially have a high frequency but this quickly reduces to the stabilised frequency. "Reverse" varieties of planar and circular waves can also be formed at the later stages of the droplet's lifetime, where these waves are curved away from the wave source.

This information allowed the characteristics of droplets of different compositions to be evaluated and wave patterns to be predicted when specific components are changed. It is found that when H_2SO_4 is increased in concentration the droplets increase in frequency and the total wave count slightly increases while other properties such as amplitude and lifetime are reduced. $NaBrO_3$ increases the frequency, but is found to reduce the lifetime of the droplet and amplitude of each peak. Malonic acid uniquely increases the total wave count and hence the lifetime without as significantly changing the frequency or amplitude. This is corroborated by the $NaBrO_3$ experiment in Figure 5.1, which shows that if the malonic acid concentration is held constant the total wave count is also constant despite increasing $NaBrO_3$. Ferroin is found to reduce the frequency when its concentration is increased while at the same time reducing the droplet lifetime and total wave count while increasing the wave amplitude, which is the opposite effect of the previous components. It is also observed that the $NaBrO_3$ concentration is a limiting factor in the composition used, such that if the concentration is too low, the effects of increasing malonic acid are no longer observed. The plots of different wave characteristics also showed unique trends for each parameter as well. The frequency and amplitude characteristics correspond to similar trends for the studies conducted in BZ of homogeneous aqueous solution in existing

literature, though existing literature did not tend to analyse individual peaks over such a long period of time or until the solutions become fully exhausted.

When pure malonic acid BZ droplets are coupled in arrays, it is found that the BZ arrays are stable even when the concentrations of $NaBrO_3$, malonic acid and ferroin are changed. Fusions are usually only observed in the initial hour of the experiment, after which the remaining droplet interfaces remain stable for several hours. In addition, a significant change in wave pattern is observed. While single droplets usually have waves that start from random positions at PMMA walls or the middle of the droplet, coupled droplets have a higher probability of having wave sources at the droplet interfaces. Waves do not reliably propagate through the interface for significant distances. However, it is observed that the droplets oscillate independently, such that oscillations would randomly go in and out of phase and is indistinguishable from two uncoupled droplets. Statistical analysis of these coupled droplets showed no significant differences in trends for the wave characteristics. Analysis of arrays using different droplet lifetimes in Section 6.2 showed that interfaces with droplets of a longer lifetime consistently act as the preferred wave source where more than one droplet interface is present.

This was solved using the MA-CHD BZ mixture, which formed waves that propagate reliably through all interfaces. These droplets have similar phases as those in the pure malonic acid BZ droplets, except that they have additional complex oscillation behaviour especially before the late phase and emit benzoquinone and hydroquinone once exhausted. The conclusions on the chemicals emitted were made based on analysis in Figure 7.3 (B) and literature [71]. These turn the oil a dark colour but do not significantly affect the BZ wave behaviour. These droplets can also propagate waves through interfaces with MA BZ droplets, but it is observed that only droplets with a direct interface with the MA-CHD droplet have this effect, and not the entire array. Long 20-droplet arrays showed waves are still able to travel through the entire length. It is also observed that only droplets in the middle phase can propagate waves, whereas droplets in other phases cannot have waves propagate through the interfaces at all, which is an interesting observation that is worth exploring to gain further insight in the BZ reaction mechanism.

This is expanded to non-linear Y-shaped arrays in Section 7.5, which have meeting points consisting of three droplets coupling to three linear arrays at the same time. These

experiments concluded that the waves can be split from one path to two and that these waves travel through the entire length of the array in the same way. However, the meeting points are also observed to form unique behaviours, as the droplets have slightly different oscillation, refractory and excitable times. This allows the droplets to excite each other and oscillate in a “spiral” pattern resulting from each compartment being slightly out of phase at the interfaces but otherwise acting as a continuous solution once inside. These meeting points can then act as wave sources as these oscillations are a significantly higher frequency that other self-oscillations due to each droplet exciting each other the moment it is possibly excitable.

In Section 7.5, the limits of this technology are then explored by using these droplets in a maze array, which showed that very large arrays consisting of 399 droplets could be formed and remained stable for several hours. The versatility of the laser cutting rapid prototyping technique is also demonstrated with the “fish” structure. By using multiple layered PMMA structures, it is possible to form freestanding structures normally impossible with the laser cutting technique. These freestanding structures enabled loop arrays to be formed, which allowed the waves to interact with earlier positions as “feedback” into itself. This demonstrates the versatility of the laser cutting method for the definition of droplet network topology.

Initial efforts are made to couple other droplets with BZ to control its behaviour. This is impossible in fully mixed free solutions and is significantly easier to control using this method structuring droplets-in-oil. By using initiator droplets of a lower ferroin concentration as in Section 7.6, those regions acted as wave sources due to the higher frequency of those droplets. Unique behaviours are also discovered such as the “over-excited” state, which is where a droplet coupled with the initiator droplet achieves the same high frequency as the initiator droplet but is unable to transfer waves through the bilayer to the rest of the array similar to droplets in the initial or late phases. Further investigation could yield new insight into the BZ reaction mechanism. H_2SO_4 mixed with $NaBrO_3$ also able to initiate droplets, but only the first wave initiated goes through the entire array, with the directly coupled droplets becoming “over-excited” droplets after this. H_2O_2 is stable in arrays only when mixed with BZ droplets and effectively inhibits of the droplet, creating regions where waves cannot propagate through. This is especially useful as the region propagates through subsequent interfaces in the array. Bromine gas

producing droplets are found to form a dark precipitate at the aqueous-oil interface but with little effect on the wave behaviour. It is also incompatible for use with asolectin in hexadecane oil as the asolectin reacts to form a dark brown precipitate and reduce the range of the bromine gas. Moreover, these droplets are unstable when coupled in arrays.

Finally, for the eventual goal of automating the droplet generating and structuring process, initial work is done on using MA BZ droplets in a PDMS microfluidic chip in Chapter 8. These efforts showed that arrays of different compositions can be mixed and positioned accurately in situ. The significant problem of CO_2 gas bubble formation inside such devices was also mitigated by using a higher PDMS to curing agent ratio for chip manufacture. In this case, arrays of up to 4 BZ droplets are tested and observed until they are exhausted, where coupling is the same as for standard MA BZ droplets of the same composition, i.e. with waves from the droplet interface without wave propagation.

A publication is to be submitted titled “Towards Functional Droplet Architectures: a Belousov-Zhabotinsky Medium for Networks” discussing the behaviour of MA and MA-CHD BZ droplets in arrays from this project. A future publication is also planned to discuss the observation of BZ droplet arrays inside the millifluidic chip. A manuscript was prepared discussing the laser cutting and droplet-in-oil techniques of this project to test an alternative method of chemical computing using bromine and iodine gas under oil. Bromine and iodine gas was used under oil to cause colour changes in potassium iodide and starch droplets and signalling cascade reactions. This was published as “Fabricating millifluidic reaction-diffusion devices: Droplet-in-oil networks structured by laser cutting” in the 2016 IEEE Symposium Series on Computational Intelligence (SSCI) [167]. This paper was then presented in the IEEE SSCI conference in Athens, Greece in December 2016. A short summary of this work is included in Appendix C.

Other compartmentalisation methodologies and reactions were also investigated and are included in the Appendices. Initial work was done to structure BZ solution inside laser-cut fibreglass networks with complex topology and with different BZ compositions. Enzymes were also tested as a computing substrate using the glucose oxidase and horseradish peroxidase reaction, forming colour changes both in fibreglass and as coupled droplets-in-oil.

The characterisation work of the BZ droplets of different composition in these different topologies allows insight into how future unconventional computing devices can function using the droplet-in-oil system. These behaviours can allow for the design and control of more accurate devices in the future using these substrates, but also give further understanding into the coupling of other systems. When combining the rapid prototyping technologies discussed with an even greater variety of droplet compositions and automated processes, interactions that are even more interesting can be explored for use in this field. It is hoped that these efforts will help advance the field for more detailed studies for the eventual development of an unconventional computing device using droplet-in-oil technology.

List of References

[1] J. Holley, A. Adamatzky, L. Bull, B. De Lacy Costello, and I. Jahan, "Computational modalities of Belousov–Zhabotinsky encapsulated vesicles," *Nano Communication Networks,* vol. 2, pp. 50-61, 2011.

[2] S. Thutupalli, S. Herminghaus, and R. Seemann, "Bilayer membranes in micro-fluidics: from gel emulsions to soft functional devices," *Soft Matter,* vol. 7, pp. 1312-1320, 2011.

[3] P. A. Merolla, J. V. Arthur, R. Alvarez-Icaza, A. S. Cassidy, J. Sawada, F. Akopyan*, et al.*, "Artificial brains. A million spiking-neuron integrated circuit with a scalable communication network and interface," *Science,* vol. 345, pp. 668-73, 2014.

[4] P. Dittrich, "Chemical Computing," in *Unconventional Programming Paradigms*. vol. 3566, J.-P. Banâtre, P. Fradet, J.-L. Giavitto, and O. Michel, Eds., ed: Springer Berlin Heidelberg, 2005, pp. 19-32.

[5] E. Katz, *Biomolecular Information Processing: From Logic Systems to Smart Sensors and Actuators*: Wiley, 2013.

[6] E. Katz, "Biocomputing - tools, aims, perspectives," *Curr Opin Biotechnol,* vol. 34, pp. 202-8, 2015.

[7] M. J. Booth, V. Restrepo Schild, F. G. Downs, and H. Bayley, "Functional aqueous droplet networks," *Mol Biosyst,* vol. 13, pp. 1658-1691, 2017.

[8] J. Gorecki, J. N. Gorecka, Y. Igarashi, and K. Yoshikawa, "Information Processing with Structured Chemical Excitable Medium," in *Natural Computing*. vol. 1, Y. Suzuki, M. Hagiya, H. Umeo, and A. Adamatzky, Eds., ed: Springer Japan, 2009, pp. 48-69.

[9] K. Torbensen, S. Ristori, F. Rossi, and A. Abou-Hassan, "Tuning the Chemical Communication of Oscillating Microdroplets by Means of Membrane Composition," *Journal of Physical Chemistry C,* vol. 121, pp. 13256-13264, 2017.

[10] K. Torbensen, F. Rossi, S. Ristori, and A. Abou-Hassan, "Chemical communication and dynamics of droplet emulsions in networks of Belousov-Zhabotinsky micro-oscillators produced by microfluidics," *Lab on a Chip,* vol. 17, pp. 1179-1189, 2017.

[11] L. Gyorgyi, T. Turanyi, and R. J. Field, "Mechanistic Details of the Oscillatory Belousov-Zhabotinskii Reaction," *Journal of Physical Chemistry,* vol. 94, pp. 7162-7170, 1990.

[12] I. R. Epstein, "Coupled chemical oscillators and emergent system properties," *Chem Commun (Camb),* vol. 50, pp. 10758-67, 2014.

[13] A. M. Zhabotinsky, "A history of chemical oscillations and waves," *Chaos,* vol. 1, pp. 379-386, 1991.

[14] V. K. Vanag and I. R. Epstein, "Pattern formation in a tunable medium: the Belousov-Zhabotinsky reaction in an aerosol OT microemulsion," *Phys Rev Lett,* vol. 87, p. 228301, 2001.

[15] V. Horvath, P. L. Gentili, V. K. Vanag, and I. R. Epstein, "Pulse-coupled chemical oscillators with time delay," *Angew Chem Int Ed Engl,* vol. 51, pp. 6878-81, 2012.

[16] S. Weiss and R. D. Deegan, "Weakly and strongly coupled Belousov-Zhabotinsky patterns," *Phys Rev E,* vol. 95, p. 022215, 2017.

[17] A. Toth and K. Showalter, "Logic Gates in Excitable Media," *Journal of Chemical Physics,* vol. 103, pp. 2058-2066, 1995.

[18] A. A. Cherkashin, V. K. Vanag, and I. R. Epstein, "Discontinuously propagating waves in the bathoferroin-catalyzed Belousov-Zhabotinsky reaction incorporated into a microemulsion," *J Chem Phys,* vol. 128, p. 204508, 2008.

[19] O. Steinbock, P. Kettunen, and K. Showalter, "Chemical wave logic gates," *Journal of Physical Chemistry,* vol. 100, pp. 18970-18975, 1996.

[20] J. Holley, I. Jahan, B. De Lacey Costello, L. Bull, and A. Adamatzky, "Logical and arithmetic circuits in Belousov-Zhabotinsky encapsulated disks," *Phys Rev E Stat Nonlin Soft Matter Phys,* vol. 84, p. 056110, 2011.

[21] J. Guzowski, K. Gizynski, J. Gorecki, and P. Garstecki, "Microfluidic platform for reproducible self-assembly of chemically communicating droplet networks with predesigned number and type of the communicating compartments," *Lab Chip,* vol. 16, pp. 764-72, 2016.

[22] P. H. King, G. Jones, H. Morgan, M. R. R. de Planque, and K.-P. Zauner, "Interdroplet bilayer arrays in millifluidic droplet traps from 3D-printed moulds," *Lab on a Chip,* vol. 14, pp. 722-9, 2014.

[23] S. H. Jo, T. Chang, I. Ebong, B. B. Bhadviya, P. Mazumder, and W. Lu, "Nanoscale memristor device as synapse in neuromorphic systems," *Nano Lett,* vol. 10, pp. 1297-301, 2010.

[24] J. Greenman, I. Ieropoulos, and C. Melhuish, "Perfusion anodophile biofilm electrodes and their potential for computing," *From Utopian to Genuine Unconventional Computers,* p. 67, 2006.

[25] T. Nakagaki, H. Yamada, and A. Toth, "Intelligence: Maze-solving by an amoeboid organism," *Nature,* vol. 407, pp. 470-470, 2000.

[26] A. Adamatzky, "Route 20, Autobahn 7, and Slime Mold: Approximating the Longest Roads in USA and Germany With Slime Mold on 3-D Terrains," *IEEE Trans Cybern,* vol. 44, pp. 126-36, 2014.

[27] S. Basu, Y. Gerchman, C. H. Collins, F. H. Arnold, and R. Weiss, "A synthetic multicellular system for programmed pattern formation," *Nature,* vol. 434, pp. 1130-4, 2005.

[28] M. Amos, "Population-based microbial computing: a third wave of synthetic biology?," *International Journal of General Systems,* vol. 43, pp. 770-782, 2014.

[29] X. Zhang, Q. Wang, A. Adamatzky, F. T. S. Chan, S. Mahadevan, and Y. Deng, "An Improved *Physarum polycephalum* Algorithm for the Shortest Path Problem," *The Scientific World Journal,* vol. 2014, p. 9, 2014.

[30] S. Tsuda, M. Aono, and Y. P. Gunji, "Robust and emergent *Physarum* logical-computing," *Biosystems,* vol. 73, pp. 45-55, 2004.

[31] S. Tsuda, K.-P. Zauner, and Y.-P. Gunji, "Robot Control: From Silicon Circuitry to Cells," in *Biologically Inspired Approaches to Advanced Information Technology*. vol. 3853, A. Ijspeert, T. Masuzawa, and S. Kusumoto, Eds., ed: Springer Berlin Heidelberg, 2006, pp. 20-32.

[32] O. Feinerman, A. Rotem, and E. Moses, "Reliable neuronal logic devices from patterned hippocampal cultures," *Nature Physics,* vol. 4, pp. 967-973, 2008.

[33] M. Yu, Y. Huang, J. Ballweg, H. Shin, M. Huang, D. E. Savage*, et al.*, "Semiconductor nanomembrane tubes: three-dimensional confinement for controlled neurite outgrowth," *ACS Nano,* vol. 5, pp. 2447-57, 2011.

[34] L. M. Adleman, "Molecular computation of solutions to combinatorial problems," *Science,* vol. 266, pp. 1021-4, 1994.

[35] E. Shapiro and Y. Benenson, "Bringing DNA computers to life," *Scientific American,* vol. 294, pp. 44-51, 2006.

[36] A. E. Friedland, T. K. Lu, X. Wang, D. Shi, G. Church, and J. J. Collins, "Synthetic gene networks that count," *Science,* vol. 324, pp. 1199-202, 2009.

[37] E. Winfree, F. Liu, L. A. Wenzler, and N. C. Seeman, "Design and self-assembly of two-dimensional DNA crystals," *Nature,* vol. 394, pp. 539-44, 1998.

[38] Y. Benenson, "Biomolecular computing systems: principles, progress and potential," *Nat Rev Genet,* vol. 13, pp. 455-68, 2012.

[39] N. Goldman, P. Bertone, S. Chen, C. Dessimoz, E. M. LeProust, B. Sipos*, et al.*, "Towards practical, high-capacity, low-maintenance information storage in synthesized DNA," *Nature,* vol. 494, pp. 77-80, 2013.

[40] R. A. Copeland, *Enzymes: A Practical Introduction to Structure, Mechanism, and Data Analysis*: Wiley, 2004.

[41] B. D. Hames and N. M. Hooper, *Biochemistry*: Garland Science, 2011.

[42] E. Katz and V. Privman, "Enzyme-based logic systems for information processing," *Chem Soc Rev,* vol. 39, pp. 1835-57, 2010.

[43] R. de la Rica and M. M. Stevens, "Plasmonic ELISA for the ultrasensitive detection of disease biomarkers with the naked eye," *Nat Nanotechnol,* vol. 7, pp. 821-4, 2012.

[44] G. Strack, M. Ornatska, M. Pita, and E. Katz, "Biocomputing security system: concatenated enzyme-based logic gates operating as a biomolecular keypad lock," *J Am Chem Soc,* vol. 130, pp. 4234-5, 2008.

[45] T. K. Tam, M. Pita, M. Ornatska, and E. Katz, "Biofuel cell controlled by enzyme logic network — Approaching physiologically regulated devices," *Bioelectrochemistry,* vol. 76, pp. 4-9, 2009.

[46] Y. Elani, R. V. Law, and O. Ces, "Vesicle-based artificial cells as chemical microreactors with spatially segregated reaction pathways," *Nat Commun,* vol. 5, p. 5305, 2014.

[47] A. Adamatzky, B. De Lacy Costello, and T. Asai, *Reaction-Diffusion Computers*: Elsevier Science, 2005.

[48] A. Adamatzky and B. De Lacy Costello, "Experimental logical gates in a reaction-diffusion medium: the XOR gate and beyond," *Phys Rev E Stat Nonlin Soft Matter Phys,* vol. 66, p. 046112, 2002.

[49] D. Margulies, C. E. Felder, G. Melman, and A. Shanzer, "A molecular keypad lock: a photochemical device capable of authorizing password entries," *J Am Chem Soc,* vol. 129, pp. 347-54, 2007.

[50] S. Rochat and K. Severin, "Pattern-based sensing with metal-dye complexes: sensor arrays versus dynamic combinatorial libraries," *J Comb Chem,* vol. 12, pp. 595-9, 2010.

[51] M. P. Nikitin, V. O. Shipunova, S. M. Deyev, and P. I. Nikitin, "Biocomputing based on particle disassembly," *Nat Nanotechnol,* vol. 9, pp. 716-22, 2014.

[52] A. M. Turing, "The Chemical Basis of Morphogenesis," *Philosophical Transactions of the Royal Society of London. Series B, Biological Sciences,* vol. 237, pp. 37-72, 1952.

[53] D. Tolmachiev and A. Adamatzky, "Chemical processor for computation of Voronoi diagram," *Advanced Materials for Optics and Electronics,* vol. 6, pp. 191-196, 1996.

[54] R. J. Field, "Limit cycle oscillations in the reversible Oregonator," *The Journal of Chemical Physics,* vol. 63, pp. 2289-2296, 1975.

[55] S. W. Wright, "Tick Tock, a Vitamin C Clock," *Journal of Chemical Education,* vol. 79, p. 40A, 2002.

[56] I. R. Epstein and K. Showalter, "Nonlinear Chemical Dynamics: Oscillations, Patterns, and Chaos," *The Journal of Physical Chemistry,* vol. 100, pp. 13132-13147, 1996.

[57] K. J. Lee, W. D. McCormick, Q. Ouyang, and H. L. Swinney, "Pattern formation by interacting chemical fronts," *Science,* vol. 261, pp. 192-4, 1993.

[58] V. K. Vanag and I. R. Epstein, "Design and control of patterns in reaction-diffusion systems," *Chaos,* vol. 18, p. 026107, 2008.

[59] H. Haken, "Self-organization," *Scholarpedia,* vol. 3, p. 1401, 2008.

[60] I. R. Epstein, J. A. Pojman, and O. Steinbock, "Introduction: Self-organization in nonequilibrium chemical systems," *Chaos,* vol. 16, p. 037101, 2006.

[61] D. Lebender and F. W. Schneider, "Logical Gates Using a Nonlinear Chemical Reaction," *Journal of Physical Chemistry,* vol. 98, pp. 7533-7537, 1994.

[62] A. Zhabotinsky, "Belousov-Zhabotinsky reaction," *Scholarpedia,* vol. 2, p. 1435, 2007.

[63] W. Jahnke and A. T. Winfree, "Recipes for Belousov-Zhabotinsky Reagents," *Journal of Chemical Education,* vol. 68, pp. 320-324, 1991.

[64] D. Suzuki and R. Yoshida, "Effect of initial substrate concentration of the Belousov-Zhabotinsky reaction on self-oscillation for microgel system," *J Phys Chem B,* vol. 112, pp. 12618-24, 2008.

[65] R. Yoshida, S. Onodera, T. Yamaguchi, and E. Kokufuta, "Aspects of the Belousov–Zhabotinsky Reaction in Polymer Gels," *The Journal of Physical Chemistry A,* vol. 103, pp. 8573-8578, 1999.

[66] E. Koros and M. Orban, "Uncatalysed oscillatory chemical reactions," *Nature,* vol. 273, pp. 371-372, 1978.

[67] C. Luengviriya, J. Luengviriya, M. Sutthiopad, P. Porjai, B. Tomapatanaget, and S. C. Muller, "Excitability of the ferroin-catalyzed Belousov-Zhabotinsky reaction with pyrogallol," *Chemical Physics Letters,* vol. 561, pp. 170-174, 2013.

[68] A. T. Winfree, "The Prehistory of the Belousov-Zhabotinsky Oscillator," *Journal of Chemical Education,* vol. 61, pp. 661-663, 1984.

[69] K. Kurin-Csörgei, A. M. Zhabotinsky, M. Orbán, and I. R. Epstein, "Bromate−1,4-Cyclohexanedione−Ferroin Gas-Free Oscillating Reaction. 1. Basic Features and Crossing Wave Patterns in a Reaction−Diffusion System without Gel," *The Journal of Physical Chemistry,* vol. 100, pp. 5393-5397, 1996.

[70] K. Kurin-Csörgei, A. M. Zhabotinsky, M. Orbán, and I. R. Epstein, "Photosensitive, Bubble-free, Bromate−1,4-Cyclohexanedione Oscillating Reactions. Illumination Control of Pattern Formation," *The Journal of Physical Chemistry A,* vol. 101, pp. 6827-6829, 1997.

[71] I. Szalai and E. Körös, "The 1,4-Cyclohexanedione−Bromate−Acid Oscillatory System. 3. Detailed Mechanism," *The Journal of Physical Chemistry A,* vol. 102, pp. 6892-6897, 1998.

[72] M. Orban and E. Koros, "Chemical oscillations during the uncatalyzed reaction of aromatic compounds with bromate. 1. Search for chemical oscillators," *The Journal of Physical Chemistry,* vol. 82, pp. 1672-1674, 1978.

[73] R. M. Noyes, R. Field, and E. Koros, "Oscillations in chemical systems. I. Detailed mechanism in a system showing temporal oscillations," *Journal of the American Chemical Society,* vol. 94, pp. 1394-1395, 1972.

[74] R. J. Field, E. Koros, and R. M. Noyes, "Oscillations in chemical systems. II. Thorough analysis of temporal oscillation in the bromate-cerium-malonic acid system," *Journal of the American Chemical Society,* vol. 94, pp. 8649-8664, 1972.

[75] P. M. Wood and J. Ross, "A Quantitative Study of Chemical Waves in the Belousov-Zhabotinsky Reaction," *Journal of Chemical Physics,* vol. 82, pp. 1924-1936, 1985.

[76] T. Biancalani, D. Fanelli, and F. Di Patti, "Stochastic Turing patterns in the Brusselator model," *Phys Rev E Stat Nonlin Soft Matter Phys,* vol. 81, p. 046215, 2010.

[77] P. K. Becker and R. J. Field, "Stationary Concentration Patterns in the Oregonator Model of the Belousov-Zhabotinskii Reaction," *Journal of Physical Chemistry,* vol. 89, pp. 118-128, 1985.

[78] T. Turanyi, L. Gyorgyi, and R. J. Field, "Analysis and simplification of the GTF model of the Belousov-Zhabotinskii reaction," *The Journal of Physical Chemistry,* vol. 97, pp. 1931-1941, 1993.

[79] S. M. Blagojević, S. R. Anić, and Ž. D. Čupić, "Influence of most important radicals on the numerically simulated belousov-zhabotinsky oscillatory reaction under batch conditions," *Russian Journal of Physical Chemistry A,* vol. 85, pp. 2274-2278, 2011.

[80] A.-M. Petrascu, M. H. J. Koch, and H.-D. Försterling, "Effect of Oxygen on the Belousov−Zhabotinsky Reaction at Low Cerium Concentrations," *The Journal of Physical Chemistry A,* vol. 103, pp. 6757-6765, 1999.

[81] A. Cadena, N. Perez, J. S. Agreda, and D. Barragan, "Understanding the induction period of the Belousov-Zhabotinsky reaction," *Journal of the Brazilian Chemical Society,* vol. 16, pp. 214-219, 2005.

[82] R. J. Field and F. W. Schneider, "Oscillating Chemical-Reactions and Nonlinear Dynamics," *Journal of Chemical Education,* vol. 66, pp. 195-204, 1989.

[83] P. Ruoff, "Phase Response Relationships of the Closed Bromide-Perturbed Belousov-Zhabotinsky Reaction - Evidence of Bromide Control of the Free Oscillating State without Use of a Bromide-Detecting Device," *Journal of Physical Chemistry,* vol. 88, pp. 2851-2857, 1984.

[84] P. Ruoff, H. D. Foersterling, L. Gyorgyi, and R. M. Noyes, "Bromous acid perturbations in the Belousov-Zhabotinskii reaction: experiments and model calculations of phase response curves," *The Journal of Physical Chemistry,* vol. 95, pp. 9314-9320, 1991.

[85] E. Kőrös, M. Burger, V. Friedrich, L. Ladányi, Z. Nagy, and M. Orbán, "Chemistry of Belousov-type oscillating reactions," *Faraday Symp. Chem. Soc.,* vol. 9, pp. 28-37, 1974.

[86] K. P. Zauner, "Molecular information technology," *Critical Reviews in Solid State and Materials Sciences,* vol. 30, pp. 33-69, 2005.

[87] V. A. Vavilin, A. M. Zhabotinsky, and A. N. Zaikin, "A study of a self–oscillatory chemical reaction I. The autonomous system," in *Biological and Biochemical Oscillators*, A. K. Ghosh, E. K. Pye, and B. Hess, Eds., ed: Academic Press, 1973, pp. 71-79.

[88] M. Toiya, V. K. Vanag, and I. R. Epstein, "Diffusively coupled chemical oscillators in a microfluidic assembly," *Angew Chem Int Ed Engl,* vol. 47, pp. 7753-5, 2008.

[89] M. D. Eager, M. Santos, M. Dolnik, A. M. Zhabotinsky, K. Kustin, and I. R. Epstein, "Dependence of Wave Speed on Acidity and Initial Bromate Concentration in the Belousov-Zhabotinsky Reaction-Diffusion System," *Journal of Physical Chemistry,* vol. 98, pp. 10750-10755, 1994.

[90] V. K. Vanag and D. P. Melikhov, "Asymmetrical Concentration Fluctuations in the Autocatalytic Bromate-Bromide-Catalyst Reaction and in the Oscillatory Belousov-Zhabotinsky Reaction in Closed Reactor - Stirring Effects," *Journal of Physical Chemistry,* vol. 99, pp. 17372-17379, 1995.

[91] M. Menzinger and P. Jankowski, "Concentration fluctuations and stirring effects in the Belousov-Zhabotinskii reaction," *The Journal of Physical Chemistry,* vol. 94, pp. 4123-4126, 1990.

[92] A. F. Taylor, B. R. Johnson, and S. K. Scott, "Effect of oxygen on wave propagation in the ferroin-catalysed Belousov-Zhabotinsky reaction," *Journal of the Chemical Society-Faraday Transactions,* vol. 94, pp. 1029-1033, 1998.

[93] Z. Noszticzius, "Non-bromide(1-) ion-controlled oscillations in the Belousov-Zhabotinskii reaction of malonic acid," *Journal of the American Chemical Society,* vol. 101, pp. 3660-3663, 1979.

[94] R. J. Kaner and I. R. Epstein, "Induction and inhibition of chemical oscillations by iodide ion in the Belousov-Zhabotinskii reaction," *Journal of the American Chemical Society,* vol. 100, pp. 4073-4079, 1978.

[95] H. Ševčíková, I. Schreiber, and M. Marek, "Dynamics of Oxidation Belousov−Zhabotinsky Waves in an Electric Field†," *The Journal of Physical Chemistry,* vol. 100, pp. 19153-19164, 1996.

[96] H. Okano and H. Kitahata, "Modulation of the shape and speed of a chemical wave in an unstirred Belousov-Zhabotinsky reaction by a rotating magnet," *Bioelectromagnetics,* vol. 34, pp. 220-30, 2013.

[97] R. Toth, V. Gaspar, A. Belmonte, M. C. O'Connell, A. Taylor, and S. K. Scott, "Wave initiation in the ferroin-catalysed Belousov-Zhabotinsky reaction with visible light," *Physical Chemistry Chemical Physics,* vol. 2, pp. 413-416, 2000.

[98] J. Szymanski, J. Gorecki, and M. J. B. Hauser, "Chemo-Mechanical Coupling in Reactive Droplets," *Journal of Physical Chemistry C,* vol. 117, pp. 13080-13086, 2013.

[99] B. D. L. Costello, I. Jahan, M. Ahearn, J. Holley, L. Bull, and A. Adamatzky, "Initiation of waves in BZ encapsulated vesicles using light-towards design of computing architectures," *arXiv preprint arXiv:1212.2244,* 2012.

[100] C. Peralta, C. Frank, A. Zaharakis, C. Cammalleri, M. Testa, S. Chaterpaul*, et al.*, "Controlled excitations of the Belousov-Zhabotinsky reaction: Experimental procedures," *J Phys Chem A,* vol. 110, pp. 12145-9, 2006.

[101] A. Koseska, E. Volkov, and J. Kurths, "Parameter mismatches and oscillation death in coupled oscillators," *Chaos,* vol. 20, p. 023132, 2010.

[102] K. Bar-Eli, "Oscillations death revisited; coupling of identical chemical oscillators," *Phys Chem Chem Phys,* vol. 13, pp. 11606-14, 2011.

[103] J. Wang and Y. Chen, "Collective reaction behavior of an oscillating system coupled with an excitable reaction," *J Chem Phys,* vol. 124, p. 234502, 2006.

[104] M. L. Turco Liveri, R. Lombardo, M. Masia, G. Calvaruso, and M. Rustici, "Role of the Reactor Geometry in the Onset of Transient Chaos in an Unstirred Belousov−Zhabotinsky System," *The Journal of Physical Chemistry A,* vol. 107, pp. 4834-4837, 2003.

[105] A. Cadena, D. Barragan, and J. Agreda, "Bursting in the Belousov-Zhabotinsky Reaction Added with Phenol in a Batch Reactor," *Journal of the Brazilian Chemical Society,* vol. 24, pp. 2028-2032, 2013.

[106] E. J. Heilweil, M. J. Henchman, and I. R. Epstein, "Sequential Oscillations in Mixed-Substrate Belousov-Zhabotinskii Systems," *Journal of the American Chemical Society,* vol. 101, pp. 3698-3700, 1979.

[107] R. P. Rastogi, I. Das, and A. Sharma, "Sequential Oscillations in the Belousov-Zhabotinski System with Ascorbic Acid-Acetone Cyclohexanone as the Mixed Organic Substrate," *Journal of the Chemical Society-Faraday Transactions I,* vol. 85, pp. 2011-2019, 1989.

[108] R. J. Field and R. M. Noyes, "Oscillations in chemical systems. V. Quantitative explanation of band migration in the Belousov-Zhabotinskii reaction," *Journal of the American Chemical Society,* vol. 96, pp. 2001-2006, 1974.

[109] J. Jorne, "Role of Diffusion in Trigger Wave-Propagation in the Belousov-Zhabotinskii Reaction," *Journal of the American Chemical Society,* vol. 102, pp. 6196-6198, 1980.

[110] I. R. Epstein and V. K. Vanag, "Complex patterns in reactive microemulsions: self-organized nanostructures?," *Chaos,* vol. 15, p. 047510, 2005.

[111] A. S. Mikhailov and K. Showalter, "Control of waves, patterns and turbulence in chemical systems," *Physics Reports-Review Section of Physics Letters,* vol. 425, pp. 79-194, 2006.

[112] M. Bär and M. Eiswirth, "Turbulence due to spiral breakup in a continuous excitable medium," *Physical Review E,* vol. 48, pp. R1635-R1637, 1993.

[113] B. Marts, K. Martinez, and A. L. Lin, "Front dynamics in an oscillatory bistable Belousov-Zhabotinsky chemical reaction," *Phys Rev E Stat Nonlin Soft Matter Phys,* vol. 70, p. 056223, 2004.

[114] M. Marek, P. Kastanek, and S. C. Muller, "Ring-Shaped Waves of Inhibition in the Belousov-Zhabotinsky Reaction," *Journal of Physical Chemistry,* vol. 98, pp. 7452-7454, 1994.

[115] C. T. Hamik and O. Steinbock, "Excitation waves in reaction-diffusion media with non-monotonic dispersion relations," *New Journal of Physics,* vol. 5, p. 58, 2003.

[116] C. T. Hamik, N. Manz, and O. Steinbock, "Anomalous Dispersion and Attractive Pulse Interaction in the 1,4-Cyclohexanedione Belousov–Zhabotinsky Reaction," *The Journal of Physical Chemistry A,* vol. 105, pp. 6144-6153, 2001.

[117] P. H. King, C. H. Abraham, K.-P. Zauner, and M. R. R. de Planque, "Excitability Modulation of Oscillating Media in 3D-Printed Structures," *Artificial Life,* vol. 21, pp. 225-33, 2015.

[118] T. Ichino, T. Asahi, H. Kitahata, N. Magome, K. Agladze, and K. Yoshikawa, "Microfreight delivered by chemical waves," *Journal of Physical Chemistry C,* vol. 112, pp. 3032-3035, 2008.

[119] F. Sakamoto and K. Miyakawa, "Asymmetric spatiotemporal patterns of reduction waves in the Belousov-Zhabotinsky reaction," *Journal of the Physical Society of Japan,* vol. 70, pp. 2263-2266, 2001.

[120] S. Maeda, Y. Hara, R. Yoshida, and S. Hashimoto, "Control of the dynamic motion of a gel actuator driven by the Belousov-Zhabotinsky reaction," *Macromolecular Rapid Communications,* vol. 29, pp. 401-405, 2008.

[121] R. Yoshida, T. Takahashi, T. Yamaguchi, and H. Ichijo, "Self-oscillating gel," *Journal of the American Chemical Society,* vol. 118, pp. 5134-5135, 1996.

[122] R. Yoshida and T. Ueki, "Evolution of self-oscillating polymer gels as autonomous polymer systems," *Npg Asia Materials,* vol. 6, p. e107, 2014.

[123] S. Maeda, Y. Hara, R. Yoshida, and S. Hashimoto, "Chemical robot; Design of self-walking gel," in *Intelligent Robots and Systems, 2007. IROS 2007. IEEE/RSJ International Conference on*, 2007, pp. 2150-2155.

[124] J. Gorecki, K. Yoshikawa, and Y. Igarashi, "On chemical reactors that can count," *Journal of Physical Chemistry A,* vol. 107, pp. 1664-1669, 2003.

[125] H. Nagahara, T. Ichino, and K. Yoshikawa, "Direction detector on an excitable field: field computation with coincidence detection," *Phys Rev E Stat Nonlin Soft Matter Phys,* vol. 70, p. 036221, 2004.

[126] H. Kitahata, A. Yamada, S. Nakata, and T. Ichino, "Propagation of photosensitive chemical waves on the circular routes," *J Phys Chem A,* vol. 109, pp. 4973-8, 2005.

[127] B. de Lacy Costello, R. Toth, C. Stone, A. Adamatzky, and L. Bull, "Implementation of glider guns in the light-sensitive Belousov-Zhabotinsky medium," *Phys Rev E Stat Nonlin Soft Matter Phys,* vol. 79, p. 026114, 2009.

[128] E. Villar Álvarez, J. Carballido-Landeira, J. Guiu-Souto, P. Taboada, and A. P. Muñuzuri, "Modulation of volume fraction results in different kinetic effects in Belousov–Zhabotinsky reaction confined in AOT-reverse microemulsion," *The Journal of Chemical Physics,* vol. 134, p. 094512, 2011.

[129] V. K. Vanag and D. V. Boulanov, "Behavior of the Belousov-Zhabotinskii Oscillator in Reverse Micelles of AOT in Octane," *Journal of Physical Chemistry,* vol. 98, pp. 1449-1453, 1994.

[130] A. Kaminaga, V. K. Vanag, and I. R. Epstein, "Wavelength halving in a transition between standing waves and traveling waves," *Physical Review Letters,* vol. 95, p. 058302, 2005.

[131] M. Toiya, H. O. González-Ochoa, V. K. Vanag, S. Fraden, and I. R. Epstein, "Synchronization of Chemical Micro-oscillators," *Journal of Physical Chemistry Letters,* vol. 1, pp. 1241-1246, 2010.

[132] N. Tompkins, N. Li, C. Girabawe, M. Heymann, G. B. Ermentrout, I. R. Epstein*, et al.*, "Testing Turing's theory of morphogenesis in chemical cells," *Proc Natl Acad Sci U S A,* vol. 111, pp. 4397-402, 2014.

[133] J. Gorecki, K. Gizynski, J. Guzowski, J. N. Gorecka, P. Garstecki, G. Gruenert*, et al.*, "Chemical computing with reaction-diffusion processes," *Philos Trans A Math Phys Eng Sci,* vol. 373, 2015.

[134] N. Tompkins, M. C. Cambria, A. L. Wang, M. Heymann, and S. Fraden, "Creation and perturbation of planar networks of chemical oscillators," *Chaos,* vol. 25, p. 064611, 2015.

[135] J. Guzowski and P. Garstecki, "Droplet clusters: exploring the phase space of soft mesoscale atoms," *Phys Rev Lett,* vol. 114, p. 188302, 2015.

[136] K. M. Doll, K. E. Vermillion, G. F. Fanta, and Z. Liu, "Diffusion coefficients of water in biobased hydrogel polymer matrices by nuclear magnetic resonance imaging," *Journal of Applied Polymer Science,* vol. 125, pp. E580-E585, 2012.

[137] S. Odake, K. Hatae, A. Shimada, and S. Iibuchi, "Apparent Diffusion Coefficient of Sodum Chloride in Cubical Agar Gel," *Agricultural and Biological Chemistry,* vol. 54, pp. 2811-2817, 1990.

[138] A. Axelsson and B. Persson, "Determination of effective diffusion coefficients in calcium alginate gel plates with varying yeast cell content," *Applied Biochemistry and Biotechnology,* vol. 18, pp. 231-250, 1988.

[139] G. F. Itamunoala, "Effective Diffusion Coefficients in Calcium Alginate Gel," *Biotechnology Progress,* vol. 3, pp. 115-120, 1987.

[140] I. R. Epstein and B. Xu, "Reaction-diffusion processes at the nano- and microscales," *Nat Nanotechnol,* vol. 11, pp. 312-9, 2016.

[141] S. K. Bathina, "Image Analysis of Compartmentalized Excitable Chemical Media," MSc in Artificial Intelligence, Faculty of Physical and Applied Sciences, University of Southampton, United Kingdom, 2011.

[142] N. Vahabi, "Image Processing for Monitoring Wet Computing Structures," MEng Computer Science With Artificial Intelligence, Faculty of Physical and Applied Sciences, University of Southampton, United Kingdom, 2012.

[143] A. M. Seddon, P. Curnow, and P. J. Booth, "Membrane proteins, lipids and detergents: not just a soap opera," *Biochim Biophys Acta,* vol. 1666, pp. 105-17, 2004.

[144] H. Bayley, B. Cronin, A. Heron, M. A. Holden, W. L. Hwang, R. Syeda*, et al.*, "Droplet interface bilayers," *Mol Biosyst,* vol. 4, pp. 1191-208, 2008.

[145] G. Villar, A. D. Graham, and H. Bayley, "A tissue-like printed material," *Science,* vol. 340, pp. 48-52, 2013.

[146] D. Miller, P. J. Booth, J. M. Seddon, R. H. Templer, R. V. Law, R. Woscholski*, et al.*, "Protocell design through modular compartmentalization," *J R Soc Interface,* vol. 10, p. 20130496, 2013.

[147] M. Jimenez, A. Martos, E. J. Cabre, A. Raso, and G. Rivas, "Giant vesicles: a powerful tool to reconstruct bacterial division assemblies in cell-like compartments," *Environ Microbiol,* vol. 15, pp. 3158-68, 2013.

[148] M. S. Friddin, N. P. Smithers, M. Beaugrand, I. Marcotte, P. T. F. Williamson, H. Morgan*, et al.*, "Single-channel electrophysiology of cell-free expressed ion channels by direct incorporation in lipid bilayers," *Analyst,* vol. 138, pp. 7294-8, 2013.

[149] B. Schlicht and M. Zagnoni, "Droplet-interface-bilayer assays in microfluidic passive networks," *Sci Rep,* vol. 5, p. 9951, 2015.

[150] M. A. Czekalska, T. S. Kaminski, S. Jakiela, K. Tanuj Sapra, H. Bayley, and P. Garstecki, "A droplet microfluidic system for sequential generation of lipid bilayers and transmembrane electrical recordings," *Lab Chip,* vol. 15, pp. 541-8, 2015.

[151] P. Carreras, R. V. Law, N. Brooks, J. M. Seddon, and O. Ces, "Microfluidic generation of droplet interface bilayer networks incorporating real-time size sorting in linear and non-linear configurations," *Biomicrofluidics,* vol. 8, p. 054113, 2014.

[152] X. Niu, S. Gulati, J. B. Edel, and A. J. deMello, "Pillar-induced droplet merging in microfluidic circuits," *Lab on a Chip,* vol. 8, pp. 1837-41, 2008.

[153] T. Wauer, H. Gerlach, S. Mantri, J. Hill, H. Bayley, and K. T. Sapra, "Construction and manipulation of functional three-dimensional droplet networks," *ACS Nano,* vol. 8, pp. 771-9, 2014.

[154] P. H. King, J. C. Corsi, B.-H. Pan, H. Morgan, M. R. R. de Planque, and K.-P. Zauner, "Towards molecular computing: Co-development of microfluidic devices and chemical reaction media," *Biosystems,* vol. 109, pp. 18-23, 2012.

[155] Ridout Plastics Co. Inc. (2018, 23/1/2018). *Chemical Resistance of Plexiglass Acrylic*. Available: http://www.eplastics.com/Plastic/plastics_library/Chemical-Resistance-of-Plexiglass-Acrylic

[156] The Editors of Encyclopædia Britannica. (2018, 8/2/2018). *Membrane*. Available: https://www.britannica.com/science/membrane-biology

[157] B. Balinov, P. Linse, and O. Söderman, "Diffusion of the Dispersed Phase in a Highly Concentrated Emulsion: Emulsion Structure and Film Permeation," *Journal of Colloid and Interface Science,* vol. 182, pp. 539-548, 1996.

[158] G. Jones, J. C. Corsi, P. H. King, H. Morgan, M. R. R. de Planque, and K.-P. Zauner,"Droplet-to-Droplet Communication in the Lipid-Enclosed Belousov-Zhabotinsky Reaction," unpublished.

[159] A. Savitzky and M. J. E. Golay, "Smoothing and Differentiation of Data by Simplified Least Squares Procedures," *Analytical Chemistry,* vol. 36, pp. 1627-1639, 1964.

[160] N. Li, J. Delgado, H. O. Gonzalez-Ochoa, I. R. Epstein, and S. Fraden, "Combined excitatory and inhibitory coupling in a 1-D array of Belousov-Zhabotinsky droplets," *Physical Chemistry Chemical Physics,* vol. 16, pp. 10965-10978, 2014.

[161] I. C. Chen, O. Kuksenok, V. V. Yashin, A. C. Balazs, and K. J. Van Vliet, "Mechanical Resuscitation of Chemical Oscillations in Belousov-Zhabotinsky Gels," *Advanced Functional Materials,* vol. 22, pp. 2535-2541, 2012.

[162] V. Klika and M. Grmela, "Mechano-chemical coupling in Belousov-Zhabotinskii reactions," *J Chem Phys,* vol. 140, p. 124110, 2014.

[163] T. Wilke, M. Schneider, and K. Kleinermanns, "1,4-Hydroquinone is a Hydrogen Reservoir for Fuel Cells and Recyclable via Photocatalytic Water Splitting," *Open Journal of Physical Chemistry,* vol. 03, pp. 97-102, 2013.

[164] F. Samiee, F. N. Pedron, D. A. Estrin, and L. Trevani, "Experimental and Theoretical Study of the High-Temperature UV-Visible Spectra of Aqueous Hydroquinone and 1,4-Benzoquinone," *J Phys Chem B,* vol. 120, pp. 10547-10552, 2016.

[165] S. P. Desai, D. M. Freeman, and J. Voldman, "Plastic masters-rigid templates for soft lithography," *Lab Chip,* vol. 9, pp. 1631-7, 2009.

[166] A. Lamberti, S. L. Marasso, and M. Cocuzza, "PDMS membranes with tunable gas permeability for microfluidic applications," *RSC Advances,* vol. 4, pp. 61415-61419, 2014.

[167] K. M. Chang, M. R. R. de Planque, and K. P. Zauner, "Fabricating millifluidic reaction-diffusion devices: Droplet-in-oil networks structured by laser cutting," in *2016 IEEE Symposium Series on Computational Intelligence (SSCI)*, 2016, pp. 1-7.

Appendix A Detailed petri dish stand schematic

The schematics for the pieces of the petri dish stand are shown in Figure S 1. This apparatus is placed on top of the light source and glass surface protector underneath the camera and is used to keep the petri dish in position with a fixed tilt to allow droplets to fall into position using gravity. The top layers consist of two sheets of PMMA and are used to keep the petri dish centred. The Bottom layer has a smaller diameter hole in the middle to support the petri dish with a 5 mm wide plastic ring under the edge. The bottom layer also has protractor markings and is used in conjunction with the markings on PMMA wafers to ensure they are always aligned with the angle of the tilt. All these layers have holes cut in the corners for the metal weights that hold the setup in position. Metal weights have PDMS cured on the underside to provide friction and a softer surface for contact on the glass surface protector. Tilt rulers are placed underneath the bottom layer sandwiched between the two weights to tilt the setup at a fixed angle, and can be pushed deeper to form a larger tilt. These rulers have markings to measure how deeply they are pushed under the petri dish stand.

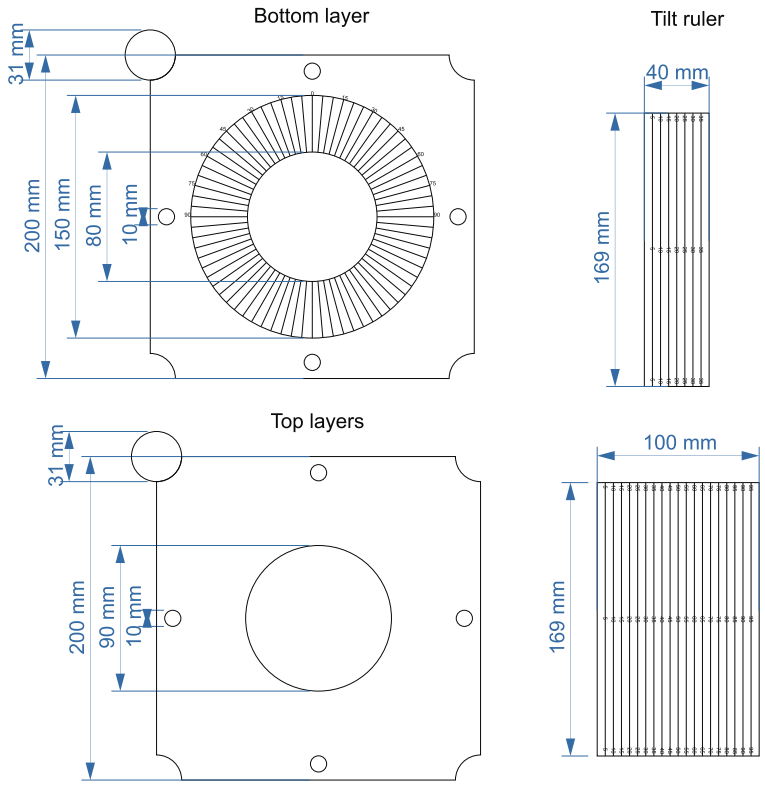

Figure S 1 Petri dish stand schematic.

Appendix B Enzyme experiments

Experiments using enzymes are conducted in fiberglass as well as in droplets as another potential substrate for unconventional computing. The glucose, glucose oxidase (GOx), horseradish peroxidase (HRP) and 2,2'-azino-bis(3-ethylbenzothiazoline-6-sulfonic acid) diammonium salt (ABTS) reaction is used to produce a green colour change.

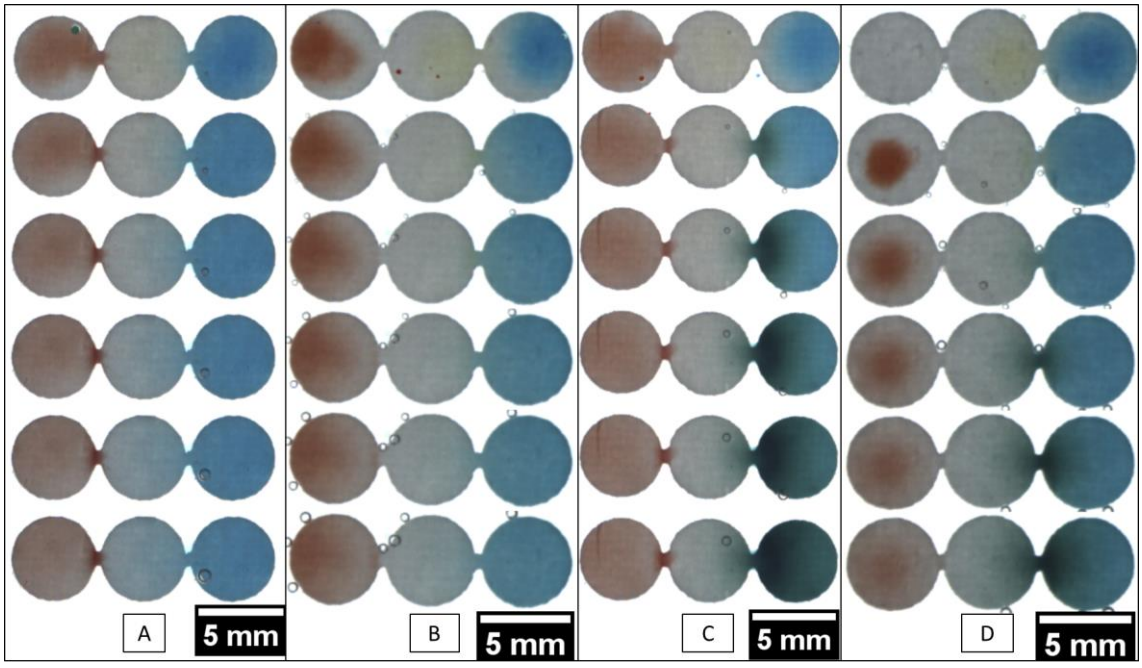

Figure S 2 Enzyme experiments with fiberglass with substrates missing and substrate added at different time. (A) Only dyes added. (B) All substrates except glucose added. (C) All substrates added. Green colour development seen. (D) All substrates added but glucose added 1 hour later. Colour development delayed. All images taken at 1-hour intervals.

In fiberglass, these substrates are used as 250 mM glucose, 2 U/ml of GOx, 2 U/ml HRP and 10 mM ABTS. The solutions are each dyed to distinguish between different substrate solutions. Glucose is dyed with 1 mM Direct Red 23 (red), GOx with quinacrine dihydrochloride (yellow) and HRP with ABTS solution with erioglaucine disodium salt (blue) (all from Sigma Aldrich). This test is conducted in fiberglass of different designs of fiberglass solution sections of 10 mm in size with 5 mm separating channels between them. An optimised size of 5 mm in size with no separating channels is then used. Dyes are also observed to diffuse over time at approximately 1 mm/hour for blue dye and 0.4 mm/hour

for red dye. An experiment was also conducted using NaOH and HCl with fiberglass soaked with universal indicator solution for similar diffusion observations. The results of fiberglass experiments performed with substrates missing and with substrates added at different times are shown in Figure S 2. Similar experiments performed with larger scale fiberglass structures needed at least 10 hours before a significant colour development is observed.

In droplets in the millifluidic chip, these substrates are used as 1 mM glucose, 1 U/ml of GOx, 1 U/ml HRP and 1 mM ABTS. It is observed that glucose cannot pass through the interface to form a colour change when placed in a separate droplet, but H_2O_2 can do so. A significant green colour development can be observed on the chip over 60 minutes. This confirms the literature that glucose is unable to pass through droplet interfaces without α-hemolysin while H_2O_2 is small enough to pass through. The chip tests also show that high concentration H_2O_2 solution cannot be used in microfluidic systems as it produces oxygen gas bubbles that can disrupt the microfluidic flows. Images of these coupled droplets and their space-time plot is shown in Figure S 3.

These initial tests show that enzyme reactions are compatible both in fiberglass, in the millifluidic chip and droplet-in-oil arrays in the asolectin in hexadecane oil system without significant modification. These could be used in the future as another substrate for unconventional computing in these systems.

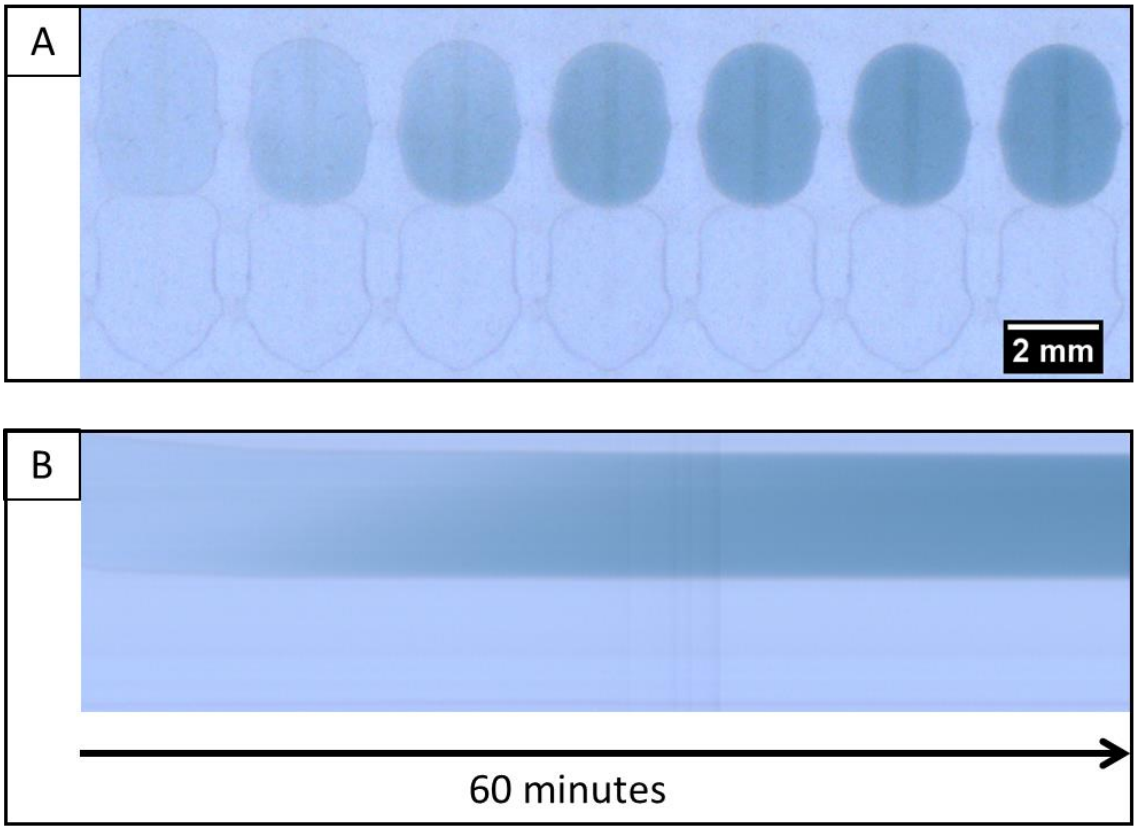

Figure S 3 Photo and space-time plot of enzyme reaction droplets in millifluidic chip. Transparent droplet is a 1 mM H_2O_2 droplet while green droplet contains 1 U/ml HRP and 1 mM ABTS. Green colour development of ABTS seen. Photos taken at 10-minute intervals.

Appendix C BZ in fiberglass

BZ solution is also tested in complex fiberglass topologies. This allowed loop designs to be fabricated without the need for multiple layers of PMMA as in the “fish” design. Fiberglass experiments are performed under hexadecane oil without asolectin. MA-CHD BZ 0.08 M H_2SO_4, 0.56 M NaBrO3, 0.09 M MA, 2 mM ferroin and 0.28 M CHD is typically used, as the normal BZ composition produces waves with too high a frequency to observe and analyse. Examples of topologies tested is shown in Figure S 4.

By using these fiberglass structures under oil, BZ wave patterns can be observed for at least 5 hours to overnight without evaporating. The oil turns yellow due to exposure to MA-CHD BZ, but this does not significantly affect wave patterns. In addition, as the oil has no asolectin additional solution can be added and fused into the existing solution in the fiberglass without forming droplet emulsions or interfaces. However, as the added solutions are not mixed homogenously with the entire structure as it is still constrained by the fiberglass. Biased or unbiased silver wire can also be pushed through the oil to touch the surface of the solution without any obstruction, though care must be taken as the fiberglass is fragile and can be moved if too much force is applied. This is not possible with droplet-in-oil arrays as the interfaces are even more fragile and the array will fuse if force is applied to them.

These structures were tested with both MA BZ and MA-CHD BZ, but with little difference except that the wave width for MA-CHD BZ has a larger width and higher contrast in the low frequency phase. Sometimes waves are observed to disappear while propagating through the fiberglass structure, even though the MA-CHD BZ solution is homogeneous throughout, similar to waves that fail to propagate through interfaces in large droplet arrays. Changing the volume of solution between one section and the other as in the diode design of connected triangles does not prevent wave propagation in any direction BZ is in the low frequency phase with waves of high contrast and large width. However, in the ring structures it is observed that high frequency waves of a low contrast in the initial phase are unable to propagate through these small connections and also do not seem to propagate to the cut edges of the fiberglass. In comparison, lower frequency waves with a higher contrast and wider width are able to propagate.

Using both electrically biased and unbiased silver wire is able to form a high frequency wave source, but these waves have a low contrast and are unable to propagate through small connections similar to waves in the initial phase. When used with only thicker connections it still does not propagate very far through the solution and disappears. This is similar to if BZ solution with higher H_2SO_4 were added to a small section of the fiberglass without allowing the solutions to be mixed homogenously.

When placed in loop topologies the wave pattern produced usually forms a wave source at one point, which propagates in both paths of the loop and interacts at a meeting point. As the wave speed along both directions is not identical, the meeting point can change over time. It is also possible for waves propagating through one path to disappear and stop propagating, allowing the wave in the remaining path to feed back to the wave source and form a clockwise or anti-clockwise wave.

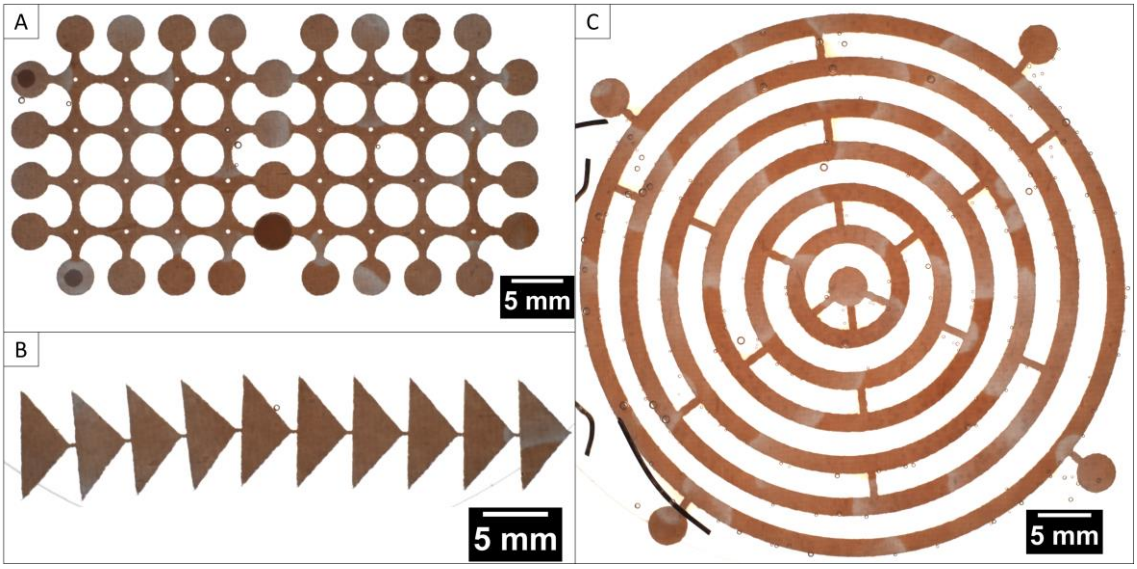

Figure S 4 MA-CHD BZ in fiberglass of different topologies. (A) Loop with many meeting points. Darker circles contain BZ with different concentration of BZ components and change behaviour of BZ in that region. (B) “Diode” type design with significantly larger surface area at one end. (C) Rings with many connections.

Separate pieces of fiberglass soaked with BZ of different composition can be placed on top of a section of the fiberglass topology to change the behaviour there. BZ that is freshly mixed was attempted to be used as wave sources in the top-left and bottom-left of Figure S 4 (A), but the results are inconclusive. Another piece with BZ without H_2SO_4 was placed

in the bottom connector in between both structures. This caused waves to disappear as they propagate through that piece of fiberglass initially. However, as time goes on the wave is able to propagate further and further through this solution without H_2SO_4 as the solution mixes through diffusion. Eventually, the connector is able to propagate waves again.

These initial tests show that fiberglass is compatible with both MA and MA-CHD BZ and can be observed for several hours. These structures can also be interacted with by touching the surface with a silver wire or adding solution through the oil. This shows another substrate where BZ can be used for study in complex topologies.

Appendix D Bromine reaction-diffusion networks

Producing bromine and iodine under the oil allows its flow to be compartmentalised and focused into different parts of millifluidic devices without excessive losses into the atmosphere. While it is incompatible with asolectin in hexadecane oil, droplets in pure hexadecane can be used to produce these halogens to interact with other droplets when they have made contact. This is also the method used to determine if the coloured oil produced with these droplets is bromine and iodine. The same procedure for producing bromine is used as in 6.5, where KBr is substituted with KI if iodine is to be produced. Example experiments shown in Figure S 5. These experiments were published as "Fabricating millifluidic reaction-diffusion devices: Droplet-in-oil networks structured by laser cutting," in the 2016 IEEE Symposium Series on Computational Intelligence (SSCI) [167]. This paper was then presented in the IEEE SSCI conference in Athens, Greece in December 2016.

When bromine is generated under oil, the oil around the droplet turns yellow-orange or brown in colour and propagates away from the droplet. When the bromine makes contact with other droplets it reacts with the chemicals dissolved in the aqueous solution. In the case of DI water, KBr and malonic acid droplets, no colour change is observed. However, if bromine interacts with 1 M KI droplets, the droplets turn yellow. If the bromine is of a high concentration and reacts for a long time, the oil surrounding the KI droplet turns purple, indicating iodine is produced and displaced into the oil.

If iodine is generated the oil is purple instead. When iodine reacts with 10 mg/ml starch droplet in DI water or 1 M KBr solution, the starch droplet turns black, but this reaction is slow and takes at least one hour. If iodine reacts with 1 M KI solution, the KI droplet turns yellow similar to the reaction with bromine, indicating iodine is also displaced. If iodine reacts with 10 mg/ml starch droplet in 1 M KI solution, the starch droplet is observed to turn black much faster.

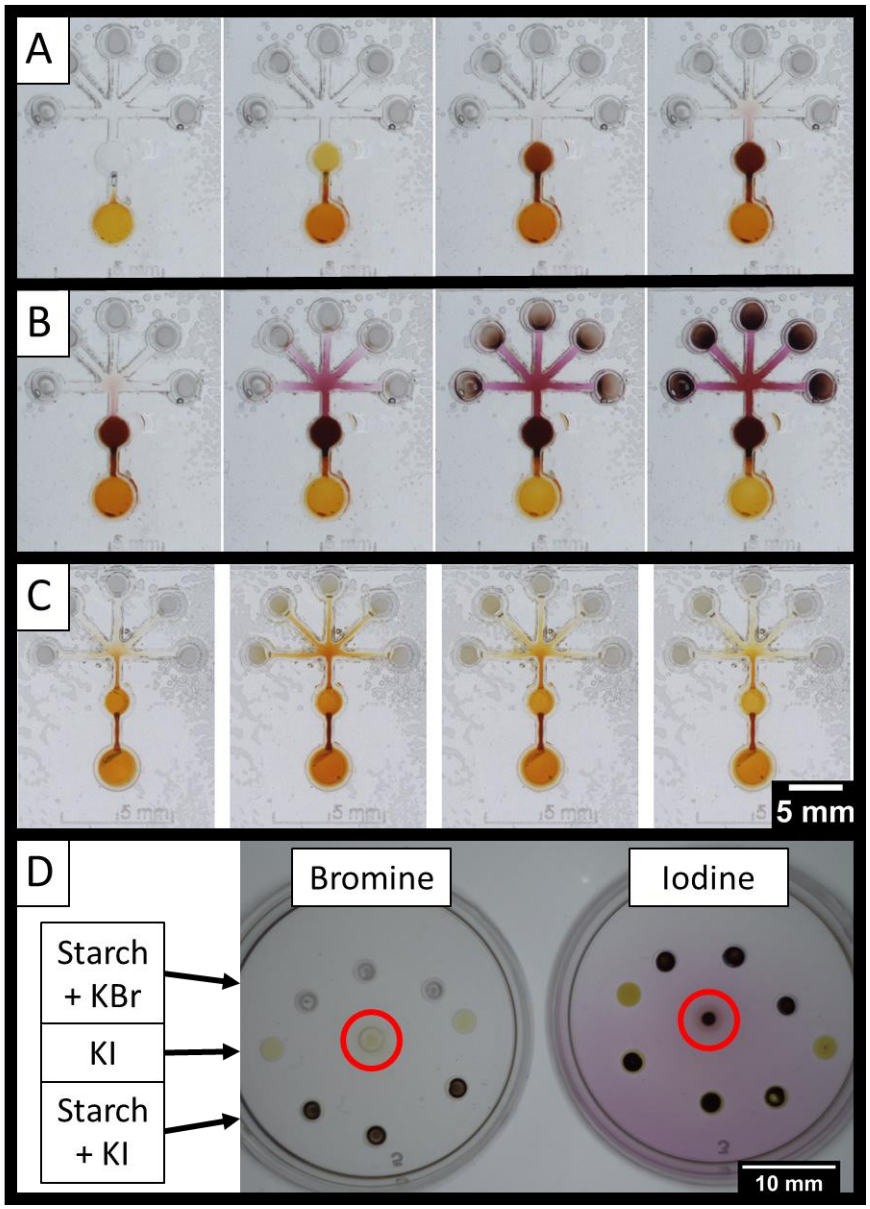

Figure S 5 Signalling cascade reaction network and control tests of reaction bromine and iodine gas under oil. All starch droplets contain 10 mg/ml starch in DI water and all KI and KBr droplets contain 1 M concentration. Images reproduced from [167]. (A) Bromine generated at bottom droplet diffuses and reacts with pure KI droplet forming iodine. Pictures taken at 10-minute intervals. (B) Iodine generated diffuses and reacts with starch droplets in DI water. Pictures taken at 60-minute intervals. (C) Control experiment where bottom and middle droplet both produce bromine, where starch droplets do not turn black. Pictures taken at 60-minute intervals. (D) Control experiment where left petri dish produces bromine and right experiment produces iodine. Only starch droplets with KI turn black in left petri dish, showing different reactions when bromine and iodine are used. Image taken approximately 50 minutes after bromine and iodine generated. Bromine and iodine generating droplets highlighted with red circles.

Laser-cut PMMA is used to structure the oil into a reaction network for the bromine and iodine to diffuse and propagate to the other aqueous droplets. These designs are solvent bonded to a PMMA base to form a liquid-tight seal. Bromine and iodine are observed to stain and damage the PMMA surfaces, but are able to block them from propagating into other channels through the PMMA.

Using these mechanisms, a signalling cascade experiment is performed where bromine is generated and reacted with a KI droplet to produce iodine, which then diffuses and reacts with starch droplets turning it black. If any components are missing from this reaction, the starch colour change cannot occur. This reaction must also occur in sequence, as not enough iodine is produced if the bromine were placed in the middle compartment.

With these experiments, a prototype device using bromine and iodine generating droplets is designed and tested. This demonstrates that complex networks can be fabricated to use these mechanisms to cause unique reactions using the topology of the network.